Effect of a Pressurised CO_2 Environment on Deformation and Failure Behaviour of Type 316H Steel Under Creep Conditions

A thesis submitted to The University of Manchester for the degree of
Doctor of Philosophy
in the Faculty of Science and Engineering
2020

Janis Cakstins

Department of Mechanical, Aerospace and Civil Engineering

Contents

Final word count (estimated by LaTeX): 36,864

Abstract

Stainless steel components in the UK advanced gas-cooled reactors (AGR's) are known to undergo microstructural changes near the surface due to the reactor carbon dioxide environment. Carburisation tends to increase the material's elastic modulus, yield strength and creep resistance and decrease creep ductility. Over the years of operation, small microcracks have been discovered in bifurcation welds that been carburised. R5, the current assessment procedure used for structural integrity assessments, does not consider the effects of carburisation, hence fails to predict creep/creep-fatigue crack initiation. This has led to a simplified approach for assessing such structures. The simplified approach suggests treating the structure as globally homogeneous but with reduced ductility. However, an alternative approach would be to treat the carburised component as a bi-metallic structure consisting of two homogeneous materials with different material properties. This work presents a detailed insight of the effects of carburisation on creep strain and creep damage accumulation, and assesses the validity of the proposed approaches by analytical and finite element modelling. Analytical models have shown that carburisation will lead to increased stress in more creep resistant regions resulting in reduced stress in the bulk section. An analytical solution for a pressurised cylindrical pressure vessel is presented where graded material properties can be implemented for creep lifetime assessment. At the steady state carburisation provide the benefit of reduced creep strain rate and reduced stress triaxiality for internally pressurised carburised cylinders. However, results show that for a small area fraction carburised carburisation cannot extend the time for damage initiation. Finite element models have been used to assess the effects of material being carburised before and after the load application and the impact of bi-metallic assumption. The graded material properties of the carburised layer were found using artificial neural networks that were trained by feeding results from a large-scale Abaqus parametric study. Research has shown material carburisation before the load application can result in either a conservative or non-conservative assessment. Carburisation after the load application shows that the proposed homogeneous assumption will result in a conservative assessment.

Declaration

I declare that this thesis was composed by myself, that the work contained herein is my own except where explicitly stated otherwise in the text, and that no portion of the work referred to in the thesis has been submitted in support of an application for another degree or qualification of this or any other university or other institute of learning.

Copyright

Dedications

To my newborn son Janis and my wife Anna. You are my inspiration, motivation and the love of my life.

To my mum Irena and dad Janis. Without you, your unconditional love and support I would not be the person I am today.

Manam jaundzimušajam dēliņam Jānim un manai sievai Annai. Jūs esat mana iedvesma, motivācija un mūža mīlestība.

Manai mammai Irēnai un tētim Jānim. Bez Jums, Jūsu neviltotās mīlestības un atbalsta es nebūtu tas cilvēks, kas esmu šodien.

Acknowledgements

First and foremost, I would like to express my gratitude to my supervisor Prof. Robert Ainsworth for offering his continuous support and encouragement throughout this project. When I started my PhD, I often felt frustrated with my lack of progress and not fully understanding the topic as much as I should as a postgraduate student. Prof. Ainsworth has always been supportive and willing to offer his help, even with the silliest questions I have asked. He has always been open to new ideas and guided me in the right direction, making me more confident in pursuing independent research. Bob, your guidance has been invaluable!

I am thankful to my supervisor Dr. Meini Su for support. Meini has helped me with preparation for my first conference and always provided constructive feedback on my work.

I want to thank the Centre for Doctoral Training in Materials for Demanding Environment (CDT in M4DE) and EDF Energy for sponsoring this project. CDT in M4DE has given me many opportunities to expand my professional competencies by making me step out of my comfort zone and completing professional training outside my line of work. I want to extend my gratitude to EDF Energy, especially to Marc Chevalier and Dave Dean. Our constructive meetings and your technical assistance have ensured I remain focused and stay on track with my project. I am also grateful to people from EDF Energy R&D, especially Philippe Martinuzzi and Jefri Draup for assisting me at various stages of my PhD.

Many thanks go to Dr. Alan Jappy from Fraser Nash Consultancy for his help on evaluating my work and sharing his concerns regarding my FE models.

Last but not least, I want to thank my wonderful wife Anna for being my sunshine on a rainy day.

List of Figures

List of Tables

Nomenclature

The next list describes all of the abbreviations and symbols that will be later used within the body of the document.

Abbreviations

AGR	Advanced Gas-cooled Reactor
ANN	Artificial neural network
BP	Back propagation
C	Carburising
DCNN	Deep convolution neural network
ENVISINC	Environmental Impact on the Structural Integrity of Nuclear Components
FE	Finite element
FEA	Finite element analysis
FEM	Finite element method
FG	Functionally graded
IS	Inner surface
LM	Levenberg-Marquardt
MDF	Multiaxial ductility factor
ML	Machine learning
NN	Neural network, same as ANN
OS	Outer surface
PC	Pre-carburised

RPROP	Resilient propagation
SH	Strain hardening
SVM	Support vector machine
TH	Time hardening
UTS	Ultimate tensile strength

Greek symbols

$\bar{\dot{\varepsilon}}^c$	Equivalent creep strain rate
$\bar{\sigma}$	Equivalent stress or von Mises stress; in machine learning can indicate mean value
β	Constant
χ	Activation function
$\dot{\rho}$	Radial steady state creep displacement rate
$\dot{\varepsilon}^c, \dot{\varepsilon}^c_{min}$	Minimum creep strain rate
$\dot{\varepsilon}^c_b$	Creep rate of the bulk
$\dot{\varepsilon}^c_c$	Creep rate of the carburised layer
$\dot{\varepsilon}^c_i$	Principal creep strain rates (i = 1, 2, 3 or i = t, r, z in cylindrical coordinates denoting hoop, radial and axial directions respectively)
$\dot{\varepsilon}^c_{ij}$	Creep strain rate tensor
$\dot{\varepsilon}^{in}$	Inelastic strain rate
$\lambda(x)$	Scalar function of position x
ω^c	Creep damage
ω^t	Total damage due to the environment and creep
ω^{env}	Damage due to the environment
ϕ	Some convex function of degree one in σ_{ij}/σ_0
σ	Stress
σ_1	Stress in material 1

σ_2^*	Averaged stress in material 2 with distributed material properties
σ_c	Stress in the carburised layer
σ_h	Hydrostatic stress
σ_i	Principal creep strain rates (i = 1, 2, 3 or i = t, r, z in cylindrical coordinates denoting hoop, radial and axial directions respectively)
σ_0	Reference stress
σ_{ij}	Stress tensor
θ	Temperature
θ_m	Melting temperature
ε_f^*	Multiaxial strain to failure
ε^c	Creep strain
ε_{ij}^c	Creep strain tensor
ε^e	Elastic strain
ε^p	Plastic strain
ε^t	Total strain
ε_c	Total strain in the carburised layer
ε_f	Creep failure strain
ε_L	Lower shelf ductility
ε_U	Upper shelf ductility
$\varepsilon_{f'}$	Intrinsic ductility or the Monkman-Grant constant
a_i	Neural network output of each hidden node
w_i, w_{ij}	Neural network weight factors

Latin symbols

ΔG^o	Gibbs energy
$\dot{D}^c$	Creep energy dissipation rate
$\dot{u}$	Steady state displacement rate

$\mathbf{H}$	Hessian matrix
$\mathbf{J}$	Jacobian matrix
A	Material constant – creep law multiplier
A'	Material constant
A_1, A_2	Creep law multiplier of material 1 or 2 respectively
A_2^*	Averaged creep law multiplier in material 2 with distributed material properties
A_b	Creep law multiplier of the bulk material
A_c	Creep law multiplier of the carburised layer
A_o	Reference creep law multiplier
b	Neural network bias term
B'	Material constant
C	Constant
c	Concentration
C_{MG}	Intrinsic ductility or the Monkman-Grant constant
C_{MMG}	Modified Monkman-Grant constant
D_c	Carbon diffusivity in steel
D_c	Diffusivity of carbon
E	Young's modulus
E_b	Young's modulus of the bulk material
E_c	Young's modulus of the carburised layer
E_{CE}	Cross entropy error function
E_{MSE}	Mean squared error function
J	Diffusion flux
$K(\mathbf{x}_i, \mathbf{x}_j)$	Kernel function
L	Loss function or performance function

loc	Location variable
m	Material constant – exponent; or the number of data points (matrices, vectors)
n	Material constant – creep stress exponent; or the number of data points (matrices, vectors)
P	Applied load
p	Pressure
p_i, p_e	Internal radius and external pressure
Q	Creep activation energy
R	Boltzman's constant
r	Radius
r_i, r_e	Internal radius and external radius
r_{int}	Radius at the interface
S	Surface
S_i	Intermediate output in neural network
S_1, S_2	Area of material 1 or 2 respectively
T	Stress triaxiality, $\sigma_h/\bar{\sigma}$
t	Time
T_0	Reference stress triaxiality
t_f	Time for creep damage initiation
t_f^c	Time for creep damage initiation in carburised material at the surface
t_f^N	Normalised time for damage initiation with respect to the homogeneous model using uniaxial ductility
t_f^{N*}	Normalised time for damage initiation with respect to the homogeneous model using multiaxial ductility
t_c	Time for carburisation to occur
t_{end}	Time at the end of simulation

t_{red}	Redistribution time
V	Volume
z	Neural network output value

Chapter 1

Introduction

1.1 Nuclear power in the UK

The United Kingdom opened its first nuclear power station in the 1950s, and until the present day, the UK's energy market relies on nuclear power as one of the primary power sources. Today nuclear energy supplies about one-fifth of the UK's electricity demand. Nuclear energy is a carbon-free energy source which does not require a daily supply of new fuel compared to conventional fossil fuel energy sources, e.g. gas turbines [1].

The UK in 2008 signed the Climate Change Act [2] which is an ambitious plan to reduce its greenhouse gas emissions by 80% from 1990 levels by 2050 [3]. Considering that the power generation industry contributes a quarter to the total UK's greenhouse gas emissions [3], to achieve this target the UK must make a transition to carbon-neutral energy generation. Additionally, the energy demand is predicted to be increased due to social factors (population growth) and economic factors (GDP growth). Therefore, nuclear energy will play a significant role in supplying the UK's energy market with secure, affordable and carbon-neutral energy to meet the UK's ambition for low-carbon power, economic growth, and account for the ever-growing population.

Currently in the UK there are seven stations operating pairs of advanced gas-cooled reactors (AGRs) and one pressurised water reactor, all operated by EDF Energy. The first AGR started operating in 1976 and the last in 1988 [4]. These reactors have been in service for 30-40 years and now they are approaching the end of their design lifetimes.

To meet the UK's forecasted energy demand and environmental targets it is important to utilise the existing resources efficiently. Hence there is ongoing research to extend the lifetime of the existing reactors as long as the operation remains safe and cost effective [5].

1.2 Advanced Gas-Cooled Reactors

A schematic diagram of the AGR power production process is illustrated in Figure 1.1. The power generation process in AGRs is the same as in any other nuclear power plant where energy is generated by nuclear fission. The reactor core is cooled using gas or water as a coolant, which is then sent to boilers where the heat is transferred to water, which is turned into super-heated steam and is then sent to turbines for power generation [6].

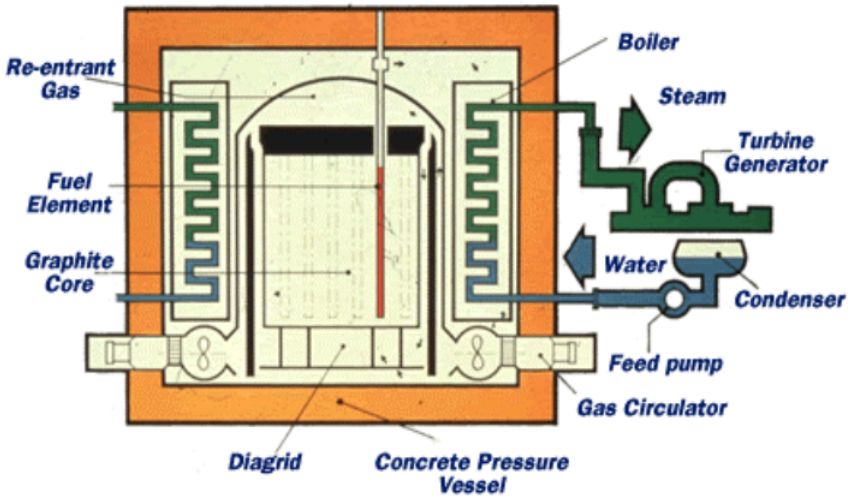

Figure 1.1: A schematic diagram of AGR [6].

The main components of the AGR are the graphite core and the boiler units that are enclosed in a concrete pressure vessel. AGRs use enriched uranium oxide as a fuel source for the nuclear fission process and graphite bricks as a neutron moderator [7]. AGRs are unique to the UK because they use a carbon dioxide rich gas as the primary coolant. Using CO_2 gas, instead of water in light-water reactors, allows operation at higher temperatures. Carbon dioxide leaving the core is at 650^oC and the high temperature gives the power plant an excellent electrical efficiency of ~ 42% [1] [8].

The graphite core is a critical component of the AGR power-plant because, within this component, the nuclear reaction occurs, hence the integrity of the reactor is of paramount importance. The boiler unit is another important component because it removes heat from the cooling agent and produces superheated steam which is sent to the electric turbine for electricity production. Advanced gas-cooled reactors in the UK have two basic boiler arrangements. One is a single cavity arrangement which uses platen boilers (Figure 1.2a) that are positioned around the core. The

[1] In perspective, AGR predecessor MAGNOX reactors operated at 360^oC, with an overall efficiency of < 34%.

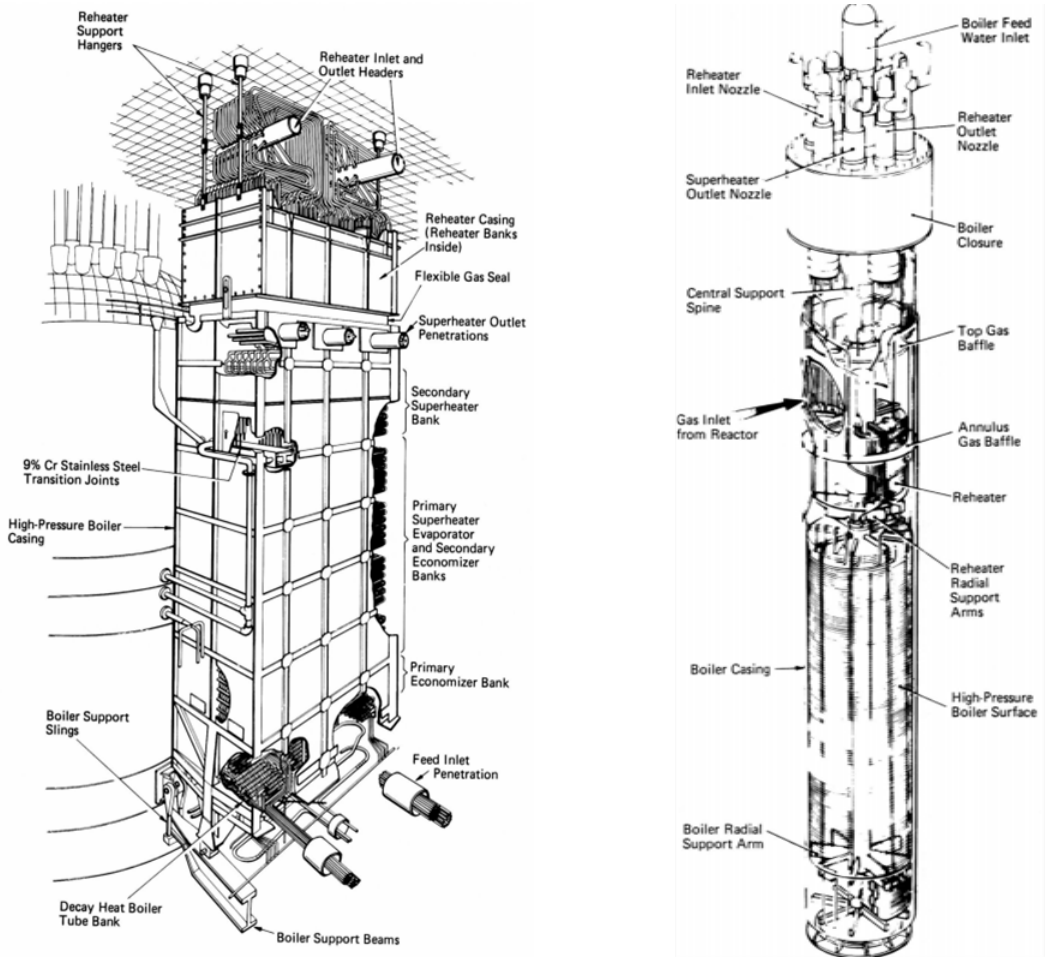

(a) Platen boiler unit; (b) Pod boiler unit.

Figure 1.2: Design of boilers for AGRs, taken directly from [9].

second arrangement uses pod boilers (Figure 1.2b) which are enclosed within the walls of the concrete pressure vessel. AGR boilers operate in counter-flow where the CO_2 coolant gas is cooled by flowing downwards outside the tubes and steam flowing upwards within the tubes [9]. Boilers operate at a temperature up to ~ 650^oC and pressure of ~ 160 bar.

The main materials used in boiler construction are the 300 series austenitic stainless steels (mainly type 316H), Esshete 1250 austenitic stainless steel, and $9\%Cr - 1\%Mo$ ferritic alloy steels. These steels are capable of maintaining desirable mechanical properties at high temperatures. Type 316 stainless steels are used mainly in reheater and secondary superheater, and $9\%Cr$ steels used mainly in the evaporator and primary superheater [9, 10].

In all of the AGRs, the boilers are enclosed in the concrete pressure vessel; hence, boiler inspections can only occur during shutdown periods. Additionally, being located within the concrete pressure vessel makes it difficult or even impossible to replace some of the boiler parts [11]. Considering that the boilers have been in

service for more than 250,000 hours, and operating at high temperatures, certain material problems have arisen during boiler operation.

1.3 Material degradation mechanisms in AGR boilers

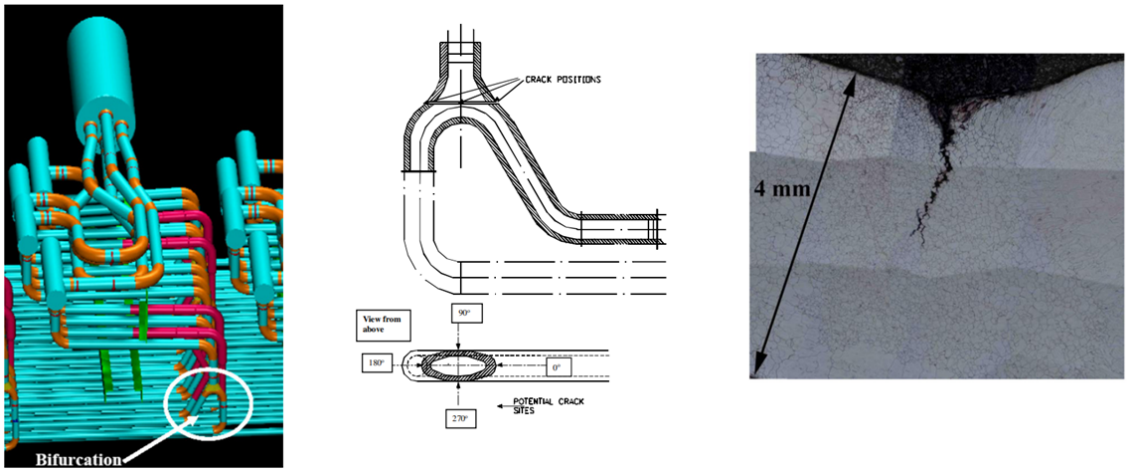

Figure 1.3: Creep-fatigue damage in bifurcation welds, taken directly from [11].

As discussed, boilers operate in a high temperature CO_2 environment over prolonged periods of time. Under such conditions components are prone to several degradation mechanisms:

- Creep and creep-fatigue. Creep is a time dependent deformation mechanism where a material forms voids and microcracks due to prolonged exposure to high-temperature and load. Creep-fatigue is a synergetic degradation of a material due to creep and fatigue (damage due to cyclic load) [11, 12];
- Oxidation. AGR coolant gas is corrosive mixture of carbon dioxide, water vapour, methane, carbon monoxide and hydrogen. Austenitic stainless steels under certain conditions are susceptible to corrosion which results in metal loss [13, 14];
- Carburisation. Exposure to a high temperature corrosive CO_2 environment can give a rise to a hardened carburised layer, which forms due to carbon diffusion into the metal [15];
- Fretting. Fretting is wear of a component (e.g. by contact between components) [16];
- Thermal ageing. Irreversible changes in material, structure of a material exposed to high temperatures [17, 18];

- High cycle fatigue [11].

The impact of carburisation in the AGRs has only been recognised in recent years. Due to advances in defect inspection technologies, there is a capability of detecting microcracks in structures. In 2006, inspections revealed existing microcracks in the bifurcation welds (Figure 1.3) within AGR boilers and tailpipe-pintle welds [19]. A detailed metallographic examination revealed creep dominated crack growth on the carburised surface [11]. A detailed creep and creep-fatigue crack initiation was carried out; however, the results could not predict crack initiation. Therefore, this raised concerns regarding the capability of predicting crack initiation uaing the existing structural integrity assessment procedures [11, 19].

1.4 Assessment procedure for nuclear components and current challenges

There are different assessment methodologies available for evaluating the structural integrity of a component operating at high temperature. The ASME-NH code is used mainly in the USA for design. The RCC-MR design code is used in France. However, in the UK power industry uses the 'R5 Procedures' for structural integrity assessments of the AGRs [20].

The R5 procedure is not a design code but is a best practice guide for performing in-service structural integrity assessment. The procedure contains simplified methods for stress analysis which are a compromise between the pessimism in elastic analysis and the cost and complexity involved in cyclic inelastic computation [21]. R5 is split into a number of volumes which each contain step-by-step instructions to perform an assessment of a component for which the lifetime might be limited by [20–22]:

1. excessive plastic deformation
2. creep rupture;
3. ratcheting or incremental plastic collapse due to a loading sequence;
4. creep deformation enhanced by cyclic load;
5. initiation of cracks in initially defect free material by creep and creep-fatigue mechanisms;
6. the growth of cracks by creep, creep-fatigue mechanisms.

R5 volume 2/3 deals with creep-fatigue crack initiation for defect free structures; volume 4/5 assesses creep-fatigue crack growth; volume 6 consider the performance of dissimilar welds; and volume 7 presents a procedure for the assessment of safe operating life of welded ferritic pipework or vessels [21].

Considering the problem regarding the creep/creep-fatigue crack initiation in tailpipe-pintle welds, it is evident that R5 is not always capable of predicting crack initiation where it occurs. This has caused a concern regarding R5 applicability for austenitic stainless steel component assessment because R5 does not currently consider the potential synergistic effects of the creep-carburisation interaction.

An extensive 3-year research project called: Environmental Impact on the Structural Integrity of Nuclear Components (ENVISINC) had been carried out to investigate the impact of carburisation on stainless steel components. The ENVISINC project aimed to provide an understanding of carburisation and provide an updated R5 Volume 2/3 assessment methodology for carburised components which were not addressed in the previous versions of the assessment procedure [23, 24]. The outcome of the ENVISINC project has been simplified to provide an advice for carburised material treatment within R5 Volume 2/3 assessments. Most of the material testing performed within the scope of the ENVISINC project has been done on already carburised specimens. However, in AGRs, metal is being carburised while the structure is under load. Hence this raises important questions regarding the validity and use of the results obtained in a laboratory setting. Furthermore, from the limited amount of data, it is now proposed to treat carburised structures as homogeneous but with locally reduced creep ductility. Additionally, there is high uncertainty regarding the material properties of the carburised layer and how the mismatch in material properties could influence the structural integrity assessment. Therefore, in order to improve the current understanding of the synergistic effects of creep and carburisation and provide advice for the treatment of components containing carburised material, there is a need for more detailed research.

1.5 Research Aims and Objectives

The research aims and objectives of this project are summarised below.

1.5.1 Aims

- Investigate the mechanical response of components and specimens with a carburised layer during both steady-state creep and the stress redistribution phase in terms of stress, stress state and global and local creep deformation.
- Investigate the impact of material pre-treatment and property distribution on

ductility measurements and creep damage calculation.

- Provide bounds for the conditions under which a carburised layer could extend/reduce the time to creep damage initiation, and when an analysis using homogeneous properties is a reasonable assumption.

- Provide advice for structural integrity assessments dealing with carburised structures.

1.5.2 Objectives

- Develop analytical solutions for predicting the effect of distributed creep properties on the local and global creep response for uniaxial conditions and for a pressurised cylinder.

- Produce finite element (FE) models to investigate the response of a functionally graded specimen with predefined material properties, and the response of a specimen where the material properties are changing over time to account for carburisation while being subjected to load.

- Gather data from parametric studies of pre-carburised specimens during the initial (time independent) loading to numerically predict the distributed tensile properties of a carburised layer.

- Perform a FE parametric study considering the creep response of a carburised specimen assuming variability in material properties and from the gathered data develop a model capable of identifying the range of applicability for the treatment of carburisation.

- Perform a creep analysis of a bifurcation weld structure considering the effects of carburisation assuming various distribution profiles. Compare the results to reference model assuming an homogeneous structure but with locally reduced creep ductility.

1.6 Thesis outline

Chapter 2 presents a literature review of the materials creep, carburisation and machine learning methods used in the following chapters. Creep phenomena are considered for creep deformation and failure under uniaxial and multiaxial states of stress. Some creep constitutive equations are presented together with lifetime estimation

laws together with the theory of creep ductility of materials. The environmental-assisted degradation section outlines oxidation and carburisation degradation mechanisms in Type 316H stainless steels. In addition, this outlines the current advice regarding the treatment of a carburised layer in structural integrity assessments. Finally, machine learning concepts such as artificial neural networks and support vector machines are introduced so that the reader is familiar with the research methodology used in Chapter 4.

Chapter 3 presents analytical solutions of creeping carburised structures in the steady state. An energy method solution, based on a proposal by Prof. Ainsworth, derives an inequality which shows that a hardened layer with reduced creep rates leads to globally reduced creep deformation. A steady state solution of a 2-bar model is modified to account for a material property distribution. Finally, an analytical solution of concentric pressurised cylinders is presented where the effects of carburisation on multiaxiality are investigated.

Chapter 4 consists of three studies. The first study considers the effects of carburisation of a 3-D uniaxial specimen based on an actual creep test. The study investigates the effects of material pre-treatment and constructs an argument of how pre-carburisation could lead to over-conservative creep ductility estimates. The second study shows how artificial neural networks can be used to determine carburised layer material properties when sufficient data have been gathered from parametric studies. The third study uses the predicted material properties to perform a parametric study on a uniaxial creep specimen assuming a range of creep material properties. The results from creep analysis are analysed, and machine learning techniques are used to construct a support vector machine classifier capable of identifying the safety bounds of carburised material.

Chapter 5 considers an AGR plant bifurcation weld geometry under internal and external pressure. The bifurcation weld models the effects of carburisation (pre-carburised material and carburising material). The carburising models consider different timescales of carburisation. Additionally, the effects of different carburised layer material property distributions are considered. The carburised model data are compared with the reference (homogeneous) model. Based on the results, conditions under which the creep damage assessment using homogeneous analysis becomes non-conservative are identified.

Chapter 6 provides advice for carburised material testing and carburised structural assessment based on the findings from Chapters 3 – 5.

Chapter 2

Literature review

2.1 Creep phenomena

2.1.1 General remarks

Creep has been observed for centuries in rock and ice sliding. However, it has become more relevant since the industrial revolution, when humans learned how to harness heat and transform it into mechanical energy. For over 100 years scientists and engineers have known that creep phenomena can occur when a material is subjected to constant stress or load over an extended period of time. One of the first scientists who investigated creep phenomena was Percy Phillips [25]. Phillips could not explain why steel wire response did not follow a similar response to rubber. Five years later Andrade [26] set the scene for describing creep phenomena by looking at the viscous flow of various metal wires that were loaded beyond yield. Andrade noticed that the extension becomes viscous and proportional to time and depends on the applied load. A concise historical overview of creep phenomena focused mainly on grain boundary sliding has been provided by Langdon [27].

In most undergraduate courses it is taught that creep is a stress, temperature and time-dependent phenomenon that becomes relevant at elevated temperatures, usually above $0.5\theta_m$ where θ_m is the melting temperature. A major concern of creep is that it can cause catastrophic failure, if sufficient creep strain is accumulated in a structure. In most practical applications above $0.5\theta_m$ creep has to be accounted for, while below $0.5\theta_m$ creep can be neglected. However, in the power industry components can be subjected to complex loading conditions over a prolonged period of time ($> 10^5$ hr), and creep at lower temperatures can not be neglected.

Creep deformation can be addressed at either the microscale — intragranular and intergranular creep deformation; or the macro scale — continuum models for creep deformation. In this report, creep phenomena are addressed at the continuum scale

and an overview of creep deformation under uniaxial as well as multiaxial states of stress is presented.

2.1.2 Creep under uniaxial state of stress

Creep deformation

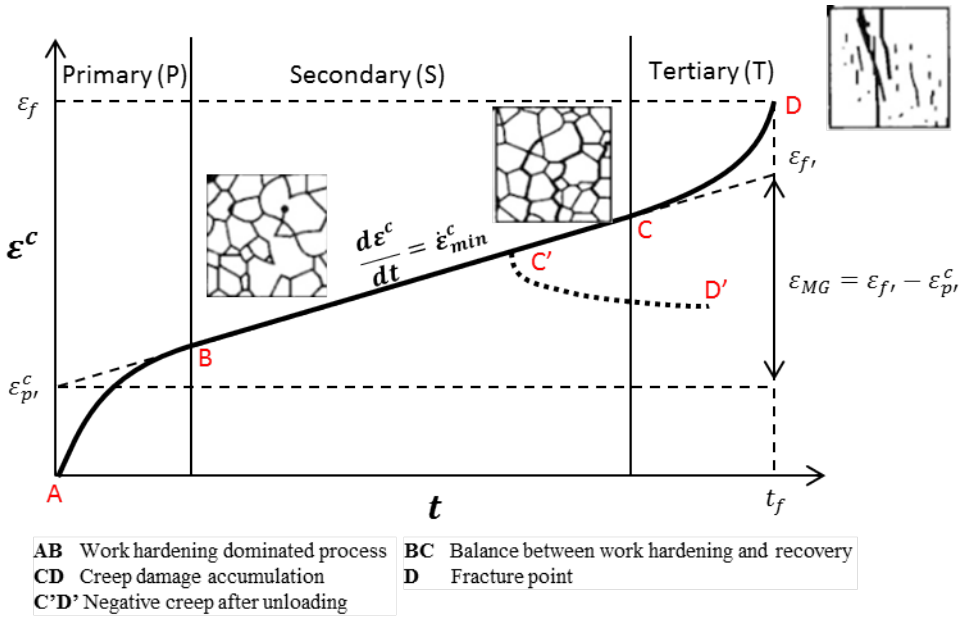

Figure 2.1: A typical creep curve obtained from a standard forward creep test under constant load. Figure adapted from [12]

A typical creep curve is presented in Figure 2.1; such a curve is obtained from a standard creep test when a material specimen is subjected to constant load at a constant temperature over prolonged time. In the laboratory, in order to obtain creep data within a reasonable time, creep is usually accelerated from service conditions by performing tests at either higher temperature or at higher load. From a microstructural viewpoint in a polycrystalline material, such as Type 316H stainless steel, creep occurs due to the motion of dislocations, diffusion of vacancies within grains or at grain boundaries, or due to grain boundary sliding. The dominant mechanism depends on the load and temperature.

The typical creep curve can be split into 3 regions. (1), primary or transient creep (AB), is a work hardening dominated process. The initial point A represents the start of the creep test, when there is no creep strain in the material, but the total strain, ε^t, is the sum of elastic (ε^e) and plastic strain (ε^p), where $\varepsilon^t(t = 0) = \varepsilon^e + \varepsilon^p$. During this stage the creep rate is reducing due to the accumulation of dislocations (work hardening). The reduction of creep rate continues until a balance between work hardening and thermally activated recovery is achieved.

Then follows region (2), secondary or steady creep (BC) during which annealing is in equilibrium with work hardening, and the material starts to develop intergranular damage. Region (3) tertiary or accelerating creep (CD), is a stage during which microstructural damage starts to outweigh work hardening. Microstructural damage leads to necking, voiding, cracking and eventually to failure (D).

Region (3) may also be associated with the reduction of specimen cross-sectional area leading to increased stress in a load-controlled test. If the applied load or stress is released during the test, some creep strain can be recovered (C'D'), this is known as creep recovery, anelasticity or elastic after effect [28]. This occurs because elastic strain is still present in the material from the initial loading [12, 29].

The most common expression used to describe primary and secondary creep is the Bailey-Norton law:

$$\varepsilon^c = A\sigma^n t^m \tag{2.1}$$

where A, m, n are temperature dependent material constants, σ is the applied stress and t is time. The derivative of Eq. 2.1 with respect of time is called the time-hardening (TH) law (Eq. 2.2). This can be used to predict the creep strain of a structure under the variable load of Figure 2.2a (Figure 2.2b). By expressing time as a function of creep rate and creep strain and substituting back into Eq. 2.1 a strain-hardening (SH) law is obtained (Eq. 2.3) [30], leading to the response under variable load in Figure 2.2.

$$\dot{\varepsilon}^c_{TH} = Am\sigma^n t^{m-1} \tag{2.2}$$

$$\dot{\varepsilon}^c_{SH} = mA^{1/m}\sigma^{n/m}\left(\varepsilon^c\right)^{(m-1)/m} \tag{2.3}$$

In practice both TH and SH laws are used, but the SH law has been observed to predict better creep behaviour of metals and polymers compared to the TH law [30, 31].

Other common phenomenological creep laws are the omega model, which is a modified version of the Bailey-Norton law with an added exponential term that can be used to model secondary and tertiary creep [32]; the hyperbolic sine law, used to characterise the creep response over high and low stresses [33]; the theta projection model which has been used to capture all three stages of creep [34, 35]. Nevertheless, the Bailey-Norton creep law is the most widely used phenomenological creep law due to its simplicity. As primary creep for many applications occurs early in the total lifetime, it does not contribute significantly to total strain and can be excluded. Alternatively, the primary creep contribution, ε^c_p in Figure 2.1, can be included in a modified secondary creep law describing the average strain rate. Hence Eq. 2.1 is

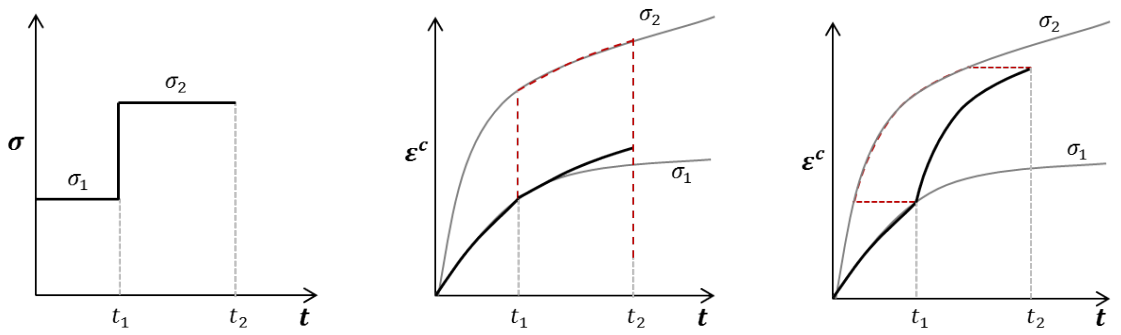

(a) Stress at different time; (b) An example of time-hardening law; (c) An example of strain-hardening law.

Figure 2.2: SH and TH laws for creep strain accumulation.

often simplified to $\varepsilon^c = A\sigma^n t$ by assuming $m = 1$, whic simplifies the TH (Eq. 2.2) and SH (Eq. 2.3) expressions and makes them both equal to $\dot{\varepsilon}^c = A\sigma^n$ [36].

Microstructural mechanisms

At different temperatures and stress levels, different microstructural mechanisms dominate creep deformation. Figure 2.3a shows a generic creep deformation map with most dominant creep deformation mechanisms: grain boundary diffusion (Coble creep); lattice diffusion (Nabarro-Herring creep); dislocation creep and dislocation glide. At high stresses ($\sigma >> \sigma_{0.2}$) dislocation glide is the dominant deformation mechanism. Dislocations move on their active slip planes while other parts of the crystal remain unaltered. Glide is not particularly temperature dependent, hence it is difficult to separate plastic deformation from creep deformation at high stresses.

Usually, creep at high stresses occurs due to a combination of dislocation climb and glide, this is referred to as dislocation creep and is the most relevant mechanism in engineering applications. During dislocation creep ($10^{-5}G < \sigma < 10^{-3}$ and $T > 0.5T_m$) at high stress, dislocations are capable of gliding along their respective slip planes. Dislocation motion is hindered by precipitates and second phase particles, for example, 316H stainless steel contains higher carbon content. Carbon forms carbides that act as obstacles to dislocation movement. However, at higher temperatures due to high thermal energy present in the system, dislocations can move to different slip planes and continue their motion. Dislocation climb is governed by atomic diffusion, and it occurs at a slower rate compared to dislocation motion due to glide. Therefore dislocation climb is the rate-limiting step that controls the creep rate. However, almost all of the accumulated creep strain will be due to dislocation glide [37]. Dislocation creep can be expressed by modifying 2.1 by including an

activation energy for creep:

$$\varepsilon^c = A'\sigma^n \exp\left(\frac{-Q}{R\theta}\right)t^m \tag{2.4}$$

where A' is the creep law multiplier,n is creep stress exponent, Q is creep activation energy, R is Boltzman's constant, and T is temperature.

At high temperatures and low stress, there is not sufficient driving force for dislocations to move around by glide and vacancy (or atom) diffusion becomes the dominant mechanism. At high temperatures when tensile stress is applied to a polycrystalline material, atoms diffuse towards the direction of applied stress. Consequently, vacancies diffuse in the opposite direction (towards compressive stress) towards the grain boundaries [37]. This is called Nabarro-Herring creep [38, 39], and total strain to failure for this type of creep mechanism is lower compared to the dislocation dominated creep mechanism.

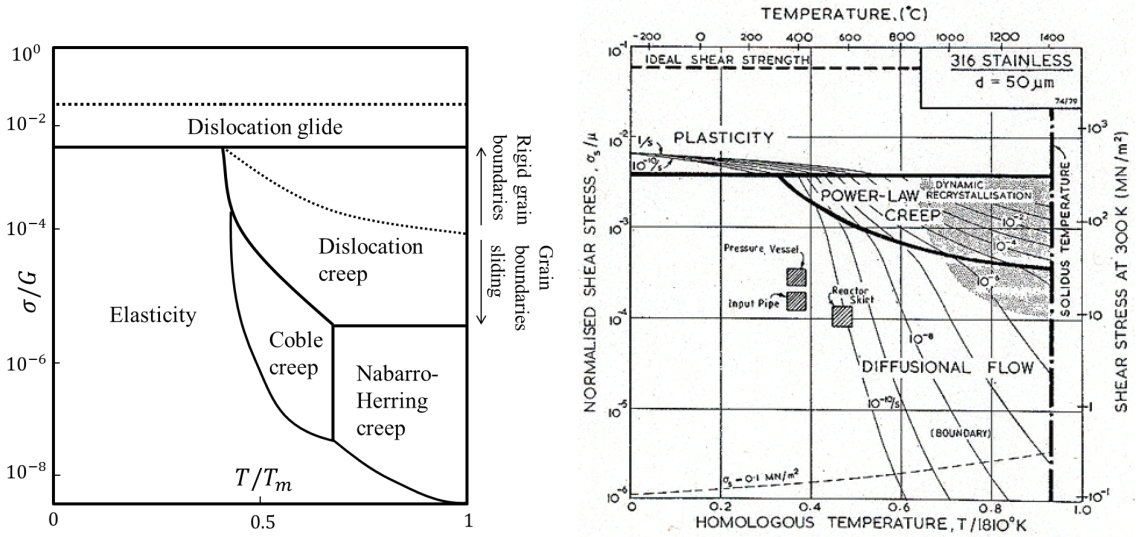

(a) A generic creep deformation map;

(b) Creep deformation map of Type 316 stainless steel [40].

Figure 2.3: Dominant creep mechanisms at various temperatures and stresses.

Coble creep [41] is also a diffusional creep mechanism but compared to Nabarro-Herring creep it is driven by grain boundary diffusion. During Coble creep, diffusion occurs not within the grain, but at the grain boundaries. Grain boundaries are less tightly packed, and vacancies can travel more easily along the grain boundaries than elsewhere when the load is applied. Hence this is preferred deformation mechanism for many materials, such as metals and ceramics at lower stress and lower temperatures.

Grain boundary sliding (GBS) is another mechanism that occurs in polycrystalline materials [27, 42]; it can be regarded as a consequence of other mechanisms

(e.g. Coble or Nabarro-Herring creep) usually due to the vicinity of diffusion. As material deforms due to either stress directed diffusion or dislocation glide and climb, individual grains deform. In order to prevent the deformed grains from leaving voids between them, grain boundary sliding may take place in response to external stress. Grain boundary sliding occurs when two grains slide over each other to remain in contact [39].

Although from a continuum mechanics standpoint creep occurs in any material at any temperature when subjected to load, in practice at low load levels and low temperatures the effects of creep can be neglected. In Figure 2.3a the elasticity region indicates that in that region the response of the material will mainly be elastic and for most applications effects of creep can be ignored. Frost and Ashby [40] constructed creep deformation maps for various metals including nickel, lead and 316 stainless steel. The creep deformation map of 316 is presented in Figure 2.3b.

Creep stress dependence

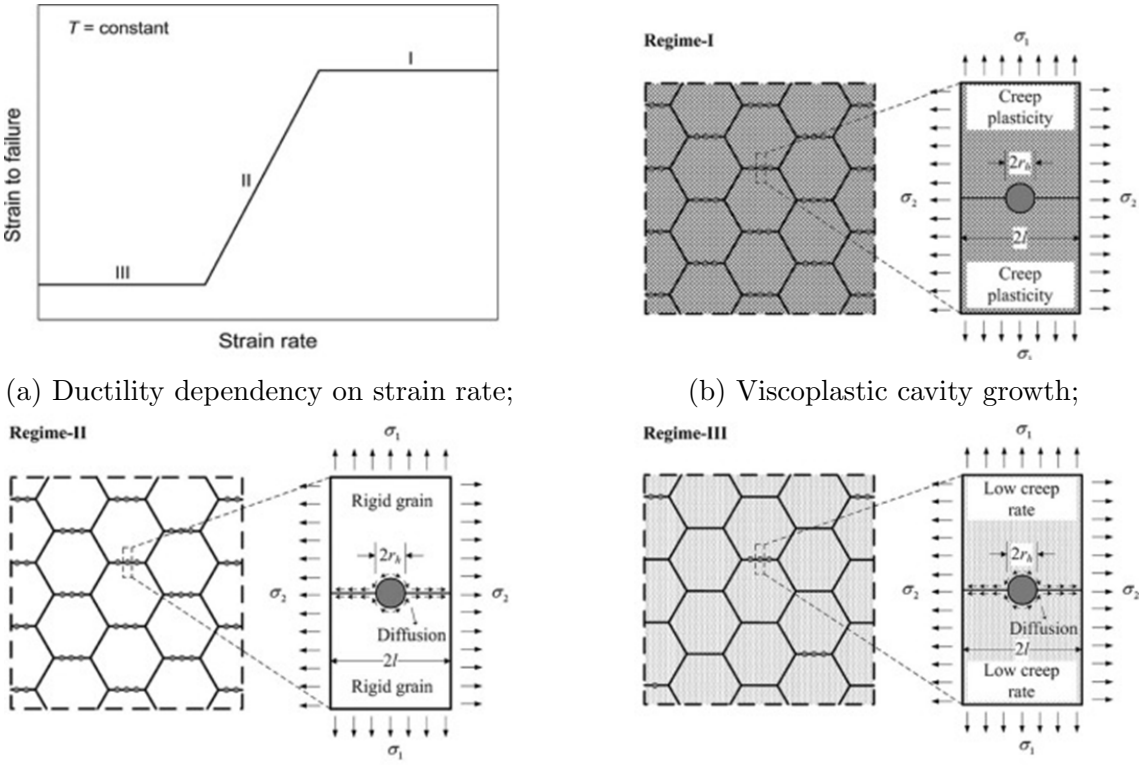

(a) Ductility dependency on strain rate;

(b) Viscoplastic cavity growth;

(c) Diffusion controlled cavity growth;

(d) Constrained diffusion cavity growth.

Figure 2.4: Ductility dependency on strain rate, directly taken from [43]

It is widely accepted that creep fracture is caused by growth and coalescence of voids at grain boundary triple points or by nucleation of cavities. Depending on applied stresses voids can either grow by viscoplastic deformation at higher stresses,

or vacancy diffusion to grain boundaries at lower stresses. Hales [44] provided a schematic representation of three distinct regions which consider strain rate effects on ductility in uniaxial creep specimens. A schematic representation of the three regimes is shown in Figure 2.4a; this shows that at higher creep strain rates (higher stresses) creep ductility has an upper bound value. Creep cavity growth at the upper bound (Regime-I, Figure 2.4b) is controlled by viscoplastic deformation of the surrounding matrix which results in a constant strain to failure. At lower strain rates there is a transition region (Regime-II, 2.4c) where creep ductility drops. In this region, the surrounding matrix is assumed to be rigid, and cavity growth is controlled by vacancy diffusion from the surrounding matrix on the grain boundaries. As the creep strain rate drops the lower bound is reached where the creep strain to failure is independent of applied stress (Regime-III, Figure 2.4d). In this region, the cavitation distribution is assumed to be uniform and non-cavitated area deformation is assumed to be slow enough to constrain the diffusion cavity growth. [43].

Holdsworth [45] proposed a fourth region after investigating creep strains to rupture for ferritic steels. The fourth region is where the strain to rupture starts to increase due to over-aging – changes in the microstructure reduces the rate of cavity nucleation and growth leading to increased ductility [46]. However, any microstructural changes in the metal can influence creep deformation rate. Research on thermal ageing on 316H stainless steel [17] indicate that thermal-aging increase creep deformation rate due to precipitation of second phase particles (carbides), which dissolved in the metal matrix provide resistance to dislocation motion.

Ductility and rupture prediction

Creep failure can be estimated either by time or strain to failure. A common approach is by characterising strain to failure and constructing ductility models that account for various temperatures, stresses and strain rates. There are several empirical ductility models available to describe stress-level effects- the Evans-Wilshire model [47], Trunin-Golobova-Loginov model [43, 48], the Soviet model, Spindler stress modified ductility exhaustion model [49, 50]. The R5 procedure currently uses Spindler's stress modified ductility exhaustion approach:

$$\varepsilon_f = min\left(\varepsilon_U, max\left(\varepsilon_L, \beta_0 \exp\left(\frac{\beta_1}{T}\right)(\dot{\varepsilon}^{in})^{\beta_2}\sigma^{\beta_3}\right)\right) \tag{2.5}$$

where ε_U and ε_L are the upper and lower shelf ductility values (Figure 2.4), σ is the stress, $\dot{\varepsilon}^{in}$ is the inelastic strain rate, $\beta_i\,(i = 1, 2, 3)$ are material constants and T is the temperature. Although the description is empirical by nature, it states that damage is a function of strain rate, stress, and temperature and is hence related to

the mechanistic models outlined in 2.1.2 [51].

The three regimes of 316H stainless steels have been identified from a range of datasets of uniaxial creep tests. Mehmanparast [52, 53] investigated the creep ductility of 316H subjected to various temperatures (550^oC-700^oC). The data for 550^oC was only available at higher stresses. Hence the lower bound ductility was estimated by assuming a similar three regime tendency and extrapolating the data (Figure 2.5a). A simplified ductility model can be fitted to describe the stress level

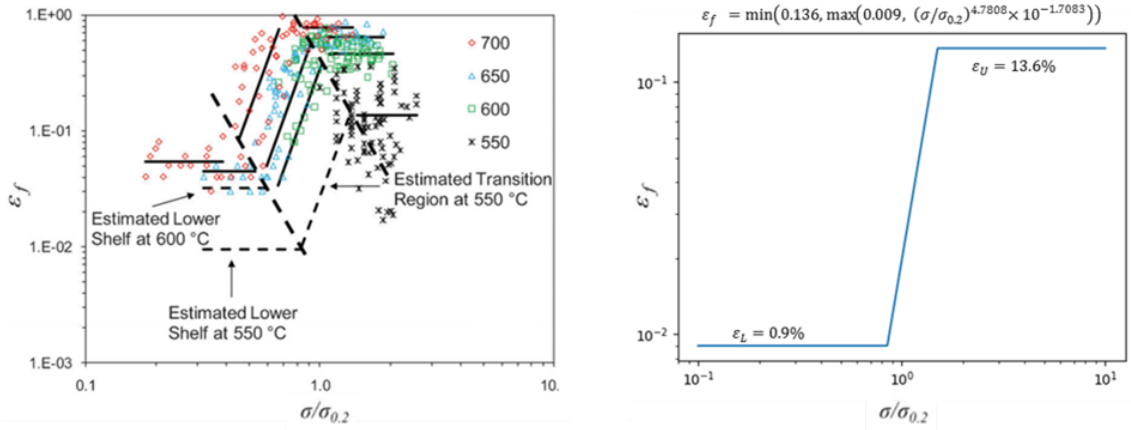

(a) Estimated ductility values at various temperatures [53];

(b) Fitted ductility model at 550^oC;

Figure 2.5: Upper and lower shelf creep ductility of 316H and fitted model.

dependency of 316H stainless steel at the temperature of interest – 550^oC. From the data of Mehmanparast [53], the upper shelf and lower shelf values have been estimated to be 13.6% and 0.9%, respectively; hence the ductility model is presented in Figure 2.5b and is as follows

$$\varepsilon_f = min\left(0.136, max\left(0.009, \left(\frac{\sigma}{\sigma_{0.2}}\right)^{4.7808} \times 10^{-1.7083}\right)\right) \tag{2.6}$$

However it has to be mentioned, that the lower bound value of type 316H steel at 550^oC is highly uncertain due to lack of data points and acquisition of such data would require unreasonably long testing times.

Intrinsic ductility or the Monkman-Grant constant, $\varepsilon_{f'}$, (Figure 2.1) can be used as a practical indicator of creep ductility [46]. By extrapolating the secondary regime of the creep curve in Figure 2.1,the strain difference from the y-axis intercept and intrinsic ductility is called the Monkman-Grant ductility. The Monkman-Grant relationship is an empirical equation (Eq. 2.7) which states that the product of

rupture time and minimum creep strain is constant:

$$C_{MG} = \dot{\varepsilon^c}_{min} t_f = \varepsilon_{f'} \tag{2.7}$$

$$C_{MMG} = \frac{\dot{\varepsilon^c}_{min} t_f}{\varepsilon_f} \tag{2.8}$$

This relationship (Eq. 2.7) assumes that secondary creep dominates the creep life and that the creep ductility is independent of applied stress and temperature and can be used to extrapolate the rupture life at different stresses [12, 54]. Modified Monkman-Grant relationship has been proposed by Dobes and Milicka [55] where creep strain rate dependency is included in the relationship (2.8), and this relationship is used for metals where tertiary creep can not be ignored.

Nevertheless, the R5 [21] procedure calculates the damage due to creep using ductility exhaustion:

$$\omega^c = \int \frac{d\varepsilon^c}{\varepsilon_f(\dot{\varepsilon}^c, T)}, \tag{2.9}$$

where $\varepsilon_f(\dot{\varepsilon}^c, T)$ is the corresponding ductility at the appropriate temperature and creep strain rate; ω^c is the creep damage over component's lifetime. The component is assumed to fail due to creep when the damage term, ω^c, reach unity.

2.1.3 Creep under multiaxial state of stress

Creep deformation

Creep under multiaxial stress conditions can be described using the classical theory of plasticity. As in plasticity, creep deformation can be regarded as incompressible, hence applying the same analogy, the multiaxial creep deformation becomes:

$$\frac{\dot{\varepsilon}_1^c}{\sigma_1 - 0.5\,(\sigma_2 + \sigma_3)} = \frac{\dot{\varepsilon}_2^c}{\sigma_2 - 0.5\,(\sigma_3 + \sigma_1)} = \frac{\dot{\varepsilon}_3^c}{\sigma_3 - 0.5\,(\sigma_1 + \sigma_2)} = \frac{\bar{\dot{\varepsilon}}^c}{\bar{\sigma}} \tag{2.10}$$

where $\dot{\varepsilon}_i^c$ – principal creep strain rates ($i = 1, 2, 3$), σ_i – principal stresses ($i = 1, 2, 3$), $\bar{\sigma}$ – von Mises or equivalent stress, and $\bar{\dot{\varepsilon}}^c$ is equivalent creep strain rate.

Before individual principal creep strain rate components can be calculated a creep law from uniaxial creep tests can be applied to multiaxial deformation by assuming an arbitrary creep rate expression of a form of Eq. 2.1:

$$\bar{\dot{\varepsilon}}^c = A\bar{\sigma}^n f(t) \tag{2.11}$$

where $f(t)$ is some time function.

Multiaxial ductility

As the creep damage is often associated with void growth, creep damage accumulation is often analogous to plastic damage accumulation in metals. In the previous section, 2.1.2, the void growth and creep ductility were discussed regarding applied stress. However, it is known that the void growth is influenced by the state of stress. Bridgman [56] noticed that under high hydrostatic compressive stress materials are more ductile during plastic deformation. Later Rice and Tracey [57] based on McClintock's work [58] proposed a physically based multiaxial ductility model considering spherical void growth due to rigid plastic deformation:

$$(MDF)_{R\&T} = \left(\frac{\varepsilon_f^*}{\varepsilon_f}\right)_{R\&T} = \exp\left(\frac{1}{2} - \frac{3}{2}\frac{\sigma_h}{\bar{\sigma}}\right) \tag{2.12}$$

where MDF stands for multiaxial ductility factor, $\varepsilon_f^*, \varepsilon_f$ is the multiaxial and uniaxial strain to failure, σ_h is the hydrostatic stress and $\bar{\sigma}$ is the equivalent stress.

A different model has been proposed by Cocks and Ashby [59] where the growth of grain boundary cavities by power-law creep of surrounding material can be expressed as

$$\left(\frac{\varepsilon_f^*}{\varepsilon_f}\right)_{C\&A} = \sinh\left(\frac{2}{3}\frac{n-0.5}{n+0.5}\right) \Big/ \sinh\left(\frac{2\sigma_h}{\bar{\sigma}}\frac{n-0.5}{n+0.5}\right) \tag{2.13}$$

where n is the creep exponent from Eq. 2.1. For most engineering materials the value of n lies between 5-10, hence Yatomi and Nikbin [60] have modified the Cocks and Ashby model by approximating $(n-0.5)/(n+0.5)$ as between 0.818 and 0.905. Assuming the value of $(n-0.5)/(n+0.5)$ to be constant, Eq. 2.13 can be rewritten approximately as follows

$$\left(\frac{\varepsilon_f^*}{\varepsilon_f}\right)_{Y\&N} = \frac{0.61}{\sinh\left(\sqrt{3}\sigma_h/\bar{\sigma}\right)} \tag{2.14}$$

The current version of the R5 procedure uses the Spindler fraction (Eq. 2.15) [50]. Spindler considered various data of multiaxial creep strains to failure for Type 304 and 316 steels. Spindler looked at various plastic hole growth and mixed mechanism models and compared them to creep test data of 304 and 316 stainless steel. He concluded that diffusion-controlled and constrained cavity growth models would give a conservative prediction for creep damage when in a biaxial stress state where the ratio of σ_2/σ_1 approaches unity. Conversely the Cocks and Ashby model would give a non-conservative prediction as $\sigma_2/\sigma_1 < 0$. As the Rice and Tracey model was consistent with the experimental data for $-1 < \sigma_2/\sigma_1 < 1$, it was used by Spindler

to develop a semi-empirical model which is implemented in the current version of the R5 procedure [21]:

$$\left(\frac{\varepsilon_f^*}{\varepsilon_f}\right)_{Spindler} = \exp\left[p\left(1-\frac{\sigma_1}{\bar{\sigma}}\right)+q\left(\frac{1}{2}-\frac{3}{2}\frac{\sigma_h}{\bar{\sigma}}\right)\right] \tag{2.15}$$

where σ_1 is the maximum principal stress, p and q are the Spindler constants. For 316 stainless steel (Spindler-I): p=0.15 and q=1.25, and for 304 stainless steel (Spindler-II): p=2.38 and q=1.04. The ratio of hydrostatic stress, $\sigma_h = \frac{\sigma_1+\sigma_2+\sigma_3}{3}$, over deviatoric stress, $\bar{\sigma}$, is called the stress triaxiality. Different ductility models are shown

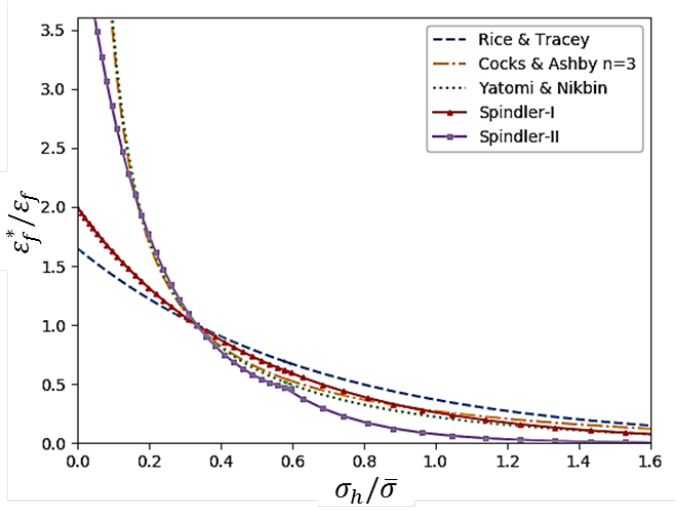

Figure 2.6: Comparison of different multiaxial ductility models.

in Figure 2.6, and they all show similar behaviour – increasing stress triaxiality, reduces the multiaxial ductility. All of the models have the same point of intersection at $\sigma_h/\bar{\sigma} = \frac{1}{3}$. The point of intersection represents the uniaxial creep test, to which is the value of multiaxial strain at failure is normalised, hence the MDF at $\sigma_h/\bar{\sigma} = \frac{1}{3}$ is unity.

Eq. 2.9 can be modified to account for stress state by

$$\omega^{c*} = \int \frac{d\varepsilon^c}{\varepsilon_f^*(\dot{\varepsilon}^c, T)}, \tag{2.16}$$

where $\varepsilon_f^*(\dot{\varepsilon}^c, T)$ is the multiaxial ductility at the corresponding creep strain rate and temperature. This can easily be obtained by multiplying the uniaxial ductility (Eq. 2.5) by the multiaxial ductility factor (Eq. 2.15).

Figure 2.6 indicates that the multiaxial ductility increases with a reduction in stress triaxiality – material increase in ductility. Most of the attention in research has been focused on studying metal failure under high stress triaxialities [57, 58, 61]. However, in recent years, it has been observed that reduced ductility to fail-

ure can also occur in metals subjected to low stress triaxialities ($\sigma_h/\bar{\sigma} < \frac{1}{3}$) [62–69]. Tvergaard [63] showed numerically that voids in the presence of a shear stress can collapse and form microcracks that can rotate and elongate under continued shearing. Wierzibicki and Bao [64] identified that ductility will reduce in the region $0 < \sigma_h/\bar{\sigma} < \frac{1}{3}$ due to combined tension and shear deformation. At stress triaxialities $\sigma_h/\bar{\sigma} < 0$ ductility will increase due to increasing compressive stress state until $\sigma_h/\bar{\sigma} = -\frac{1}{3}$. This is believed to be a cutoff point where no damage is expected due to high compressive stresses.

Creep in pressure vessels

An analytical solution for a pressurised thick-walled cylinder is presented to provide a better appreciation of the analytical solution presented in chapter 3. There are plenty of resources available that deal with component lifetime assessment under creep conditions. Notable resources on creep stress analysis for practical applications have been written by the following authors [12, 29, 70] . The analytical solution presented is an expanded version of the axisymmetric creep stress analysis from Webster and Ainsworth [12].

Consider a cylinder with inner and outer radii of r_i, r_e under internal and external pressure (p_i, p_e) and under plane strain conditions. Initially, when such a cylinder is loaded, based on applied load, it will deform either elastically or plastically. If there is no plastic deformation within the structure, the stress state in the cylinder will follow Lame's equations [71]. However, when elastic stresses in the cylinder exceeds yield, stress redistribution will start to occur prior to creep. The fully redistributed stress state in the axisymmetric structure under plane strain conditions for a material obeying an arbitrary creep law in the form of Eq. 2.11 can be calculated using the following formulae:

$$\sigma_t = \frac{(p_i - p_e)\left((r_i/r)^{2/n}(2/n-1)+1\right)}{1-(r_i/r_e)^{2/n}} - p_i \tag{2.17}$$

$$\sigma_r = \frac{(p_i - p_e)\left(1-(r_i/r)^{2/n}\right)}{1-(r_i/r_e)^{2/n}} - p_i \tag{2.18}$$

$$\sigma_z = \frac{1}{2}(\sigma_t + \sigma_r) \tag{2.19}$$

where $\sigma_{t,r,z}$ are hoop, radial and axial stresses.

Stress redistribution is a critical phenomenon, because, for structures where stresses are distributed non-uniformly, regions with high stress can relax and shed more load to regions of lower stress. Stress redistribution is particularly significant when considering complex geometries. Stress redistribution occurs in pressurised

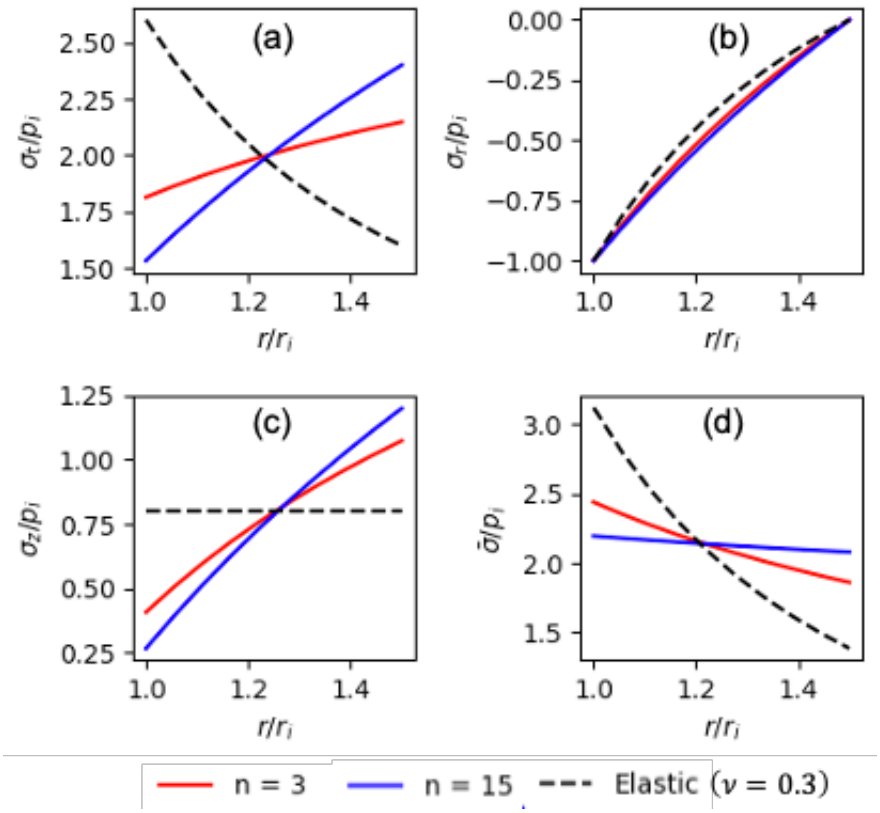

Figure 2.7: Stress state in a pressurised thick-walled cylinder ($r_e : r_i = 1 : 1.5$) after initial elastic loading (blue) and during fully redistributed steady-state creep. (a) Hoop stress; (b) radial stress; (c) axial stress; (d) von Mises stress across the thickness.

cylinders due to either creep or plastic response. The fully redistributed stress response the internally pressurised cylinder ($p_e = 0$) is shown in Figure 2.7. The stress in the cylinder is not uniform. If the pipe is loaded elastically, the stress state under plane strain conditions subjected to internal pressure is shown with the dashed line in Figure 2.7. As the highest equivalent stress state is at $r = r_i$, there creep strain will accumulate the fastest according to Eq. 2.11. Over time stress will relax near the inner radius and more load will be shed towards the outer radius. After stress redistribution, the stress state through the thickness is determined by the creep law exponent, n. In order to calculate the time for stress to redistribute, a numerical approach is needed.

Due to the multiaxial state of stress present in the cylinder, failure is not only governed by accumulated creep strain but is also influenced by multiaxial ductility factor. Figure 2.8 shows the stress triaxiality ($\sigma_h/\bar{\sigma}$), and Spindler's multiaxial ductility factor ($\varepsilon_f^*/\varepsilon_f$) of the same internally pressurised cylinder as Figure 2.7. Although the highest creep strain is expected at the inner radius, it does not necessarily mean that damage will initiate at that location because ductility may be enhanced there due to reduced stress triaxiality.

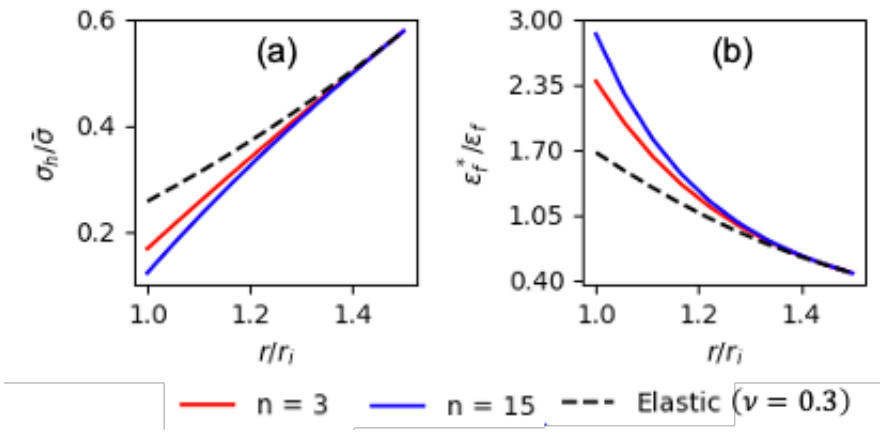

Figure 2.8: Stress triaxiality (a) and Spindler's multiaxial ductility (b) across the thickness of internally pressurised cylinder ($r_i : r_e = 1 : 1.5$).

2.2 Environment-assisted degradation

2.2.1 General remarks

As AGR's operate in a high temperature CO_2 environment the material needs to offer good mechanical properties and an appropriate resistance to any environmental damage. Type 316H stainless steels in an oxidising environment can form a passive oxide layer (Cr_2O_3) at the surface that will protect the metal from further oxidation. This is achieved due to increased chromium content (16% – 18%), hence stainless steels are a good material of choice for designing structures that will be operating at corrosive AGR environment. However the increased chromium content restricts the face-centred cubic (fcc) austenite (γ) phase formation. The fcc structure of γ-phase offers higher ductility compared to α-phase due to its closed-packed planes that enable dislocation movement. Hence in order to retain the desired mechanical behaviour of the γ-phase nickel (Ni) and manganese (Mn) are added to steels to remain austenitic even at room temperatures [72].

C	Si	Mn	S	P	Ni	Cr	Mo	Co	B
0.05	0.49	1.56	0.009	0.021	11.35	16.9	2.26	0.009	0.003

Table 2.1: Chemical composition (wt.%) of Type 316H stainless steel taken from ex-service superheater header material [13].

As discussed in chapter 2.1, Type 316H SS has an improved creep resistance due to the increased carbon content that impedes dislocation motion and provides protection against creep and creep-fatigue crack initiation and growth. However in recent years, due to improvements in defect inspection technology, the plant operators have noticed small crack like defects on the surface. More detailed metallurgical investigation has revealed that 316H components have undergone microstructural

changes due to interaction with the environment that has caused an increased hardness at the surface due to oxidation and carburisation [19]. The current R5 Volume 2/3 assessment procedure [21] does not consider defect initiation in a case hardened materials, hence this has raised an important questions about how environmental degradation mechanisms can influence creep and creep-fatigue crack formation and growth.

An extensive 3-year research project called: Environmental Impact on the Structural Integrity of Nuclear Components (ENVISINC) investigated CO_2 environment impact on stainless steel. The ENVISINC project aimed to provide an understanding of carburisation and provide an updated R5 Volume 2/3 assessment methodology which could be applied to carburised components, which were not included in the previous versions of this assessment procedure [23]. The following section presents current understanding of factors influencing oxidation and carburisation of austenitic stainless steels and critically analyses the current advice on structural integrity assessment.

2.2.2 Oxidation

All steels exposed to an oxygen rich environment will oxidise given enough time. The kinetics of oxidation will mainly depend on diffusion and interfacial processes. In practice, predicting damage due to oxidation is often a complex task because metal alloys can react with more than one reactive component, (e.g. oxygen, water vapour, carbon monoxide), metals can react to gasses, solids and liquids, and any changes in the reactant concentration or partial pressures will influence the rate of corrosion. Additionally the rate of oxide formation can be influenced by the state of stress of the material and surface finish, hence increasing the complexity in predicting the oxidation behaviour. However the basic principles of corrosion are based on the second law of thermodynamics that can be found in most introductory textbooks covering metal corrosion [73–75]. The general equation of metal (M) oxidation is

$$\frac{2a}{b}M + O_2 \rightarrow \frac{2}{b}M_aO_b, \tag{2.20}$$

where a, b are reaction coefficients. Eq. 2.20 involves 2 redox reactions – reduction of oxygen: $\frac{1}{2}O_2 + 2e^- \rightarrow O^{-2}$; oxidation of the metal: $M \rightarrow M^{+\frac{2b}{a}} + \frac{2b}{a}e^-$).

The equilibrium state in Eq. 2.20 will be determined from the standard free energy formation of the metal oxide. The standard free energy or Gibbs energy (ΔG^o) of a metal oxide oxidising in the gas environment can be expressed as

$$\Delta G^o = RT \ln P_{O_2} \tag{2.21}$$

where R is the ideal gas constant, T is the temperature (K), and P_{O_2} is the partial pressure of oxygen. By knowing the Gibbs free energy of oxide formation it is possible to predict what type of oxides are most likely to form using the Ellingham diagram (Figure 2.9).

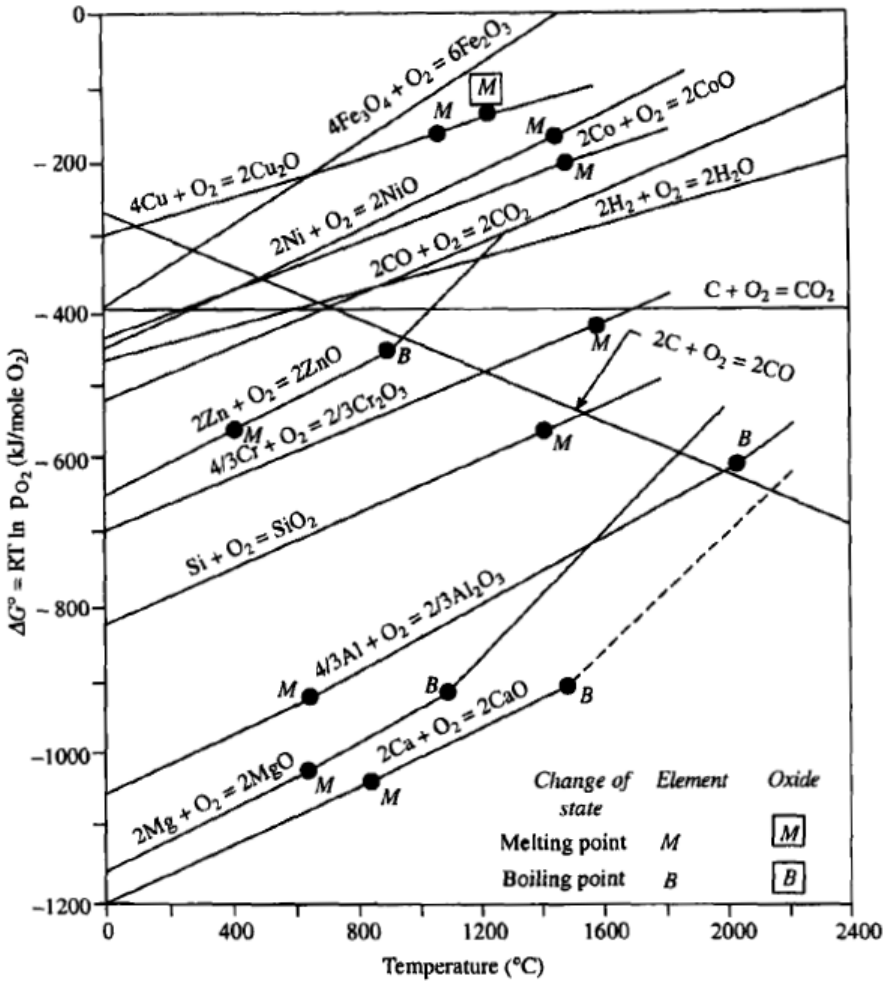

Figure 2.9: Standard free energy of formation of oxides at different temperatures [74].

Iron is a transition metal, hence it can have more than one oxidation state, however it mainly has two: +2 and +3. The oxidation state will depend on the available Gibbs free energy which will determine the thermodynamic stability of the oxide formation. As a metal oxidises, it is more difficult for oxidising agents to penetrate through the oxide layer, hence reducing the available oxidising agents (O_2, CO). Such changes can give rise to different oxide formations, hence iron surface can form layers of different oxides. Haematite (Fe_2O_3) usually forms at the surface due to higher oxygen availability and it has an oxidation state of +3. Deeper in the material as oxygen concentration is reduced haematite reduces to magnetite (Fe_3O_4) which is a spinel oxide consisting of one Fe^{+2} and two Fe^{+3} ions. At temperatures $> 570^oC$ iron can reduce to +2 oxidation state and form Wüstite (FeO).

As the Gibbs free energy of an oxide formation becomes more negative, the more stable is the oxide. From Figure 2.9 it can be seen that Cr_2O_3 is more stable than Fe_2O_3 oxide (more stable < $\Delta G^o_{Cr_2O_3}$ < ΔG^o_{FeO} < $\Delta G^o_{Fe_3O_4}$ < $\Delta G^o_{Fe_2O_3}$ < less stable), therefore steels containing >16 wt%Cr should be protected by formation of the passive Cr_2O_3 layer. However the evidence suggests [76, 77] that in an AGR high temperature CO_2/CO environment the protective chromium layer gets depleted. The depletion of this protective oxide causes duplex oxide to grow (Figure 2.10). The duplex oxide formation in a high temperature CO_2 environment has been widely studied for $9Cr-1Mo$ steel [78–84]. $9Cr-1Mo$ is a ferritic steel and the exact mechanism of the oxide growth in the AGR environment are still not completely understood.

Duplex oxide consists of outer magnetite and Cr-rich inner spinel ($(Fe,Cr)_3O_4$) layers. Magnetite forms by outward diffusion of Fe ions (Eq. 2.22). Magnetite is a porous layer that allows for inward diffusion of oxidising species (CO_2/CO and H_2O/H_2). The cavities that are formed by outward diffusion of Fe ions are filled by the growth of the inner Cr-rich spinel (Eq. 2.23) [85]. As the Cr-rich spinel oxide formation involves CO_2/CO, carbon can be injected in the base material. However the composition of this oxide will depend on the oxidising agent potential of the environment [75].

$$3Fe + 2O_2 \rightleftarrows Fe_3O_4 \tag{2.22}$$

$$3(Fe,Cr) + 4O + xC \rightleftarrows (Fe,Cr)_3O_4 + xC \tag{2.23}$$

It is known that duplex oxide formation is influenced by several factors including chromium and silicon contents, microstructure [86], surface finish [13, 17, 78, 87], gas composition and pressure [78], dislocation and vacancy concentration [88], temperature [78, 79, 87] and applied load [13]. Although austenitic stainless steels do not initiate a breakaway reaction [79], unless the temperature exceeds 900°C [77], it has been known that the duplex oxide formation plays an important role in 316H carburisation process [76]. Magnetite can form in the CO_2 environment by several mechanisms but mainly it forms by iron reacting with the carbon dioxide gas (Eq. 2.24). This reaction within the porous oxide scale produce carbon monoxide which can deposit carbon molecules into the base metal according to the Boudouard reaction (Eq. 2.25) [84].

$$3Fe + 4CO_2 \rightarrow Fe_3O_4 + 4CO \tag{2.24}$$

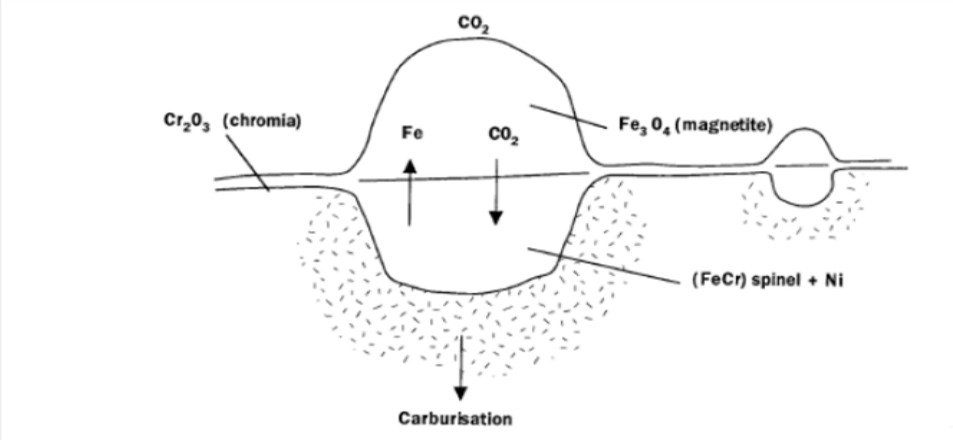

(a) Depletion of Cr_2O_3 and the growth of the duplex oxide;

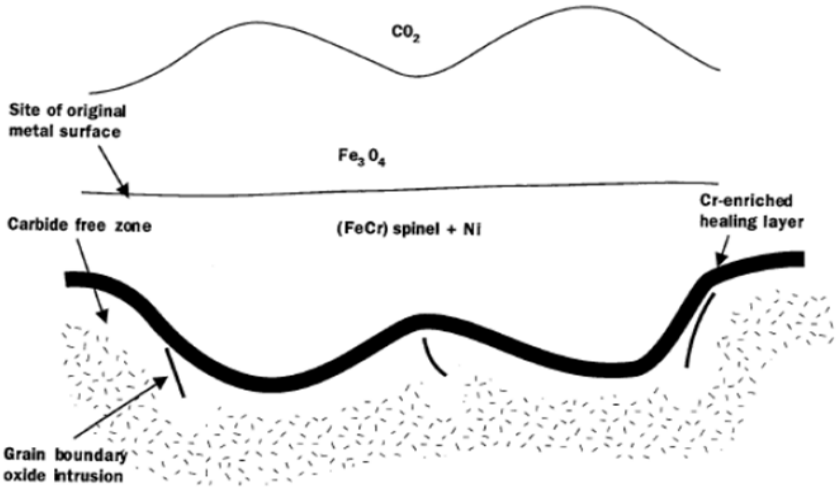

(b) Formed duplex oxide with an internal oxidation zone (healing layer).

Figure 2.10: Schematic diagram of duplex oxide formation with Cr rich healing layer [89].

2.2.3 Carburisation

Carburisation of steels is a well-known industrial process that has been used to enhance fatigue and wear properties of steel components. Usually carburisation of steel is accomplished around 950°C or above. Higher temperatures enhance carbon diffusion into the metal lattice. Non-austenitic stainless steels at higher temperatures change from bcc to fcc structure which enables higher diffusivity and solubility of interstitial carbon atoms [90].

In the AGR environment ($CO_2/CO/CH_4/H_2/H_2O$) carburisation can occur in several ways (2.25–2.27). Carburisation is an endothermic reaction and the most dominant mechanism of carburisation is believed to be the Boudouard reaction 2.25 [73,

85, 91].

$$2CO \rightarrow C + CO_2 \tag{2.25}$$

$$CO + H_2 \rightarrow C + H_2O \tag{2.26}$$

$$CH_4 \rightarrow C + 2H_2 \tag{2.27}$$

From chemical reactions (2.25 –2.27), it can be seen that carburising agents are CO and CH_4 gases and decarburising agents are CO_2 and H_2O. For a commercial carburisation process (e.g. gear carburisation), the gas composition together with temperature and pressure is carefully controlled to maximise active carbon potential. The active carbon potential is defined as the carbon that is available at the metal surface for chemical reaction to take place and it is calculated by considering reaction kinetics of carburisation under particular conditions [91].

To estimate carbon concentration in the metal, mass transfer of carbon from gas to metal has to be considered. Figure 2.11 shows a basic schematic of 3 stages of carburisation. The first stage is carbon transport from the carburising atmosphere to the steel surface. The concentration of carbon at the steel surface (C_s) is not the same as in the bulk gas (C_p) because there is a boundary layer with a mass transfer coefficient (β) that limits carbon atom flux (J) to the surface.

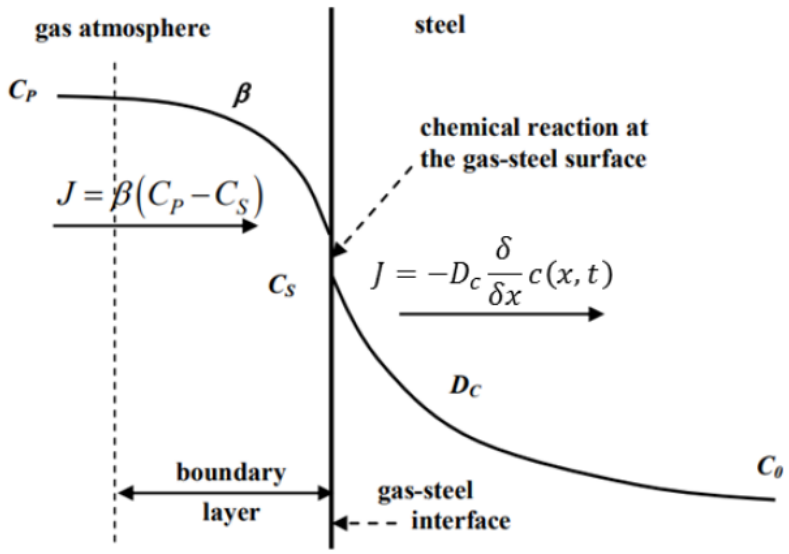

Figure 2.11: A schematic diagram of carbon mass transfer, directly taken from [91].

The second stage of carburisation is chemical reactions between gas and metal surface with main carburising reactions described in Eqs. 2.25-2.27. The third and final stage is carbon diffusion into the metal surface [91], and as carburisation is a diffusion driven process in an idealised scenario, it can be modelled using Fick's laws

of diffusion (Fick's first law – Eq. 2.28; Fick's second law – Eq. 2.28 in 1-D):

$$J = -D_c \cdot \frac{dc}{dx} \tag{2.28}$$

$$\frac{\delta c(x,t)}{\delta t} = D_c \cdot \frac{\delta^2 c(x,t)}{\delta x^2} \tag{2.29}$$

where J is the diffusion flux, c is the carbon concentration, D_c is the carbon diffusivity in steel, and x is location. In Figure 2.11, the first Fick's law of diffusion is presented, where carbon molar flux is a function of carbon diffusivity in steel (D_c), and rate of change of concentration through the thickness (for the 1-dimensional problem). It has to be noted that Fick's first law of diffusion can only be applied for steady-state diffusion. Hence it has little significance for practical applications [92].

In the AGR's, the carburisation mechanism is significantly more complex because carburisation is induced by oxidation as explained in section 2.2.2. Carburising agents (e.g. CO) are produced during iron oxidation (Eq. 2.24) that are then introduced into the metal matrix. However, a chromium rich healing layer (Figure 2.10b) may form between the metal-oxide interface [93]. This healing prevents parent metal from further oxidation and carburisation. However it has been observed that at certain temperatures ($480^oC - 600^oC$) the healing layer may never form and result in continuous oxidation/carburisation of a component throughout its life [76].

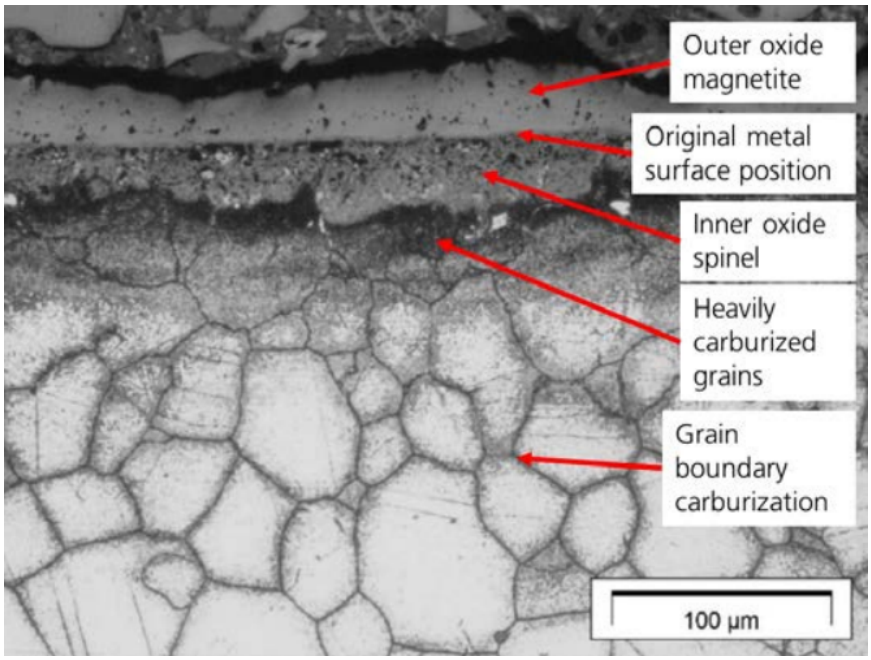

Figure 2.12: Carburised Type 316H stainless steel, directly taken from [15].

Figure 2.12 show an etched carburised 316H steel, it shows the approximate duplex oxide size of $50\mu m$. Under the duplex oxide the first layer of grains are

heavily carburised. Below the first grain layer, carburisation occurs heavily at the grain boundaries. Similar to $9Cr-1Mo$ steel, carburisation on the grain boundaries forms chromium rich carbides ($M_{23}C_6$, M_7C_3) [15, 94] which cause further chromium depletion and makes this region more susceptible to corrosion [95].

Due to the carbide formation, the carburised material has an increased hardness at the surface below the duplex oxide. According to Chevalier [15] the hardness of carburised material (with $250\mu m$ thickness that have been measured by micro-hardness indentation) ranges from 180 Hv (at the base material or bulk) to 450 Hv (near the duplex oxide). Palko [13] also measured hardness of a carburised 316H material and found 450 Hv hardness near the oxide interface. Ex-service bifurcations and tailpipes that have been in service for > 100 kh [24], and pre-conditioned material [96] show elevated hardness up to 600 Hv.

From a structural integrity point of view, elevated hardness due to carburisation indicates changes in material properties. It is known [76] that carburisation increases Young's modulus, yield strength, tangent modulus (slope of the stress-strain curve in the plastic region), creep resistance and reduces creep ductility. Previous attempts have been made to study how microstructural changes due to carburisation will influence creep damage accumulation in 316H stainless steel.

Using Fick's second law of diffusion Biglari and Nikbin [97–99] proposed a novel numerical approach to investigate coupled diffusion-creep damage evolution in the microstructure. It was assumed by these authors that coupled damage could be modelled by linearly separating creep and environmental-induced damage:

$$\omega^t = \omega^c + \omega^{env} \tag{2.30}$$

where ω^t is total damage, ω^c is creep damage, and ω^{env} is environmental damage due to carburisation. The environmental damage term is calculated assuming a critical carbon concentration. In their research, material properties were related to carbon concentration assuming that corresponding material property (e.g. E) scale according to increasing carbon concentration. However their research focused on developing a crack growth model at grain level using the finite element model. For practical applications it is desirable to develop a simplified approach to account for damage initiation for carburised components.

2.2.4 Accounting for carburisation in R5: current understanding

Currently R5, the high temperature assessment procedure [21], can not predict damage initiation due to the synergistic effects of the environmental and creep/creep-

fatigue mechanisms. Instead oxidation is treated as metal loss due to the oxide having low load bearing capacity [15, 76]. This is a conservative assumption because at low stresses the oxide will have some load bearing capability. Nevertheless, as the duplex oxide is usually $50-100\,\mu m$ thick [14, 24, 79, 96], such an assumption is reasonable. Contrarily, the carburised layer thickness can vary up to $500\,\mu m$, hence treating carburised layer as metal loss would be overly pessimistic. The results from the ENVISINC project have been analysed and summarised to provide the carburised material property inputs for a simplified assessment methodology [24].

Hardness

The severity and depth of carburisation in ex-service material have been measured indirectly by micro-hardness testing [23, 76]. The term "severity" means the elevation of hardness compared to bulk and "depth" is the depth of the material with increased hardness. The carburised surface shows a significant increase in hardness compared to bulk material (≈180 Hv) [13, 14, 23, 76, 96, 100]. Typically the measured hardness of uncracked sections of bifurcations and tailpipes is 300 Hv. However regions which have cracked have shown increase in hardness up to 600 Hv. In practice, defining the depth of carburised layer is based on hardness measurements as evaluated by the increased hardness relative to bulk material. Chevalier [76] defined the carburised layer depth as the region over which the Vickers hardness is 10% greater than the bulk value. Although such a definition does not measure carburisation directly, it provides a useful indication of the depth and severity of carburisation. Younes [14] demonstrated that the elevated hardness profile is directly associated with elevated carbon concentration and is defined by diffusion of carbon from the surface.

Monotonic tensile properties

It is known that carburisation increases Young's modulus, yield stress and ultimate tensile strength (UTS) of a material [23, 24, 90, 101]. Hardness measurements have been used to determine local mechanical properties of the carburised layer [14, 102]. Zhao [102] developed an indentation method to measure the elastic modulus of the surface modified layer of 18CrNiMo7-6 steel alloys. Younes used [14] load controlled nanohardness tests to measure the increase in elastic modulus of carburised 316H steel. Younes found an increase in elastic modulus by 25% relative to the bulk at room temperature at a distance of 50 microns from the carburised material surface.

The measure of hardness have been shown to correlate to yield stress and carbon concentration [103, 104]. Work by Kimmins [104] focused on the effects of thermal

ageing on 316/316H stainless steel and fitted a linear model (Eq. 2.31) to 0.2% proof stress data of an ex-service material (at 525^oC) and room temperature Vickers hardness measurements.

$$\sigma_{0.2} = 1.73(Hv) - 106(\pm 42\,MPa) \tag{2.31}$$

In Eq. 2.31 $\sigma_{0.2}$ is the 0.2% proof stress, Hv is the measured Vickers hardness, and $(\pm 42\,MPa)$ represents the upper and lower bound 95% confidence interval to the data.

The reported hardness data through the depth of the carburised layer can be used to estimate carburised layer proof stress from 2.31. The reported hardness values through the depth of carburised layer are 180Hv - 450 Hv [76], 240 Hv - 430 Hv [13], 200 Hv - 600 Hv [14], 170 Hv - 600 Hv [100] 240 - 600 Hv [96]. Eq. 2.31 suggests that with peak hardness of 300 Hv - 600 Hv the estimated 0.2% proof stress is 371 - 974 MPa. According to R66 [105] the 0.2% proof stress for the bulk is 131 MPa, hence Eq. 2.31 predicts proof stress elevation by a factor of 2.8 - 7.4. It has to be noted that Eq. 2.31 was obtained by analysing thermally aged material data and the work does not consider the effects of carburisation. Therefore, Eq. 2.31 can only provide a qualitative indication of the possible range and variability in yield stress.

Chevalier [24] and Wisbey [23] have estimated the monotonic tensile properties of the carburised layer by analysing the global response of carburised specimens. The effect of the increase in yield stress and UTS on the global response will depend on the area fraction carburised. Wisbey [23] assuming carburised layer consists of a homogeneous material calculated 0.2% proof stress $\sigma_{0.2}$ = 516 MPa (193% increase from the bulk value). Chevalier [24] analysed monotonic tensile data of carburised 316H and fitted a Ramberg-Osgood model (Eq. 2.32) for a homogeneous carburised surface layer for stress values: $140\,MPa < \sigma < 270\,MPa$. From the data it was estimated that the average 0.2% proof stress is 400 MPa and that the Young's modulus (E_c) is 205 GPa, with total strain in the carburised layer described by

$$\varepsilon_c = \frac{\sigma_c}{205000} + \left(\frac{\sigma_c}{1304}\right)^{\frac{1}{0.19}} \tag{2.32}$$

Creep deformation and ductility

Carbide precipitation leads to composition changes and deterioration of creep properties [17, 90, 106–108]. It is known that 316H forms $M_{23}C_6$ carbide precipitates at the grain boundaries which lead to a decreased concentration of solute elements

for the austenitic matrix. Formation of $M_{23}C_6$ leads to reduced fracture toughness and reduces corrosion resistance [108]. Formation of $M_{23}C_6$ carbides and other second phase particles increase the resistance to dislocation motion and leads to loss of ductility [14, 17, 108]. Heterogeneous microstructure that arise from formation of these second phase particles creates strain misfits in the matrix which provide suitable places for crack initiation [109].

Data from one creep test is available on a Type 316H carburised specimen with a characteristic carburisation depth of $250\,\mu m$, regarding the minimum creep deformation [24]. A hollow 316H carburised specimen with 6 mm internal and 7 mm external diameter was tested at 260 MPa. The observed minimum creep rate was a factor of 6.4 slower compared to virgin material. By comparing the creep response of uncarburised material at various stresses and assuming a Norton creep law, the creep law exponent (n) and creep law multiplier (A_o) of the bulk material were found to be $n = 10.18$ and $A_o = 8.876 \times 10^{-35}$. In analysis of the hollow specimen, the carburised layer was treated as homogeneous material with no material property gradation through the thickness. Assuming that the creep law exponent in the carburised layer remains unchanged and the creep rate is reduced by some factor, the creep law for a homogeneous carburised layer under uniaxial loading was then deduced

$$\dot{\varepsilon}_c^c = A_c \sigma_c^n = \frac{A_o}{22} \sigma_c^n \tag{2.33}$$

where A_c is the creep law multiplier of the carburised layer and σ_c is the stress in carburised layer.

Although evenly distributed carbon atoms can improve resistance to dislocation movement [90], carbide precipitation on the grain boundaries has been shown to have a detrimental effect on creep ductility and corrosion resistance [96, 110]. Chevalier [24] reports that the creep ductility of the carburised layer is 1%, but in creep life analysis a conservative estimate of 0.75% should be used. However it has to be emphasised that this has been estimated by considering interrupted creep tests of pre-carburised specimens. Pre-carburised refers to being was preconditioned to achieve the characteristic carburisation depth of $200 - 250\,\mu m$ prior to any mechanical testing. This ductility was obtained by observing the crack depth at various creep strains, and the conservative estimate of the ductility was made when the average crack length was 80% of the carburised layer thickness. In the analysis of Chevalier [24] it is also reported that although the cracking in the carburised layer occurred early in the creep test, the ductility of the bulk was not significantly affected. The current advice on the carburised 316H material is that the lower bound ductility is reduced by a factor of 3.5 from that of bulk material at all temperatures.

As only one data point has been taken, there is a high uncertainty regarding the actual carburised layer ductility value. It has to be noted that creep response [23, 24, 96] and creep ductility [24] measurements have been measured by looking at the global response of the carburised specimens.

Summary of the key assumptions in the carburised structure assessment methodology

The key assumptions in the current simplified methodology for R5 carburised component assessment are

- Perform creep damage analysis treating the carburised structure as globally homogeneous with locally reduced creep ductility. The ductility of the carburised layer should be reduced by factor of 3.5 (from [105] the lower bound creep ductility of Type 316H is ε_f = 2.6%, hence ε_f^c = 0.75%).
- Alternatively, assume a bi-metallic structure where the carburised layer is treated as homogeneous having tensile properties according to Eq. 2.32, creep deformation properties according to Eq. 2.33, and creep ductility of 0.75%.

Treating a carburised structure as globally homogeneous is preferable for structural integrity assessments because it allows use of the established assessment procedures. However, as the carburised material is inhomogeneous near the surface, clearly the homogeneous assumption could lead to erroneous analysis. Treating the carburised layer as homogeneous but with different material properties from the bulk could improve the quality of structural integrity assessments. However, to evaluate when simplified assumptions are appropriate, a detailed analysis is needed to understand where over-conservativism or under-conservativism may arise. Given the uncertainty in the available materials data and the assumptions in determination of the carburised layer material properties, the existing assumptions should be critically re-evaluated.

2.3 A brief introduction to supervised learning algorithms

2.3.1 General remarks

Machine learning (ML) is a subset within Artificial Intelligence (AI) which focuses on teaching computers to find patterns in data without being specifically programmed to do so [111]. The two major subsets of the ML field are supervised and unsupervised learning. Supervised machine learning is a construction of algorithms where

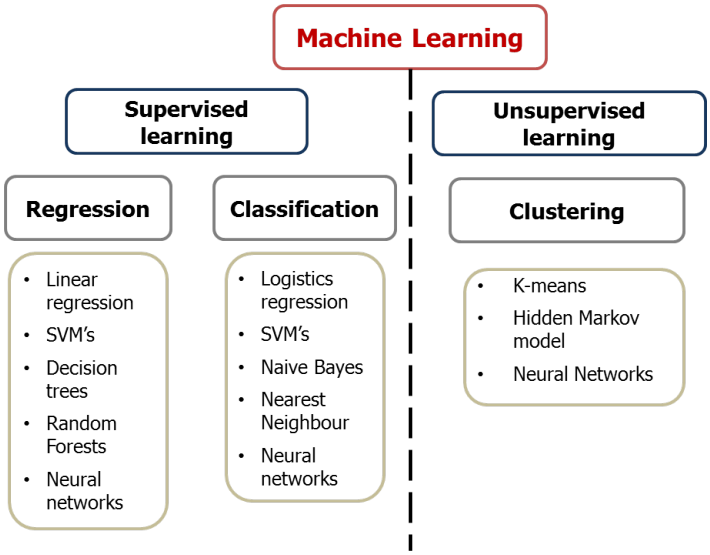

Figure 2.13: Supervised vs unsupervised ML algorithms.

two sets of data are provided – training data and target data [112]. Training data are used to train the model to make some sort of prediction and target data are the values which the model is trying to predict by minimising the error function. Supervised learning can be divided into two major subsets – classification and regression. Classification algorithms would try to predict in which category would a given N-dimensional data point fall, e.g. a simple binary classification problem would be predicting whether or not a structure will fail due to creep-fatigue when exposed to given service conditions (load cycles, temperature, etc.) over its design lifetime. In classification the output variables are discrete values (-1 – will fail; 1 – will not fail). On the other hand, regression would output a continuous value based on the input. A simple example of a regression would be a stress-strain curve prediction of a material under different parameters (temperatures, chemical composition, grain size, etc.). The important factor, besides choosing the right algorithm, would be providing sufficient good quality input data (e.g. stress-strain curves).

Unsupervised learning is a construction of algorithms where algorithms are capable of finding patterns in data where the target values are not provided. A simple diagram of ML subcategories is shown in Figure 2.13 together with the most common algorithms. The purpose of this chapter is to introduce the reader to two supervised learning algorithms: Support Vector Machines (SVM's) and Artificial Neural Networks (ANN's). The material presented here is a summary of the following references: SVM's [112–117] and ANN's [111, 118–120].

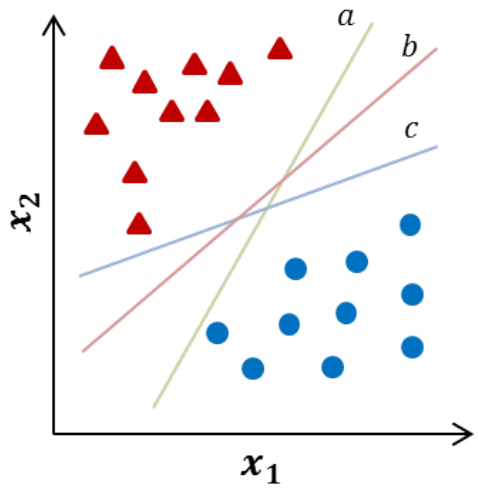

(a) Linearly separable classes can have infinite boundaries;

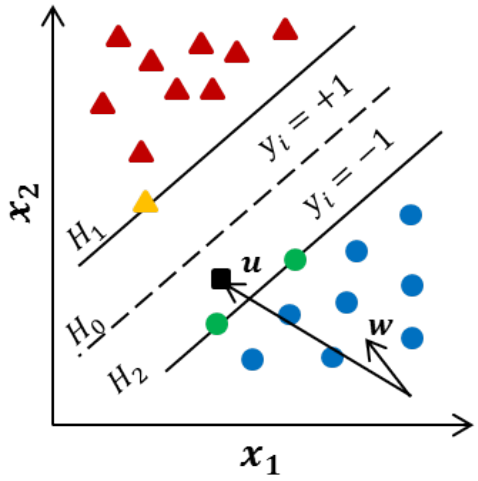

(b) Finding the optimum hyperplane to classify unknown data (■);

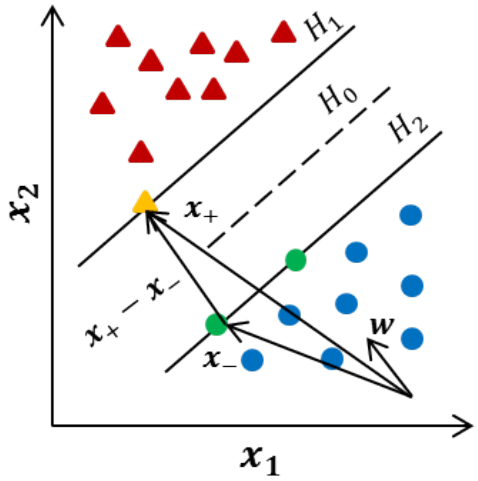

(c) Finding the largest separation margin between support vectors

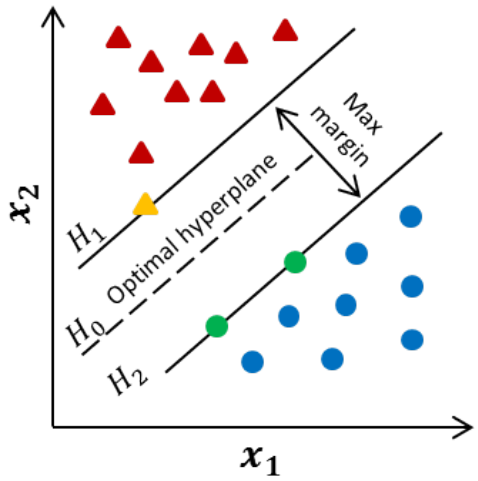

(d) The optimum hyperplane with the highest margin.

Figure 2.14: A schematic representation of SVM decision boundary for binomial classification assuming 2-dimensional parameter space.

2.3.2 Support vector machines

Support vector machines (SVM's) are one of the most popular algorithms that were introduced in the 1990s and they are used for classification and regression problems [115, 116]. Consider a classification problem where an engineer wants to predict failure of a material based on certain parameters. For this theoretical example only 2 parameters will be considered – applied stress (x_1) and temperature (x_2). Figure 2.14a is a schematic representation of the problem, where x_1 and x_2 are applied stress and temperature respectively and red triangles (▲) indicate material did not fail and blue circles (●) – material failed. Theoretically there is an infinite number of hyperplanes (a, b, c) that could be drawn to linearly separate the two

classes. However the objective is to find the optimal hyperplane that would have the maximal margin from the closest data points that separate these two groups (Figure 2.14b) [117].

Consider two parallel planes, H_1 and H_2, that are drawn so that they just touch the nearest data point(s), these are called support hyperplanes (Figure 2.14b). There can be drawn another plane at median distance between both (H_0), which will be the decision boundary that will classify data points either $+1$ for the positive samples (did not fail) or -1 for the negative samples (did fail). Consider this as a road where there is some unknown data point (■), and the objective is to find on which side of the "road" this point lies. Let's say there is some vector $\mathbf{w}$ perpendicular to these planes and vector, $\mathbf{u}$, pointing at (■) from the same origin as $\mathbf{w}$. The projection of $\mathbf{u}$ on $\mathbf{w}$ can give information on which side of the "road" the point will be

$$\mathbf{w} \cdot \mathbf{u} + b < 0 \tag{2.34}$$

where b is the threshold or the bias term which is the shortest distance to the median plane. Eq. 2.34 is the decision rule which will determine whether point (■) will be classed as $+1$ or -1. However as the objective is to also find the maximum margin between support hyperplanes, more constraints are needed to calculate b and $\mathbf{w}$ [113]. The support hyperplanes, H_1 and H_2, are defined by the support vectors, $\mathbf{x}_-$ and $\mathbf{x}_+$, with points denoted as ● and ▲ (Figure 2.14c) which of course are known from the provided data. Eq. 2.34 can be rewritten for the support vectors, $\mathbf{x}_-$ and $\mathbf{x}_+$, such that

$$\mathbf{w} \cdot \mathbf{x}_+ + b \geq +1 \tag{2.35}$$

$$\mathbf{w} \cdot \mathbf{x}_- + b \leq -1 \tag{2.36}$$

where $\mathbf{x}_-$ and $\mathbf{x}_+$ are the negative and positive sample support vectors. The Eqs. 2.35-2.36 can be rewritten as

$$y_i(\mathbf{w} \cdot \mathbf{x}_i + b) - 1 = 0 \tag{2.37}$$

by introducing the term y_i that will be either ± 1 and $\mathbf{x}_i$ are the parameters (e.g. x_1, x_2). The support vectors $\mathbf{x}_-$ and $\mathbf{x}_+$, contain the information about the width of the "street" and this can be found by taking a dot product between the difference of these vectors and the unit normal vector of $\mathbf{w}$. The dot product of $\mathbf{x}_-$ and $\mathbf{x}_+$ can be expressed from Eq. 2.37 such that

$$(\mathbf{x}_+ - \mathbf{x}_-) \cdot \frac{\mathbf{w}}{\|\mathbf{w}\|} = \frac{2}{\|\mathbf{w}\|}. \tag{2.38}$$

Eq. 2.38 represents the function that needs to be maximised subjected to constraints in Eq. 2.37 to obtain the hyperplane with the maximum margin between the two support hyperplanes (Figure 2.14d). The maximisation of Eq. 2.38 is the same as $\min \frac{1}{2}\|\mathbf{w}\|^2$. The function is squared so that the problem can be solved using quadratic programming where efficient algorithms exist for solving quadratic classification and/or regression problems [113, 114, 121]. This is a quadratic constrained optimisation problem with inequality constraints where the saddle point can be found using the Langragian (L):

$$L(\mathbf{w}, b, \alpha_i) = \underbrace{\frac{1}{2}\|\mathbf{w}\|^2}_{\text{Objective function}} \underbrace{- \sum_{i=1}^{m} \alpha_i \left(y_i[\mathbf{w} \cdot \mathbf{x}_i + b]\right)}_{\text{Inequality constraint}} \tag{2.39}$$

where α_i are Lagrange multipliers. This is a dual function which implied that $L(\mathbf{w}, b, \alpha_i)$ is either minimised with respect to primal variables $(\mathbf{w}, b)$, or maximised with respect to dual variables, α_i, [113]. Taking the partial derivatives $(\nabla L(\mathbf{w}, b, \alpha_i))$ with respect to primal variables and equating to 0, and substituting the resulting equalities back into Eq. 2.39 eliminates $\mathbf{w}$ and b. The maximum margin hyperplane (Figure 2.14d) is found by maximising the new function $W(\alpha_i)$:

$$W(\alpha_i) = \sum_{i=1}^{m} \alpha_i - \frac{1}{2} \sum_{i=1}^{m} \sum_{j=1}^{m} y_i y_j \left(\mathbf{x}_i \cdot \mathbf{x}_j\right). \tag{2.40}$$

As it can be seen from 2.40 the maximisation only depends on the dot products of $\mathbf{x}_i \cdot \mathbf{x}_j$ and as $L(\mathbf{w}, b, \alpha_i)$ is a convex function, the maximum of $W(\alpha_i)$ will always result in finding the global maximum.

In practical applications it might be difficult to find a linear boundary to separate data (Figure 2.15a). This can be overcome by mapping the input to a new function $\chi(\mathbf{x}_i)$ which has a higher number of variables than the input vector [116]. This is done using a Kernel function $K(\mathbf{x}_i, \mathbf{x}_j)$:

$$K(\mathbf{x}_i, \mathbf{x}_j) = \chi(\mathbf{x}_i) \cdot \chi(\mathbf{x}_j). \tag{2.41}$$

The remarkable feature of this function is that, as maximisation only depends on dot products, it is only necessary to know the kernel function. The inner product of Eq. 2.41 is computed in lower dimensional input space, hence there is no need to construct the χ vectors or even know the transformation function itself [114]. An example of a polynomial kernel is

$$K_P(\mathbf{x}_i, \mathbf{x}_j) = \left(\mathbf{x}_i \cdot \mathbf{x}_j + 1\right)^d \tag{2.42}$$

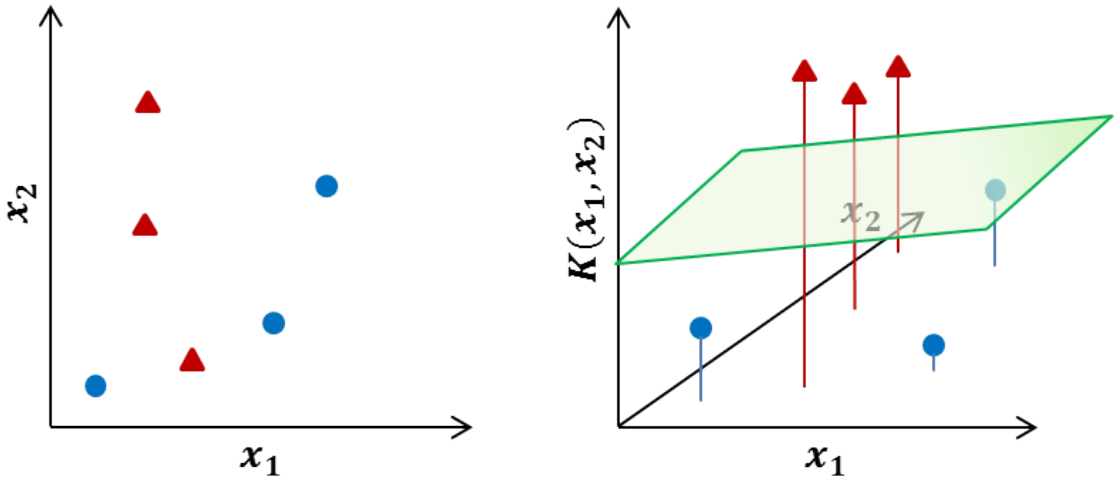

(a) Linearly inseparable data points;

(b) Feature transformation to another space using a kernel function;

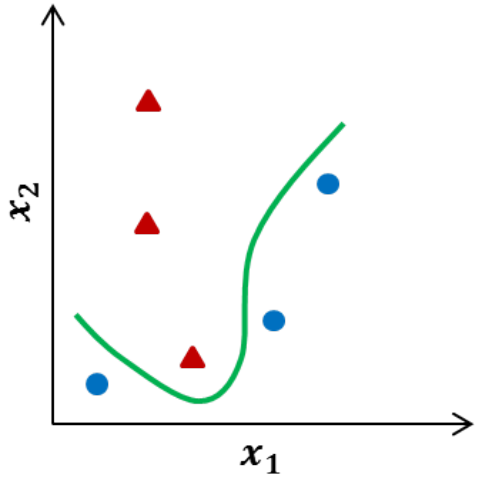

(c) Decision boundary of linearly inseparable data points.

Figure 2.15: A schematic representation of how linearly inseparable data points are transformed to another space where they become linearly separable.

where d is the degree of the polynomial. Other popular kernels are: Gaussian radial basis function (RBF), and sigmoidal kernel [117]. However the choice of kernel function will depend on the given data set. A major advantage of SVM's over other machine learning techniques (e.g. ANN's) is that the global minimum will always be found because of the convexity of $L(\mathbf{w}, b, \alpha_i)$ (Eq. 2.39), whereas ANN's can get stuck in local minimum points.

2.3.3 Artificial neural networks

The motivation for artificial neural networks (ANN's) is based on the principle of biological neural networks in our brains that are capable of analysing, and recognising

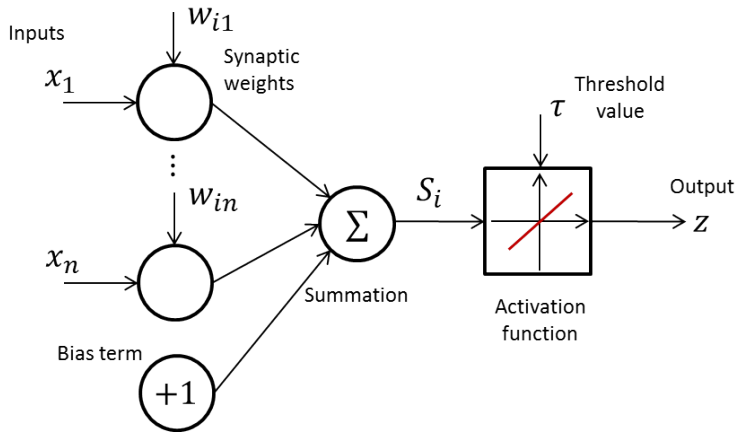

Figure 2.16: A simple mathematical model of neural networks with n inputs, one output using linear activation function.

patterns based on the path path the electric signals have taken to reach our brain [120]. Neural networks can be trained to approximate any function (continuous [122] or discrete) given sufficient training data together with appropriate architecture.

ANN's were introduced in 1943 by McCulloch and Pitts [123], who showed that binary neurons could compute any arithmetic or logical function. In 1958 the first neural network model was created by Rosenblatt [124] who discovered how to update weights of neural networks [119]. Since the 1960s many discoveries were made within neurocomputing research, however practical applications were limited by the available computing power [120]. The neural network method gained popularity after Krizhevsky, Sutskever, and Hinton won the ImageNet classification challenge in 2012 [125]. They built a deep convolution neural network (DCNN) able to classify images of 1000 different objects and animals using 60 million parameters and achieving an error rate of 37.5% (62.5% chance the DCNN will correctly classify the image).

Research regarding metallic creep using ANN is limited. One of the major obstacles in using ANN's is obtaining relevant data sets that can be used to train the model [119]. However ANN's have been used to predict creep rupture life of steels based on chemical composition, stress and temperature [126, 127]; low cycle fatigue and creep-fatigue life prediction [128–130]; and creep curves from accelerated creep tests [131].

A simple neural network (NN) model is shown in Figure 2.16, where x_j are the input vectors (n in total) and they are multiplied by some weight factor, w_{ij}. All of the inputs multiplied by their respective weight factors are summed together with some additional bias term, b, where they produce some intermediate output, S_i, that

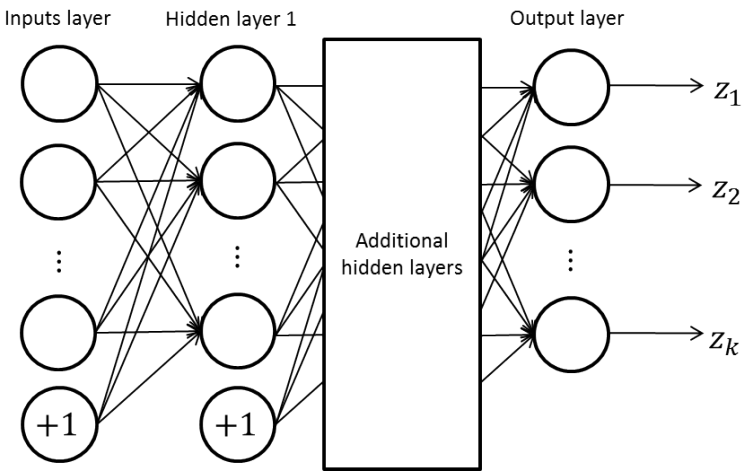

Figure 2.17: A neural network consisting of multiple hidden layers and multiple outputs.

goes into an activation function:

$$S_i = b + \sum_{j=1}^{n} w_{ij} x_j. \tag{2.43}$$

In the activation function the input is compared to some threshold value, τ. If the input exceeds the threshold value then the neuron will be "activated" and it will output an appropriate output value. The activation functions will either produce a discrete output (1 or 0) for classification problems, or a continuous output for regression problems. In general, the output of a NN is a function of inputs, weight factors and thresholds – $z_i = f(x_j, w_{ij}, \tau)$. The objective of a neural network is to approximate some function with inputs and their respective outputs (y_i) by minimising the error between the predicted values and the actual values. As the inputs of the neural network are known, the weight factors and threshold must be somehow calculated. This can be done by constructing some sort of performance function that compares the predicted values with actual values. An example of a simple performance function or loss function, L, is

$$L = -\|y_i - z_i\|^2, \tag{2.44}$$

where the square term is to make L a quadratic function for computational efficiency and minus sign for convenience purposes. The maximisation of this function will be a procedure of finding the partial derivatives with respect to their input variables. The process starts with randomly assigning some weight values to w_{ij} and calculating the resulting output. The next step is to update the weight factors so that with the next iteration the computed output value will be closer to the actual output. This

involves using the chain rule, to find partial derivatives of the loss function with respect to weights. The process of gradient computation is usually performed using backpropagation (BP), resilient propagation (RPROP) or the Levenberg-Marquardt learning (LM) algorithms. These algorithms calculate every partial derivatives with respect to network inputs and network parameters. Then the values of the weights can be updated accordingly to minimise the loss function [116, 118].

A more complex feed forward neural network model is shown in Figure 2.17. In this model each layer receives an input from the previous layer and the process of updating each neuron weight factor is the same as outlined above. To find the best network for approximating the given function, an appropriate architecture must be chosen. This includes choosing the appropriate activation functions, learning algorithms and the number of input and hidden layers [120].

Chapter 3

Analytical solutions of creeping non-homogeneous bodies

3.1 Introduction

Creep lifetime assessment is a complex task which often requires detailed finite element calculations. However, for steady state problems, some closed-form solutions exist which can assist in high-temperature assessments. The current advice for assessing carburised components is to treat them as homogeneous structures but with reduced creep ductility. As carburisation locally reduces the creep rate for a given stress, this advice should be conservative for assessing the global deformation; hence it should be critically re-evaluated to reduce unnecessary conservatism in the assessment procedure. Additionally, there is high uncertainty regarding the carburised layer creep properties. From a limited number of tests, *average* properties have been estimated. The *average* property assumption is based on material uniformity. As carburisation is a diffusion-driven process, such an assumption is not accurate. However, the uniform layer assumption could be a reasonable simplification if there was evidence that the shape of the function describing the carburised layer material property distribution does not significantly influence the creep assessment. As many components in the AGRs undergo microstructural changes which result in the formation of a carburised layer, there is a need for simplified analytical solutions that can predict the local and global creep response and provide an insight into how carburisation alters the local stress state. The following chapter first provides a proof that a local increase of creep resistance leads to a non-homogeneous structure globally creeping slower than the corresponding homogeneous structure. Then closed-form analyses of a functionally graded uniaxial bar and a functionally graded cylinder are presented.

3.2 Mathematical description of creeping non-homogeneous structures

Consider a structure of volume, V, surface, S, with negligible body forces. This is subject to an applied load, P_i, over part, S_p, of S and to zero surface velocities over the remainder , S_u of S. All deformations are assumed small so that changes in geometry may be neglected. For simplicity of presentation, the structure is assumed to be at uniform temperature but a non-uniform temperature can be treated by taking creep strain rates as an increasing function of temperature.

The stress-strain relationship ($\dot{\varepsilon}^c = A\sigma^n$) of a specimen under constant uniaxial stress at elevated temperature can be written in a dimensionless form normalised to any normalising stress, σ_0, and corresponding creep rate, $\dot{\varepsilon}_0^c$,

$$\frac{\dot{\varepsilon}^c}{\dot{\varepsilon}_0^c} = \left(\frac{\sigma}{\sigma_0}\right)^n. \tag{3.1}$$

Considering only the homogeneous part of the structure at any state of stress, σ_{ij}, and at steady state creep conditions, the total strain rate, $\dot{\varepsilon}_{ij}$ is equal to $\dot{\varepsilon}_{ij}^c$. Elastic and plastic strain rates are zero as the stress, σ_{ij} is constant. Eq. 3.1 can be written in more general form as

$$\dot{\varepsilon}_{ij}^c\left(\frac{\sigma_{ij}}{\sigma_0}\right) = \dot{\varepsilon}_0^c\phi^n\left(\frac{\sigma_{ij}}{\sigma_0}\right)\frac{\partial\phi(\sigma_{ij}/\sigma_0)}{\partial(\sigma_{ij}/\sigma_0)} \tag{3.2}$$

where $\dot{\varepsilon}_0^c$, σ_0, n are constants and ϕ is a convex function which is homogeneous of degree one in σ_{ij}/σ_0 and has a value of unity for uniaxial stress σ_0 [132]. The creep energy dissipation rate per unit volume, $\dot{D}^c$, is defined from Eq. 3.2 as

$$\dot{D}^c\left(\frac{\sigma_{ij}}{\sigma_0}\right) = \sigma_{ij}\dot{\varepsilon}_{ij}^c = \sigma_0\dot{\varepsilon}_0^c\phi^{n+1}\left(\frac{\sigma_{ij}}{\sigma_0}\right). \tag{3.3}$$

As ϕ is convex and homogeneous of degree one in σ_{ij}/σ_0, it follows [133] that any two states of stress, $\sigma_{ij}^{(1)}$, $\sigma_{ij}^{(2)}$ and associated creep strain rates, $\dot{\varepsilon}_{ij}^{c(1)}$, $\dot{\varepsilon}_{ij}^{c(2)}$ satisfy

$$\dot{D}^c\left(\frac{\sigma_{ij}^{(2)}}{\sigma_0}\right) - \dot{D}^c\left(\frac{\sigma_{ij}^{(1)}}{\sigma_0}\right) \geq (n+1)[\sigma_{ij}^{(2)} - \sigma_{ij}^{(1)}]\dot{\varepsilon}_{ij}^{c(1)}. \tag{3.4}$$

Consider that $\sigma_{ij}^{(1)}$ is the equilibrium stress field in steady state creep in the structure which is entirely of the homogeneous material defined above. Then, the virtual work

equations lead to

$$\int_{S_p} P_i \dot{u}_i^{(1)} dS = \int_V \sigma_{ij}^{(1)} \dot{\varepsilon}_{ij}^{c(1)} dV = \int_V \dot{D}^c \left(\frac{\sigma_{ij}^{(1)}}{\sigma_0} \right) dV = \int_V \sigma_{ij}^{(2)} \dot{\varepsilon}_{ij}^{c(1)} dV \tag{3.5}$$

where $\dot{\varepsilon}_{ij}^{c(1)}$ is a strain field compatible with $\dot{u}_i^{(1)}$, the steady state displacement rate conjugate to the load, P_i. In Eq. 3.4, $\sigma_{ij}^{(2)}$ is any stress field in equilibrium with the load P_i. Combining Eq. 3.5 with inequality Eq. 3.4 leads to

$$\int_V \dot{D}^c \left(\frac{\sigma_{ij}^{(2)}}{\sigma_0} \right) dV \geq \int_V \dot{D}^c \left(\frac{\sigma_{ij}^{(1)}}{\sigma_0} \right) dV \tag{3.6}$$

which is the well known result that the steady state stress field $\sigma_{ij}^{(1)}$ leads to less creep energy dissipation rate integrated over the volume than any other equilibrium stress field; i.e. $\sigma_{ij}^{(1)}$ is the stress field which minimises the creep energy dissipation rate integrated over the volume.

Now consider the same structure subjected to the same load but in which the material properties in a part of the structure differ from the homogeneous properties above and in this part the creep strain rate is described by

$$\dot{\varepsilon}_{ij}^{c^*} = \lambda(x) \dot{\varepsilon}_0^c \phi^n \left(\frac{\sigma_{ij}}{\sigma_0} \right) \frac{\partial \phi(\sigma_{ij}/\sigma_0)}{\partial(\sigma_{ij}/\sigma_0)} \tag{3.7}$$

where $\lambda(x)$ a scalar function of position x and the superscript "*" is used to denote the non homogeneous material properties which differ from Eq. 3.2. Specifically, it is assumed that the material is stronger in this part of the structure so that

$$0 \leq \lambda(x) \leq 1 \tag{3.8}$$

where unity holds in that part of the structure made of the homogeneous material. In this structure, the equilibrium stress field in steady state creep will differ from $\sigma_{ij}^{(1)}$ and is here denoted as $\sigma_{ij}^{(2)}$. Then the work equations lead to

$$\int_{S_p} P_i \dot{u}_i^{(2)} dS = \int_V \sigma_{ij}^{(2)} \dot{\varepsilon}_{ij}^{c^*(2)} dV = \int_V \dot{D}^{c^*} \left(\frac{\sigma_{ij}^{(2)}}{\sigma_0} \right) dV \tag{3.9}$$

where $\dot{\varepsilon}_{ij}^{c^*(2)}$ is a strain rate field compatible with $\dot{u}_i^{(2)}$, the steady state displacement rate conjugate to the load, P_i, in this structure consisting of non-homogeneous material and $\dot{D}^{c^*}(\sigma_{ij}/\sigma_0)$ is the creep energy dissipation rate per unit volume for the material described by the creep law of Eq. 3.7. Inequality 3.4 still holds when

multiplied by scalar, $\lambda(x)$, and can be written

$$\dot{D}^{c^*}\left(\frac{\sigma_{ij}^{(1)}}{\sigma_0}\right) - \dot{D}^{c^*}\left(\frac{\sigma_{ij}^{(2)}}{\sigma_0}\right) \geq (n+1)[\sigma_{ij}^{(1)} - \sigma_{ij}^{(2)}]\dot{\varepsilon}_{ij}^{c^*(2)}. \tag{3.10}$$

Integrating this inequality over the volume noting that $[\sigma_{ij}^{(1)} - \sigma_{ij}^{(2)}]$ is a stress field in equilibrium with zero load and $\dot{\varepsilon}_{ij}^{c^*(2)}$ is compatible strain rate field then leads to

$$\int_V \dot{D}^{c^*}\left(\frac{\sigma_{ij}^{(1)}}{\sigma_0}\right) dV \geq \int_V \dot{D}^{c^*}\left(\frac{\sigma_{ij}^{(2)}}{\sigma_0}\right) dV \tag{3.11}$$

which shows, in accord with inequality 3.4, that the steady state stress field, now $\sigma_{ij}^{(2)}$, leads to less creep energy dissipation rate, now defined in terms of the creep law of Eq. 3.7, integrated over the volume than any other equilibrium stress field. Thus, that result applies irrespective of whether or not the creep properties are independent of position. This could be due to variations in temperature, for example, or as a result of changes in material properties due to carburisation, which is the topic of interest here.

Combining Eq. 3.9 and Eq. 3.11 leads to

$$\int_{S_p} P_i \dot{u}_i^{(2)} dS \leq \int_V \dot{D}^{c^*}\left(\frac{\sigma_{ij}^{(1)}}{\sigma_0}\right) dV \tag{3.12}$$

In view of inequality Eq. 3.8

$$\dot{D}^{c^*}\left(\frac{\sigma_{ij}}{\sigma_0}\right) \leq \dot{D}^{c}\left(\frac{\sigma_{ij}}{\sigma_0}\right) \tag{3.13}$$

and hence, using Eq. 3.5, inequality 3.12 can be written

$$\int_{S_p} P_i \dot{u}_i^{(2)} dS \leq \int_V \dot{D}^{c^*}\left(\frac{\sigma_{ij}^{(1)}}{\sigma_0}\right) dV \leq \int_V \dot{D}^{c}\left(\frac{\sigma_{ij}^{(1)}}{\sigma_0}\right) dV = \int_{S_p} P_i \dot{u}_i^{(1)} dS \tag{3.14}$$

Therefore, the creep law of Eq. 3.7 with inequality Eq. 3.8 leads to reduced creep deformation relative to the creep law of Eq. 3.2. This confirms that a hardened layer with reduced creep rates at the outside of a component leads to reduced creep deformation, as expected. However, this result has several limitations. First, it applies only to steady state creep and not to the transient period before the steady state is reached. Secondly, it applies only to the volume averaged creep deformation and not to the local deformation. Finally, it covers only equivalent stresses and does not address any influence of locally constrained deformation on stress triaxiality.

3.3 Steady state creep response

To address the issues regarding the local creep deformation and locally constrained deformation on stress triaxiality, in the following section, some detailed component creep analyses are performed. First, a simple two-material structure under uniaxial loading is analysed. Then, a thick walled cylinder consisting of concentric cylinders under internal and external pressure is analysed analytically assuming plane strain conditions. These analyses give an indication of the effect of carburisation on steady state component response. The presented cylinder derivation is an extension of axisymmetric creep analysis from section 2.1.3.

3.3.1 Uniaxial loading

Determination of the stress state and compatible creep law

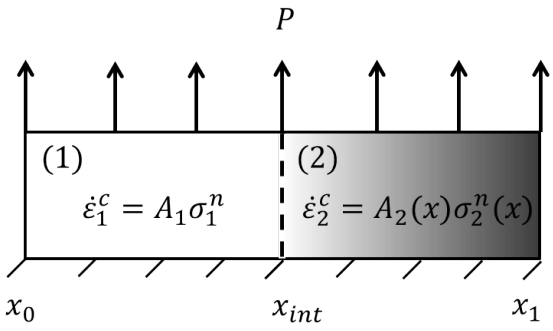

Figure 3.1: Schematic representation of a bar made of homogeneous and functionally graded parts under constant load, P.

The creep rate of many engineering materials can be approximated assuming simple Norton creep law, $\dot{\varepsilon}^c = A\sigma^n$. Consider a two material structure (Figure 3.1) where S_1 is the area of the material (1), and S_2 is the area of the material (2). On the surface there is applied a constant uniaxial load, P, so that the nominal stress, σ_{obs}, is

$$\sigma_{obs} = \frac{P}{S_1 + S_2} = \frac{S_1}{S_1 + S_2}\sigma_1 + \frac{S_2}{S_1 + S_2}\sigma_2 = (1 - a_f)\sigma_1 + a_f\,\sigma_2^* \tag{3.15}$$

where a_f is the area fraction of material (2) and σ_1 and σ_2^* are *average* stresses in each material. Consider that the structure is at steady state, so that the creep rates of both materials must be equal:

$$\dot{\varepsilon}^c = \dot{\varepsilon}_1^c = \dot{\varepsilon}_2^c \tag{3.16}$$

$$\dot{\varepsilon}_1^c = A_1\sigma_1^n = A_2^*\sigma_2^{*n} = \dot{\varepsilon}_2^c \tag{3.17}$$

If the structure in Figure 3.1 consists of two homogeneous materials with creep law multipliers of A_1 and A_2^* for materials (1) and (2) respectively, the stress state in (1), σ_1, and (2), σ_2^*, can be easily calculated using the strain compatibility Eq. 3.16 and constitutive Eqs. 3.17 [134]:

$$\sigma_1 = \frac{\sigma_{obs}}{a_f\left[(A_1/A_2^*)^{\frac{1}{n}} - 1\right] + 1} \tag{3.18}$$

$$\sigma_2^* = \frac{\sigma_{obs}}{(1-a_f)(A_2^*/A_1)^{\frac{1}{n}} + a_f}. \tag{3.19}$$

If the global creep rate is known then Eqs. 3.18–3.19 can be used to determine the creep law multiplier of each part of the two bar structure, if one of the creep law multipliers is known. However, if this problem is related to carburisation, the homogeneous assumption might not be accurate when assessing the local stress state. Although the *average* creep properties and stress state can be determined using the equations above, for more detailed analysis it is useful to estimate a functionally graded material creep law multiplier function, $A(x)$, and the compatible stress function $\sigma_2^n(x)$. Therefore, if material (2) is a functionally graded material:

$$\dot{\varepsilon}_2^c = A_2(x)\sigma_2^n(x), \tag{3.20}$$

the stress in the part (2) cannot be assumed to be uniform because the creep law multiplier $A(x)$ is not uniform, hence the stress function must satisfy the creep strain compatibility Eq. 3.16 to ensure a uniform deformation rate. Eq. 3.19 can only be used to determine the *average* stress in part (2) assuming an *average* creep law multiplier. For a functionally graded structures where the creep property distribution $A(x)$ is not known, certain assumptions must be made regarding the shape of such a function. However, the *average* stress, σ_2^*, in the functionally graded material can be expressed as

$$\sigma_2^* = \frac{\sigma_1}{x_1 - x_{int}} \int_{x_{int}}^{x_1} \left[\frac{A_1}{A_2(x)}\right]^{\frac{1}{n}} dx \tag{3.21}$$

$$= \frac{\sigma_2^*}{x_1 - x_{int}} \int_{x_{int}}^{x_1} \left[\frac{A_2^*}{A_2(x)}\right]^{\frac{1}{n}} dx \tag{3.22}$$

$$= \frac{1}{x_1 - x_{int}} \int_{x_{int}}^{x_1} \left[\frac{\dot{\varepsilon}^c}{A_2(x)}\right]^{\frac{1}{n}} dx \tag{3.23}$$

$$= \frac{\sigma_{obs}}{x_1 - x_{int}} \int_{x_{int}}^{x_1} \left[\frac{A_1}{fA_2(x)}\right]^{\frac{1}{n}} dx \tag{3.24}$$

where x_1, x_{int} denote the boundary of material (2) in Figure 3.1. The factor, f, is the reduction or increase in the creep rate compared to a homogeneous structure

of material (1) under the same loading conditions: $\dot{\varepsilon}^c = A_2(x)\sigma_2^n(x) = (A_1/f)\sigma_{obs}^n$. If the average creep law multiplier A_2^* is known, the compatible $A_2(x)$ distribution can be easily calculated using 3.22.

3.3.2 Single thick walled cylinder analysis

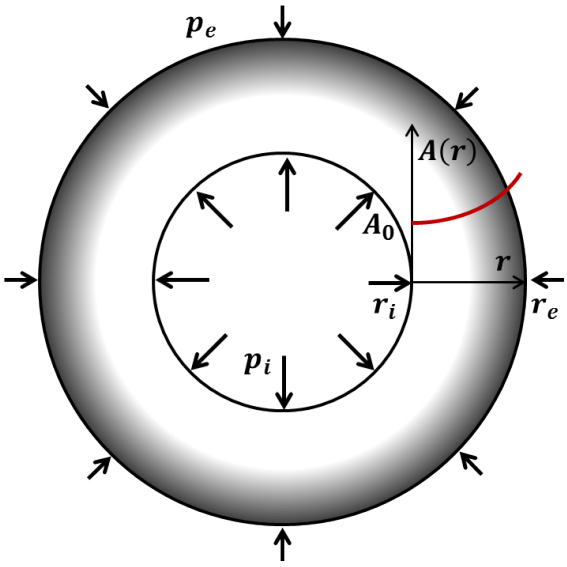

Figure 3.2: Schematic representation of a single internally and externally pressurised functionally graded cylinder.

Consider a pressurised cylinder (Figure 3.2) with internal and external radii r_i and r_e respectively. This cylinder is subjected to internal and external pressure (p_i and p_e), hence the boundary conditions are

$$\begin{aligned} \sigma_r(r_i) &= -p_i \\ \sigma_r(r_e) &= -p_e \end{aligned} \tag{3.25}$$

where σ_r is radial stress. From axisymmetric analysis equilibrium is satisfied if

$$\frac{\partial \sigma_r}{\partial r} = \frac{\sigma_t - \sigma_r}{r} \tag{3.26}$$

where r is radius and σ_t is hoop stress. The compatibility equations to preserve axial symmetry in the steady state creep are

$$\dot{\varepsilon}_t^c = \frac{\dot{\rho}}{r} \tag{3.27}$$

$$\dot{\varepsilon}_r^c = \frac{\partial \dot{\rho}}{\partial r} \tag{3.28}$$

where $\dot{\rho}$ is the radial steady state creep displacement rate; $\dot{\varepsilon}_t^c$ and $\dot{\varepsilon}_r^c$ are the hoop and radial creep strain rates respectively. From the Levy-Mises flow rule and com-

patibility Eqs. 3.27 – 3.28, it can be shown that

$$\dot{\varepsilon}_t^c = -\dot{\varepsilon}_r^c = \frac{C}{r^2} \tag{3.29}$$

where C is a constant. In order to obtain an explicit equation to characterise the stress state at steady state creep, a simple power-law creep law is introduced which is assumed to vary with radial position to describe a functionally graded material:

$$\bar{\dot{\varepsilon}}^c = A(r)\bar{\sigma}^n(r)f(t) = A_o\left(\frac{r}{r_i}\right)^m \bar{\sigma}^n(r)f(t) \tag{3.30}$$

where $\bar{\dot{\varepsilon}}^c$ is the equivalent creep strain rate, $A(r) = A_o(\frac{r}{r_i})^m$ is the position dependent creep law multiplier function, A_o and m are material constants, and $f(t)$ is some function of time, which at steady state is assumed to be a constant ($f(t) = F_o$). The functional form of $A(r)$ has been chosen based on the fact that such a function provides a continuous increase/decrease of creep law multiplier through the cylinder with respect to some reference value, A_o, and the derivative of such a function can be easily calculated. As carburisation is driven by diffusion, $A(r) = A_o(\frac{r}{r_i})^m$ will not provide a realistic property distribution through the cylinder. However section 3.3.3 shows that assuming a concentric cylinder structure any functional form of $A(r)$ can be implemented. Assuming $A(r) = A_o(\frac{r}{r_i})^m$ and using a time hardening creep equation, the radial and hoop creep strain rates can be expressed as

$$\dot{\varepsilon}_t^c = -\dot{\varepsilon}_r^c = \frac{\sqrt{3}}{2}A_o\left(\frac{r}{r_i}\right)^m \bar{\sigma}^n(r)F_o = \frac{C}{r^2}. \tag{3.31}$$

From the von Mises stress definition under plane strain conditions, the axial stress, σ_z, is

$$\sigma_z = \frac{1}{2}(\sigma_t(r) + \sigma_r(r)) \tag{3.32}$$

$$\bar{\sigma} = \frac{\sqrt{3}}{2}(\sigma_t(r) - \sigma_r(r)) \tag{3.33}$$

and Eq. 3.30 becomes

$$\sigma_t - \sigma_r = C_1 r^{-\frac{m+2}{n}} = C_1 r^{-k} \tag{3.34}$$

where $k = (m+2)/n$ and C_1 are constants. C_1 can be obtained by combining Eq. 3.34 and the equilibrium equation (Eq. 3.26) and imposing boundary conditions

(Eq. 3.25). Therefore solving for radial and hoop stress

$$\sigma_r = (p_i - p_e)\frac{(r_i/r)^k - 1}{(r_i/r_e)^k - 1} - p_i \tag{3.35}$$

$$\sigma_t = (p_i - p_e)\frac{(r_i/r)^k(1-k) - 1}{(r_i/r_e)^k - 1} - p_i \tag{3.36}$$

Eqs. 3.35 – 3.36 show that the stress distribution at steady state creep does not depend on on the creep law multiplier, A_o, but is influenced by the exponents m and n. The general solution can be simplified to a homogeneous material by assuming $m = 0$. Using Eqs. 3.35 – 3.36, the von Mises stress of the functionally graded cylinder becomes

$$\bar{\sigma}(r) = \frac{\sqrt{3}}{2}(p_i - p_e)\frac{k(r_i/r)^k}{1 - (r_i/r_e)^k} \tag{3.37}$$

Considering a functionally graded cylinder with creep law $\bar{\dot{\varepsilon}}^c = A_o^*(r/r_i)^m\bar{\sigma}^n(r)F_o^*$ and a homogeneous cylinder with creep properties $\bar{\dot{\varepsilon}}_o^c = A_o\bar{\sigma}^n(r)F_o$, it can be shown that the reduction/increase of creep rate is independent of radial location, r, and only depends on geometry and material constants:

$$\frac{\bar{\dot{\varepsilon}}^c}{\bar{\dot{\varepsilon}}_o^c} = \frac{A_o^*}{A_o}\frac{F_o^*}{F_o}\left[\frac{m+2}{2}\cdot\frac{1-(r_i/r_e)^{\frac{2}{n}}}{1-(r_i/r_e)^k}\right]^n \tag{3.38}$$

3.3.3 Concentric thick walled cylinder analysis

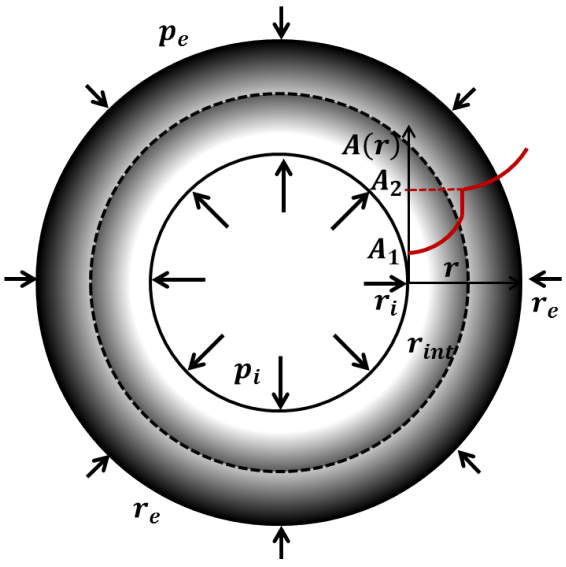

Figure 3.3: Schematic representation of two concentric internally and externally pressurised functionally graded cylinders with a mismatch in creep properties.

The analysis above assumes a radial variation of creep strain rate throughout the cylinder. However, carburisation only tends to occur near the surface of a component and therefore leads to a variation in creep properties over a limited region. To address this variability, in this section a general solution for N-concentric cylinders is derived and it can be used for any $A(r)$ distribution profile.

Before a general solution can be derived, consider a simplified case with 2 concentric thick-walled cylinders (Figure 3.3) under internal and external pressure at steady state creep in plane strain conditions and with interface r_{int}. The assumed creep laws for the inner (subscript 1) and outer (subscript 2) cylinders are

$$\bar{\dot{\varepsilon}}_1^c = A_1 \left(\frac{r}{r_i}\right)^{m_1} \bar{\sigma}_1^{n_1}(r) f_1(t), \qquad r \in [r_i, r_{int}] \tag{3.39}$$

$$\bar{\dot{\varepsilon}}_2^c = A_2 \left(\frac{r}{r_{int}}\right)^{m_2} \bar{\sigma}_2^{n_2}(r) f_2(t), \qquad r \in [r_{int}, r_e] \tag{3.40}$$

where A_1, A_2, m_1, m_2, n_1, n_2 are material constants, $\bar{\sigma}_1$, $\bar{\sigma}_2$ are von Mises stress functions, and $f_1(t)$, $f_2(t)$ are time functions (constants at steady state, $f_1(t) = F_1, f_2(t) = F_2$) of the inner and outer cylinde,r respectively. For simplicity, the creep law exponents are assumed to be equal, $n_1 = n_2 = n$. To ensure inner and outer cylinders do not overlap, radial compatibility at the interface is imposed where radial velocity of the inner cylinder, $\dot{\rho}_1$ is equal to the radial velocity of the outer cylinder, $\dot{\rho}_2$ at r_{int}:

$$\dot{\rho}_1(r_{int}) = \dot{\rho}_2(r_{int}). \tag{3.41}$$

From Eq. 3.27, it is known that $\dot{\rho} = \dot{\varepsilon}_t^c r$, hence combining with Eq.3.30 radial compatibility is satisfied when

$$\dot{\varepsilon}_{t,1}^c(r_{int}) = \dot{\varepsilon}_{t,2}^c(r_{int}) \tag{3.42}$$

As there is an interface pressure acting at r_{int}, the inner and the outer cylinders can be treated as separate internally and externally pressurised structures. The internal cylinder is subjected to internal pressure , p_i, and external pressure (at r_{int}), p_{int}. The outer cylinder is subjected to internal pressure of, p_{int}, and external pressure, p_e. The only unknown is the interface pressure, which is obtained by expanding Eq. 3.42 using the von Mises stress from Eq. 3.37 in terms of hoop and radial stresses ,

and substituting Eqs. 3.35–3.36:

$$\dot{\varepsilon}^{c}_{t,1}(r_{int}) = \frac{\sqrt{3}}{2} A_1 \left(\frac{r_{int}}{r_i}\right)^{m_1} \left[\frac{\sqrt{3}}{2}(p_i - p_{int}) \frac{k_1 (r_i/r_{int})^{k_1}}{1-(r_i/r_{int})^{k_1}}\right]^{n} F_1 \tag{3.43}$$

$$\dot{\varepsilon}^{c}_{t,2}(r_{int}) = \frac{\sqrt{3}}{2} A_2 \left[\frac{\sqrt{3}}{2}(p_{int} - p_e) \frac{k_2}{1-(r_{int}/r_e)^{k_2}}\right]^{n} F_2 \tag{3.44}$$

where $k_1 = (m_1 + 2)/n$ and $k_2 = (m_2 + 2)/n$. The stress state in the creeping concentric pressurised cylinder system is defined by the interface pressure which can be then expressed by equating Eq. 3.43 and Eq. 3.44:

$$p_{int} = \frac{C_2}{1+C_2} p_i + \frac{1}{1+C_2} p_e \tag{3.45}$$

$$C_2 = \sqrt[n]{\frac{A_1}{A_2}\frac{F_1}{F_2}\frac{k_1}{k_2}} \left(\frac{r_i}{r_{int}}\right)^{k_1} \left[\frac{1-(r_{int}/r_e)^{k_2}}{1-(r_i/r_{int})^{k_1}}\right] \tag{3.46}$$

When the inner cylinder is homogeneous ($m_1 = 0$, $k_1 = 2/n$) and at the interface the value of the creep law multiplier is the same for both cylinders ($A_1 = A_2$) and the time constants are equal ($F_1 = F_2$), the n^{th}-root term in Eq. 3.46 simplifies to unity. In such a case the stress distribution depends only on geometry and material constants n and m_2.

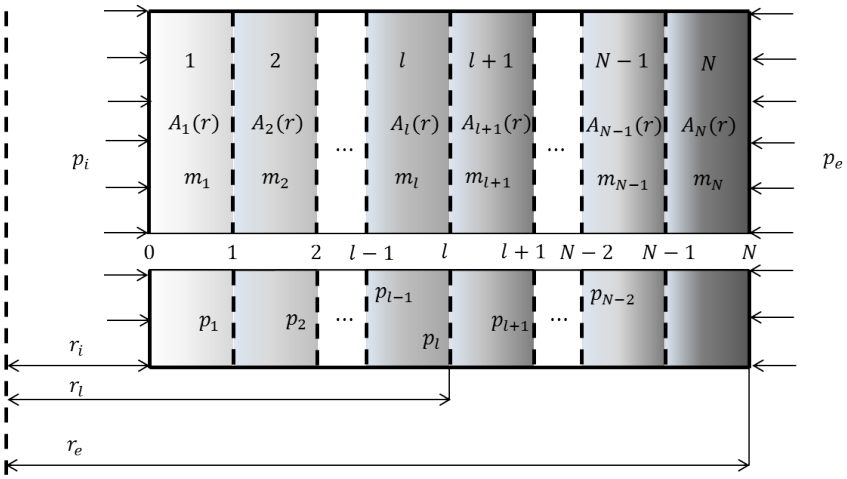

Figure 3.4: Discretisation of a pressurised cylindrical structure consisting of N-concentric functionally graded cylinders.

The proposed power-law $A(r)$ distribution has limited application due to the shape of the function. Nevertheless Eq. 3.45–3.46 can be extended to N-number of cylinders to allow a close approximation to any property distribution function. Consider the a concentric cylinder structure shown in Figure 3.4 which consists of N-concentric cylinders. Each cylinder shares a boundary at r_l ($l = 1 \rightarrow N-1$), where for N-concentric cylinders there are $N-1$ boundaries. The inner and outer

radii are denoted as r_0 and r_N, respectively. On each of the boundaries there is a corresponding interface pressure, p_l. Hence by solving for each p_l the stress state of each cylinder can be found from Eqs. 3.35–3.36. The Eqs. 3.45 – 3.46 can be rewritten as

$$p_l = \alpha_l p_{l-1} + \beta_l p_{l+1} \tag{3.47}$$

$$C_l = \sqrt[n]{\frac{A_l}{A_{l+1}}\frac{F_l}{F_{l+1}}}\frac{k_l}{k_{l+1}}\left(\frac{r_{l-1}}{r_l}\right)^{k_l}\left[\frac{1-(r_l/r_{l+1})^{k_{l+1}}}{1-(r_{l-1}/r_l)^{k_l}}\right] \tag{3.48}$$

where $\alpha_l = C_l/(1+C_l)$, $\beta_l = 1/(1+C_l)$, and $k_l = (m_l+2)/n$. The problem can easily be solved for every p_l by vectorisation – where interface pressures are expressed in matrix form and boundary conditions imposed (Eq. 3.25).

$$\begin{Bmatrix} p_1 \\ p_2 \\ \vdots \\ p_l \\ \vdots \\ p_{N-1} \end{Bmatrix} = \begin{bmatrix} 0 & \beta_1 & 0 & \cdots & 0 & 0 & 0 & \cdots & 0 & 0 \\ \alpha_2 & 0 & \beta_2 & \cdots & 0 & 0 & 0 & \cdots & 0 & 0 \\ \vdots & \vdots & \vdots & \ddots & \cdots & \cdots & \cdots & \ddots & \vdots & \vdots \\ 0 & 0 & 0 & \cdots & \alpha_l & 0 & \beta_l & \cdots & 0 & 0 \\ \vdots & \vdots & \vdots & \ddots & \cdots & \cdots & \cdots & \ddots & \vdots & \vdots \\ 0 & 0 & 0 & \cdots & 0 & 0 & 0 & \cdots & \alpha_{N-1} & 0 \end{bmatrix} \begin{Bmatrix} p_1 \\ p_2 \\ \vdots \\ p_l \\ \vdots \\ p_{N-1} \end{Bmatrix} + \begin{Bmatrix} \alpha_1 p_i \\ 0 \\ \vdots \\ 0 \\ \vdots \\ \beta_{N-1} p_e \end{Bmatrix} \tag{3.49}$$

Eq. 3.49 can be rewritten as $\mathbf{p}_{int} = \mathbf{C}\cdot\mathbf{p}_{int} + \mathbf{b}$ and solved for all interface pressures to give:

$$\mathbf{p}_{int} = (\mathbf{C}-\mathbf{I})^{-1}\cdot(-\mathbf{b}) \tag{3.50}$$

As each interface pressure is known, the stress response within such a cylinder can be found using Eqs. 3.32, 3.35– 3.36.

3.4 Results

Uniaxial loading

Creep property determination

In Chapter 2.2.4, a set of assumptions were listed regarding the methodology for the treatment of carburised stainless steels and the uncertainty associated with the limited number of material data available. For practical applications, it is preferable to avoid unnecessary complexity in analyses. Therefore, it has been hypothesised that treating the carburised layer as uniform with homogeneous material properties would be a preferable simplification.

Consider the real creep test described in section 2.2.4, where a carburised specimen with 57% area fraction carburised is crept under a stress of 260 MPa [24] which results in $A_1/A_2^* = A_b/A_c = 22$ (for $x_1 - x_{int} = 0.25\,mm$). $A_c = A_b/22$ has been obtained by Chevalier [24] assuming the 2-bar model. To investigate how creep deformation and creep life analysis is influenced by such a simplification, results have to be compared with a model accounting for changing material properties with respect to x towards the surface. This implies that certain assumptions must be made about the functional form of $A(x)$. Considering the uncertainty regarding carburised layer materials data, variability from hardness measurements, the "true" functional form of the carburised layer creep properties is unknown. The purpose of this analysis is to investigate how different functional forms of $A(x)$ that give the same global creep rate influence the local stress magnitude, state and creep damage. Therefore, to investigate the effects of the homogeneous carburised material assumption and the effects of more severe changes of $A(x)$ towards the surface 2-bar, linear and parabolic distributions are assumed. Linear and parabolic in this analysis are functions that are linear and parabolic in logarithmic space: $A(x) = A_1 10^{ax}$ or $A(x) = A_1 10^{ax^2}$, where a is a fitting constant. Table 3.1 shows the assumed functional forms of $A(x)$ with fitting constant a [1]. The parabolic function is used to qualitatively represent the effects of diffusion where there are severe material property change towards the surface and at the bulk and the carburised layer interface $A(x = x_{int}) = A_1 = A_b$. The linear functional form investigates the effects of less severe material property changes.

Name	$A(x)$	a
2-bar	$A_1/22$	N/A
Linear	$A_1 10^{ax}$	-2.5381×10^{-2}
Parabolic	$A_1 10^{ax^2}$	-3.5782×10^{-4}

Table 3.1: The assumed creep law distribution A(x) with calculated parameters using Eq. 3.22 .

Figure 3.5a shows that at steady state creep conditions, the stress in the creep-resistant carburised region increases relative to the nominal applied stress whilst in the and bulk area decreases to maintain strain rate compatibility. The increase in stress depends on the assumed creep property distribution through the functionally graded region (Figure 3.5b). The 2-bar assumption underestimates the local stress state in the more creep resistant region relative to the linear and parabolic distributions. However, note that all models will identical creep strain accumulation within

[1] Fitting constant a was obtained from Eqs. 3.21 - 3.24 using SciPy (Python) root-finding solver *fsolve*

the specimen in the steady state.

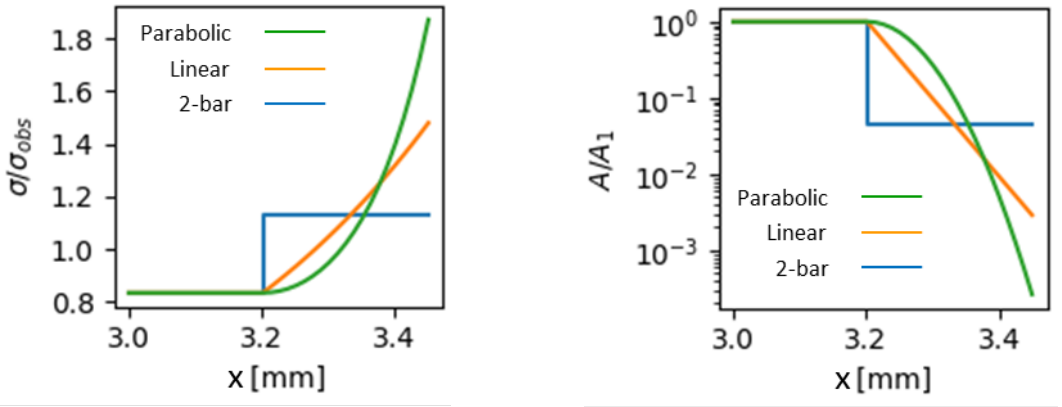

(a) Normalised stress;

(b) Normalised creep law multiplier properties.

Figure 3.5: Stress state of $a_f = 57\%$ carburised specimen at steady state creep using three different creep property distribution profiles.

Creep lifetime estimation

Considering that carburisation reduces creep ductility, it is useful to perform a simple creep lifetime estimation of carburised structures using Eq. 3.18. The creep lifetime can be estimated by making assumptions about the mismatch in creep properties (A_1/A_2^*) and considering how the lifetime of the more creep resistant structure is influenced by reducing creep ductility compared to the homogeneous structure. Assuming that the homogeneous material creep ductility is $\varepsilon_{f,1}$, the lifetime of a homogeneous structure under stress σ_{obs} is

$$t_{f,1} = \frac{\varepsilon_{f,1}}{\sigma_{obs}^n A_1}. \tag{3.51}$$

For the structure shown in Figure 3.1 and assuming that the creep ductility of the creep resistant layer is reduced by some factor, $\varepsilon_{f,2}/\varepsilon_{f,1} = 1/f_c$ ($f_c > 1$), the time for creep damage initiation in the FG material, $t_{f,2}$, is

$$t_{f,2} = \frac{1}{f_c}\left(\frac{\sigma_{obs}}{\sigma_1}\right)^n t_{f,1}. \tag{3.52}$$

Figure 3.6 shows a colour plot of normalised failure times for 0-15% carburised specimens using Eqs. 3.51–3.52. For low area fractions the carburised material gains no benefit in increased lifetime due to reduced overall creep rate, but instead sees reduced lifetime due to reduced ductility. For larger area fractions and lower effects on ductility (lower f_c) there is the potential for an increased lifetime relative to the

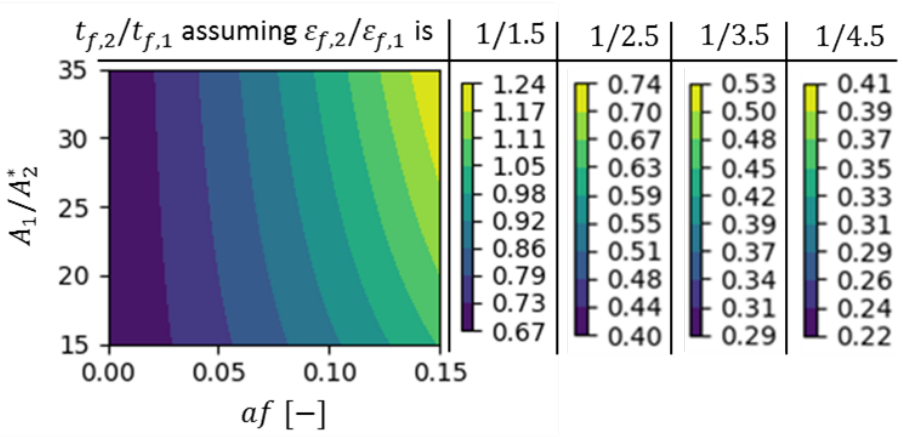

Figure 3.6: Creep damage initiation time of a carburised structure normalised to a homogeneous structure assuming various area fractions and ductility ratios.

non-carburised structure. For $\varepsilon_{f,2}/\varepsilon_{f,1} = 1/3.5$ and A_2^*/A_1 the creep lifetime can be extended when $a_f > 38\%$[2].

Pressurised carburised cylinder

Stress state

The derived equations (Eqs. 3.47-3.48) has been used to analyse the stress response in a carburised cylinder with $r_i : r_e = 1 : 1.5$ and 50% area fraction carburised. The creep distribution profiles are according to Figure 3.5b with the *average* reduction in creep law multiplier being a factor of 22. Figure 3.7 shows the redistributed stress state normalised to that in a homogeneous cylinder ($n = 10.18$ and $A_o = A_b = 8.876 \times 10^{-35}$) for each distribution profile.

Similar to Figure 3.5a, an increased resistance to creep deformation causes an increase in hoop (Figure 3.7a) and axial stress (Figure 3.7b), consequently in von Mises stress (Figure 3.7c) in the carburised region. For the given geometry the parabolic distribution profile leads to almost a doubling of stress compared to the homogeneous material. The bi-metallic cylinder (2-bar) model leads to a lower stress state towards the outer surface. However, the bulk responses for all distribution profiles are almost identical.

$$T = \frac{(\sigma_r + \sigma_t + \sigma_z)/3}{\bar{\sigma}}. \tag{3.53}$$

Figure 3.7d shows the stress triaxiality and it can be seen that an increase in the creep resistance results in a reduction of stress triaxiality, relative to that in the bulk

[2]The current suggestion for carburised layer creep deformation and creep ductility properties from [24]

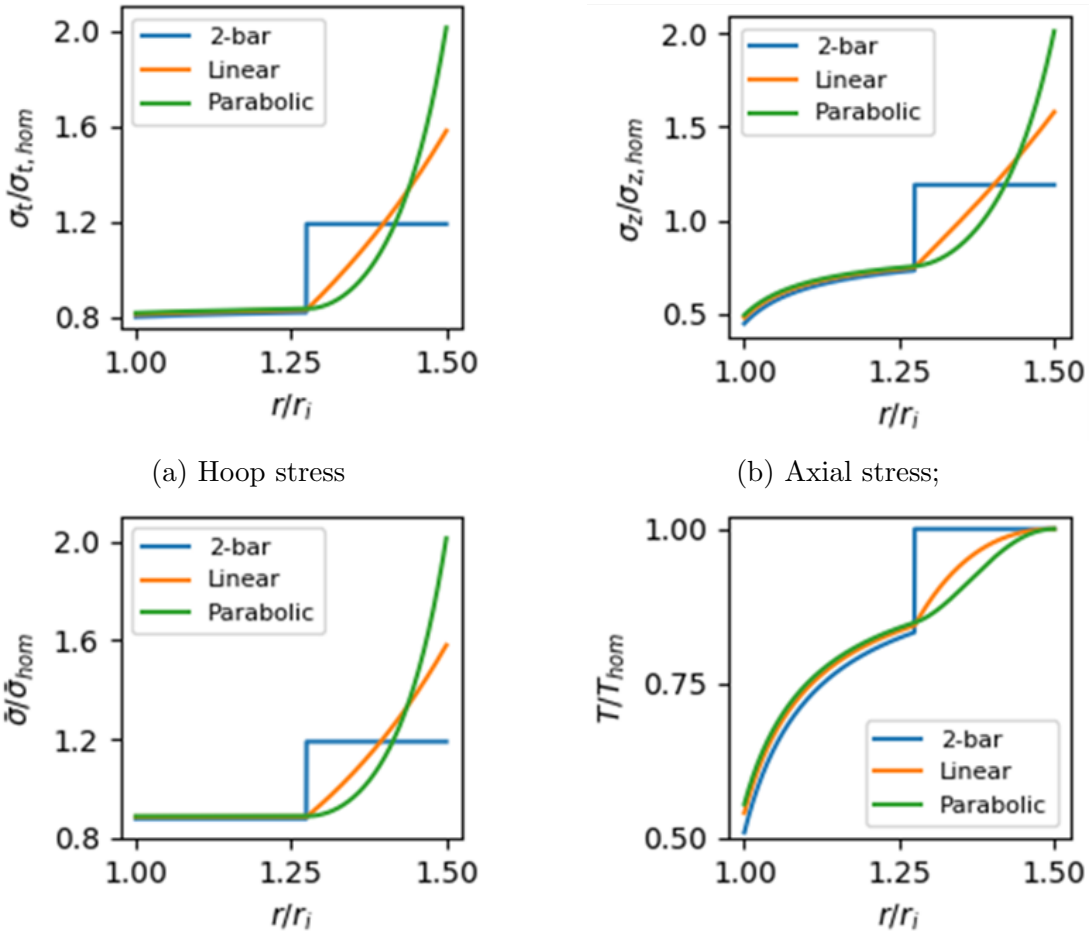

(a) Hoop stress

(b) Axial stress;

(c) von Mises stress;

(d) Stress triaxiality.

Figure 3.7: Stress state in a carburised internally pressurised cylinder assuming different creep profiles with the same *averaged* reduction in creep law multiplier.

section, T_{hom}. The *2-bar* model predicts that the stress triaxiality in the carburised layer is unchanged from the homogeneous bulk value, where as *Linear* and *Parabolic* models show gradual increases of T/T_{hom} to unity at the outer surface. The normalised stress triaxiality and von Mises stress are not equal for different models in the bulk section, and in the graphs there can be seen a slight difference between each distribution profiles. This is due to the geometric effects, as for $r_i/r_e \rightarrow 1$ the normalised von Mises stress and stress triaxiality for all distributions converge to the same solution. For smaller carburised area fraction, the differences in stress triaxiality for different creep law distribution profiles with the same *average* values become insignificant.

Creep damage estimation

To evaluate the creep damage initiation time in pressurised cylinders, the multiaxial stress must be taken into account. The Spindler fraction [50] (Eq. 2.15) has been used to modify the ductility of the material. The normalised creep damage initiation

time compared to that of the uncarburised (homogeneous) cylinder is calculated as

$$\frac{t_f^c}{t_f} = \frac{\varepsilon_f^{c*}}{\bar{\dot{\varepsilon}}_c^c} \Bigg/ \frac{\varepsilon_f^*}{\bar{\dot{\varepsilon}}_{hom}^c} \tag{3.54}$$

where t_f^c/t_f is the normalised creep damage initiation time relative to that of a homogeneous cylinder, ε_f^{c*}, ε_f^* are the multiaxial ductilities of carburised and homogeneous cylinder respectively, and $\bar{\dot{\varepsilon}}_c^c$, $\bar{\dot{\varepsilon}}_{hom}^c$ are the creep rates of carburised and homogeneous cylinders respectively. The normalised creep damage initiation time is a function of radius as stress is not uniform through the cylinder. A value of t_f^c/t_f below unity correspond to increased creep damage due to carburisation and, therefore, reduce the lifetime to damage initiation.

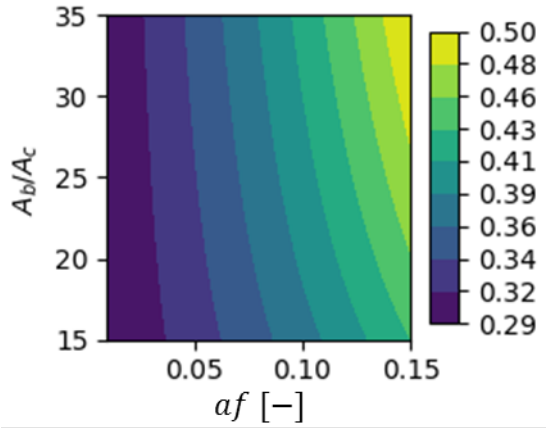

(a) At $r = r_e$ (carburised surface), $r_i : r_e = 1 : 1.1$

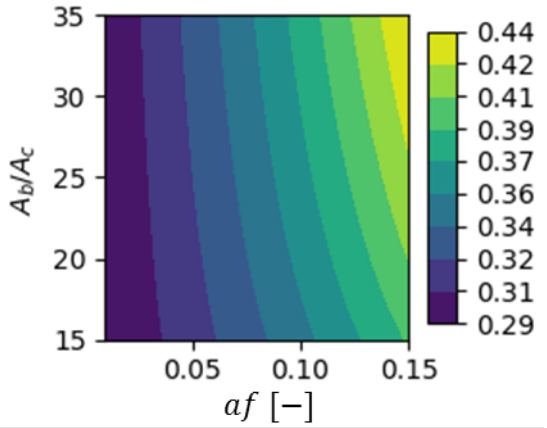

(b) At $r = r_e$ (carburised surface), $r_i : r_e = 1 : 1.5$

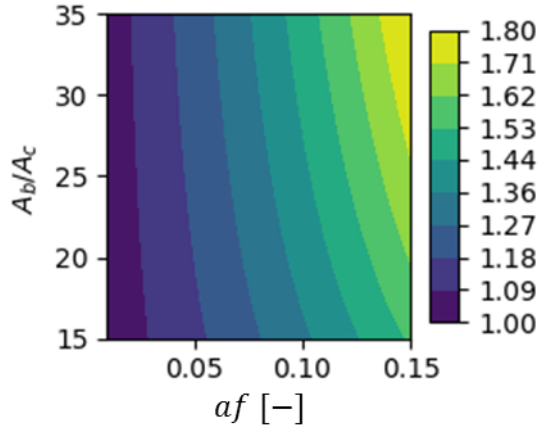

(c) At $r = r_i$ (bulk), $r_i : r_e = 1 : 1.1$

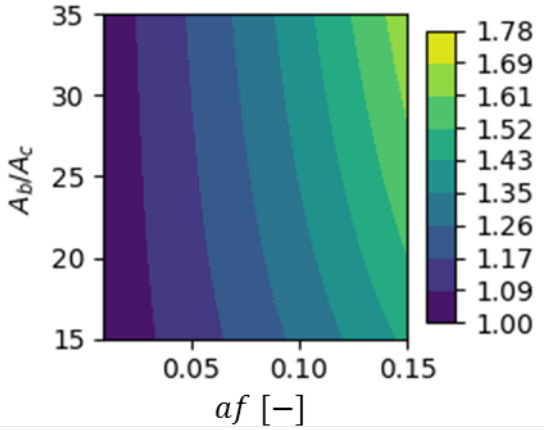

(d) At $r = r_i$ (bulk), $r_i : r_e = 1 : 1.5$

Figure 3.8: Creep damage initiation, t_f^c/t_f, assuming steady state creep and $\varepsilon_f/\varepsilon_f^c = 3.5$

Figure 3.8 shows a contour plot of Eq. 3.54 assuming the two homogeneous concentric cylinder model (Eq. 3.45–3.46, $k_1 = k_2 = 2/n$). Figures 3.8a and 3.8b

show the normalised creep damage initiation times of thin ($r_i : r_e = 1 : 1.1$) and thick ($r_i : r_e = 1 : 1.5$) cylindrical structures at the outer surface assuming the carburised layer uniaxial creep ductility is reduced by factor of 3.5. It can be seen that multiaxial effects are more predominant in thick wall pressure vessels (Figure 3.8b) and cause a reduction in creep life compared to thin components (Figure 3.8a). Despite the reduction in creep rate, the creep damage initiation at the surface is strongly influenced by the assumed creep ductility. However, the creep damage initiation in the bulk section (Figures 3.8c–3.8d) is reduced due to the combined effects of reduced stress triaxiality and the reduction in creep rate.

3.5 Summary and discussion

The analytical solutions presented in this chapter provide simplified methods for creep lifetime evaluation. The mathematical proof using bounding theorems shown in section 3.2 shows that the average creep energy dissipation rate of a non-homogeneous structure is less than that of a homogeneous structure. This leads to the conclusion that a carburised layer with a reduced creep rate will lead to a reduced overall creep deformation rate at the steady state. However, the result does not provide any information about the stress redistribution phase to the steady state, local deformation, or the influence of carburisation on local stress state, which influence multiaxial ductility.

The local stress magnitude and triaxiality effects have been investigated in section 3.3. The presented uniaxial solution is a modification of a well-known creep problem [134] with two creeping structures at steady state under uniaxial loading. The modification of the analytical expression allows the derivation of a method to estimate the local creep law properties and the uniaxial stress state assuming any creep distribution profile. The results show that more creep resistant regions (e.g.a carburised layer) have increased stress magnitude to maintain a uniform creep deformation rate in the structure. Consistent with the general theory of section 3.2, the total creep rate of a carburised structure is reduced by some factor which depends on the assumed *average* reduction in creep law multiplier and the area fraction carburised.

Carburisation leads to reduced steady state creep rate and is a positive characteristic because it could, in theory, extend the lifetime of a component. However, results indicate that this is influenced by the area fraction carburised and thet the lifetime is also strongly influenced by the assumed carburised layer creep ductility. According to the current evidence [24], the creep ductility of the carburised layer with a characteristic depth of $250\mu m$ is reduced by a factor of ≈ 3.5 compared to the bulk material. Considering the small depth of carburised layer, it can be as-

sumed that the total area fraction carburised is small compared to the component's thickness for most components. The results in section 3.4 show that small area fraction carburised is more detrimental in terms of creep lifetime compared to larger area fraction carburised because it causes the creep strain rates to be closer to the homogeneous values. Figure 3.6 shows that components with $a_f < 15\%$ do not gain any benefit from the reduced creep strain rates. However, Figure 3.6 clearly outlines where conservatism arises, if the structure is treated as homogeneous but with reduced creep ductility. A homogeneous assumption for creep deformation leads to a creep damage increase by the same factor as the reduced ductility ($t_f^c/t_f = \varepsilon_f^c/\varepsilon_f$). The uniaxial and concentric cylinder solutions take into account the benefit of reduced creep rate. For $a_f = 10\%$ with an average reduction of creep rate $A_b/A_c = 22$, and a ductility ratio $\varepsilon_f^c/\varepsilon_f = 1/3.5$ the time for damage initiation reduces by only a factor of 2.5 assuming the uniaxial model. Assuming a constant reduction of creep ductility across various a_f, the creep damage initiation time in carburised components increases with increasing a_f of carburisation.

The concentric cylinder analysis allows investigation of the effects of carburisation on stress triaxiality by considering various geometries. The analytical solution shows that at the steady state the stress response assuming various distribution profiles is comparable for thin components. For thin components, the stress state approaches the uniaxial steady state solution. Functionally graded pressure vessels under internal pressure and with a creep resistant outer surface experience a reduction in stress triaxiality at the bulk section. This can lead to increased creep ductility and reduced creep damage in the bulk section if the carburised layer remains intact. The stress triaxiality in the carburised section depends on the assumed creep distribution profile. The two homogeneous concentric cylinder model predicts unchanged stress triaxiality in the carburised layer, and hence can result in a more conservative assessment than other models.

The thickness of the pressure vessel influences the creep damage initiation time in the carburised layer. The normalised creep rate with respect to the homogeneous case in a thick component with the same area fraction carburised is higher compared to thin pressure vessels. Therefore, a thicker geometry leads to accelerated normalised creep damage accumulation in the carburised layer. Nevertheless, the creep damage in the bulk section is reduced as long as the carburised layer stays intact and provides the benefit of reduced stress triaxiality and reduced creep rate.

A major disadvantage of using analytical solutions for creep lifetime assessment is that the derived analytical solutions do not consider stress redistribution effects prior to steady state creep that arise due to the mismatch in tensile properties. A mismatch in tensile properties will influence the initial creep strain rate. The range of applicability of the proposed analytical solutios can be determined from the stress

redistribution time. Additionally, the initial loading can induce multiaxial effects that can alter the creep lifetime. It can be shown analytically that under uniaxial loading a multiaxial stress state can be induced in a cylinder with a carburised layer where the carburised layer has higher yield stress and Young's modulus (Appendix A.1). Therefore to address the limitations of the steady state solutions, a numerical approach is adopted in the following chapters to investigate the effects of carburisation.

Chapter 4

Creep analysis of uniaxial carburised specimens

4.1 Introduction

This chapter is composed of three studies where behaviour of carburised uniaxial geometries is investigated using Abaqus finite element modelling software. The first study considers a uniaxial creep specimen where the effects of carburisation on creep response are investigated at high-stress conditions. The second study considers a neural network approach to determine the carburised layer tensile properties. The third study considers creep response of a carburised structure for various area fractions carburised, various stresses, and reduced ductility factors using the calculated material tensile properties from the neural network model.

As discussed in section 2.2.3, there have been attempts to characterise carburised layer elastic, plastic and creep properties by observing the global response of carburised specimens. However the analysis in the literature did not consider detailed stress redistribution effects that might arise due to the mismatch in material properties between base and carburised materials. Additionally, as carburised layer properties cannot be measured directly, certain assumptions must be made regarding the material property distribution. In Chapter 3, it was shown that the same global response on plastic loading and steady state creep can be achieved by assuming different distribution profiles, but the question of how this might affect creep strain accumulation was not answered. Therefore, this chapter investigates which material properties influence creep strain accumulation the most at various stress levels; how material distribution profiles might influence creep redistribution; if it is possible to develop a predictive model that could approximate the stress state in a carburised component; and investigates the conditions under which the structure might gain benefit from the reduced creep strain accumulation.

4.2 Impact of material properties on accumulated creep strain

Currently, most of the carburised material mechanical testing is performed on uniaxial specimens that have been carburised before mechanical testing (pre-carburised). In AGR components, carburisation occurs during operation, i.e. components are being carburised while subjected to load. Therefore how pre-carburisation of a specimen affects measured material behaviour, and how this measured behaviour should be applied in a carburising component need to be addressed. There is still major uncertainty regarding material property distributions and how these are influenced by increased carbon concentration. It is known that carburisation increases Young's modulus, yield properties and reduces creep rate. Therefore in this chapter a qualitative study is presented on the impact of mechanical properties on measured creep behaviour of a material that has been pre-carburised and material that is being carburised during a forward creep test. The proposed model is based on Fick's second law of diffusion with changing material properties across the thickness according to carbon concentration.

4.2.1 Model description

A 3-D uniaxial specimen has been modelled under constant load where the tensile load is applied by a pin which is treated as a rigid body. Material properties at $T = 550^{o}C$ are used, and the simulation time for the creep response, t_{end}, was chosen to be 500 hours. The specimen geometry and material properties were provided by Sandor Palko who performed uniaxial tensile tests and creep tests in a custom built creep rig to investigate duplex oxide growth under creep conditions [13]. During the experiments material was subjected to carburising CO_2. The material was not pre-carburised prior to the test, instead it was carburising/oxidising over 500 hours while under constant load (equivalent to $\sigma_{eng} = 350\,MPa$).

Material property definition

The baseline material properties for 316H stainless steel that have not been carburised are taken here as those obtained by Sandor Palko from a uniaxial tensile test at $550^{o}C$ loaded to 350 MPa engineering stress or 408 MPa true stress in an inert gas environment (Argon). The baseline properties are given in Table 4.1.

Oxidation and carburisation create a hardened surface layer due to ingress of carbon. As discussed in sections 2.2.4 – 2.2.4, there is a correlation between increase in carbon concentration and changes in material properties. causes increases

E_b [GPa]	ν
157	0.3

(a) Elastic properties;

σ [MPa]	ε_b^p [%]
153.8	0
217.0	1.0
252.6	3.0
291.7	5.6
315.1	7.9
339.1	10.2
362.2	12.0
386.5	14.0
395.1	14.4
403.8	14.9
408.0	15.1
430.0	16.1

(b) Plastic properties;

A_o [–/hr]*	n
6.2892×10^{-32}	10.18

(c) Creep constants for Norton creep law.
∗ *The creep law multiplier was determined numerically*

Table 4.1: Material properties implemented in Abaqus of 316H stainless steel at 550^oC;

in yield stress and Young's modulus and reductions in creep rate and creep ductility. To define the relationship between carbon concentration and corresponding material properties, certain assumptions must be established about the diffusion process and the correlation between carbon concentration and mechanical properties. The purpose of this model is not to model the process of carburisation accurately but to provide a reasonable functional form of the non-uniform material properties through the carburised layer and investigate qualitatively how changes in material properties at the surface can influence creep tests subjected to high stresses.

The carburised layer properties are defined based on carbon concentration within the carburised layer. The carbon distribution profile over 500 hours can be approximated by using Fick's law of diffusion Eq. 2.29. The process of carburisation can be viewed as a simplified case of a semi-infinite solid with the surface exposed to carburising gas. If the carbon concentration at the surface is taken as constant and the duplex oxide layer is ignored, a solution to the problem can be found in most textbooks on diffusion, and the exact derivation can be found in [92, 99]. The resulting equation with fixed surface concentration, $c(x = 0, t) = c_s$, and for a semi-infinite body, $c(x = \infty, t) = c_0$, leads to the following solution:

$$c(x,t) = c_s - (c_s - c_0)erf\left(\frac{x}{2\sqrt{D_c t}}\right), \tag{4.1}$$

where $c(x,t)$ is the carbon concentration at position x and time t, c_0 is the initial carbon concentration in the material, D_c is the diffusivity of the carbon in steel, and $erf(x/(2\sqrt{D_c t}))$ is the error function.

Considering that the material properties are related to carbon concentration the

constant surface boundary condition ($c(x = 0, t) = c_s$) results in an already hardened surface at $t = 0$ and this is not changing with time. Such an assumption is unrealistic because at $t = 0$ the surface of the material is homogeneous, therefore, the existing equation has to be modified to account for a variable surface concentration over time. As discussed in section 2.2.1, carburisation is induced by oxidation. Oxidising species, such as CO_2/CO, diffuse through the porous oxide and cause carburisation through an exothermic reaction [73, 85, 91]. Considering that carbon-containing oxidising agents are diffusing through the oxide, Eq. 4.1 can be modified to account for the oxide layer:

$$c(x,t) = c_s - (c_s - c_0)erf\left(\frac{x + x_{ox}}{2\sqrt{D_c t}}\right); \tag{4.2}$$

$$x_{ox} = \frac{1}{t_{end}} \int_0^{t_{end}} 2\sqrt{D_c t}\, dt; \tag{4.3}$$

where x_{ox} is the thickness of the oxide layer and x is the distance from the oxide-carburised layer interface. It has to be noted that several assumptions have been made in Eqs. 4.2-4.3 about the oxide layer and carbon diffusion that need to be addressed.

In Eq. 4.2, oxide is assumed to grow according to parabolic growth kinetics [17, 99]. The thickness of the oxide layer, x_{ox}, is assumed to be constant and is calculated by integrating the parabolic rate equation over the carburisation time. As explained in section 2.2.2, oxidation of austenitic stainless steel is a complex process where the rate of oxide formation is influenced by many factors, including reactive components, state of stress, surface finish. Therefore, the presented definition of the oxide layer is a simplification that avoids the initial step change of the concentration at the surface and the metal.

Another assumption is that diffusivity of carbon oxidising agent through the oxide and diffusivity of carbon into parent material is the same and is a constant. As discussed in sections 2.2.3 and 2.2.4, carburisation can cause increased amounts of second phase particles, such as $M_{23}C_6$ carbides. Carbides form at the grain boundaries and lead to decreased concentration of solute elements. Carbide formation in 316H stainless steel slows the rate of carbon penetration into the metal by diffusion [17, 107]. This implies that the diffusivity of carbon in austenite is not constant and will change with changes in microstructure [91]. However, the purpose of this model is to obtain a material property distribution through the carburised layer that is changing with time. Therefore, the proposed diffusion model is justified for this analysis. The assumed constants of Eqs. 4.2-4.3 can be found in Table 4.2.

In this study the carburised material properties are assumed to be related to

c_s [wt%]	c_0 [wt%]	D_c [mm^2/s]	x_{ox} [mm]
0.5	0.05	1.78×10^{-9}	0.084

Table 4.2: Carburisation properties at T=550^oC, diffusivity of carbon taken from [135].

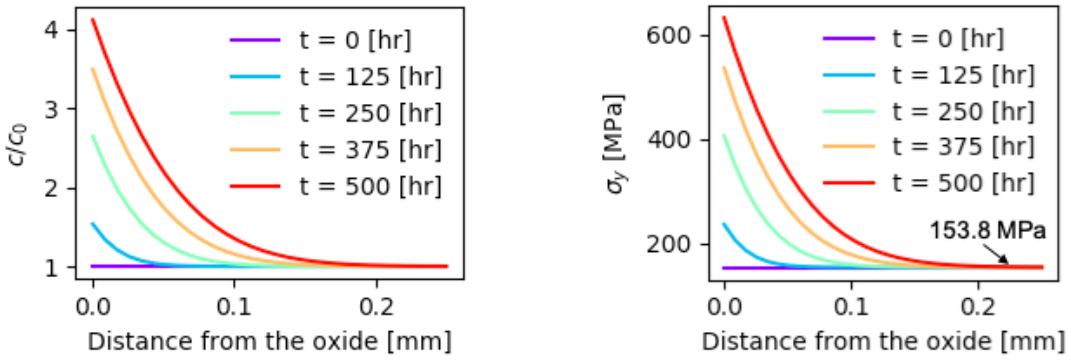

(a) Normalised carbon concentration

(b) Yield stress distribution

Figure 4.1: Representation of material property change over time according to Eq. 4.4.

carbon concentration by the following relationship:

$$M(x,t) = \left(\frac{c(x,t)}{c_0}\right)^m \times M_0 \tag{4.4}$$

$M(x,t)$ is the material property at location x (distance from the oxide) and time t. M_0 is the bulk or baseline material property (e.g. E_b), and m is an empirical constant which for this study is either 1, for Young's modulus and the stress to reach a specific plastic strain, or -1 for the creep law multiplier. An example of how yield stress is scaled is showed in Figure 4.1, where yield stress increases proportionally with carbon concentration. The plastic stress-strain response (Pl) (Table 4.1b) is scaled the same as σ_y according to carbon concentration. The creep law multiplier is taken to be inversely proportional to the carbon concentration and hence reduces with increasing carbon weight percent.

In this study two types of models are considered. In the *carburising* (C) models the material properties will change over time. In *pre-carburised* (PC) models, it is assumed that $M = M(x, t = t_{end})$, i.e. no evolution of the material properties takes place within the carburised layer. It should be noted that Eq. 4.1 with $m = \pm 1$ is not intended to be an accurate predictor of material response. Instead the effect of carburisation on Young's modulus is unlikely to be increased by factor of 4 as Figure 4.1a predicts. Instead the models are used to investigate the difference between carburising and pre-carburised models.

Model implementation in Abaqus

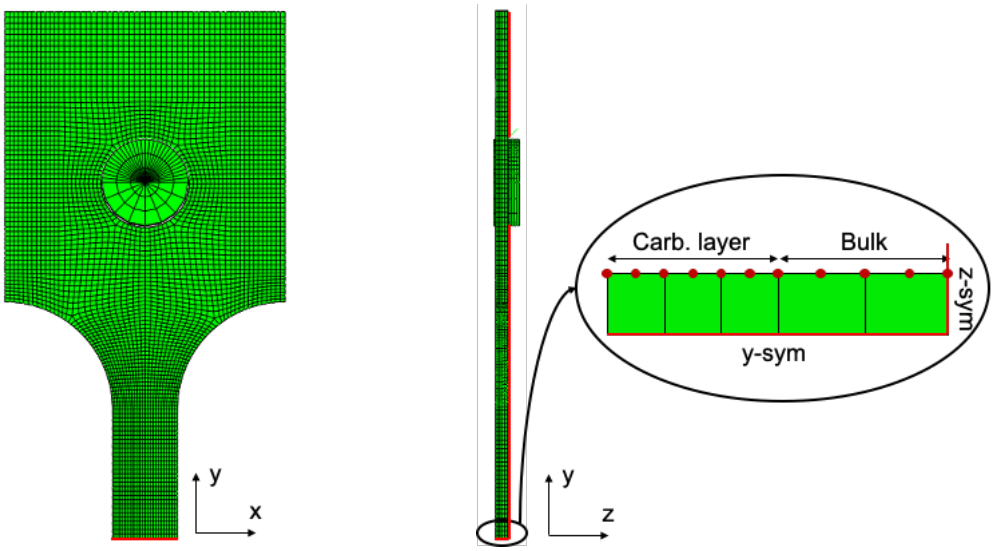

(a) Front view

(b) Side view with magnified mesh showing boundary conditions.

Figure 4.2: The implemented uniaxial specimen geometry in Abaqus.

The uniaxial creep response is solved as a 3-D non-linear contact problem with a rigid body (pin) pulling the specimen. The applied load at the pin is 1151.6 N which equates to an engineering stress of 350 MPa (true stress of 408 MPa). The specimen geometry (Figure 4.2) is in accordance with the test specimen dimensions provided by Palko [13]. The exact dimensions of the specimen can be found in Appendix B.1.1.

A quarter of the specimen has been modelled imposing appropriate boundary conditions (red lines in Figures 4.2a and 4.2b) to account for the symmetry on the x-z plane (y-sym) and x-y plane (z-sym). Quadratic coupled temperature-displacement elements with reduced integration, C3D20RT, were used in this model so that an artificial temperature field could be introduced in conjunction with the USDFLD subroutine to define material properties at 100 different time steps according to Eqs. 4.2 and 4.4. The modelled *hardened* layer spans three quadratic elements. The purpose of this study is to qualitatively investigate the effects of pre-treatment and how material properties impact the creep response and not to fit any particular carburised material data. Hence the thickness of three elements (Figure 4.2b) for the carburised layer is assumed to be sufficient to provide information about the forward creep tests of carburised specimens.

In total 15 models have been analysed, of which: one is a homogeneous model; 7 are pre-carburised; and 7 carburising. In each model a different combination of scaled material properties were used. For example, $M^*(El, Pl)$ and $M(El, Pl)$ denote the models with changed elastic and plastic properties for the pre-carburised

and carburising models, respectively.

4.2.2 Homogeneous specimen

The stress and strain response of the homogeneous specimen is considered first because this will be the reference test case. Upon initial loading the peak stress at the gauge section from the experimental data has been deduced as 408 MPa. The FEA calculated an almost identical result of 408.3 MPa at the gauge section and demonstrates that appropriate bulk material properties have been used. The multiplying creep law constant (A_o) has been estimated by comparing the experimental value of minimum creep strain rate ($\dot{\varepsilon}^c_{exp} = 2.62 \times 10^{-5}\, h^{-1}$) to the numerical ($\dot{\varepsilon}^c_{fe}$) and the creep law multiplier was adjusted accordingly. The estimated value of the creep law multiplier A_o is 6.289×10^{-32} and, at a stress of 408.3 MPa this gives a creep rate 2.3% lower than the minimum experimental strain rate in Figure 4.3e. Due to geometric non-linearity, the inelastic strain rate is not the same as the creep strain rate. Figure 4.3e shows that the inelastic strain rate, $\dot{\varepsilon}^t_{fe}$, is 21.8% larger than the recorded creep strain rate. As the material is creeping, its cross-sectional area is changing, and the lower cross-sectional area causes an increase in stress and plastic strain. At $t = t_{end}$ the final stress in the homogeneous test case was 416.0 MPa (Figure 4.3a).

Although the stresses within the homogeneous material in the gauge section are uniform, Figure 4.3b shows that towards the shoulder there is an increase in stress triaxiality. By calculating the Spindler fraction (Eq. 2.15), it can be seen that the multiaxial ductility decreases towards the shoulder. Hence, taking into consideration the stress state and triaxiality effects, the creep damage in the uniaxial specimen was calculated using Eq. 2.16, where the uniaxial creep ductility was taken as 2.6% according to R66 advice [105] (Figure 4.3d). The average damage in the gauge section is estimated to be $\omega^c = 0.51$. However, the slight increase in stress triaxiality together with stress redistribution due to geometrical effects shows a region with increased creep damage of $\omega^c = 0.526$ (the grey region in Figure 4.3d) near the specimen shoulder.

4.2.3 Carburised specimens

The results of the carburised specimen models presented in this section are normalised to the homogeneous specimen results at the same time. The presented results have been extracted from the gauge section at the most carburised point (surface) and the bulk material (centre of the specimen). The following section is a summary of models that highlight the impact of material pre-treatment and material property influence on creep strain accumulation.

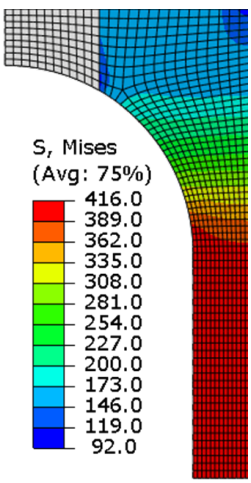

(a) von Mises stress;

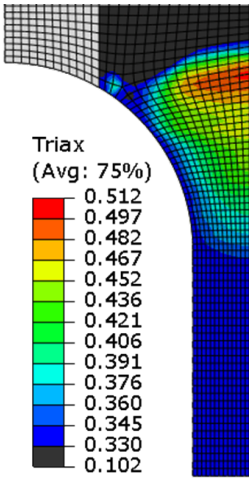

(b) Stress triaxiality;

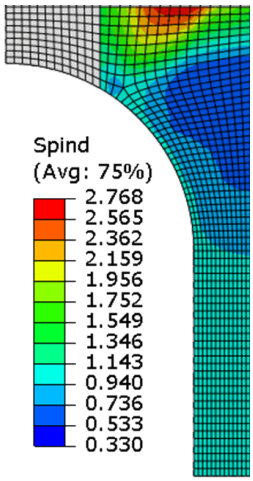

(c) Spindler's multiaxial ductility factor;

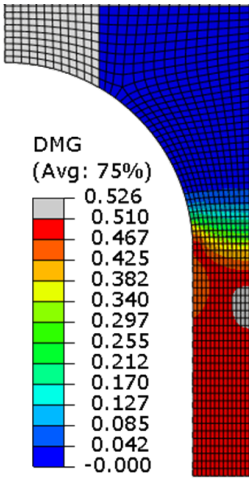

(d) Estimated damage assuming ε_f = 2.6%;

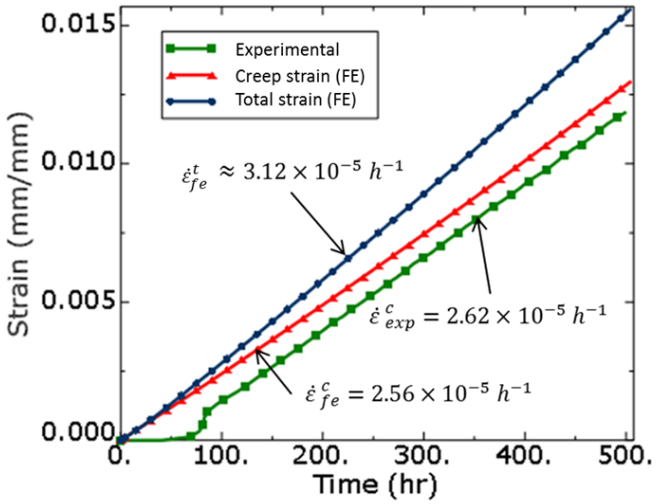

(e) Creep strain from FEA and experiment [13].

Figure 4.3: FEA results of the homogeneous specimen (4.3a - 4.3d at $t = t_{end}$ = 500 hr).

Stress response

Figure 4.4 show von Mises stress change at the surface (a,b), and bulk section (c,d) for pre-carburised (a,c) and carburising (b,d) models. For the pre-carburised models (a,c), it can be seen that the increase in material yield stress and hardening curve elevate the stress in the carburised layer to an equivalent value of 2.18–2.2 times higher than the reference (homogeneous) model. Consequently the bulk material experiences a reduction in stress ($0.76\bar{\sigma}_{hom}$). However, during creep the increased stress magnitude in the carburised layer is redistributed and stresses relaxes. From Figure 4.4 (a), the $M^*(El, Pl, Cr)$, $M^*(Pl, Cr)$ test cases show identical stress relaxation behaviour, the $M^*(El, Pl)$ case, at the surface, shows that after 500 hours the normalised stress has almost reduced to unity. $M^*(El, Cr)$ in Figure

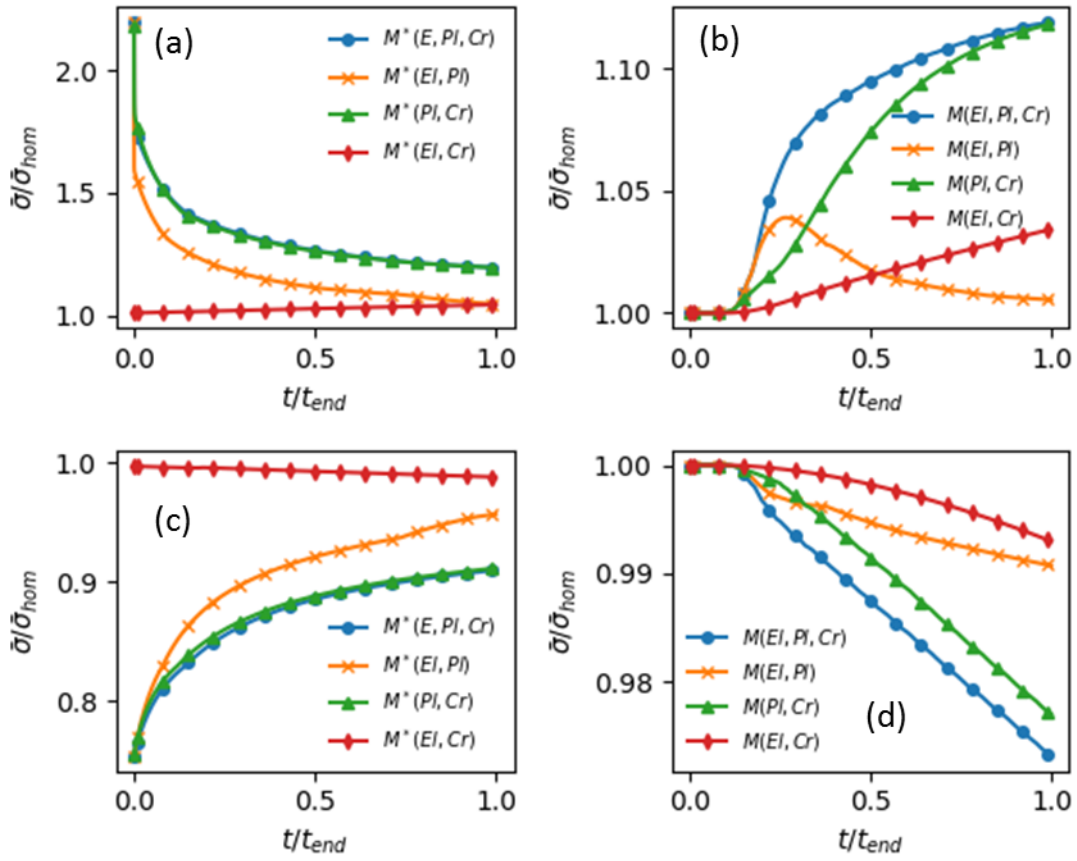

Figure 4.4: von Mises stress change over time for selected models. (a) At the surface, pre-carburised; (b) at the surface, carburising; (c) in the bulk, pre-carburised; (d) in the bulk, carburising.

4.4 (a,c) show that changes in Young's modulus initially give insignificant changes in stress response compared to the homogeneous specimen, and as time progresses the stresses in the bulk and carburised layer redistribute towards the steady state solution.

The carburising models, Figure 4.4 (b, d), show very different behaviour. Initially the stress distribution is identical to the homogeneous test case as no carburisation has occurred. However by about $t = 0.16t_{end}$ it can be seen that all models experience stress redistribution effects. The $M(El, Pl)$ test case experiences some increase in the normalised stress in the carburised layer and a decrease in stress in the bulk; however, this is due to the fact that the stress is increasing in the homogeneous case due to non-linear effects. By normalising the $\bar{\sigma}$ with the increasing $\bar{\sigma}_{hom}(0) < \bar{\sigma}_{hom}(t_{end})$, the stress appears to be decreasing in the bulk. The carburising $M(El, Pl, Cr)$ and $M(Pl, Cr)$ models approaching the steady state solution without the major stress relaxation that occurs in the $M^*(El, Pl, Cr)$ and $M^*(Pl, Cr)$ models. However, at the steady state both pre-carburised and carburising models achieve the same steady state response, as they have the same creep property distribution (Appendix

B.1, Figure B.2).

Plastic strain response

The changes in stress in the bulk material are shown in Figure 4.5. The rapid stress

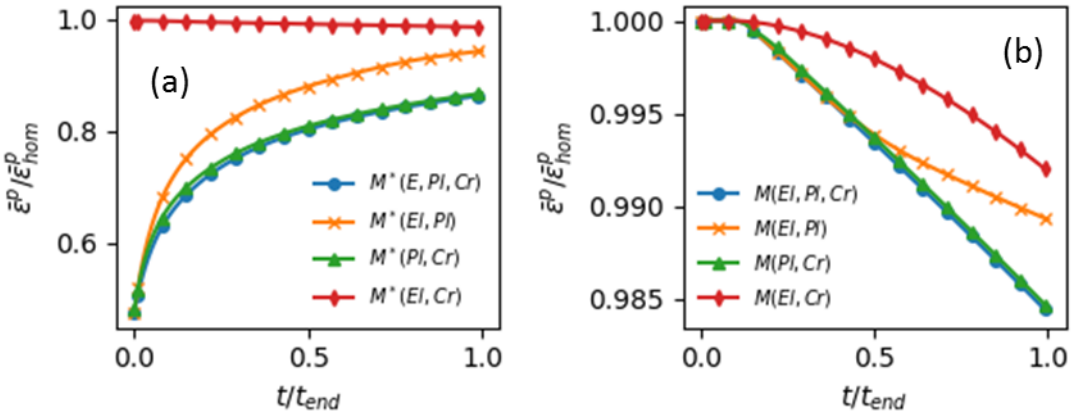

Figure 4.5: Plastic strain change in the bulk material over time for chosen models.(a) Pre-carburised; (b) carburising models.

relaxation in pre-carburised regions from the high initial stress there due to increased yield strength and hardening causes additional plastic strain accumulation in the bulk phase 4.5 (a). The decrease in normalised plastic strain for the $M^*(El, Cr)$ model is due to the homogeneous material increase in stress, hence accumulation of more plastic strain occurs. The carburising models, Figure 4.5 (b), indicate that normalised changes in plasticity in the bulk are much closer to unity. The decreasing normalised plasticity with time is again due to the normalisation with homogeneous material where plasticity is increasing. The carburised layer exhibits an increasing resistance to plastic deformation in all carburising $M(Pl)$ models.

Creep and damage response

Figure 4.6a shows how the observed total strain would be appearing in carburising and pre-carburised creep tests. It can be seen that the mismatch in plastic properties of a pre-carburised specimen would give rise to a creep response that resembles primary creep and cause 3.3 times more creep strain accumulation at t_{end} compared to a homogeneous specimen. Figure 4.6b shows the creep strain in the bulk and at the carburised surface. It can be seen that during the stress redistribution phase, the bulk part of the specimen accumulates creep strain a factor of 20 lower than the carburised surface. Additionally, the carburised layer accumulates higher creep strain, than the observed strain due to the stress relaxation process. The accumulated creep strain in Figure 4.6b for the $M^*(El, Pl, Cr)$ specimen has

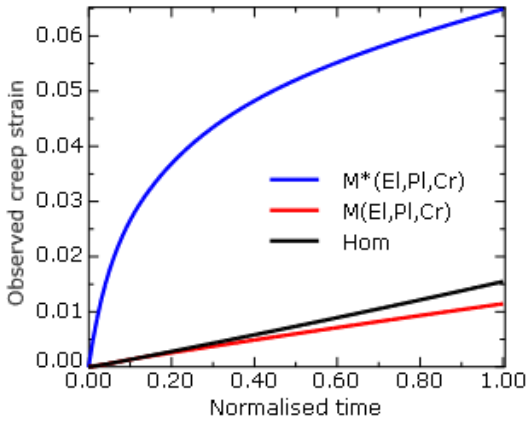

(a) Observed strain over time of the selected models;

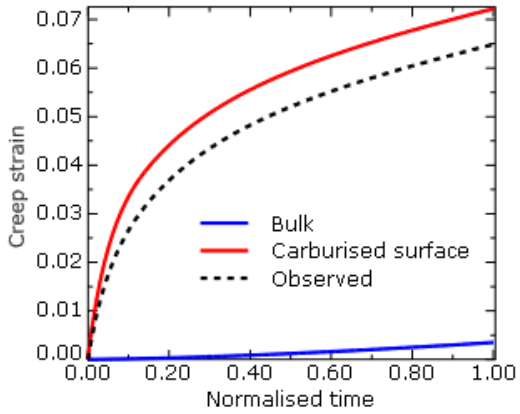

(b) Creep accumulation in pre-carburised $M^*(El, Pl, Cr)$ model;

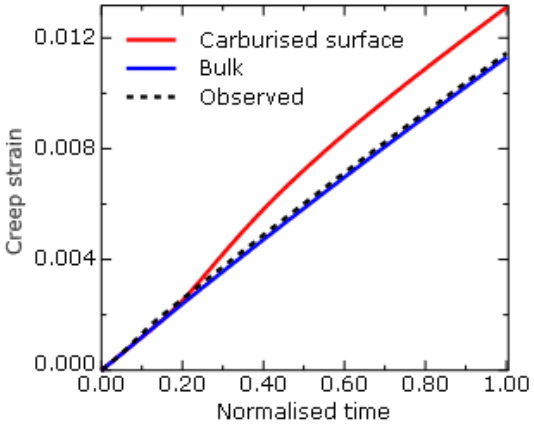

(c) Creep accumulation in carburising $M(El, Pl, Cr)$ model.

Figure 4.6: Creep strain accumulation in pre-carburised and carburising models normalised to $t_{end} = 500\,hr$.

normalised creep strain rates shown in Figure 4.7a, which show that the most carburised point of the models with scaled plastic properties initially creeps 2 orders of magnitude faster compared to the reference specimen.

Conversely, the carburising test case in Figure 4.6a, $M(El, Pl, Cr)$, shows observed total strain below that of a homogeneous specimen. The surface creep strain values (Figure 4.6c) again show additional creep strain accumulation in the most carburised point. This is again due to the stress redistribution as the tensile properties are changed, and this is reflected in the spike in the normalised creep rate, Figure 4.7b. However the key observation is that there is not a significant variation between the observed and actual creep strain values, as was seen in the pre-conditioned model. Furthermore, the normalised creep strain rate and creep strain are closer to unity and carburisation occurring after a specimen is subjected to load, leads to accumulated creep strains lower compared to a homogeneous specimen.

Multiaxial ductility is not significantly affected at the gauge section by the hard-

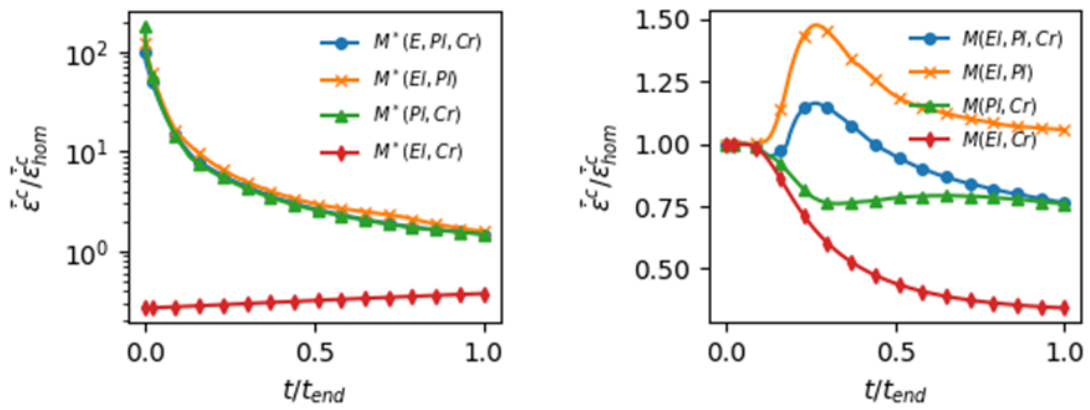

(a) Pre-carburised models; (b) Carburising models;

Figure 4.7: Normalised creep strain rate at the carburised surface of selected models.

ening effects when adapting a Spindler ductility model. The largest changes in ductility are seen in test cases with modified Young's modulus. For pre-carburised models, the ductility at the carburised layer is reduced by < 1.5% by changes in multiaxial stresses. The ductility change due to multiaxial stress effects for carburising cases is insignificant (< 0.35%).

As the multiaxial stress effects on ductility are not a major factor in this geometry, the damage accumulation was calculated assuming that the material ductility is directly proportional to the carbon content in the specimen. If the assumed creep ductility of the bulk material is ε_f, the creep ductility in pre-carburised and carburising models is calculated as

$$\varepsilon_f^c(x,t) = \left(\frac{c_0}{c(x,t)}\right) \times \varepsilon_f, \tag{4.5}$$

where $\varepsilon_f^c(x,t)$ is the uniaxial ductility within the carburised layer and for pre-carburised models, $t = 500$ hr ($\varepsilon_f^c(x = 0, t = 500\,hr) = \varepsilon_f/4.1$). The accumulation of creep damage (according to Eq. 4.5 and 2.16) in pre-carburised and carburising models is shown in Figure 4.8. Pre-carburised models indicate that creep damage in the carburised layer can reach unity within minutes of commencing the creep test. Conversely the carburising models show less severe creep damage accumulation over time even with the progressively reducing ductility in the carburised layer. The carburising test case predicts crack initiation at the surface after $0.78t_{end} - 0.85t_{end}$ compared to $0.01t_{end}$ in pre-carburised specimens with modified plastic properties. Even assuming the same creep ductility as the bulk material, the carburised surface layer in pre-carburised test cases accumulates 4.7 times more damage than a homogeneous specimen. The damage distribution through the thickness assuming unchanged ductility is shown in Appendix B.1, Figure B.3.

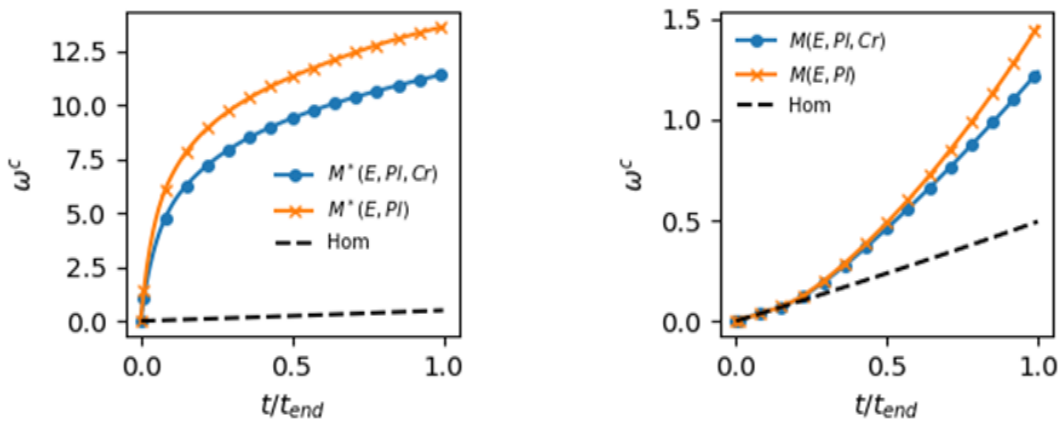

(a) Pre-carburised models; (b) Carburising models.

Figure 4.8: Creep damage accumulation in the uniaxial specimen with modified material properties, assuming ductility is a function of carbon content.

4.2.4 Summary and discussion

Homogeneous specimen results show additional plasticity accumulation during the creep phase which would be indistinguishable from the creep response. This adds significant complexity for interpretation of the creep results and makes it more difficult to fit the creep data at a particular stress level, because the stress is increasing with time due to the reduction in cross sectional area. However, due to the qualitative nature of this study, the exact value of the creep law multiplier is not that significant in this case. The purpose of this study was to investigate how changes in material's surface properties would influence the creep response.

Results clearly indicate that material pre-treatment has a significant impact on the global and local creep response of a specimen. Creep tests performed at high stresses on pre-carburised material could result in early failure of the carburised layer even if the creep ductility is the same as the homogeneous material. Considering the evidence [23, 24, 96] that carburisation occurs at grain boundaries, the creep damage will most likely be accelerated by the reduction in creep ductility due to grain boundary embrittlement. Additionally, when performing tests on pre-carburised specimens, the primary creep region will appear to be extended as carburisation accelerates the creep strain accumulation (Figure 4.6a). The numerical results showing accelerated initial creep response are in agreement with experimental observations [136] where it has been observed that carburisation accelerates the creep strain. Furthermore, the observed global creep rate can underestimate the actual creep rate in the carburised layer due to the local creep relaxation process. Hence, if the creep ductility of the carburised layer were measured as the observed total strain when the crack has reached the size of the carburised layer [24], this could underestimate the creep ductility as the local creep strain is not captured in the global response.

Results also indicate that despite the initial accelerated creep response, the system does approach to the steady state solution where the overall creep rate is reduced compared to the homogeneous test case. Therefore, it is theoretically possible that carburisation could extend the lifetime of a component, but this will depend on the creep stress redistribution time, area fraction carburised and the creep ductility of the bulk material and carburised layer.

Carburising models show completely different creep behaviour compared to pre-carburised models. Results indicate that carburisation while being subjected subjected to load reduce the overall creep rate. Damage calculations also indicate that the creep damage is closer to the damage of homogeneous material. This observation could potentially have an important implications in carburised layer creep ductility measurements. Specimens that are carburising while being subjected to load avoid the initial stress redistribution process that occurs on pre-carburised specimens. Furthermore there is much smaller variance between the accumulated creep strain in bulk and carburised layer. According to [24], pre-carburised specimens crack if the initial loading stresses are above 270 MPa, hence it makes accelerated creep tests of pre-carburised materials unfeasible. However it could be postulated based on the numerical observations that loading to the required creep stress state to prior carburisation could prevent carburised layer from premature cracking and result in more reliable ductility estimates where the observed total strain would be much closer to the actual carburised layer creep strain.

The chosen Young's modulus magnitude is not realistic because the estimates show that the carburised layer has a slight increase (30%) in Young's modulus compared to bulk material. The presented numerical models are based on mate-rial loaded to 408 MPa, but the carburised layer is known to crack above 270 MPa. Considering that no damage models were implemented in analyses and the simulated carburised layer is intact, questions arise as to how the carburised layer would behave at lower stress values. The carburised layer spans over 3 elements and given the small number of gauss points available to describe material variability, the proposed models are unlikely to represent carburised material creep response. Therefore the following section 4.3 will address these issues and whether material would material experience accelerated creep damage due to the mismatch in properties. To answer these questions, meaningful estimations of carburised layer properties must be determined; hence section 4.3 presents a method on how tensile properties of the carburised layer can be determined using artificial neural networks.

4.3 Neural networks for material property determination

Section 4.2 has outlined the complexity of interpreting the current creep results on pre-carburised specimens. As most of the tests have been performed at high stresses it is important to know the carburised materials tensile properties to interpret the creep response. As these properties cannot be measured directly, the stress-strain response has to be deduced from pre-carburised specimen global response. Previously this have been attempted by assuming carburised material is a homogeneous layer with no property gradation [23, 24]. However as shown in Chapter 3 this can underestimate the stress at the surface, where the carbon concentration is the highest, and from section 4.2 it is known that a mismatch in tensile properties can cause rapid stress relaxation with an associated accumulation of creep strain in highly stressed regions.

There is evidence that the changes in Young's modulus, yield stress and creep properties are related to the increase in carbon concentration, as has been assumed in section 4.2. However, as discussed in sections 2.2.4 and 2.2.4, there is high uncertainty regarding the material mechanical property data. One of the main questions that are addressed in this work is *"does the property distribution matter?"*. Section 2.2.4 states that for practical applications, it is preferable to treat the carburised layer as homogeneous material because such an assumption can simplify the assessment procedure. To answer this question, the exact shape of the material property distribution through the carburised layer is not that significant as long as the chosen distribution is comparable to the one that would arise from the diffusion process. Therefore, there is no reason why the material property distributions could not be simplified to linear or parabolic distributions, as described in Chapter 3.4. Using the proposed assumptions, this section investigates how carburised layer material properties can be estimated using neural networks that have been trained using data generated from finite element parametric studies.

4.3.1 Model description

The aim of this study is to develop a method to estimate the gradation of the carburised layer properties based on the global response from a circular tensile specimen. The hypothesis is that there is some correlation between material geometry, bulk material response, applied load, and recorded strain with the stress response in the carburised layer. Therefore by observing many specimens with different hardened layer properties, functions for the stress (σ_c) and stress triaxiality (T_c) within

the carburised layer could be derived:

$$\frac{\bar{\sigma}_c(loc)}{\sigma_o} = f\left(a_f, loc, \frac{r_{int}}{r_e}, \frac{r_i}{r_e}, \frac{\sigma_b}{\sigma_o}, \varepsilon_{obs}, \frac{\sigma_{obs}}{\sigma_o}\right) \tag{4.6}$$

$$\frac{T_c(loc)}{T_o} = g\left(a_f, loc, \frac{r_{int}}{r_e}, \frac{r_i}{r_e}, \frac{\sigma_b}{\sigma_o}, \varepsilon_{obs}, \frac{\sigma_{obs}}{\sigma_o}, \frac{\nu}{\nu_o}\right). \tag{4.7}$$

Here, area fraction carburised, a_f, location parameter $loc = (r - r_{int})/(r_e - r_{int})$, and the ratios, r_{int}/r_e , r_i/r_e, are parameters that define the geometry of the specimen. σ_b and σ_{obs} are the bulk and the observed stress response at the *observed* strain, ε_{obs}. The stresses are normalised to some reference stress, σ_o (e.g. the yield stress, σ_y), the stress triaxiality is normalised to the uniaxial stress triaxiality, $T_o = \frac{1}{3}$. The stress triaxiality function has an additional input which is the fractional increase or decrease in Poisson's ratio within the carburised layer ($\nu_o = 0.3$ is the bulk's value).

The proposed neural network models are just functions that can estimate the local stress magnitude and stress state within the carburised layer based on the global stress-strain response of the specimen and some additional information about the specimen geometry. The neural network used for $\bar{\sigma}_c(loc)$ and $T_c(loc)$ calculations are different. Neural networks are trained on data obtained from finite element simulations where either linear or parabolic material property functional forms are assumed for the carburised layer. The trained neural networks are used to estimate local properties of the carburised layer using real tensile test data. More details on data acquisition, material properties and neural network training are provided in the following subsections.

Data acquisition

FE geometry

A uniaxial tensile specimen was modelled in Abaqus using axisymmetric CAX8RT elements. For computational efficiency only the gauge section was modelled. Different geometries were modelled by changing the area fraction carburised and inner and outer radii. Figure 4.9 shows an example of the gauge section. The carburised layer was discretised using 12 elements, which give a total of 25 nodal values for data acquisition. In total 5 different geometries were considered with different $r_i : r_{int} : r_e$ ratios. Table 4.3 lists all of the geometries considered. Most geometries used $r_e = 3.45$, because that was reported in [24] (outer radius of $3.5mm$ with $50\mu m$ oxide). However, a very thin structure with $r_i = 10mm$, $r_e = 10.01mm$ was also considered to examine whether stress triaxiality is affected in thin carburised structures.

A monotonic tensile load was applied at the top surface (Figure 4.3) by displacement control. The maximum applied strain for each test case was $< 5\%$, this ensures

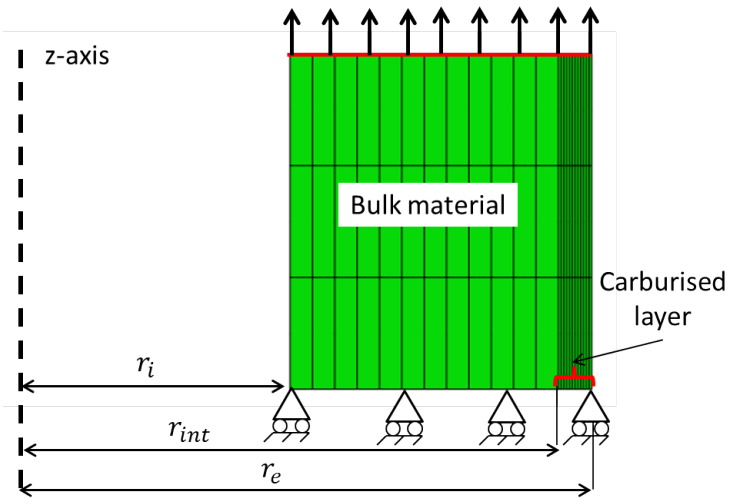

Figure 4.9: Implemented geometry in Abaqus.

r_i [mm]	r_e [mm]	Area fraction carburised (a_f) [%]
3	3.45	11.8, 23.4, 34.9, 46.2, 57.3
2.25	3.45	5.0, 9.9, 14.8, 19.6, 24.3
1.5	3.45	3.5, 7.0, 10.5, 13.9, 17.2
0	3.45	2.9, 5.7, 8.5, 11.3, 14.0
10	10.01	1.0, 5.0, 14.0, 25.0, 57.0

Table 4.3: Implemented geometry in Abaqus for the tensile specimen.

that calculations do not need to consider non-linear geometric effects that may arise due to high strains.

Material properties

To create a neural network that is capable of estimating the local stress-strain properties from a given global response requires training the model using an appropriate data set. In order to provide such a data set, a training set must be obtained that contains the necessary information about how global response is influenced by the local changes of elastic and plastic properties.

The bulk material properties used for this study was taken directly from [24], where the uniaxial tensile response is described by a Ramberg-Osgood fit. The equation that describes uniaxial tensile behaviour for bulk material up to 270 MPa is

$$\varepsilon_b^t = \varepsilon_b^e + \varepsilon_b^p = \frac{\sigma}{E_b} + \left(\frac{\sigma}{A'}\right)^{B'} \tag{4.8}$$

where E_b = 157 GPa, A' = 374.3 MPa and B' = 8.7873.

As described in section 2.2.4, a Ramberg-Osgood model was also used to de-

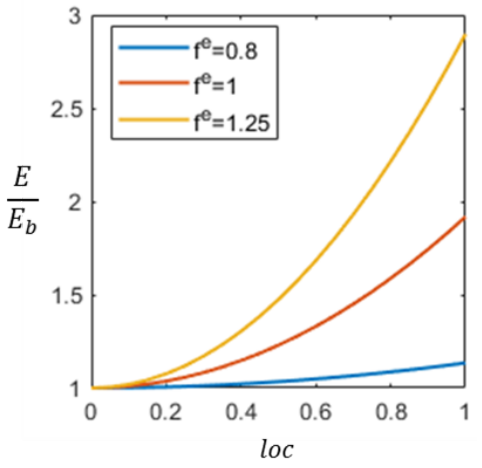

(a) Young's modulus;

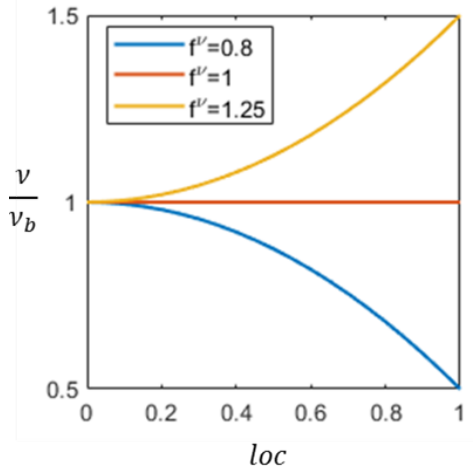

(b) Poisson's ratio

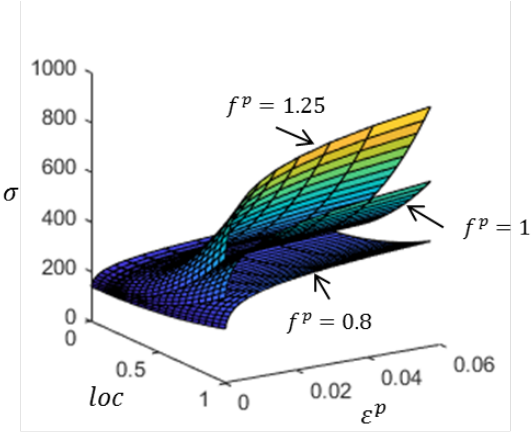

(c) Stress and plastic strain.

Figure 4.10: An example of changing material properties assuming parabolic distribution profile through the carburised layer.

termine the parameters that describe the *average* carburised layer properties. In this FE study the carburised layer is modelled assuming a Ramberg-Osgood model where Young's modulus, $E_c(loc)$, and plastic deformation parameters, $A_c'(loc)$, and $B_c'(loc)$, are changed assuming linear and parabolic distribution profiles through the carburised layer:

$$\varepsilon_c^t = \varepsilon_c^e + \varepsilon_c^p = \frac{\sigma_c(loc)}{E_c(loc)} + \left(\frac{\sigma_c(loc)}{A_c'(loc)}\right)^{B_c'(loc)}. \tag{4.9}$$

The position within the carburised layer is defined by the location/position parameter, *loc*, which is 0 at the bulk-carburised layer interface and 1 at the surface.

The equations describing how material properties were modified through the layer are given in Table 4.4. a^e, a^p are parameters that provide reasonable magnitudes of material property change through the thickness. Parameters were sampled

Property	Linear	Parabolic
$E_c(loc)$	$a^e_{lin} loc + E_b$	$a^e_{par}[loc]^2 + E_b$
$\sigma(\varepsilon^p_c, loc)$	$a^p_{lin} loc + A'[\varepsilon^p_b]^{1/B'}$	$a^p_{par}[loc]^2 + A'[\varepsilon^p_b]^{1/B'}$
$\nu_c(loc)$	$a^\nu_{lin} loc + \nu_b$	$a^\nu_{lin}[loc]^2 + \nu_b$

Table 4.4: Linear and parabolic material property distribution implementation in Abaqus.

around the *average* carburised layer properties (Eq. 2.32). Material parameters were not fitted to give the *average* carburised layer response, because the objective of the neural network model is to determine the local carburised layer properties.

Changes in Poisson's ratio have also been considered, although there are no data on how Poisson's ratio might change due to carburisation. The Poisson's ratio parameters, a^ν, were fitted so that Poisson's ratio within the carburised layer is $0.15 \leq \nu_c \leq 0.45$. The proposed variation in Poisson's ratio has been chosen purely out of the scientific inquiry. Modelling such changes provides some insight on how changes in Poisson's ratio might influence the local stress state and stress magnitude.

The bulk material is assumed to be perfectly elastic below 140 MPa ($\varepsilon^p_b = 0$ at $\sigma < 140$ MPa), hence the plastic part ($\varepsilon^p_b = (\sigma/A')^{B'}$ at $\sigma \geq 140$ MPa) of Eq. 4.8 was scaled using only stresses ≥ 140 MPa. The hardening behaviour of the bulk layer was calculated by scaling the yield stress and the tangent modulus of the bulk plastic response to reach a specific plastic strain. An example of how material properties are varied through the thickness within the carburised layer is shown in Figure 4.10 and the equations for the properties a_{lin} and a_{par} are given in Table 4.5.

Linear	Parabolic
$a^e_{lin} = E_b[2.612 f^e - 2]$	$a^e_{par} = 3E_b[1.306 f^e - 1]$
$a^p_{lin} = A'[\varepsilon^p_b]^{1/B'}[2.97 f^p - 2]$	$a^p_{par} = 3A'[\varepsilon^p_b]^{1/B'}[1.486 f^p - 1]$
$a^\nu_{lin} = f^\nu - \nu_b$	$a^\nu_{par} = f^\nu - \nu_b$
$f^e = [0.8, 0.89, 0.93, 1.0, 1.08, 1.13, 1.25]$	
$f^p = [0.8, 0.89, 0.93, 1.0, 1.08, 1.13, 1.25]$	
$f^\nu = [0.15, 0.2, 0.25, 0.3, 0.35, 0.4, 0.45]$	

Table 4.5: Linear and parabolic material property distributions implemented in Abaqus.

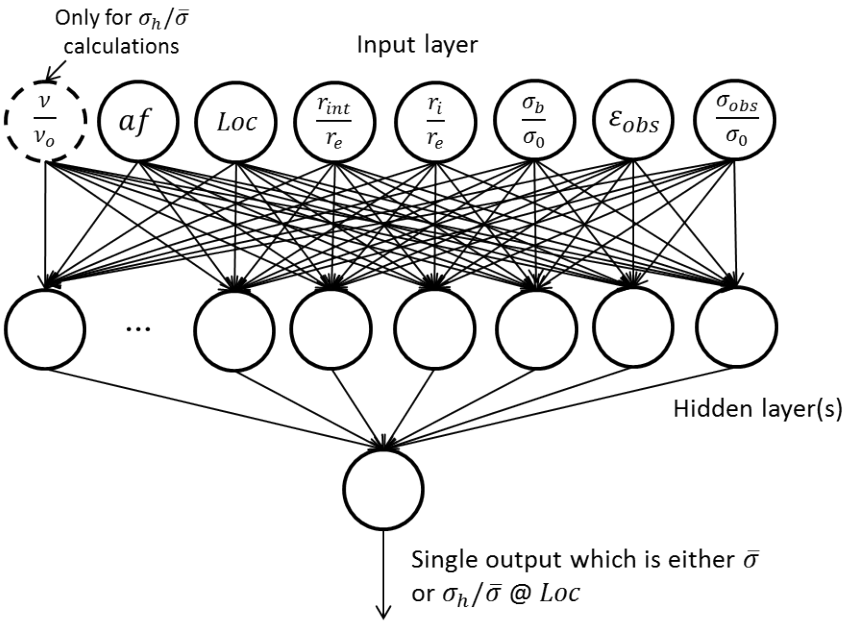

Figure 4.11: The architecture of the neural network for tensile property determination.

The NN model training and validation

For the chosen geometry a total 17150 models have been analysed, with half using parabolic material property distributions for the carburised layer and the other half using linear distribution profiles. From each study principal stresses, inelastic and elastic strains were extracted at positions in the carburised layer.

Figure 4.11 shows a neural network model used to develop an estimator for carburised layer stress and stress triaxiality. The neural networks had 7 inputs for the stress estimator and 8 inputs for the triaxiality estimator. The observed stress, σ_{obs}, was calculated from the FEA data using axial stress values, σ_z, where the applied load was obtained by integrating over the axisymmetric geometry. The neural networks were built and trained using Matlab, with separate approaches used to build carburised layer stress magnitude and triaxiality estimators.

Stress magnitude estimator

For the stress state estimator for the carburised layer a multi-layer perceptron was used as shown in Figure 4.11. This model does not use Poisson's ratio as an input, so the neural network was trained using $7 \times (\sim 10^6)$ input data variables. Finding the best neural network was trial and error approach, where different neural network architectures were considered. This is a function fitting problem and therefore only one hidden layer was used, because according to [122], only one hidden layer is needed for continuous function approximation. The neural networks were tested using 14, 21, 28 and 42 hidden layers. The hidden layers used a hyperbolic tangent

sigmoid transfer function. Hence for a single input, x_j, where x_j is a 1×7 vector, the output of each hidden node can be written as:

$$a_i^{[1]} = \chi^{[1]}\left(w_{ij}^{[1]}, x_j, b^{[1]}\right) = tanh\left(b^{[1]} + \sum_{j=1}^{n} w_{ij}^{[1]} x_j\right) \tag{4.10}$$

where $a_i^{[1]}$ is the output of each hidden node, $\chi^{[1]}$ denotes activation function, b is the bias term, $w_{ij}^{[1]}$ are the weight values that are multiplied by each input value. The $\sum_{j=1}^{n} w_{ij}^{[1]} x_j$ term determines whether or not the neurons are *activated* by the hyperbolic tangent function. The outputs from all hidden nodes, $a_i^{[1]}$, are fed into the output node which has a linear activation function that gives a continuous output:

$$\chi(w_i^{[2]}, a_i^{[1]}) = \sum_{i=1}^{n} w_i^{[2]} a_i^1 + b^{[2]} = z^{\bar{\sigma}} \tag{4.11}$$

where $w_i^{[2]}$ are the weight factors of each output from the hidden nodes ($a_i^{[1]}$). The output node calculates the output value, $z^{\bar{\sigma}}$. The Eqs. 4.10-4.11 are shown for a single set of inputs, but during actual training, all inputs are passed in a $m \times 7$ matrix, where m corresponds to the size of the training data.

The Levenberg-Marquardt back propagation algorithm was used to train the neural network model. To optimise the neural network model, a mean squared error (E_{MSE}) function was used to evaluate the performance by comparing all of the calculated output values z_i with their respective target values, y_i. For m number of outputs the error function is

$$E_{MSE} = \frac{1}{m} \sum_{i=1}^{m} (y_i^{\bar{\sigma}} - z_i^{\bar{\sigma}})^2 \tag{4.12}$$

The Levenberg-Marquardt algorithm minimises the E_{MSE} function by calculating the second order derivatives of the error function with respect to weight values by computing the Jacobian matrix using a backpropagation algorithm. The calculated Jacobian matrix is used to define the Hessian matrix for the special case of the sum of square error ($\mathbf{H} \approx \mathbf{J}^T\mathbf{J}$). The calculated second order derivatives allow the weight values to be updated to decrease the error function with each iteration [120, 137].

The data were randomly divided into training, validation and test data sets: 90%, 5% and 5% respectively. The training set is used to train the neural network model and find the weights and biases, hence 90% of the data were used to build the model. The validation data are used to evaluate the performance of the neural network. The validation set are not used during the training stage and this prevents

the neural network from overfitting the data. The set can also give an indication when the training is not showing any progress. The test data are used to test different configurations of the neural network and to give an indication of whether or not the data set has been poorly divided, e.g. if the validation set error is different from the training set error [138].

Triaxiality estimator

The stress triaxiality estimator was trained using $8 \times (\sim 1.6 \times 10^6)$ input variables. Initially, this was treated as a regression fitting problem, but this approach was unsuccessful, as explained in the following section. Nevertheless, a working neural network model was build by treating this as a classification problem, where instead of predicting a continuous stress triaxiality value, the stress triaxialities were split into 5 classes (Table 4.6).

Class	Triaxiality ratio	Description
1	$T/T_o > 1.1$	Severe increase in $\sigma_h/\bar{\sigma}$
2	$1.025 < T/T_o \leq 1.1$	Increase in $\sigma_h/\bar{\sigma}$
3	$0.975 < T/T_o \leq 1.025$	Insignificant change in $\sigma_h/\bar{\sigma}$
4	$0.9 < T/T_o \leq 0.975$	Decrease in $\sigma_h/\bar{\sigma}$
5	$T/T_o \leq 0.9$	Severe decrease in $\sigma_h/\bar{\sigma}$

Table 4.6: Assumed classes for building stress triaxiality classifier

In total 6 architectures were tested from which: two had a single hidden layer with 21 and 28 hidden nodes; two had two hidden layers with (21, 7) and (28, 14); and two had (7,7,7) and (14, 7, 7) configuration. Each hidden layer used the hyperbolic tangent activation function (Eq. 4.10), however the output layer used the normalised exponential function (or $softmax$ function) which gives a probability of each class from 0 to 1. For a single input, the output is a vector whose values correspond to probability value of each class

$$z_i^{\bar{\sigma}} = \chi^{[l]}\left(w_{ij}^{[l]}, a_j^{[l-1]}, b^{[l]}\right) = \frac{\exp\left(b^{[1]} + \sum_{j=1}^{n} w_{ij}^{[1]} x_j\right)}{\exp\left(\sum_{i=1}^{n}\left[b^{[1]} + \sum_{j=1}^{n} w_{ij}^{[1]} x_j\right]\right)} \tag{4.13}$$

Subscript, l, in Eq. 4.13 is the l^{th} layer that correspond to the output layer for $l-1$ number of hidden layer architecture. The stress triaxiality output vector, z_i^T, will give $n = 5$ values – probability values for each triaxiality class. The performance or the error function, which is minimised with each iteration, in this problem has been chosen to be the cross entropy function, E_{CE}, and considering n by m outputs the

error function is shown in Eq. 4.14. The error function, E_{CE}, is minimised using the scaled conjugate gradient backpropagation method [137].

$$E_{CE} = \frac{1}{m}\sum_{j=1}^{m}\sum_{i=1}^{n}\left(y_{ij}^{T}\ln z_{ij}^{T} + (1-y_{ij}^{T})\ln(1-z_{ij}^{T})\right). \tag{4.14}$$

4.3.2 The NN performance

Stress state estimator

The output of the neural network is the normalised von Mises stress within the carburised layer at *loc*. Figure 4.12 shows the performance data of the best performing stress state estimator for the parabolic distribution which was the network with 28 hidden nodes. Figure 4.12a shows the error histogram with the difference between the target value, $y_i^{\bar{\sigma}}$, and calculated output, $z_i^{\bar{\sigma}}$. The error histogram has been plotted using a log-scale because of the small deviation from the 0 value. By looking at

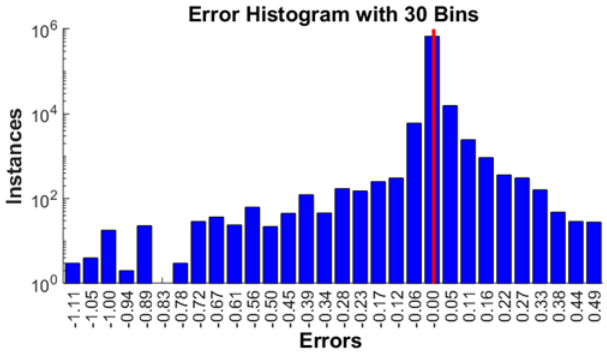

(a) Error histogram, where $Error = y_i - z_i$;

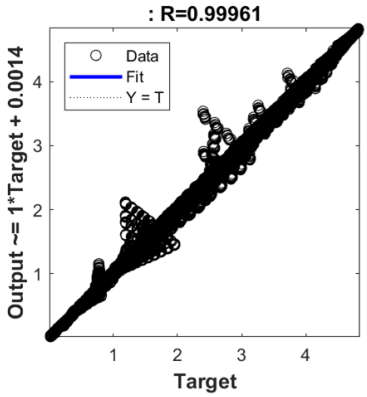

(b) The correlation coefficient of ~ 10^6 data points;

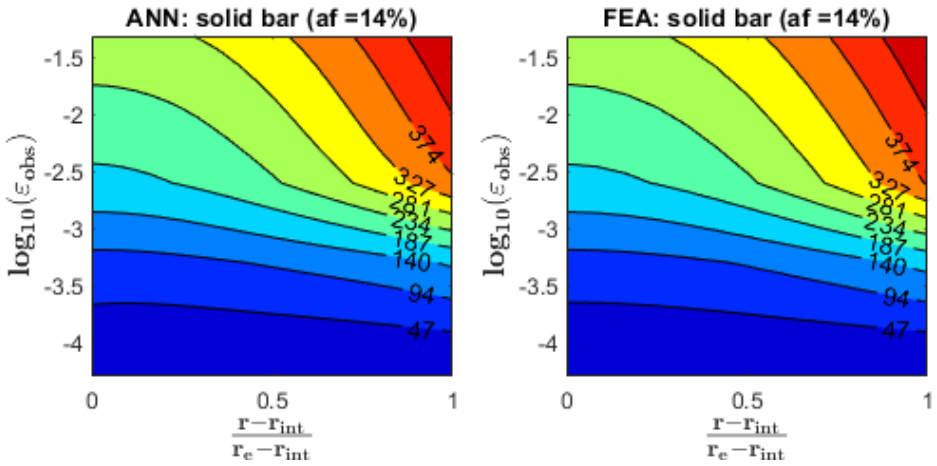

(c) Comparison between ANN and FEA calculated results through the carburised layer for 14% area fraction carburised solid bar.

Figure 4.12: The performance of the stress state estimator.

the error histogram, it can be seen that almost all data > 99% are concentrated at the zero error (red) line.

Architecture	E_{MSE} (validation)	E_{MSE} (training)
14	5.0E-05	4.0E-05
21	3.2E-05	3.3E-05
28	2.9E-05	2.7E-05
42	1.3E-05	1.0E-05

Table 4.7: Performance indicators for the parabolic distribution von Mises stress neural network.

Table 4.7 shows the calculated mean squared error functions for the training and validation data sets. Clearly the neural network with 42 hidden nodes has performed the best. However the neural network did not provide a good generalisation when the input parameters were real life data including some noise. As the test data used have been taken from the finite element models, the neural network is trained on *noise free* data, hence the 42 hidden node neural network has been overfitted. The 28 hidden node neural network has been chosen as the best performing model for generalising a uniaxial model that can use real life tensile test data and this will be discussed in section 4.3.3.

The regression plot (Figure 4.12b) shows the correlation between the outputs and target values (normalised to σ_o). There are two distinct triangle-shaped regions where the neural network was not able to approximate the solution. The region around $1.2 < Target < 2$ was identified to be the yield stress region close to the bulk material (at $loc \sim 0$). The second region, $Target \approx 3$, was the region of the yield stress values towards the outer surface. Nevertheless, it has to be noted that Figure 4.12b shows all $\sim 10^6$ output values, the values away from the regression line correspond to $\ll 0.01\%$ of total data points. The remarkable precision of the neural network is shown in Figure 4.12c where the von Mises stress has been calculated through the carburised layer. The trained NN gives an almost identical solution to the finite element predictions.

The training performance of the neural network assuming a linear property gradation can be found in Appendix B.2. In general, the linear neural network was more easily able to find a generalised solution than the parabolic neural network and the regression curve showed an almost perfect fit for all tested architectures.

Triaxiality estimator

Developing the stress triaxiality estimator using a linear regression approach was

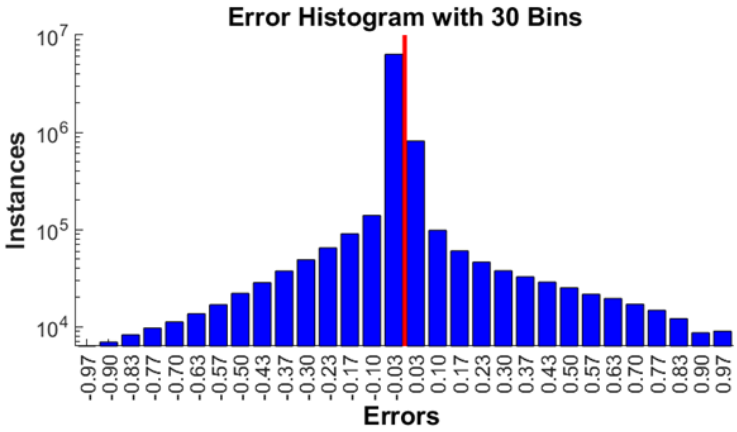

(a) Error histogram, where $Error = y_i^T - z_i^T$;

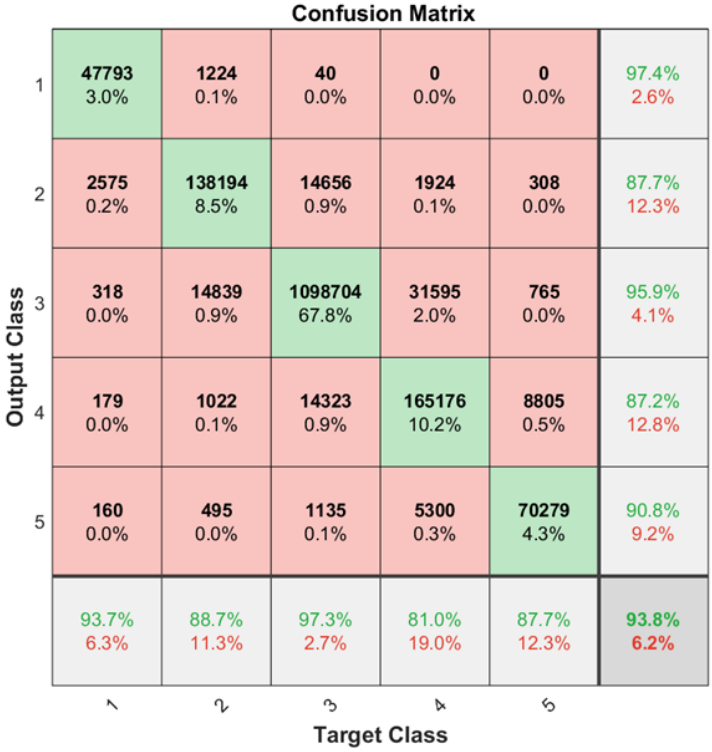

(b) Confusion matrix of the triaxiality classifier, where classes are (1) $T/T_o > 1.1$; (2) $1.025 < T/T_o \leq 1.1$; (3) $0.975 < T/T_o \leq 1.025$; (4) $0.9 < T/T_o \leq 0.975$; (5) $T/T_o \leq 0.9$;

Figure 4.13: The performance of the triaxiality estimator.

problematic, because the data were highly biased towards the uniaxial stress triaxiality value of $T/T_o = 1$. This means that most of the data were close to unity: 84% of all data were between $0.99 < T/T_o < 1.01$, and 95% between $0.95 < T/T_o < 1.05$. A neural network could provide model with 84% accuracy by always giving the output as unity. This is not very useful for the cases where stress triaxiality values have changed significantly. Therefore, the data set was reduced by excluding the majority of the inputs that corresponded to $T/T_o = 1$. By doing this the data set contained a higher percentage of the data points that would give either a reduction

or an increase in stress triaxiality. Additionally, this problem was simplified to a classification problem where the neural network was trained to identify the regions with changed triaxiality rather than predict the specific value (Table 4.6).

The best performing classifier based on its accuracy was with the model using [24, 14] hidden layer architecture and the performance of this NN model is summarised in Figure 4.13. The model with [24, 14] hidden nodes was able to accurately classify 93.8% of the data. Figure 4.13b shows a confusion matrix of the [24, 14] neural network and this provides more insight of how the model classifies/misclassifies the data. The values on the right-hand column show the recall (Eq. 4.15), whereas values on the bottom row show the precision (Eq. 4.16).

$$Recall = \frac{T^{(n)}}{T^{(n)} + F^{(n)}} \tag{4.15}$$

$$Precision = \frac{T^{(n)}}{T^{(n)} + F^{(n)}} \tag{4.16}$$

The green cells show the correctly classified instances, $T^{(n)}$, where n is the class number and the red cells show incorrectly classified instances. Recall (sensitivity) is the fraction of correctly labelled relevant instances over the total number of the retrieved instances of the same predicted class, $T^{(n)} + F^{(n)}$ (correct and incorrect instance of the same output class). Considering the first output class, 47793 entries have been correctly classified, and 1224+40 instances have been incorrectly classified as class (1); therefore, the recall of (1) is 97.4%. The precision (positive predicted value) is a fraction of correctly classified instances over the total number of instances that should have been of the same class, $T^{(n)} + F^{(m)}$ (correct and incorrect instance of the same target class), where m are the rest of the output classes [139].

Architecture	Accuracy	E_{CE}
21	89.8%	5.00E-02
21, 7	88.4%	5.29E-02
28	88.8%	5.40E-02
28, 14	93.8%	3.23E-02
7, 7, 7	87.7%	5.97E-02
14, 7, 7	89.2%	5.24E-02

Table 4.8: Performance indicators for the parabolic distribution neural network triaxiality classifiers.

The [28, 14] ANN had the highest recall and precision values out of all tested models. However, based on the confusion matrix it can be seen that the neural

network is most likely to incorrectly classify the *reduced* triaxiality class (4) (see Table 4.8) where the precision is lowest at 81%.

4.3.3 Tensile response

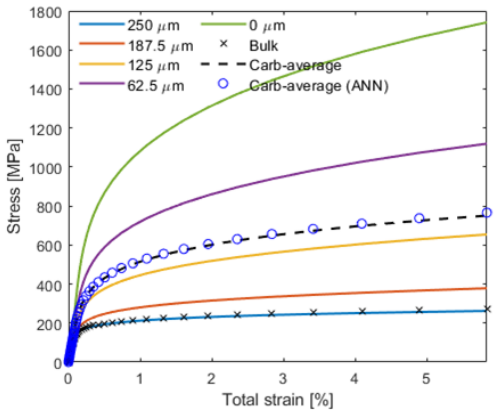

(a) Predicted stress strain curves compared with the *average* model 2.32.

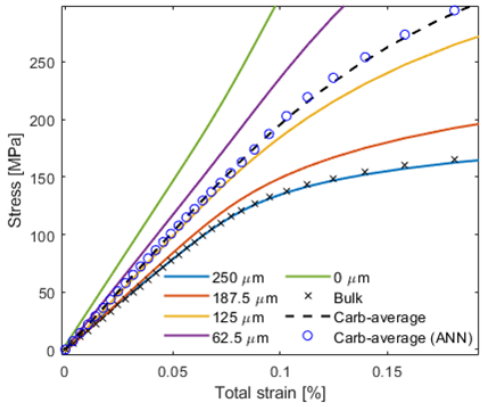

(b) The elastic response;

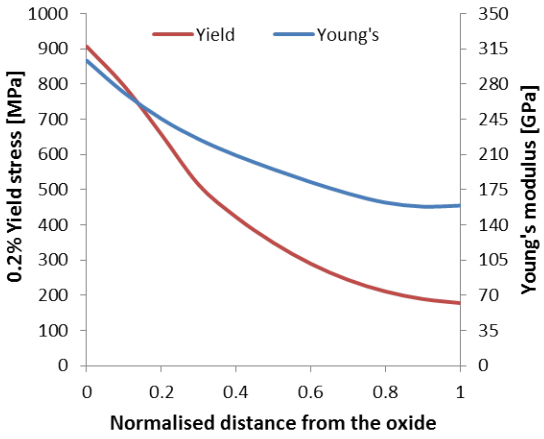

(c) The predicted 0.2% proof stress and Young's modulus values for the carburised layer.

Figure 4.14: ANN model for carburised layer stress strain response under uniaxial loading.

The von Mises neural network has been tested to predict the stress-strain response of the carburised layer using the observed stress strain curve according to a real test from [24], where the observed stress is the combination of bulk and carburised material response averaged over surface area it acts on. The stress estimator was tested by using Eq. 4.8 and Eq. 2.32 to calculate the global stress response assuming a_f = 14%:

$$\sigma_{obs} = (1 - a_f)\sigma_b + a_f\sigma_c. \tag{4.17}$$

Figure 4.14a shows the output of the parabolic distribution neural network assuming a solid uniaxial specimen of r_e = 3.45mm and carburised layer thickness of 250μm. The solid lines are stress-strain curves of the carburised layer at different locations away from the surface. The neural network predicts the same stress-strain behaviour as the bulk at 250μm away from the surface, which is one of the indicators for neural network validity. Secondly, the *average* stress-strain curve of the carburised layer can be calculated from the ANN model by integrating the stress-strain curves over the thickness and compared with the *averaged* estimate from [24]. The calculated ANN *averaged* stress response through the carburised layer (denoted as "*Carb-average (ANN)*") is almost identical with the σ_c from Eq. 2.32 (denoted as "*Carb-average*").

It was observed that the biggest difference between the ANN and reference *Carb-average* values is at high strain values (2% − 3%). At low strain values (Figure 4.14b) the neural network was able to predict the initial elastic response and yield almost identically to the reference data. Figure 4.14c shows the mapped 0.2% proof stress and Young's modulus through the carburised layer. For the parabolic distribution the estimated 0.2% proof stress range is between 178 and 907 MPa and Young's modulus between 159 and 303 GPa.

The results for a linear distribution profile can be found in Appendix B.2 Figure B.6. This neural network does not predict as severe yield and Young's modulus variations as the NN model trained on parabolic data. The neural Young's modulus range for the linear NN is 157 - 253 GPa and the 0.2% yield stressrange is 178 – 548 MPa. From these results it can be said that the mismatch between the outer surface and the bulk for the linear property distribution is not as severe as for a parabolic distribution, which is as expected.

4.3.4 Stress triaxiality change

For geometries with r_e = 3.45 mm and unchanged Poisson's ratio (ν_b = ν_c = 0.3), there was not a noticeable change in stress triaxiality through the carburised layer for the given geometry. However, if a Poisson's ratio variation through the carburised layer is assumed, this can lead to induced non-axial stresses in the cylinder under axial load (discussed in Chapter 3). If the bulk material is in the fully plastic region ν_b = 0.5 and the carburised layer is elastic (ν_c = 0.3) the elastic stresses in the carburised layer can be underestimated.

Figure 4.15 shows how stress triaxiality changes within the carburised layer for two different parabolic Poisson's ratio variations. With a decreasing Poisson's ratio during elastic loading the stress triaxiality at the outer surface reduces compared to pure uniaxial loading, Figure 4.15a. The opposite can be observed if the ν_c is

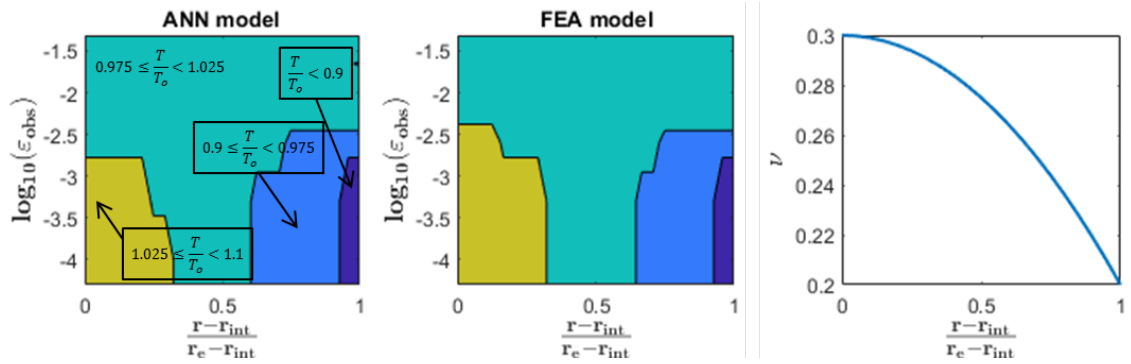

(a) Decreasing Poisson's ratio.

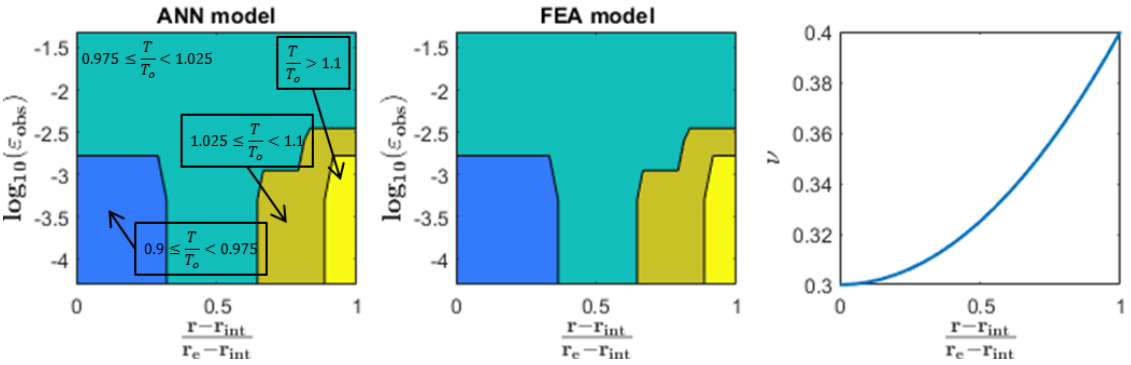

(b) Increasing Poisson's ratio.

Figure 4.15: ANN model to predict the stress triaxiality in carburised layer under uniaxial loading for 57% area fraction carburised hollow specimen.

increasing towards the outer surface, Figure 4.15b. The results are consistent with the analytical solution from Chapter 3 where 2 concentric homogeneous cylinders were considered under axial load.

For most cases the neural network model performance provided a good generalisation for approximating stress triaxiality. However, from the confusion matrix as discussed in section 4.3.2, it has up to a 19% chance of incorrectly classifying some data. An example of such a poor prediction is given in Appendix B.2 Figure B.5, where the neural network predicts a severe decrease in stress triaxiality for a model where the stress triaxiality was not changed significantly $T/T_o \approx 1$.

4.3.5 Summary and discussion

It has been shown that neural networks can be used as highly accurate tools for function approximation. As the carburised layer material property distribution is unknown, a trained neural network can rapidly give a prediction avoiding time consuming finite element modelling. However, the neural network must be trained in the first place using appropriately sampled data.

Although the proposed neural network has been shown to be a good tool for approximating material properties within the carburised layer, the neural network

results should be treated with caution. The NN models were trained using data provided by finite element analysis and were capable of solving the problem with great accuracy with respect to FE results. Predicting the stress triaxiality using the proposed neural network showed the importance of appropriate data sampling. Although most of the time the neural network was capable of predicting the appropriate triaxiality, in some cases the best model gave completely unreasonable results (Figure B.5) indicating that it was not capable of generalising the problem for all geometries. However the tensile property ANN was validated using a known *averaged* carburised layer response with $\sigma_{obs} - \varepsilon_{obs}$ data that the neural network had not *seen* before. Furthermore, based on the validation data set error and the regression data, the trained NN showed that it is capable of approximating the von Mises stress within the carburised layer with the same accuracy as the FEA.

In reality materials data will have some variability in its mechanical response that current finite element analysis has not considered. This variability can arise from material pre-treatment, history effects, testing error etc. The remarkable feature of neural networks is that, if such variability could be introduced in the training data set, the output of the trained neural network would correspond to the most probable scenario. This means that the proposed model could be improved by introducing some uncertainty in the bulk material properties in the finite element parametric models. This approach could make a neural network a more robust tool for determining material properties when new carburised material data are provided.

By changing Poisson's ratio in the carburised material it has been identified that any mismatch in the Poisson's ratio could result in a reduction or increase in stress triaxiality. If the carburised layer has lower stress triaxiality than the bulk, then during the elastic loading carburised layer will have reduced stress triaxiality on the outer surface. This observation is significant when considering damage formation at the surface. If carbon ingress has the potential to increase Poisson's ratio on elastic loading, then the surface could experience a reduction in multiaxial ductility due to increased stress triaxiality. Currently there is no evidence showing whether carbon ingress in Type 316H stainless steel causes any changes in Poisson's ratio. However, even if Poisson's ratio has not changed there can still be induced non-axial stresses if the bulk material is in the fully plastic regime (ν_b = 0.5) and the carburised layer is elastic (ν_c = 0.3). This study has shown that for the given geometry and the material properties according to Eq. 2.32, the stress triaxiality would be the same as for pure uniaxial loading. Nevertheless, the implemented geometry only considers the gauge section of the tensile specimen. If the geometry of a hollow tensile specimen were implemented, there would be additional constraints for the radial deformation of the gauge section due to the clamped ends.

The significance of these neural network models is their ability to produce candi-

date solutions for carburised material tensile properties. The estimated stress-strain curves through the thickness depend on the initial assumption about the carburised layer tensile property distribution profile. Therefore, to answer the proposed question of whether or not the functional form of carburised layer properties matter, creep analysis must be performed assuming different functional forms. The presented neural networks have been shown to estimate solutions that will give an appropriate global response. Chapters 4.4 and 5 use these results as an input to investigate the effects of material property distribution profiles on creep deformation.

4.4 Creep damage classification in carburised structures

Section 4.2 outlined the issues of performing creep measurements on pre-carburised specimens at high stresses. The mismatch in tensile properties leads to an increased local stress that causes rapid stress relaxation in the carburised layer. Assuming carburisation reduces creep ductility, it was shown that rapid stress relaxation would cause enhanced damage accumulation in the carburised layer and cause early damage initiation. However, only a single stress value was considered, and there is no evidence that under different loading conditions and for different area fractions of carburised material, the response will be the same.

Section 4.3 showed that there could be many material property distribution profiles that would give the same global $\sigma_{obs} - \varepsilon_{obs}$ response upon initial loading. However the creep response had not been investigated using these material properties. Additionally, for engineering applications where assessment procedures, e.g. R5, are used, robust simplified analysis is preferred over complicated finite element models. Therefore, it has been proposed that a carburised structure could be treated as a homogeneous one but with reduced creep ductility to account for creep damage initiation. In order to investigate the range of applicability of such an assumption in this section, a more detailed creep analysis is presented by modelling a uniaxial axisymmetric specimen with different creep property gradations. The artificial neural network results from the previous section 4.3 are used as an input to define carburised layer tensile properties. The local creep strains at various observed strains are considered and the characteristic creep ductility of the carburised layer is estimated using the reference creep crack size data. A parametric study is considered where Young's modulus, creep law multiplier and load are changed. The gathered data from the parametric study are used to build a support vector machine (SVM) classification model that can estimate if the time to failure is higher or lower than for a homogeneous structure to reach the same strain. Note, the present study con-

siders pre-carburised specimens, although similar analyses could be performed for specimens carburising under load.

4.4.1 Model description

Uniaxial model

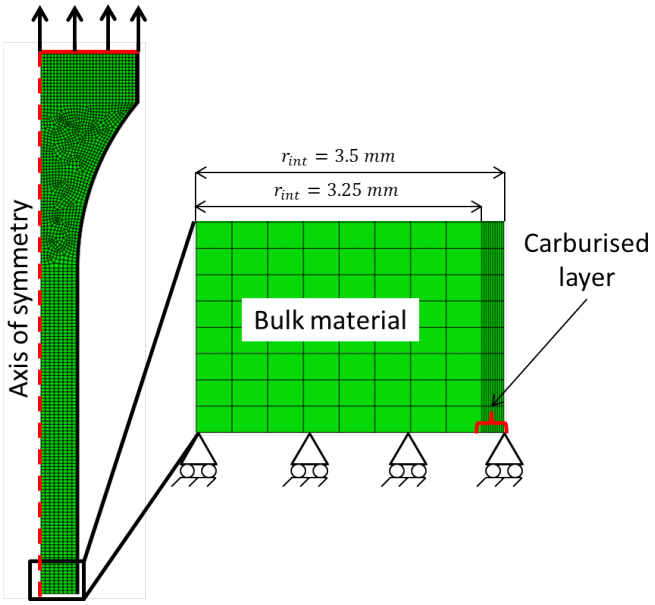

Figure 4.16: Uniaxial creep specimen model.

The geometry of the carburised ($a_f \approx 14\%$) specimen is shown in Figure 4.16. Axisymmetric CAX8RT elements were used in this study. The assumed tensile property distributions through the carburised layer are: parabolic (NN model, Figure 4.14a); linear (NN model, Figure B.6); and homogeneous (denoted as *2-bar* model, Eq. 2.32). The bulk tensile properties are according to Eq. 4.8. The assumed creep property distributions are also parabolic, linear and homogeneous (according to Figure 3.5b). An additional test case is considered assuming a combination of parabolic tensile properties and a homogeneous creep distribution profile. The creep test is modelled under an applied stress of 270 MPa for 10k hours (t_{end} = 10^4 hr). The value of 270 MPa has been chosen because at this stress interrupted creep tests have been analysed by Chevalier [24] using pre-carburised specimens with the same geometry as shown in Figure 4.16.

Simplified uniaxial model

A simplified geometry of the uniaxial model is shown in Figure 4.17. In this model the gauge dimensions are not the same as Figure 4.16. However, ensuring the same

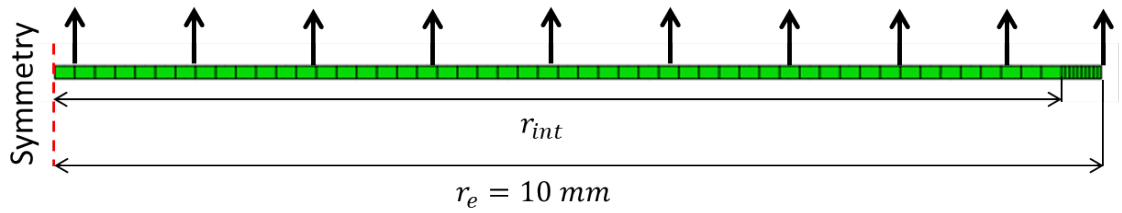

Figure 4.17: Simplified uniaxial geometry where area fraction was varied with changing r_{int}.

area fraction carburised, the local stress response will be the same under uniaxial loading conditions. Additionally this model is used to determine the range of applicability of the assumption that carburised structures can be treated as homogeneous but with reduced creep ductility. Therefore, with appropriate kinematic constraints, a simple test case can be considered under uniaxial loading where area fraction carburised is varied as a function of radius.

The simplified model was used to run a series of parametric studies assuming parabolic tensile and creep distribution profiles within the carburised layer (NN model, Figure B.6). The Young's modulus, creep law multiplier, area fraction carburised (a_f), and applied stress (σ_{obs}) have been varied in the model.

As real structures have a small area fraction carburised due to the depth of the carburisation ($0.25 - 1mm$), the chosen area fractions carburised are 2.5% – 15%. The loading conditions (σ_{obs}) have been chosen to be between 140 – 260 MPa. The *average* Young's modulus values in the literature are cited as 176 GPa [23] and 205 MPa [24]; therefore Young's modulus has been chosen to be 176 – 239 GPa. The *average* reduction in creep law multiplier have been cited as A_o/A_c = 22 [24]. However as there is uncertainty regarding this value, the range of A_o/A_c has been chosen to be 17.9 - 30.8. The parameters used in this study are summarised in Table 4.9. In total, this results in 972 models. The collected data have been used to

Parameter	Factor
E_c [GPa]	[176, 205, 239]
A_o/A_c [-]	[17.9, 20.4, 22.0, 24.7, 27.5, 30.8]
σ_{obs} [MPa]	[140, 155, 170, 185, 200, 215, 230, 245, 260]
a_f [%]	[2.5, 5, 7.5, 10, 12.5, 15]

Table 4.9: Parameters used for the parametric FE study.

build a support vector machine classifier (section 2.3.2) that is capable of predicting whether or not the carburised layer will reach the assumed creep failure strain, ε_f^c, before the homogeneous specimen reaches the same strain under the same loading conditions (more details in section 4.4.2).

4.4.2 Results

Stress state

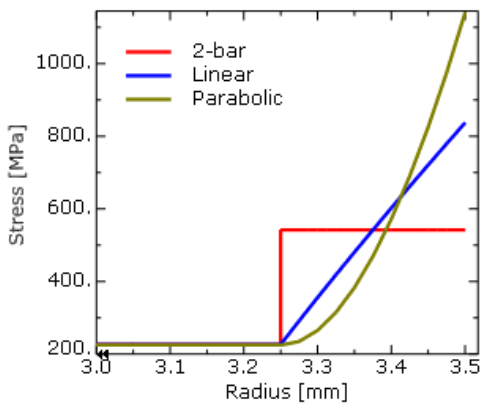

(a) Mises stress at $t = 0$;

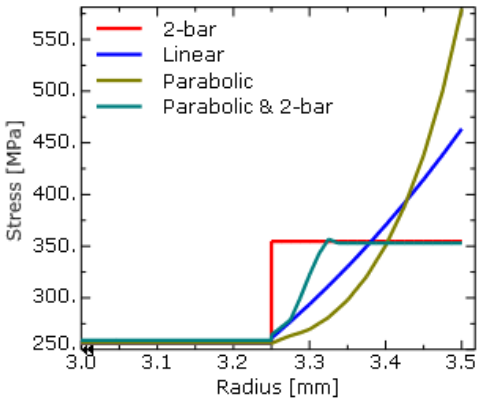

(b) Mises stress at $t = t_{end}$;

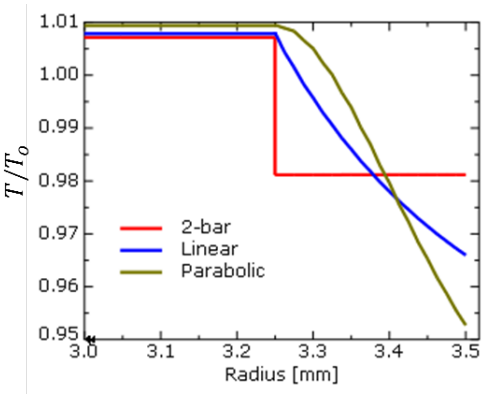

(c) Stress triaxiality at $t = 0$.

Figure 4.18: Stress state through the thickness for assumed distribution profiles (carburised region).

The stress distribution assuming the actual a_f = 14% uniaxial specimen geometry loaded at 270 MPa is shown in Figure 4.18. Figure 4.18a and 4.18b shows the stress through the thickness of the carburised region upon initial loading and after 10k hours, respectively. All models initially ($t = 0$) give the same stress state in the bulk region (227 MPa) which ensures that the global stress response is the same. Similarly at $t = t_{end}$ all models give the same bulk stress response (256 MPa), which indicate that although each model has a different creep property distribution profile, the global steady-state creep rate is the same. By comparing the initial and final stresses for the *Parabolic & 2-bar* model can be seen that initially the stress distribution follows that of a *Parabolic* model, however at fully redistributed state the stress will be homogeneous through the carburised layer. On average the stress in carburised layer after redistribution reduced by factor of 1.53 compared to the stress upon the initial loading.

The calculated stress triaxiality shows that initially there is some reduction in T/T_o for the given geometry, however, it is less than 5% at the outer surface. At $t = t_{end}$ the normalised stress triaxiality was unity which indicates that any stress triaxiality effects for uniaxial loading conditions of this geometry can be neglected. Therefore this further simplifies the creep damage analysis of the parametric creep study.

Creep strain accumulation

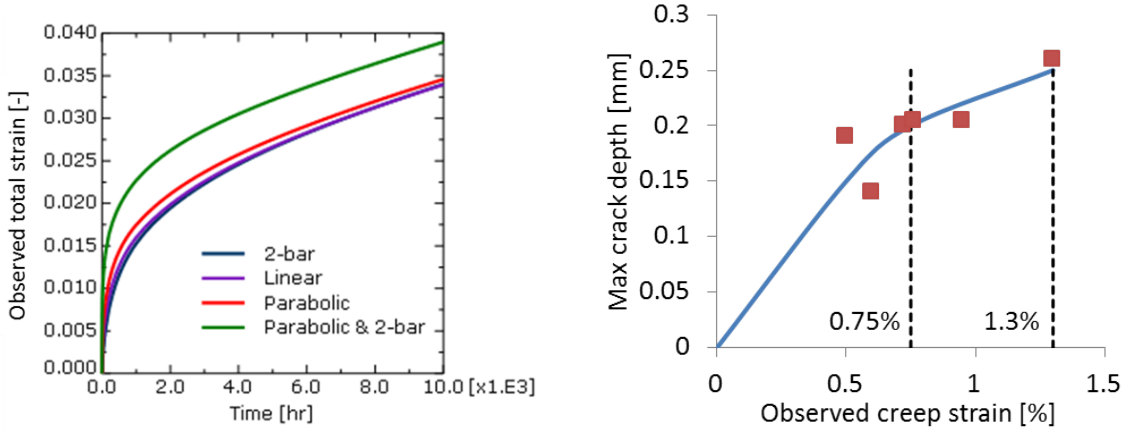

(a) Total strain accumulation over time;

(b) Crack depth vs creep strain, adapted directly from [24].

Figure 4.19: Creep strain accumulation and the carburised layer creep ductility reference data.

During stress redistribution phase pre-carburised specimens experience a reducing creep strain rate that resembles primary creep. Figure 4.19a illustrates this phenomenon where the observed total strain is plotted against time. By comparing the global response of all 4 cases, the *Parabolic & 2-bar* model accumulates the most creep strain ($\varepsilon^c_{obs}(t_{end})$ = 3.9%) during the stress redistribution phase ($\varepsilon^c_{obs}(t_{end})$ = 3.9%). *Parabolic* ($\varepsilon^c_{obs}(t_{end})$ = 3.5%), *Linear* ($\varepsilon^c_{obs}(t_{end})$ = 3.4%) and *2-bar* ($\varepsilon^c_{obs}(t_{end})$ = 3.4%) models are comparable to each other, but the *Parabolic* model would give the highest creep strain accumulation initially. Therefore the *Parabolic* model is the second most conservative test case. Despite showing an accelerated creep behaviour initially at t_{end} all models have achieved the minimum creep rate of $\dot{\varepsilon}^c_{obs}(t_{end}) \approx 1.069 \times 10^{-6}$ [-/hr] which makes the carburised model creep rate by a factor of 1.69 slower compared to the homogeneous/non-carburised model creep rate.

In order to make a meaningful creep ductility estimation of the carburised layer the local creep strains must be considered. Figure 4.19b shows the data from interrupted creep tests of pre-carburised specimens at 240 - 270 MPa [24]. The ductility

of the carburised layer can be estimated by examination of the local creep strains at a particular ε^c_{obs} at the depth that corresponds to the observed crack size. Based on Figure 4.19b the observed strains of interest are ε^c_{obs} = 0.75% and ε^c_{obs} = 1.3%. Figure 4.20 shows the local creep strain accumulation of each test case for the selected observed strains.

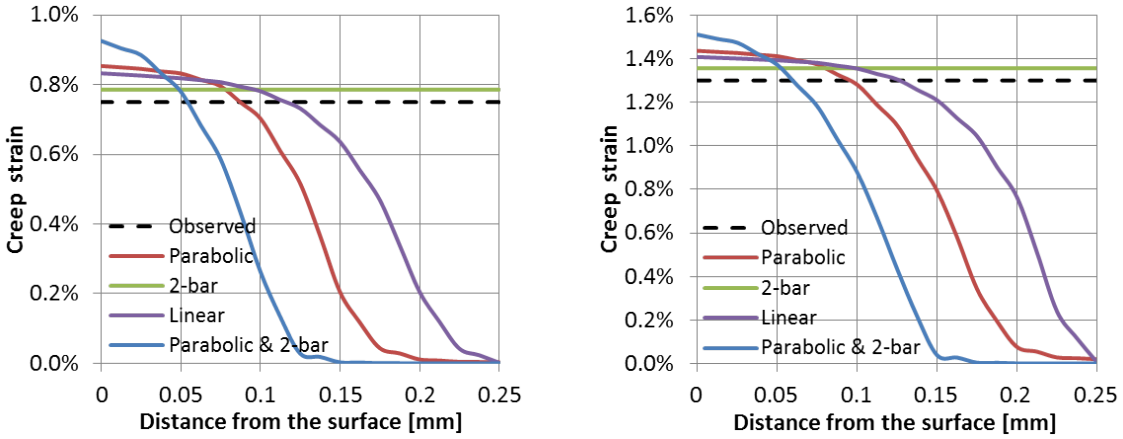

(a) Creep accumulation for ε^c_{obs} = 0.75%; (b) Creep accumulation for ε^c_{obs} = 1.3%.

Figure 4.20: Creep strain accumulation in the carburised layer for different distribution profiles.

Unsurprisingly the maximum creep strain (ε^c_{max}, Eq. 4.18) is accumulated at the surface. In all test cases the maximum creep strain at the surface exceeds the observed total strain; however the accumulated creep strain in the bulk section is insignificant as the strain accumulation there is dominated by plastic strain due to the increasing stress. In order to correlate the crack size to the *average* ductility of the carburised layer, certain assumptions must be made regarding the characteristic ductility. In this study the characteristic creep strains have been estimated by assuming that the creep strain to failure of the carburised layer is either the averaged value between the maximum and minimum creep strains (ε^c_{mid}, Eq. 4.19) or the average creep strain value (ε^c_{ave}, Eq. 4.20) over the crack depth, x_c (Figure 4.19b). For values of ε^c_{obs} = 0.75% and 1.3% the values of x_c are 200μm and 250μm respectively. A summary of the characteristic creep strain values, $\varepsilon^c_{max}, \varepsilon^c_{mid}, \varepsilon^c_{ave}$, is given in Table 4.10.

$$\varepsilon^c_{max} = max(\varepsilon^c(\varepsilon^c_{obs}, \{x\})) \qquad x \in [0, x_c] \qquad (4.18)$$

$$\varepsilon^c_{mid} = \frac{1}{2}\left(max(\varepsilon^c(\varepsilon^c_{obs}, \{x\})) + min(\varepsilon^c(\varepsilon^c_{obs}, \{x\})\right) \qquad x \in [0, x_c] \qquad (4.19)$$

$$\varepsilon^c_{ave} = \frac{1}{x_c}\int_0^{x_c} \varepsilon^c(\varepsilon^c_{obs}, x)dx \qquad (4.20)$$

The *2-bar* model has no variation across the thickness. Using this simplified

Test case	ε^c_{obs} = 0.75%			ε^c_{obs} = 1.3%		
	ε^c_{max}	ε^c_{mid}	ε^c_{ave}	ε^c_{max}	ε^c_{mid}	ε^c_{ave}
2-bar	0.79%	0.79%	0.79%	1.36%	1.36%	1.36%
Linear	0.83%	0.42%	0.51%	1.41%	0.71%	1.08%
Parabolic	0.85%	0.43%	0.34%	1.44%	0.73%	0.86%
Parabolic & 2-bar	0.93%	0.46%	0.16%	1.51%	0.76%	0.51%

Table 4.10: The characteristic creep strains of the carburised layer according to Eqs. 4.18–4.20.

model the estimated creep ductility can be taken as any of the ε^c_{ave}, ε^c_{mid} values. The corresponding creep ductility of the carburised layer is approximately the same as the observed strain increase. Conversely, by comparing the ε^c_{mid} values for the other cases, all of the characteristic creep strain values are 0.42% − 0.46% (at ε^c_{obs} = 0.75%) or 0.71% − 0.76% (at ε^c_{obs} = 1.3%), i.e. approximately 60% of the observed strain increase. The ε^c_{ave} would give more conservative approximation for models like *Parabolic & 2-bar* because in this model at 150μm the creep strains are insignificant compared to the surface values.

Creep damage classification

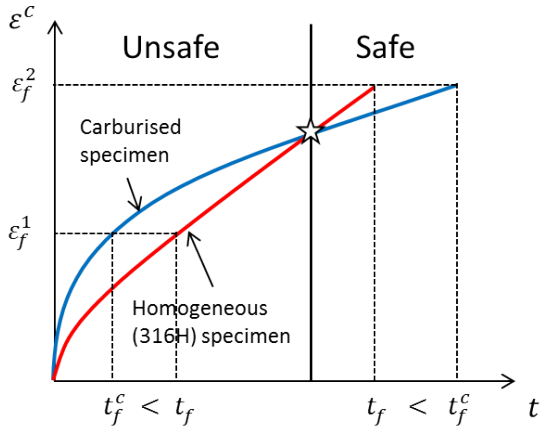

Figure 4.21: Illustration of how *safe* and *unsafe* regions are determined.

By using the characteristic ductility values, the range of applicability of simplified assumptions can be determined from the gathered parametric study data. In the previous sections it has been determined that carburisation causes accelerated creep deformation during the initial stress redistribution phase. However at the fully redistributed state the steady-state creep rate is lower than that of a homogeneous specimen. Based on this information there is a point of intersection where creep curves of the carburised specimen will intersect with these of the homogeneous specimen. If the carburised material response is compared to the homogeneous material, the response is illustrated in Figure 4.21. The ☆ symbol shows the point

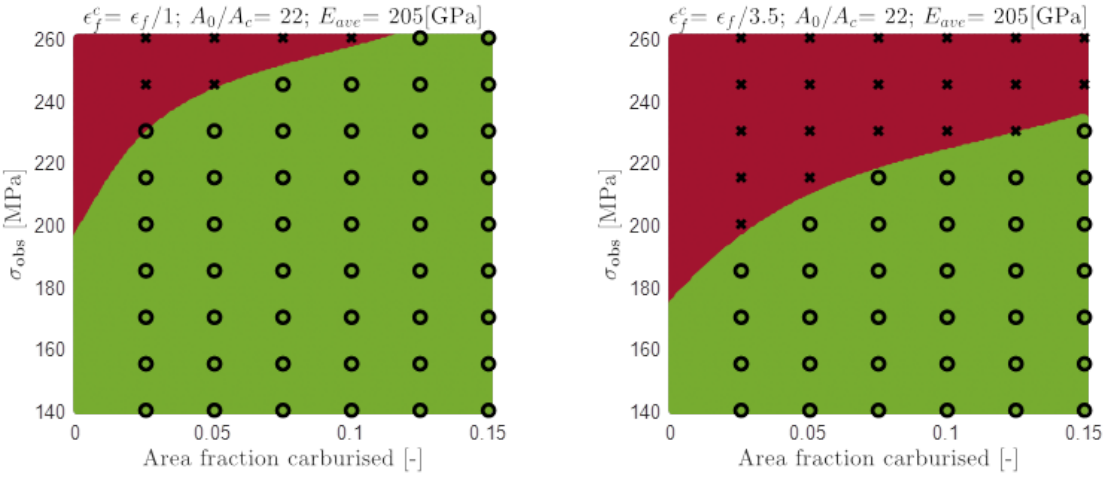

(a) ε_f^c = 2.6%

(b) ε_f^c = 0.75%;

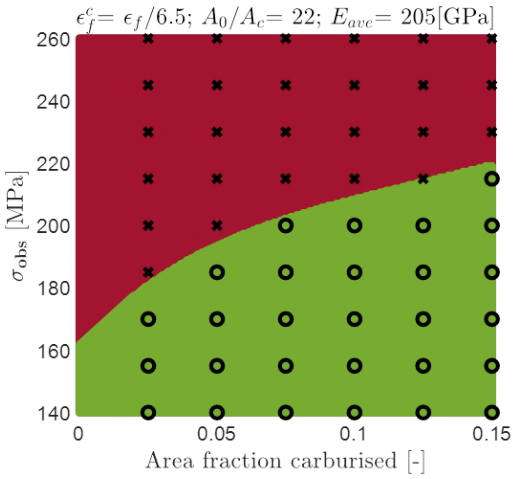

(c) ε_f^c = 0.4%

Figure 4.22: Classification of *safe* (green) and *unsafe* (red) creep operating regions using ε_{mid}^c (Eq. 4.19) as the safety criterion.

of intersection of the carburised and homogeneous specimen apparent creep curves. Assuming that the carburised layer ductility is reached before the point of intersection ($\varepsilon_f^c = \varepsilon_f^1$) then the time for the carburised layer to reach ε_f^1 is smaller than for the homogeneous specimen to reach the same creep strain. In this scenario ignoring the effects of carburisation and treating the carburised structure as homogeneous but with reduced ductility would lead to a higher lifetime estimation than it actually is. Therefore this region is denoted as the **unsafe** region. Conversely, if the creep ductility of the carburised layer falls after the ☆ point (e.g. $\varepsilon_f^c = \varepsilon_f^2$), then by treating the carburised structure as homogeneous but with reduced ductility would be a conservative approach for lifetime estimation. Therefore, every point on the right from the point of intersection (Figure 4.21) is classified as **safe**.

The SVM classifier has been built based on the above safe and unsafe criterion and using ε_{mid}^c as the characteristic creep ductility value. Figure 4.22 shows the

results from the SVM model with FE data points of the selected models. The boundary that separates the safe and unsafe regions has been fitted for a 5-dimensional parameter space, where the parameters are the data from Table 4.9 and the assumed carburised layer creep ductility ($\varepsilon_f^c/\varepsilon_f \in [1; 0.05]$). The vertical axis is the observed applied stress, and the horizontal axis represents the area fraction carburised. The points × and ○ denote the unsafe and safe points based on the FE analysis, and the red (unsafe) and green (safe) regions are the SVM model predictions. The overall accuracy of correctly classifying data of the SVM model was 99.6%.

Figure 4.22 only shows the data of a carburised structure that has average Young's modulus of 205 GPa and $A_o/A_c = 22$. Irrespective of the assumed creep ductility, A_o/A_c or the average Young's modulus all of the models show that with increasing area fraction carburised, the threshold of the safe region increases. Considering no change in creep ductility (Figure 4.22a), the FE data predict that the safe-unsafe region boundary for $a_f = 2.5\%$ is somewhere between 230 MPa and 245 MPa. The trained SVM model predicts that for the same ε_f^c, below ≈ 197 MPa the homogeneous assumption will give conservative lifetime estimates for thick-walled structures with insignificant area fraction carburised. If $a_f > 12\%$ then the safe region extends up to 260 MPa.

Considering the case with the current suggestion for the carburised ductility value (Figure 4.22b), the lower bound value is ≈ 175 MPa and for $a_f = 15\%$ it is $\sigma_{obs} < 232$ MPa. By changing the average Young's modulus from 176-239 MPa the safe-unsafe boundary changed only by ±5 MPa. Even assuming the reduction of creep ductility is a factor of 6.5 (Figure 4.22c) the analysis still indicates that a conservative lifetime estimation would be obtained for stresses below 160 MPa if the structure was treated as a homogeneous structure with reduced ductility value.

A similar stress model has been built using the maximum creep strain (ε_{max}^c, Eq. 4.18) as the creep ductility criterion and the results can be found in Figures 4.23 and 4.24. As the maximum creep strain is used, these results would provide more conservative safe-unsafe boundary estimation. However even by assuming the reduction of creep ductility by factor of 8, the model predicts that below $150 - 160$ MPa for $a_f = 1\%$ and $195 - 20$ MPa for $a_f = 15\%$ it is acceptable to use the homogeneous assumption to determine the creep damage initiation within the carburised layer (Figure 4.23). Figure 4.23 also shows the sensitivity of the safe-unsafe boundary to the assumed Young's modulus of the carburised layer. Assuming no reduction in creep ductility, the changes in the boundary are insignificant. However, even by assuming severe reduction in ductility, the changes in the boundary vary by ±5 MPa compared to the assumed $E_c = E_{ave} = 205$ GPa value

Figure 4.24 shows that changes in the creep deformation rate does not influence the boundary of the safe-unsafe region. If value of $A_0/A_c = 16$, then the boundary of

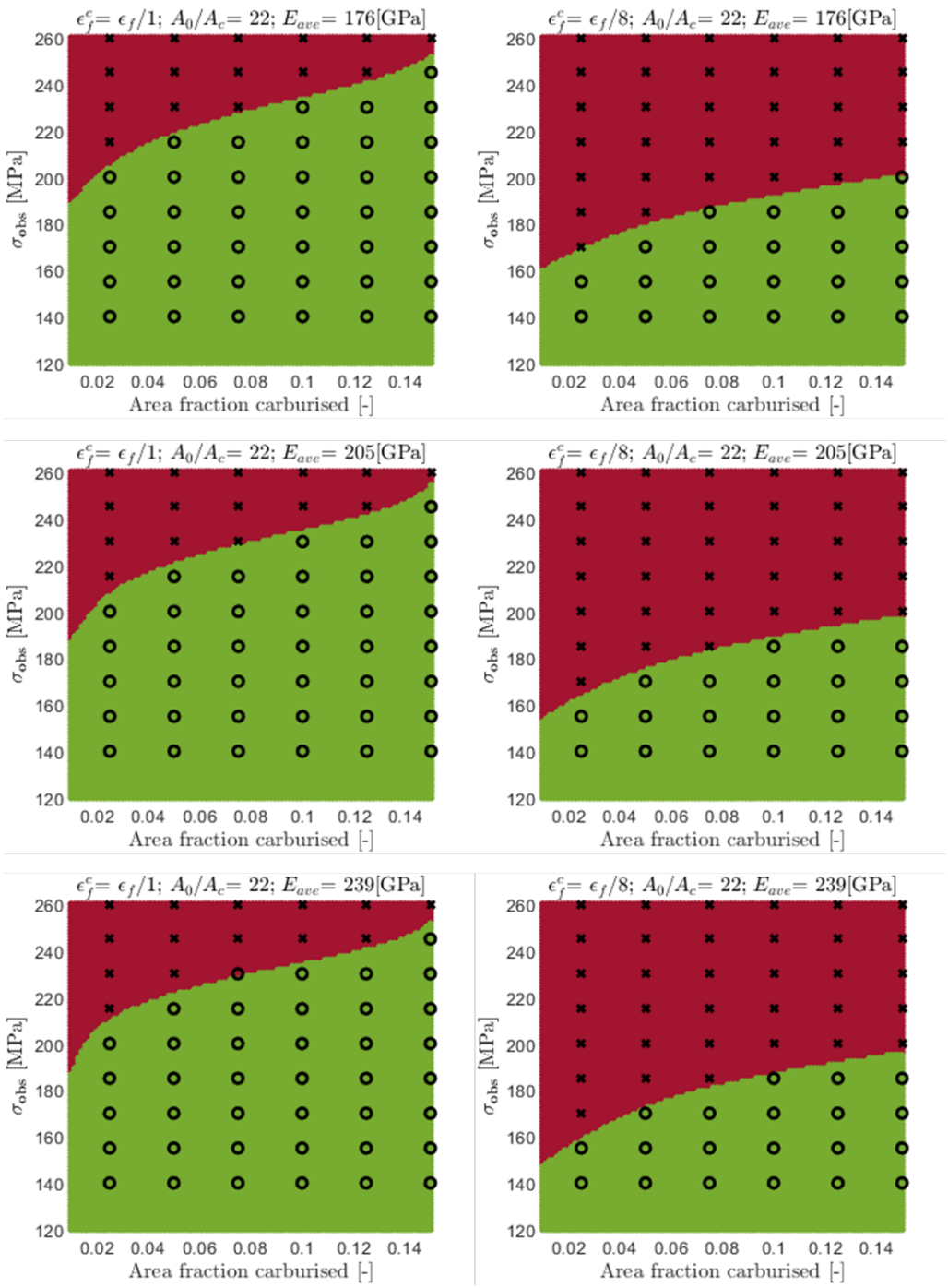

Figure 4.23: Classification of *safe* and *unsafe* creep operating regions using maximum creep strain as the safety criterion (changes due to reduced ductility and mismatch in Young's modulus).

10% area carburised specimen is around 230 MPa. Whereas, if value of A_0/A_c = 28, the boundary is around 238 MPa. Hence the assumed value of the reduction in creep law multiplier are not that important for determination of the safe/unsafe boundary [1]. By changing the reduction in the creep law multiplier, A_0/A_c, it was found that a higher reduction in creep rate only slightly increases the safe boundary threshold.

[1] The data points denoted as x's and o's represent only the A_o/A_c = 22 points

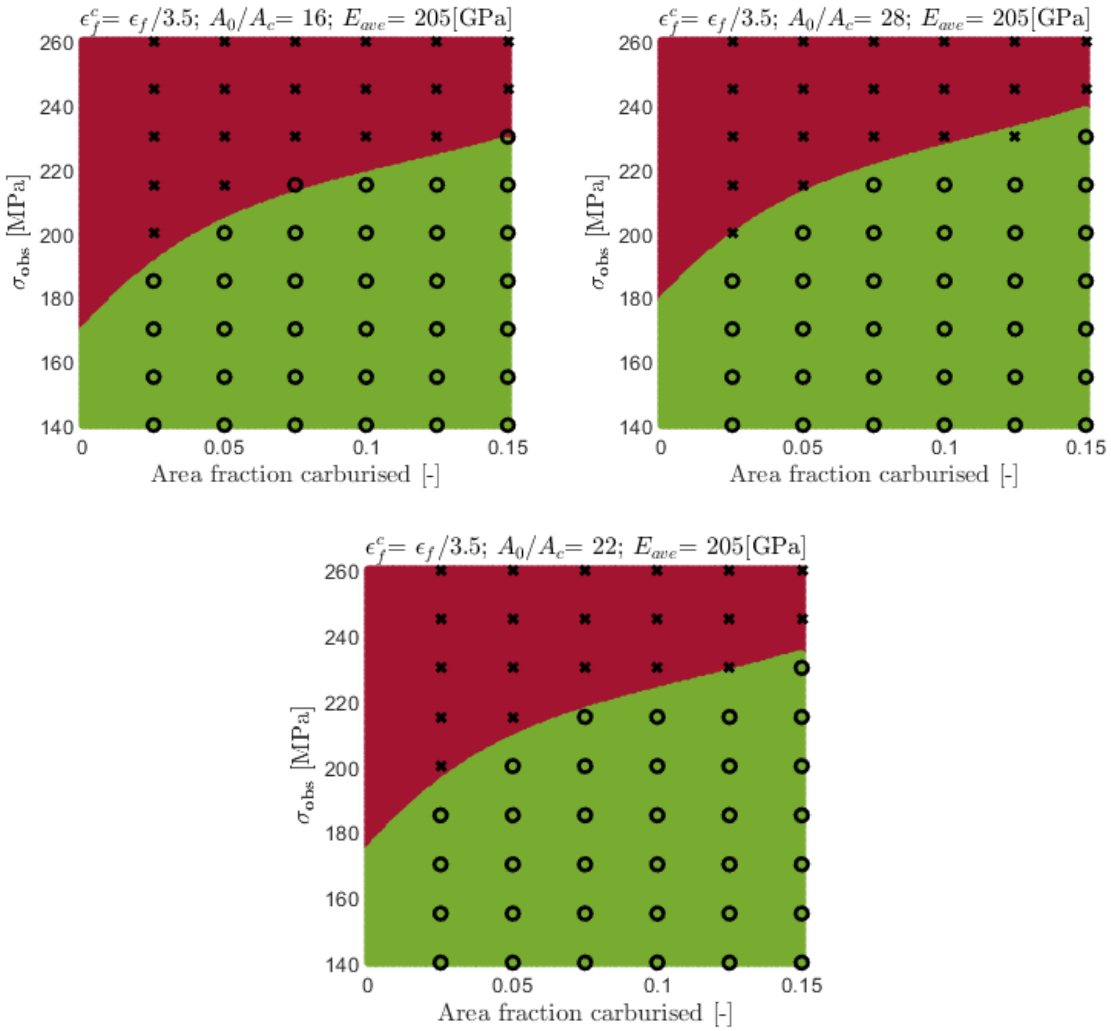

Figure 4.24: Classification of *safe* and *unsafe* creep operating regions using maximum creep strain as the safety criterion (changes due to reduced creep law multiplier).

Assuming ε^c_{max} as the ductility criterion and taking the reduction in creep rate as $16 < A_0/A_c < 28$ ($\varepsilon^c_f = 0.75\%$; $E_{c,ave} = 205\,GPa$) the change in the safe-unsafe boundary was only 8 MPa.

From the acquired data, the redistribution times, t_red, were calculated. By considering all of the models where the carburised material creep rate is reduced by a factor of 22, the time needed to reach redistributed stress state is around $\sim 10^5$ hours. The time needed to reach the failure strain is less than the time needed to reach a complete stress redistribution.

4.4.3 Summary and discussion

It is difficult to interpret the creep ductility of the carburised layer from the data. The creep ductility, ε^c_f, in the study presented in this chapter has been treated as

a single value. However, if creep ductility of the carburised layer, ε_f^c, is a function of carbon concentration, stress magnitude, stress state and microstructure, such an assumption is likely to be inaccurate. The present study indicates that the observed increase in strain in a carburised specimen can overestimate the average creep strain in the carburised layer. Although locally some parts accumulate higher creep strains compared to the global response, the analysis showed that depending on the carburised layer creep ductility definition, the creep ductility can be either underestimated or overestimated. By considering the creep strain across the whole crack depth, and assuming the ε_{mid}^c or ε_{ave}^c the creep ductility can be lower than predicted from the global response. On the contrary, the ε_{max}^c definition can overestimate creep ductility. The 2-bar model shows higher creep strain accumulation in the carburised layer, hence the creep ductility of the carburised layer is most likely higher than predicted by [24]. However, engineering applications the present study shows that even if conservative characteristic creep ductility definitions are used (ε_{mid}^c, ε_{ave}^c), for a 250μm carburised layer, a creep ductility of 0.75% is an acceptable assumption based on crack size of 250μm and ε_{obs}^c = 1.3%.

An important observation is that with increasing area fraction carburised the boundary of the safe-unsafe region increases in a simplified model using homogeneous analysis. This can be explained by considering the total deformation of the specimens. A specimen with higher area fraction carburised leads to reduced global deformation. Therefore, the total strain for high a_f carburised structures will be smaller compared to low area fraction carburised structures.

It has been shown that the reduction in creep rate in the carburised material is not of major importance for finding the boundary for the safe-unsafe region. This further emphasises the importance of accurate tensile property determination which has been shown to have a significant impact on the creep stress redistribution process which is the key factor determining the lifetime of carburised structures. The boundary of the safe-unsafe regions only corresponds to the ratio of times required for carburised and homogeneous structures to reach the same creep strain. However another metric could be implemented that would describe the ratio of the time required for carburised material to reach a certain failure strain versus a homogeneous material to reach a different failure strain (e.g. 2.6%). This approach was examined in this analysis. However the results indicated that between 140-260 MPa the carburised layer always reach failure before the homogeneous material. Thus, it would not be conservative to use homogeneous deformation analysis with homogeneous material ductility for pre-carburised specimens.

The presented study only considers pre-carburised specimens, therefore, a similar case study could be considered where carburisation kinetics are taken into account, similar to the study proposed in section 4.2. Additionally considering various

a_f, A_o/A_c, $\sigma_{obs}\, E_c$ parameters the redistribution time (t^c_{red}) could be calculated. It can be postulated that if the time to failure for the carburised layer is greater than the time to reach the minimum creep strain ($t^c_{red} < t^c_f$) rate, then

$$\varepsilon^c_c(t) = \varepsilon^c_c(t^c_{red}) + \dot{\varepsilon}^c_c \cdot (t - t^c_{red})$$

The minimum creep strain rate, $\dot{\varepsilon}^c_c$, of the carburised structure is known from the analytical solution (section 3.3.1 and 3.3.3), and the creep strain at the redistribution time $\varepsilon^c_c(t^c_{red})$ could be found from various parametric studies for various loading conditions and a_f carburised. The proposed analysis would determine conditions where carburisation could extend the lifetime of the structure.

The safe/unsafe regions identified by the creep damage classification show the same observation that was identified in section 4.2. At high stresses even by assuming no reduction in creep ductility, the carburised layer will accumulate more creep strain and leads to earlier damage initiation. The analysis shows that simplified creep analysis, where the structure is treated as homogeneous with reduced ductility, should not be used in such circumstances. In the unsafe region time to failure of the homogeneous structure exceeds the time to failure of the carburised structure. However, the present analysis has identified the region at which the homogeneous assumption with reduced ductility becomes acceptable.

Chapter 5

Analysis of bifurcation pipework

5.1 Introduction

As discussed in section 2.2.3, carburisation is influenced by factors such as temperature, gas composition, pressure, surface finish, and stress state. Although carburisation of stainless steels is a complex process and its kinetics in AGR environment are not fully understood, in terms of structural integrity assessments, engineers are interested in how carburisation will impact lifetime assessment of components susceptible to carburisation and creep damage.

Bifurcation welds in AGR's are known to be susceptible to creep crack growth [19]. Furthermore, recent research has been attempting to predict surface crack initiation considering the effects of pipe cold-forming, welding and in-service operation [140]. However, analysis considering a homogeneous structure without the effects of carburisation has failed to predict microcrack initiation at the hardened surface. Therefore, there is a need for an assessment methodology that is capable of predicting damage initiation on the hardened outer layer.

One of the proposed assessment methods is to assume a homogeneous structure but with reduced creep ductility. It is known from previous chapters that such an assumption can lead to an underestimate of the time to failure, particularly if the creep analysis is based on pre-carburised material. If the carburisation occurs while the material is subjected to in-service loading conditions, then the effects of reduced creep strain can offer an extended lifetime compared to that predicted with a simplified homogeneous assumption with reduced creep ductility. However, for real component assessment the homogeneous assumption greatly simplifies the analysis procedure. Therefore there is a need to investigate the range of applicability of this assumption.

The objective of this chapter is to understand how carburisation influences the structural integrity assessment of an in-service pipework joint. The bifurcation

pipework is modelled using Abaqus finite element software using different material property distributions. Additionally, simplified models for capturing in-service carburisation have been proposed. The performance of various carburised models are compared with the reference/homogeneous model, where the effects of carburisation are ignored, but material ductility is reduced by some factor. Finally, the effects of carburisation depth are investigated by modelling the carburised structure with a carburised layer thickness of 0.25 mm and 1 mm.

5.2 The bifurcation pipework joint model

The bifurcation pipework joint geometry and loading conditions have been taken from earlier investigations of the effects of manufacturing history on creep-fatigue damage accumulation of the same geometry [140]. The following model does not consider the effects of manufacturing, defects or residual stresses in the heat affected zone. The models assumes constant loading conditions, a temperature of $550^{o}C$, and uniform bulk material (Type 316H stainless steel).

5.2.1 Implementation in Abaqus

The discretised geometry of the component that has been used in FEA is shown in Figure 5.1. The component combines the flow of superheater steam of two inlet tubes from bent tubing (denoted as 1) into a single outlet tube (denoted as 2). The inlet tubes have 38.1 mm outside diameter and 4.06 mm wall thickness; the outlet tube has 50.8 mm outside diameter and 5.38 mm wall thickness. The transition stub (denoted as 3) joins the outlet tube with the bent tubing. A more detailed engineering drawing of the geometry can be found in [140].

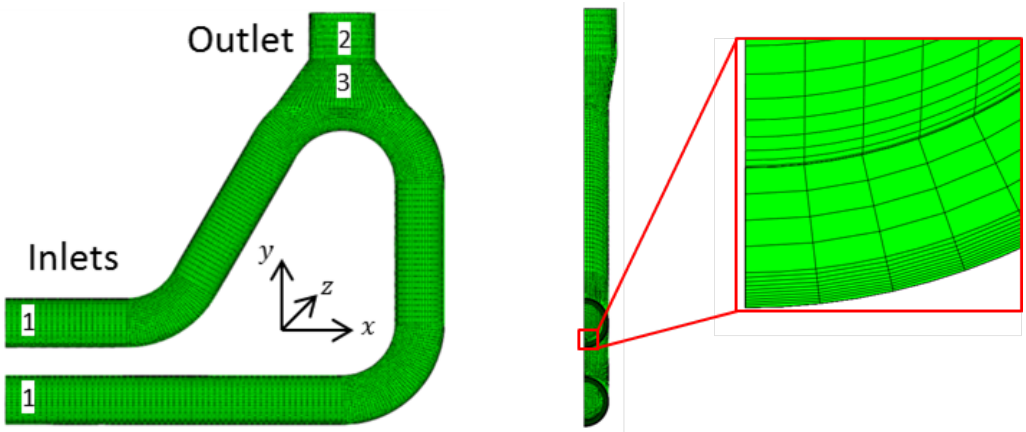

(a) Front view;

(b) Side view and carburised layer discretisation.

Figure 5.1: The bifurcation pipework joint geometry implementation in Abaqus.

Half of the geometry has been modelled to save computation time. Therefore, z-symmetry boundary conditions (Figure 5.1a) have been applied. The ends of the inlet tubes have been constrained in the x-direction and the outlet end has been constrained in the y-direction respectively to allow tube ends to expand. The loading conditions of in-service operation have been applied: an internal pressure (p_i) of 16.8 MPa and external pressure (p_e) of 3.9 MPa. The model does not consider cyclic loading conditions or other system loads, e.g. boiler expansion and rotation at the boiler inlet ends.

To analyse such a structure the mesh refinement has to be sufficiently small to account for the thin carburised layer with variations in material properties. The optimal mesh size has been found by carrying out a small mesh sensitivity analysis to achieve a sufficiently refined mesh where results do not change significantly with higher refinement and computation time is within reasonable limits. The model consists in total of 58920 thermally coupled quadratic brick 20-node elements (C3D20RT). The outer surface has been discretised using eight elements to account for up to 1 mm carburisation depth (Figure 5.1b).

5.2.2 Material properties and model description

Reference model

The bulk material tensile properties of Type 316H stainless steel at $T = 550^oC$ are described by Eq. 4.8, and the creep properties used are the same as those listed in section 2.2.4. The following material properties were used to calculate the results for the reference/homogeneous test case:

$$\varepsilon_b = \varepsilon_b^e + \varepsilon_b^p = \frac{\sigma}{157000} + \left(\frac{\sigma}{374.3}\right)^{8.7873} \tag{4.8}$$

$$\dot{\varepsilon}_b^c = 8.876 \times 10^{-35} \sigma^{10.18}. \tag{5.1}$$

Pre-carburised models

The pre-carburised (denotes as PC) models, similar to pre-carburised models from Chapters 3 and 4, assume 3 different property distribution profiles: *2-bar*, *linear*, and *parabolic*. Creep property distribution profiles can be found in Chapter 3, Figure 3.5. The tensile properties for the carburised part of the model are *2-bar* according to Eq. 2.32:

$$\varepsilon_c = \frac{\sigma_c}{E_c} + \left(\frac{\sigma_c}{1304}\right)^{\frac{1}{0.19}}; \tag{2.32}$$

The *parabolic* tensile properties for the model are according to results from Chapter 4, Figure 4.3.3; and for the *linear* assumption according to Figure B.6 in Appendix B.2.2.

Two carburisation depths have been considered. Three models consider the characteristic carburised layer depth of 0.25 mm (area fraction carburised: 5.2%–6.8%), and three with 1 mm (area fraction carburised: 20.4%–26.8%). The pre-carburised simulations examine if the carburisation distribution profile influences the creep damage calculation, and where conservativism might arise if the pre-carburised assumption is used for structural integrity assessment.

Carburising models

The carburising models (denoted as C) assume that at the start of the simulation the structure is uncarburised and consists of pure Type 316H stainless steel material. Given the size of the model, it was found to be impractical to implement the carburisation kinetics as was done in section 4.2.

According to [14], carburisation of the Type 316 steel tubes develops rapidly over about 18k hours and then slows down up to 48k hours. The purpose of the models is not to model carburisation kinetics accurately, but to investigate how carburisation times influence creep damage assessment. Therefore, a simplified assumption has been made that carburisation occurs instantly at either $t_c = 2 \times 10^3$ or $t_c = 2 \times 10^4$ hours of operation. Before t_c, the material is assumed to be homogeneous, at t_c there is a step-change in carburisation kinetics and the outer surface of the structure becomes carburised according to 2-bar, linear, or parabolic material definitions described above. Although such a step-change is not realistic, an argument can be made based on the results from section 4.2, such that, by assuming a reduced creep ductility of the carburised layer from the start (which is base material when $t < t_c$) the overall creep damage accumulation in the proposed model will be higher compared to the model with more realistic carburisation kinetics. Therefore, the proposed carburising model will be more pessimistic as the structure does not experience any benefits of the reduced creep rate due to carburisation (see $M(El, Pl, Cr)$ in Figure 4.6a). Hence, if $t < t_c$ the carburised layer has base tensile and creep deformation properties, but creep ductility is reduced, and if $t \geq t_c$ the carburised layer has carburised creep deformation, creep ductility and tensile properties.

In total 8 carburising (C) models have been analysed of which half assume carburisation depth of 0.25 mm or 1 mm, and *2-bar* or *parabolic* material property distribution profiles.

5.2.3 Calculation of creep damage

The calculation of creep damage is based on the creep strain output from the FE models and a ductility exhaustion model. An implicit integration scheme was used in the FEA using a creep error tolerance value of 1×10^{-7}.

The ductility exhaustion model is described in detail in sections 2.1.2 and 2.1.3, where creep damage is calculated using the ductility exhaustion approach (Eq. 2.9):

$$\omega^c = \int \frac{d\varepsilon^c}{\varepsilon_f(\dot{\varepsilon}^c)}. \tag{2.9}$$

In Eq. 2.9 creep damage is calculated based only on the equivalent creep strain, hence to account for ductility reduction due to increased stress triaxiality Eq. 2.16 is used,

$$\omega^{c*} = \int \frac{d\varepsilon^c}{\varepsilon_f^*(\dot{\varepsilon}^c)}, \tag{2.16}$$

where Spindler's multiaxial ductility factor (Eq. 2.15) with $p = 2.38$ and $q = 1.04$ is used to calculate the modified creep ductility (ε_f^*) according to the stress state.

The analysis does not include ductility dependence on the stress magnitude, because the purpose of this chapter is to investigate the relative effects of carburisation compared to the reference (homogeneous) model. Hence the creep ductility of the base material is assumed to be $\varepsilon_f = 2.6\%$. The time for creep damage initiation has been calculated based on ω^c and ω^{c*} damage estimates when damage parameter reaches unity and normalised as:

$$t_f^N = \frac{t_f(\varepsilon_f)}{t_f^{hom}(\varepsilon_f = 2.6\%)} \tag{5.2}$$

$$t_f^{N*} = \frac{t_f(\varepsilon_f)}{t_f^{hom}(\varepsilon_f = 2.6\%)}. \tag{5.3}$$

In section 4.4.2 Table 4.10 the characteristic uniaxial creep ductility values of the carburised layer where estimated to be ~ 0.45% and ~ 0.75%. According to the proposed advice on creep damage calculations for R5, a creep ductility value of 0.75% is suggested compared to 2.6% for base material. Therefore, in this study the assumed creep ductility values of the carburised layer are $0.26\% \leq \varepsilon_f \leq 2.6\%$. A more detailed damage accumulation over time are presented for the carburised layer creep ductility values estimated in section 4.4.2, where $\varepsilon_f = 2.6\%, 0.75\%, 0.45\%$.

5.3 Results

The following set of results have been gathered at the point which sustains the most creep damage in the structure. For all models the maximum damage point was the same. Therefore, a comparison has been made between the homogeneous/uncarburised model (denoted as *Hom*) and PC/C models.

5.3.1 Creep damage initiation in a homogeneous structure

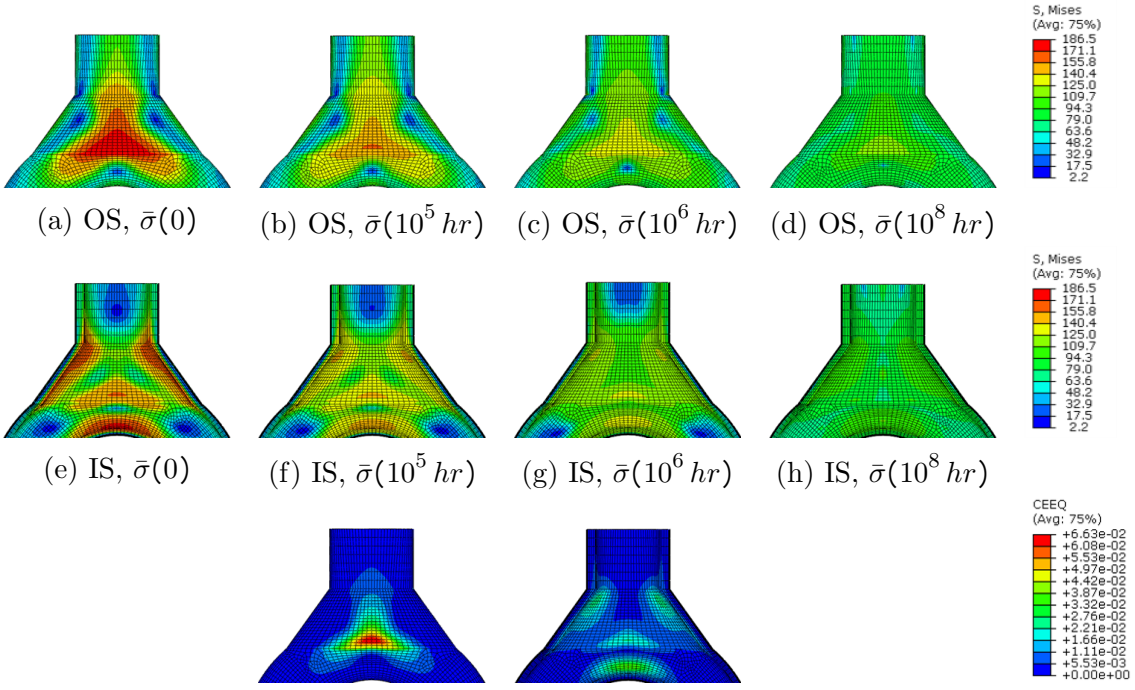

(a) OS, $\bar{\sigma}(0)$ (b) OS, $\bar{\sigma}(10^5\,hr)$ (c) OS, $\bar{\sigma}(10^6\,hr)$ (d) OS, $\bar{\sigma}(10^8\,hr)$

(e) IS, $\bar{\sigma}(0)$ (f) IS, $\bar{\sigma}(10^5\,hr)$ (g) IS, $\bar{\sigma}(10^6\,hr)$ (h) IS, $\bar{\sigma}(10^8\,hr)$

(i) OS, $\bar{\varepsilon}^c(10^8\,hr)$ (j) IS, $\bar{\varepsilon}^c(10^8\,hr)$

Figure 5.2: Contour plots of von Mises stress and creep strain at various times at the outer surface (OS) and inner surface (IS).

According to the current assessment advice for carburised structures assessment [24], carburised structures are treated as homogeneous but with locally reduced ductility. Therefore this section presents a damage calculation based on this assumption and investigates how the creep damage initiation time might change.

Figure 5.2 shows contour plots of von Mises stress change over time and accumulated creep strain at the point with the maximum creep strain. The maximum creep strain is accumulated on the outer surface at the transition stub and bent tubing interface. Upon initial loading, the stress in the most highly stressed region is 186.5 MPa, which is above the material's 0.2% yield stress. As stresses relax in the structure, at the end of the simulation (t_{end} = 10^8 hr) the von Mises stress in the transition stub and bent tubing interface has dropped to 114.8 MPa.

Despite the long simulation time, complete stress redistribution was not achieved in the structure. The structure has very lowly stressed regions of von Mises stress value of 2.2 MPa. The stress response in the midsection of the pipe initially follows Lamé's equations [71] with a hoop stress value of 52 MPa at the inner surface at the bent tubing, and at t_{end} the stress drops to 48.7 MPa, hence steady state had not been reached.

Although full stress redistribution had not been achieved, the area of interest in these models is the maximum creep strain and creep damage accumulation. Figure 5.2i show the region of the highest accumulated creep strain: a maximum of 6.6% creep strain. Creep damage calculations have been performed assuming the material has the uniaxial creep ductility of ≤ 2.6%, and creep damage accumulation over time assuming 2.9 and 2.16 is presented in Figure 5.3.

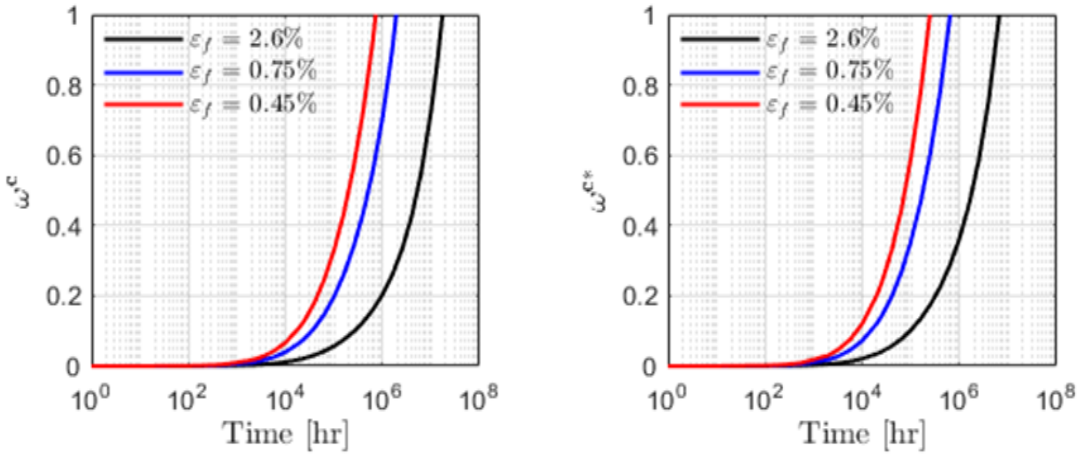

(a) Damage calculation based on equivalent creep strain;

(b) Damage calculation including multiaxial ductility factor.

Figure 5.3: Creep damage accumulation in a homogeneous structure assuming reduced ductility due to carburisation.

For the R66 [89] creep ductility of 2.6% and ignoring the effects of multiaxial stress state (Eq. 2.9), the time for creep crack initiation under the given loading conditions is 9.414×10^6 hours (> 1000 years). If the creep ductility is assumed to be reduced to 0.75% (factor of 3.5) or 0.45%, the time to failure reduces by factors of 7.8 or 18.1, respectively (Figure 5.3a).

Figure 5.3b shows creep damage accumulation according to Eq. 2.16. Considering the local stress triaxiality, the material at the most highly stressed region is under hydrostatic tension with stress triaxiality being $T(t = 0) = 0.626$ and the value of stress triaxiality is not changing significantly over time ($T(t) \approx const$). Assuming no reduction in creep ductility (ε_f = 2.6%), the time to reach creep damage initiation is 6.057×10^6 (≈690 years). However considering a reduction in creep ductility by a factor of 3.5 (ε_f = 0.75%) the time to damage initiation reduces by a

factor of 9.75. The times for creep damage to reach unity assuming different creep ductility values at the most highly stressed region, are summarised in Table 5.1.

ε_f	$t_f^{hom}(\omega^c)$ [hr]	$t_f^{hom}(\omega^{c*})$ [hr]
2.6%	9.414×10^6	6.057×10^6
0.75%	1.205×10^6	6.212×10^5
0.45%	5.204×10^5	7.018×10^4

Table 5.1: Creep damage initiation times assuming different creep ductility and creep damage models for homogeneous test case.

5.3.2 Effects of material property distribution profile

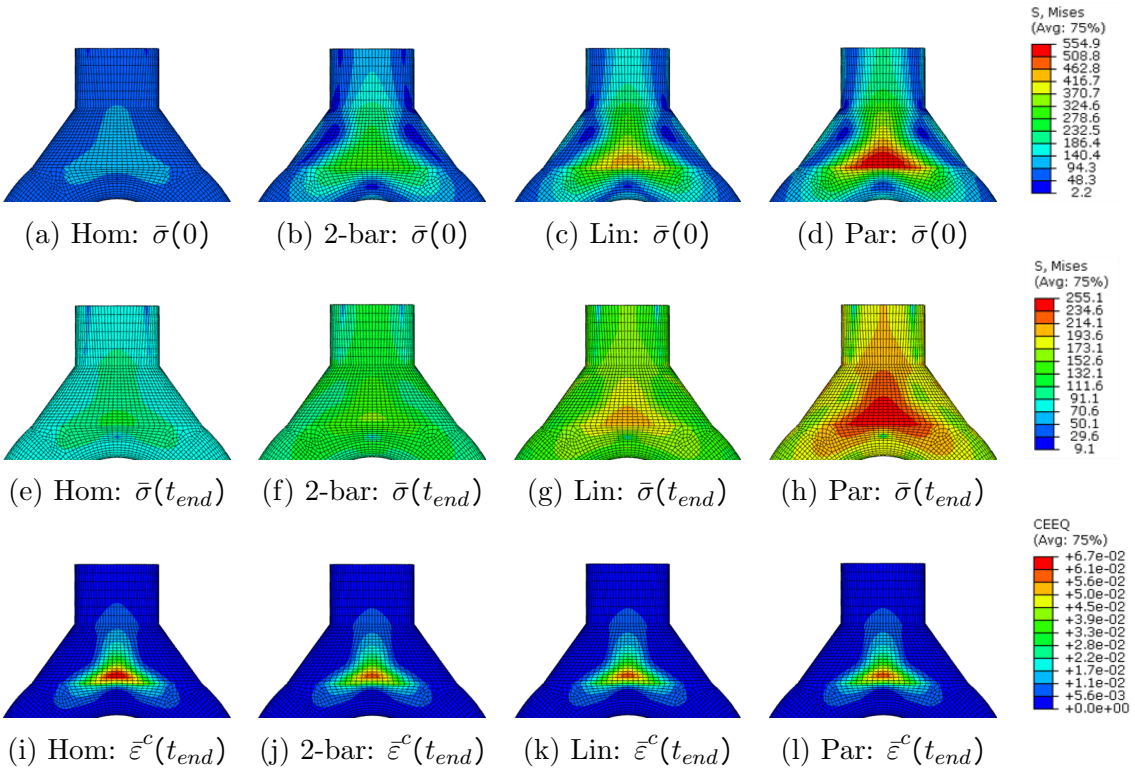

(a) Hom: $\bar{\sigma}(0)$ (b) 2-bar: $\bar{\sigma}(0)$ (c) Lin: $\bar{\sigma}(0)$ (d) Par: $\bar{\sigma}(0)$

(e) Hom: $\bar{\sigma}(t_{end})$ (f) 2-bar: $\bar{\sigma}(t_{end})$ (g) Lin: $\bar{\sigma}(t_{end})$ (h) Par: $\bar{\sigma}(t_{end})$

(i) Hom: $\bar{\varepsilon}^c(t_{end})$ (j) 2-bar: $\bar{\varepsilon}^c(t_{end})$ (k) Lin: $\bar{\varepsilon}^c(t_{end})$ (l) Par: $\bar{\varepsilon}^c(t_{end})$

Figure 5.4: Contour plots of the stress state and creep strain accumulation in homogeneous and pre-carburised bifurcation models. *Note, the scales in 5.4a-5.4h differ from those in Figure 5.2.*

Contour plots of von Mises stress and accumulated creep strain for the homogeneous structure and for models with a pre-carburised (carburised layer thickness: $0.25\,mm$) layer are shown in Figure 5.4. All of the pre-carburised models lead to an increased von Mises stress in the highly stressed region. Additionally, all of the PC models show decreasing stress with time due to stress redistribution. However, the magnitude of the stress depends on the assumed carburisation property distribution. The bi-layer (*2-bar*) assumption leads to the lowest stress of the PC models

at the point of interest ($\bar{\sigma}(0)$ = 342 MPa and $\bar{\sigma}(t_{end})$ = 199 MPa). *Linear* and *parabolic* assumptions give significantly higher initial von Mises stress: 439 MPa and 555 MPa, respectively. At t_{end}, the *parabolic* model has a stress of 255 MPa stress near the transition stub and bent tubing.

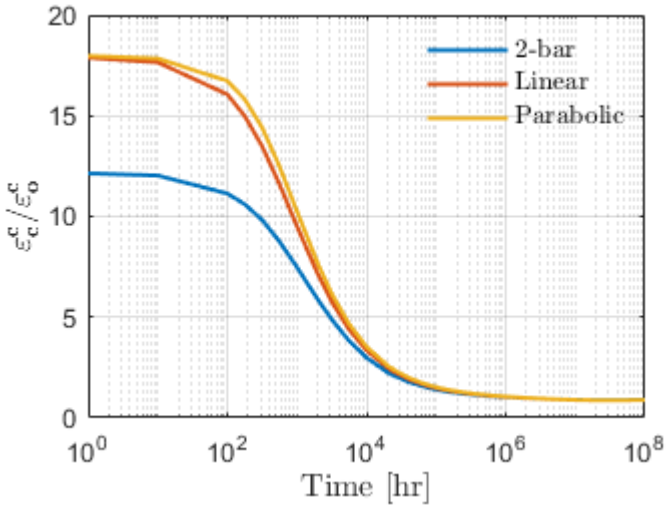

Figure 5.5: The normalised creep strain accumulation of pre-carburised models assuming different creep material property distribution profile.

Despite the enhanced von Mises stress due to the hardened outer layer, the accumulated creep strain at t_{end} for all pre-carburised models is essentially the same ($\approx$ 6%), which is 0.7% lower than the homogeneous model (Figures 5.4i – 5.4l). However, Figure 5.5 shows that the normalised creep strain is initially higher compared to the homogeneous case. The *2-bar* model at t = 1 hr has accumulated a creep strain which is a factor of 12 higher than the accumulated creep strain in the homogeneous case. The *linear* and *parabolic* assumptions leads to a factor of 18 higher creep strain. For the given loading conditions the *linear* and *parabolic* models exhibit similar creep strain response while having different stress values.

Despite the initial increase in creep strain, at $t = 10^5$ hours all of the PC models have converged to the same creep strain value which is 1.5 times higher than the homogeneous creep strain value, and after $t = 10^6$ hours the total creep strain is below that of the homogeneous model. Creep damage accumulation over time is summarised in Figure 5.6. Figures 5.6a–5.6c shows damage accumulation assuming uniaxial ductility exhaustion model based on equivalent creep strain (Eq. 2.9), and Figures 5.6a–5.6c use the ductility exhaustion model including multiaxial stress effects (Eq. 2.16).

Assuming no reduction in carburised material ductility (ε_f = 2.6%), despite the accelerated creep damage accumulation due to the increased stress the creep lifetime is extended for the pre-carburised models compared to the homogeneous model (Fig-

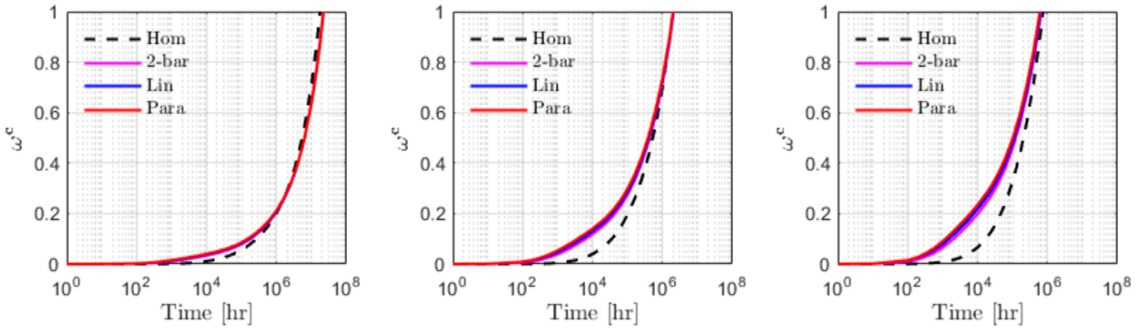

(a) $\omega^c(t, \varepsilon_f = 2.6\%)$ (b) $\omega^c(t, \varepsilon_f = 0.75\%)$; (c) $\omega^c(t, \varepsilon_f = 0.45\%)$;

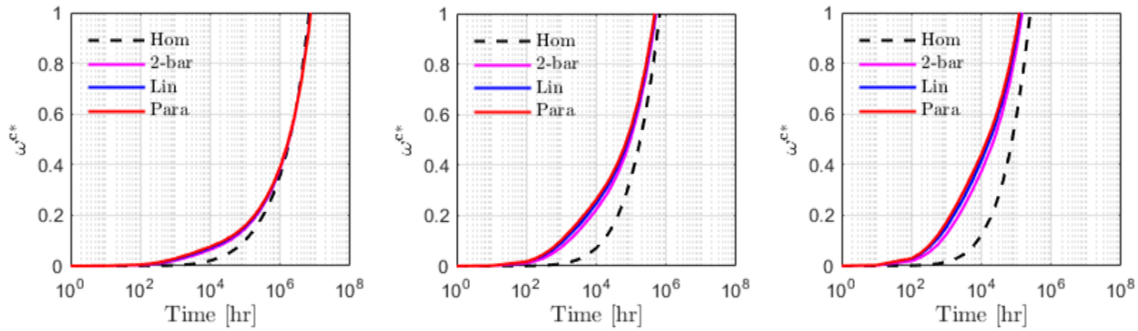

(d) $\omega^{c*}(t, \varepsilon_f = 2.6\%)$; (e) $\omega^{c*}(t, \varepsilon_f = 0.75\%)$; (f) $\omega^{c*}(t, \varepsilon_f = 0.45\%)$.

Figure 5.6: Creep damage accumulation at the surface of pre-carburised models assuming different creep ductility and damage models.

ure 5.6a and 5.6d) by a factor of ≈ 1.25, because of the reduced accumulated creep strain at long times. Allowing for a reduction in creep ductility due to multi-axiality, the time for creep damage to initiate is extended by factor of 1.1. The reduced factor is a result of the reduced times to failure (see Figure 5.2) rather than any significant triaxiality differences between the homogeneous and PC models. Hence the homogeneous model is a more conservative model for creep damage initiation assuming a creep ductility of 2.6 %.

Figures 5.6b and 5.6e show results assuming a creep ductility of 0.75%. Ignoring the effects of multi-axiality, almost identical results are obtained for the time to damage initiation using pre-carburised and homogeneous assumption (Figure 5.6b). However, including the effects of reduced creep ductility due to stress state, the time to damage initiation is reduced to a factor of $0.73 - 0.79$ of that of the homogeneous model with the same ductility.

With further reductions in creep ductility, the effects of material property distribution become more prominent and the time to damage initiation starts to differ between the PC models. Assuming a creep ductility of 0.45%, for the *2-bar* model the time to failure is 0.6 that of the homogeneous model, whereas the *parabolic* model leads to a time to failure of $0.5t_f^{hom}$ (including multiaxial effects).

The dashed lines in Figure 5.6a - 5.6f show creep damage accumulation of an

Test case	ε_f = 2.6%		ε_f = 0.75%		ε_f = 0.45%	
	t_f^N	t_f^{N*}	t_f^N	t_f^{N*}	t_f^N	t_f^{N*}
2-bar	1.24	1.11	0.13	0.08	0.05	0.03
Linear	1.26	1.10	0.13	0.08	0.05	0.03
Parabolic	1.26	1.12	0.13	0.07	0.04	0.03

Table 5.2: The normalised failure time of pre-carburised test cases according to Eqs. 5.2–5.3.

homogeneous model assuming creep ductility values the same as the carburised models: either 2.6%, 0.75% or 0.45%. A more informative way to represent the impact of the carburised layer on creep damage initiation time is to normalise the time to damage initiation with respect to the homogeneous test case with ε_f = 2.6%. The normalised times for damage to reach unity from Figure 5.6 with respect to the homogeneous model (with ε_f = 2.6%) are summarised in Table 5.2. Considering models where creep ductility of the carburised layer is 0.75%, time for creep damage initiation is significantly reduced. Although the creep ductility is reduced by a factor of 3.5, the time for damage initiation is reduced by a factor up to ≈ 14.2 (see parabolic t_f^{N*}). From Table 5.2, it can be deduced that for each creep damage model there is a ductility value at which the PC model leads to lower normalised creep damage initiation time estimates (t_f^N and t_f^{N*} is less than 1). For the given geometry and loading conditions, this ductility value at which carburisation could extend lifetime is ≈ 2.3%. A summary of how t_n^N and t_f^{N*} change for different ε_f values is summarised in a graph in Appendix C Figure C.1.

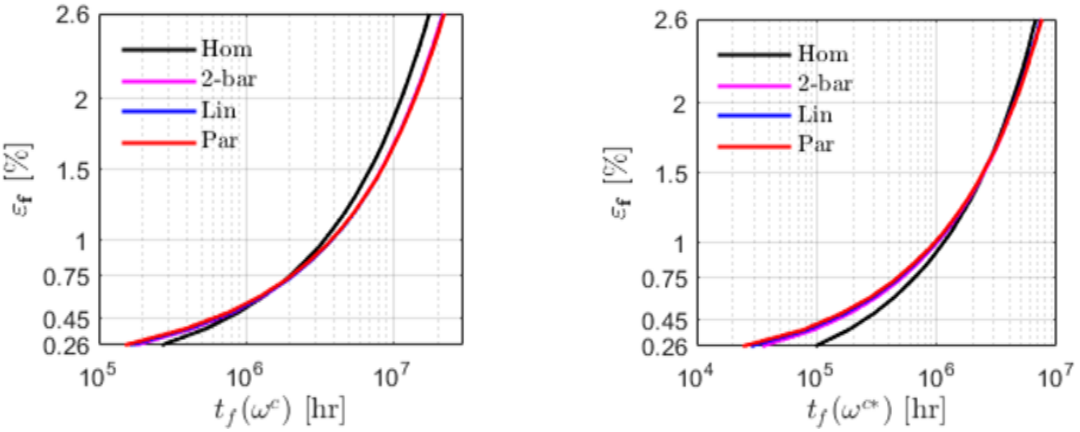

(a) Based only on equivalent creep strain; (b) Including multiaxial ductility factor.

Figure 5.7: Creep damage initiation time in pre-carburised and homogeneous test cases assuming different ductilities.

Figure 5.7 shows the time to damage initiation for creep ductility values between 0.26% and 2.6%. Figure 5.7a is according to Eq. 2.9 and Figure 5.7b according to Eq. 2.16. If the effects of multi-axiality are ignored, then for uniaxial creep

ductility values above 0.7% the homogeneous model (with reduced creep ductility) leads to more conservative damage assessment. However, for ductility below 0.7% the homogeneous assumption overestimates the time for damage initiation relative to the PC models.

Allowing for the effects of multiaxial stress state, the point where the PC curves intersect with the homogeneous curve is at ε_f = 1.5% (Figure 5.7b). Therefore, for the homogeneous model to be more conservative, uniaxial creep ductility must exceed 1.5%.

Figures 5.7a and 5.7b show that the material distribution profile has no significant influence on the creep lifetime assessment. PC curves start to differ only at low ductility values, where the *parabolic* material distribution profile is the most conservative.

5.3.3 Effects of carburisation time

As it has been established that the material property distribution profile is not that significant for uniaxial creep ductilities between 0.26% ≤ ε_f ≤ 2.6%, this section only considers the FE results using a parabolic distribution. Hence PC now refers to the *parabolic* assumption and a carburised layer thickness of 0.25 mm (as in section 5.3.2).

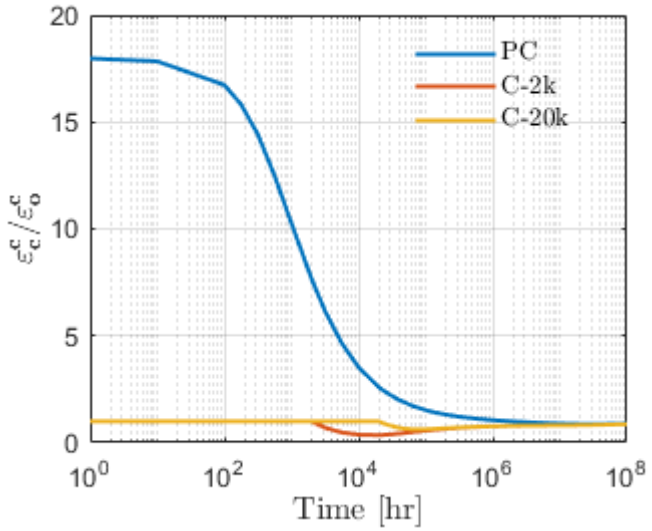

Figure 5.8: The normalised creep strain accumulation of pre-carburised and carburised models assuming pre-carburised and carburising models and carburisation depth of 0.25 mm.

Figure 5.8 compares the accumulated creep strain in pre-carburised and carburising material. *C-2k* and *C-20k* refers to carburising models that are being carburised in 2k and 20k hours respectively. Inevitably the carburising models have normalised

creep strain values of unity before the material property change occurs. After the material becomes carburised there is a reduction in the overall creep strain due to the increased carburised layer creep resistance. Both carburising models at ~ 10^5 hr converge to the same creep strain value and at 4×10^6 hr the carburising models converge to the same normalised creep strain as the pre-carburised model. The main difference between the carburising and pre-carburising models is that the normalised creep strain of the carburising models never exceeds unity.

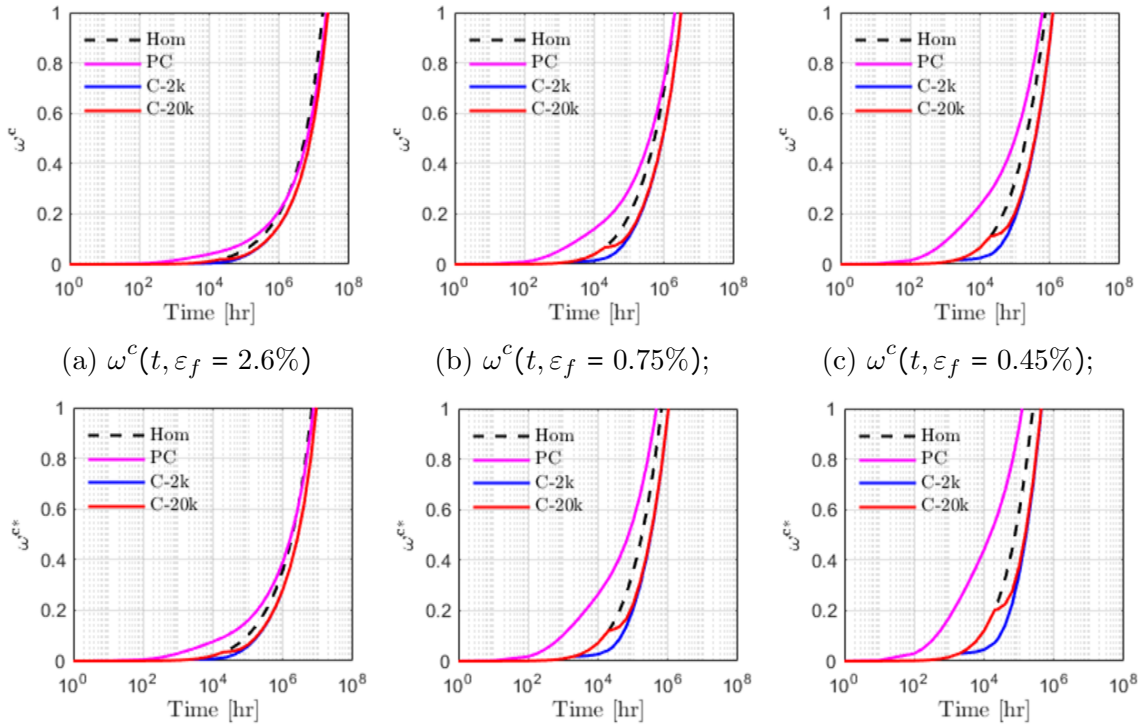

(a) $\omega^c(t, \varepsilon_f = 2.6\%)$ (b) $\omega^c(t, \varepsilon_f = 0.75\%)$; (c) $\omega^c(t, \varepsilon_f = 0.45\%)$;

(d) $\omega^{c*}(t, \varepsilon_f = 2.6\%)$; (e) $\omega^{c*}(t, \varepsilon_f = 0.75\%)$; (f) $\omega^{c*}(t, \varepsilon_f = 0.45\%)$.

Figure 5.9: Creep damage accumulation at the surface of pre-carburised and carburising models.

Test case	ε_f = 2.6%		ε_f = 0.75%		ε_f = 0.45%	
	t_f^N	t_f^{N*}	t_f^N	t_f^{N*}	t_f^N	t_f^{N*}
C-2k	1.40	1.36	0.20	0.16	0.10	0.10
C-20k	1.40	1.36	0.20	0.16	0.10	0.10

Table 5.3: The normalised failure time of carburising test cases according to Eqs. 5.2–5.3.

Similar to analysis of results in section 5.3.2, creep damage accumulation over time and normalised failure times are summarised in Figure 5.9 and Table 5.3. The reduced creep strain accumulation is reflected in the calculated time for damage initiation, where for all models t_f^N and t_f^{N*} are larger than for pre-carburised test cases (Table 5.2). This indicates that carburising while being subjected to load

can increase the time for damage initiation depending on the reduction of ductility. Comparing the results for ε_f = 0.75% shows if the creep ductility is reduced by a factor of 3.5, the time for damage initiation is reduced by a factor of ≈ 6.2 (t_f^{N*}). Table 5.3 shows that t_f^N and t_f^{N*} are comparable so that multi-axial stress effects do not reduce the normalised time for damage initiation.

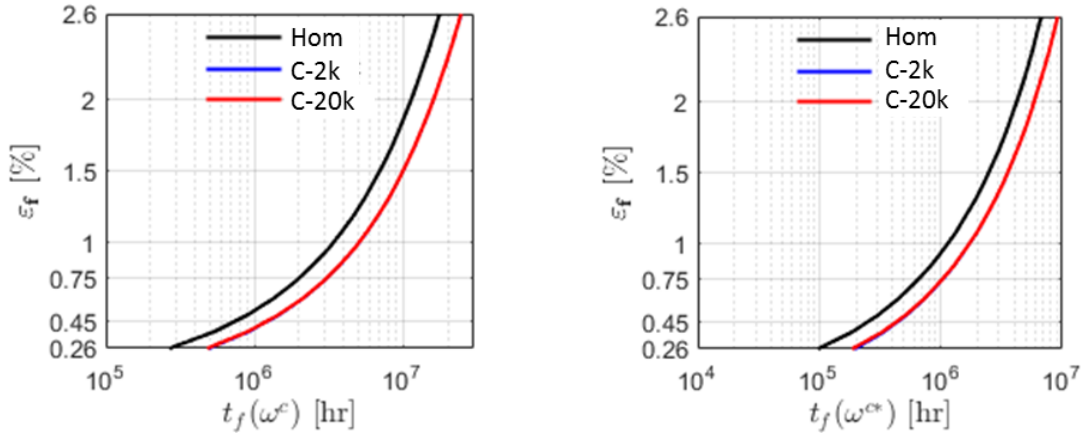

(a) Based only on equivalent creep strain; (b) Including multiaxial ductility factor.

Figure 5.10: Creep damage initiation time in carburising and homogeneous test cases assuming different ductilities.

The $\varepsilon_f - t_f$ plots in Figure 5.10 show that the homogeneous structure model for a wide range of creep ductility is more conservative in terms of t_f compared to the structure that is carburising while being subjected to load. For the assumed creep ductility values, the carburisation time does not influence the time for damage initiation.

5.3.4 Effects of carburisation depth

In this section the effects of carburisation depth are analysed by comparing the results for a carburisation depth of 0.25 mm from sections 5.3.2 and 5.3.3 to results assuming a carburised layer depth of 1 mm (20.4% ≤ a_f ≤ 26.8%). Only *parabolic* distribution profiles are presented here. Additionally, section 5.3.3 has shown that the time for creep damage initiation is the same for $C-2k$ and $C-20k$ models. Therefore, in the following section, only results for $C-2k$ models are shown and are denoted C.

Figure 5.11 shows the difference in accumulated creep strains for the 1 mm carburised models from the models with a carburisation layer of 0.25 mm depth. It can be seen that at short times the normalised creep strain is lower than in the 0.25 mm PC models (factor of, 3 and 18, respectively). This is due to lower initial stresses in the carburised layer as more load is redistributed over a larger area.

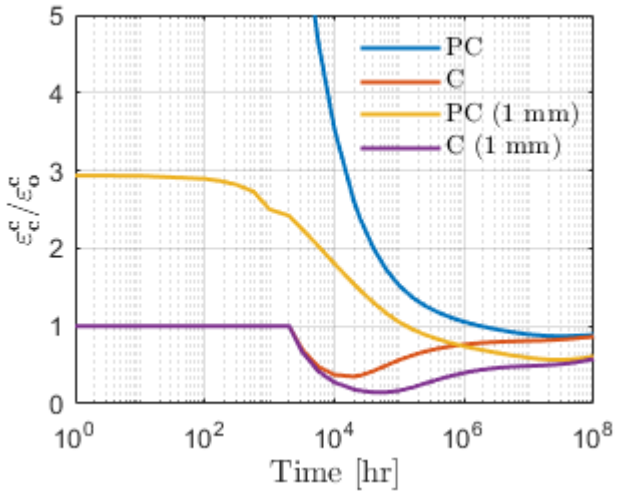

Figure 5.11: The normalised creep strain accumulation of pre-carburised and carburising models assuming carburisation depth of 0.25 mm and 1 mm.

The carburising models predict the same response initially, as they must, but after carburisation (2k hours) the 1 mm models experience a higher drop in normalised creep strain. Both of the 0.25 mm models converge to $\varepsilon_c^c/\varepsilon_o^c$ = 0.89 and the 1 mm models to $\varepsilon_c^c/\varepsilon_o^c$ = 0.61 at t_{end}.

The higher resistance to creep deformation of the 1 mm models is reflected in lower creep damage accumulation (Figure 5.12 and Table 5.4). The pre-carburised models with a carburisation depth of 1 mm have longer times for damage initiation compared to the models with carburisation depth of 0.25 mm (Tables 5.2 and 5.3). The 1 mm models have longer times for creep damage initiation compared to models with lower carburisation depth. Figure 5.4 shows that larger area fraction carburised can extend lifetime even assuming a pre-carburised structure. Hence, this makes the homogeneous assumption more pessimistic for 1 mm carburised structure. The carburising models lead to damage initiation time being extended by 3–5 times, hence indicating the importance of the kinetics of material property changes.

Test case	ε_f = 2.6%		ε_f = 0.75%		ε_f = 0.45%	
	t_f^N	t_f^{N*}	t_f^N	t_f^{N*}	t_f^N	t_f^{N*}
PC (1 mm)	2.66	2.31	0.30	0.17	0.11	0.07
C-2k (1 mm)	3.03	2.98	0.48	0.42	0.24	0.27

Table 5.4: The normalised failure time of pre-carburised and carburising test cases with 1 mm carburisation depth, according to Eqs. 5.2–5.3.

The calculated t_f curves in Figure 5.13 show that the higher area fraction carburised shifts the failure curves further to the right-hand side (dotted lines). For creep ductilities in the range of 0.1% – 2.6 % the homogeneous model becomes non-conservative only at ε_f = 0.3% relative to the PC model, which includes the effects of

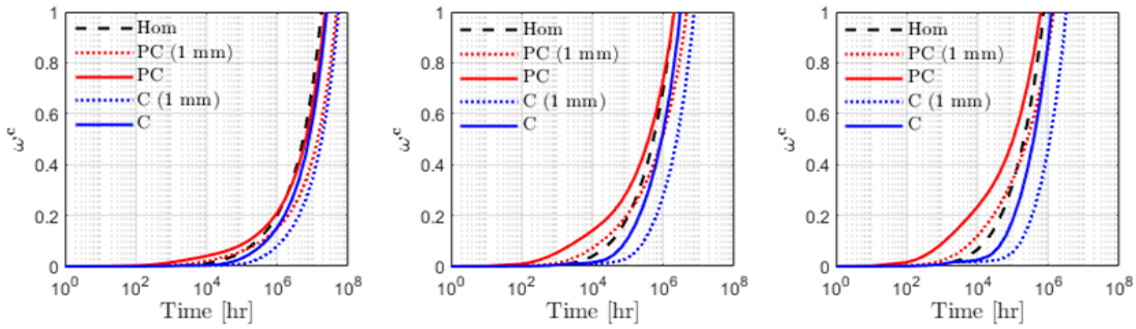

(a) $\omega^c(t, \varepsilon_f = 2.6\%)$ (b) $\omega^c(t, \varepsilon_f = 0.75\%)$; (c) $\omega^c(t, \varepsilon_f = 0.45\%)$;

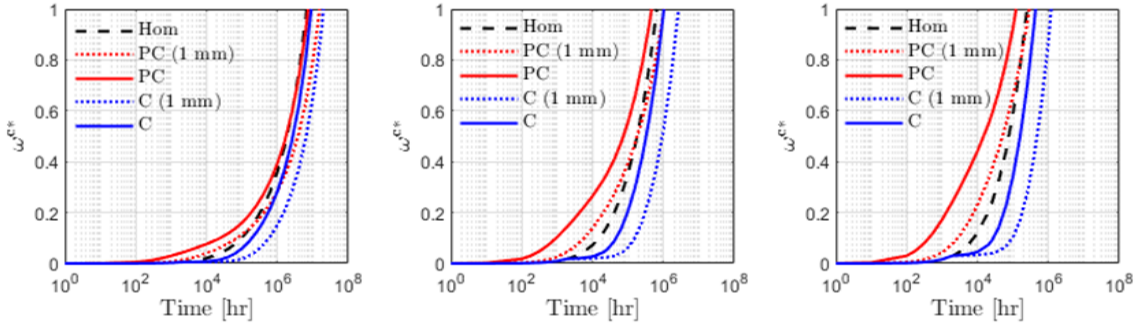

(d) $\omega^{c*}(t, \varepsilon_f = 2.6\%)$; (e) $\omega^{c*}(t, \varepsilon_f = 0.75\%)$; (f) $\omega^{c*}(t, \varepsilon_f = 0.45\%)$.

Figure 5.12: Creep damage accumulation at the surface of pre-carburised and carburising 0.25 mm and 1 mm models

multi-axiality. For carburising models, the homogeneous assumption always remains conservative assumption for the given strain ductility range, for the carburisation depth of 1 mm.

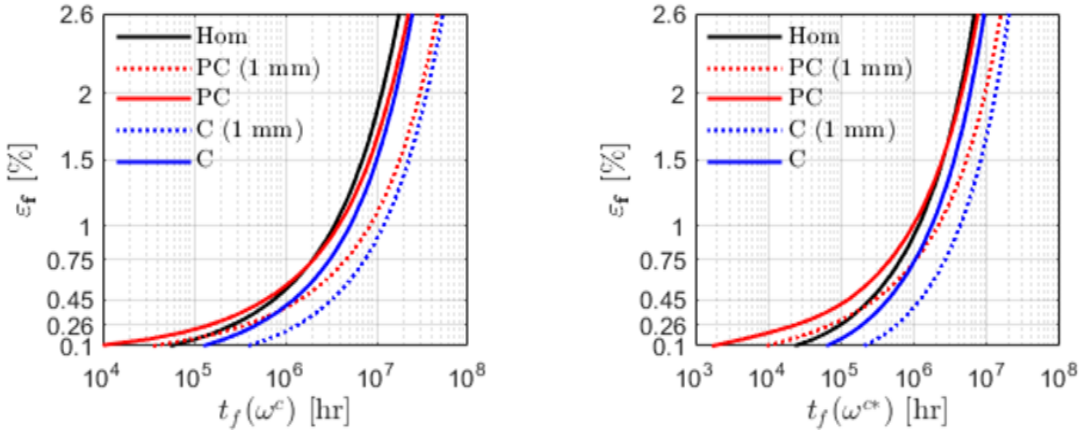

(a) Based only on equivalent creep strain; (b) Including multiaxial ductility factor.

Figure 5.13: Creep damage initiation time in pre-carburised, carburised and homogeneous test cases assuming different uniaxial ductilities and carburisation depths.

Appendix C contains additional results regarding creep damage initiation times. Due to normalisation with the homogeneous test case with fixed ductility (ε_f = 2.6%), the presented results in Tables 5.2 - 5.4 conceal some useful information.

Similar results are presented in Table C.1 where the creep damage initiation times are normalised with respect to the homogeneous test case assuming the **same** ductility. The values in Table C.1 above unity imply that if the homogeneous model is assumed _with reduced ductility, then such an assumption would give a conservative prediction compared to models where carburised layer is accounted for. In addition, Figure C.1 shows graphs of t_f^N and t_f^{N*} values assuming a range of ε_f values. Figure C.1 contains the same information as Figures 5.7, 5.10, and 5.13 and it clearly shows under what ductility assumptions the time for creep damage initiation is higher compared to non-carburised/homogeneous geometry.

5.4 Summary and discussion

The results presented in this chapter for a complex geometry have shown similar trends regarding carburised material creep as in Chapters 3 and 4. As complete stress redistribution was not reached in realistic times, creep damage calculations have shown that damage can initiate during the stress redistribution phase, and the results emphasise the limitations of analytical steady state solutions.

The analysis of the homogeneous structure predicts damage initiation in hundreds of years. However, the calculated time for damage initiation should only be used for comparison purposes to compare carburised model performance relative to the homogeneous case. The analysed problem does not consider residual stresses due to cold-forming, welding, post-weld heat treatment, and the effects of cyclic loading, which are important for structural assessment. However, the model predicts the maximum accumulated creep damage to be at the same location as analyses of the homogeneous bifurcation structure under different loading conditions in [140].

The initial assumption regarding the state of the material (pre-carburised or carburising during service) has been shown to be of major importance for structural integrity assessments. If the structure is assumed to be pre-carburised, then the carburised surface is at high stress on initial loading but stress relaxation leads to reduced stress and ultimately to reduced strain accumulation relative to the homogeneous structure. Depending on the assumed ductility and initial stress the homogeneous model, reduced creep ductility can give conservative or non-conservative lifetime estimation. For the given loading conditions, the pre-carburised models only lead to earlier damage initiation than homogeneous model when creep ductility is below 1.5% for a carburisation depth of 0.25 mm. Above a ductility of 1.5% the time for creep damage to initiate in the carburised structure is higher than for the homogeneous structure with the same ductility. For higher area fraction carburised, pre-carburised assumption shows that the structure can gain benefit from reduced creep strain rates, hence making the homogeneous model with reduced creep duc-

tility a more pessimistic approach for creep damage initiation calculation.

The pre-carburised results clearly indicate that the distributed material properties give the same accumulated creep strain results as the simplified 2-bar model. This is only true for longer time-scales ($\approx 10^4 - 10^5$) when more creep strain is accumulated in the material, hence the initial creep strain accumulation due to mismatch in material properties becomes insignificant. However, during cyclic behaviour carburised material properties can be important parameter for constructing hysteresis loops. Figure C.2 in Appendix C shows an example of stress versus strain graph for the parabolic, 2-bar and homogeneous models. It shows that regardless of which carburised material distribution is used, the bulk response remains unchanged. Hence if damage accumulation in the bulk part of the material is of interest, then the carburised layer material property distribution is not important. However, considering the carburised layer response, the difference in initial stress magnitude will lead to different relaxation behaviour and could lead to erroneous creep analyses at higher stresses.

As the structure becomes more carburised and the carburisation depth increases, the overall creep strain rate decreases. Hence all of the 1 mm models predict that with this increased carburisation depth, creep damage initiation time increases compared to the structures with a carburisation depth of 0.25 mm. It has to be noted that the same material properties have been used for 0.25 mm and 1 mm models. For higher carburisation depth, creep ductility may reduce more severely. Hence the results do not necessarily imply that higher area fraction carburised is beneficial to the structure than smaller area fraction carburised.

Limitations of the current model are that cyclic material response is not considered. As considered in [140], creep-fatigue interaction can influence the lifetime of the component. According to [15], a significant concern is that due to cyclic plasticity, the peak stresses in the carburised layer can increase with each cycle, hence accelerating creep damage accumulation. Hence with each dwell cycle, the structure could undergo the initial stress redistribution phase and accumulate higher creep strain compared to steady-state operation. Therefore, the question of how carburisation influences creep-fatigue interaction is still unknown, especially considering pre-carburised and carburising material models.

Modelling complex geometries that have been carburised significantly increases the difficulty of creep analysis. The mesh has to be refined to account for the carburised layer, especially if any property gradation is introduced. Fortunately, results show that the material property distribution profile is not that significant. The simplified bi-metallic (*2-bar*) assumption predicted the same time for creep damage initiation as the *linear* and *parabolic* distribution profiles. Hence, if a more complex FE assessment procedure is required, then a *2-bar* model may be sufficient.

Chapter 6

Advice on carburised structure assessment

In [15], advice is given on structural assessment of carburised stainless steel components. Guidance on related material properties inputs to the assessment is contained in [24]. This chapter assesses this advice and guidance based on the results obtained in this study.

6.1 Monotonic tensile properties

The monotonic tensile properties of the carburised layer play an important role in determining the stress magnitude and the total deformation of the structure. As the carburised layer is harder than the bulk material, treating a component as homogeneous and made of bulk material will result in overestimation of elastic-plastic deformation. The homogeneous assumption might be appropriate when the carburised area fraction is negligible; however, if the assessment aims to predict crack initiation, then the mismatch in tensile material properties should not be neglected.

The current advice for carburised material properties is based on a 2-bar model, assuming uniform material properties through the carburised layer. Uniaxial specimen analysis (Figure 4.18a) and bifurcation analysis (Figure C.2) have shown that the 2-bar model is an acceptable assumption for estimating the stress magnitude in the bulk section. The 2-bar assumption gives essentially the same stress and triaxiality magnitude in the bulk section as the use of more complex graded material models. However, in the carburised layer, the bi-layer assumption results in underestimated stress magnitude towards the surface (most carburised region). If cyclic creep conditions were considered, the bi-layer assumption would result in an incorrect stress at the start of the dwell (Figure C.2). However, this would reduce an over-conservatism in the homogeneous material assumption, which leads to an over-

estimate of the total strain range. The homogeneous material assumption would, therefore, underestimate the stress and overestimate the strain at the start of dwell (Figure C.2). An incorrect stress prediction will result in an erroneous creep strain and wrong hysteresis loop prediction. However, the effects of carburisation on cyclic creep behaviour were out of the scope of this project; hence, more research needs to be done to improve our understanding of the impact of the bi-layer assumption.

A parametric study has shown that the Young's modulus is not that influential for determining the conservative/non-conservative boundary (Figure 4.23), however this might not be true for cyclic response due to cyclic hardening effects. Elastic analysis (Figure A.1) and FEA analysis (Figure 4.15) of a uniaxial specimen have shown that, if the carburised layer has a lower Poisson's ratio compared to the bulk layer, then under uniaxial loading there can be reduced stress triaxiality in the carburised layer. This can occur, if the carburised layer is deforming elastically (e.g. ν_c = 0.3) and the bulk section is deforming plastically (ν_b = 0.5). The lower stress triaxiality would result in increased ductility in cylindrical specimens. Additionally, the elastic analysis (Figure A.1) has shown that the 2-bar model could underestimate the stress magnitude in the carburised layer (if the bulk is deforming plastically and the carburised layer is deforming elastically). Nevertheless, FE analysis has showed that at high stresses, the effects of stress triaxiality and non-axially induced stresses are negligible in uniaxial specimens (Figure 4.18c) and can be ignored.

6.2 Creep properties

The current advice for creep analysis of a carburised structure based on [24] is to assume a homogeneous structure consisting of bulk material but with a creep ductility reduced by a factor of 3.5. Based on a single creep test creep deformation properties have been proposed in [24], which are to reduce the creep law multiplier of the carburised layer by factor of 22 from that of bulk material. Chapters 3–5 have investigated the impact of such assumptions and compared the results to more detailed analyses, including those using graded material properties.

6.2.1 Creep deformation

Creep deformation is influenced by material condition (pre-carburised or carburising) and stress magnitude. Chapter 4 (Figure 4.6b and 4.19a) highlighted that at high stresses pre-carburised material shows accelerated creep deformation due to rapid stress relaxation in the carburised layer. The creep deformation during the stress redistribution phase depends on the assumed tensile and creep properties. Once steady state creep is reached, a carburised structure will have a reduced creep

deformation rate (Chapter 3.2), but the reduction will depend on the area fraction carburised and the assumed reduction in creep rate.

By comparing the creep deformation of components consisting of bi-layer material and graded material models, the evidence shows (Figure 5.5) that the bi-layer assumption is a valid assumption for creep lifetime estimation for longer dwell times. At longer dwell times, the effects of initially accelerated creep deformation become negligible compared to the total creep strain. However, at high stresses, the bi-layer assumption can underestimate the creep deformation rate due to the enhanced creep that arises of the high stresses induced by the mismatch in tensile properties. Whether or not the shape of the creep property distribution function within the carburising layer is important, depends on the monotonic tensile property data. If the shapes of the property distribution functions for creep and tensile properties are the same, then according to the evidence presented, the shape of the function does not matter as long as it is consistent. However, if carburisation causes severe hardening at the surface, but the reduction in creep deformation is uniform through the layer, this can result in severe creep strain accumulation at the surface (Figure 4.19a). However, as the shape of the material property distribution function is not known the bi-layer assumption remains a reasonable assumption for determining global and local creep strains.

A parametric study has shown that the exact value of the average creep law multiplier is not that important for determining at what conditions the homogeneous material assumption becomes non-conservative (Figure 4.24). However, in carburising models, the reduction in creep deformation always offers the benefit of reduced overall creep strain rate; hence for a structure carburising while under the load the homogeneous assumption will always lead to an overestimation of creep strain within the structure (Figure 5.11).

6.2.2 Creep ductility

Confidence in creep ductility value

The work presented in chapter 4 has re-evaluated the estimated creep ductility of the carburised layer (value of 0.75%), which is based on interrupted creep tests. The creep ductility in [24] was measured based on the recorded strain once a crack had reached the carburised layer thickness. The observed strain is not pure creep strain but is a combination of creep, plastic and elastic strains which arise due to stress redistribution. Hence the estimated creep ductility in [24] does not consider the local creep strain accumulation which may arise due to graded material properties and stress redistribution. Hence the finite element model in section 4.4.2 has mapped the local creep strain values at 0.75% and 1.3% to re-evaluate the ductility assumption.

The bi-layer model (2-bar) predicts 0.4% – 0.6% higher average creep strain within the carburised layer compared to the observed strain (Figure 4.20, Table 4.10); hence indicating that the actual creep ductility of the carburised layer might be higher than initially predicted. On the contrary, the graded material models all showed that the creep ductility in a carburised layer could be less than the observed strain. However, the methodology used for the characteristic creep ductility in graded models is based on average and median creep strain values. The presence of the carburised layer reduces stress in the bulk section resulting in an insignificant creep rate in the bulk section compared to the carburised layer during the redistribution phase for high area fraction carburised specimens. Hence the calculated ductilities based on median and average assumptions across the carburised layer will underestimate the creep ductility and show contradicting results compared to the 2-bar model. Nevertheless, considering the current results, the 0.75% assumption for creep ductility should remain unchanged.

The inherent conservatism in the ductility value should be re-evaluated with further modelling work. The model presented in section 4.4.2 is based on an intact specimen. As the recorded experimental data are based on a growing the crack size, simplified damage mechanics should be included in future work. With the same geometry and material properties, a new parametric study should be made that could account for increasing crack size. For thin specimens, crack propagation will result in an increased stress in the specimen and an accelerated creep rate. Matching the global strain response and crack growth with data in Table 4.10 will give a better ductility approximation. This could be achieved by introducing an element failure criterion, where element load-bearing capacity reduces to zero once a specific creep strain is reached. Such an analysis could reduce the conservatism in the ε_f = 0.75% assumption.

Homogeneous assumption re-evaluation

The analytical solution in Chapter 3 has shown that internally pressurised components with an outer carburised layer experience reduction in stress triaxiality in the bulk and unchanged stress triaxiality at the surface (Figure 3.7). The bi-layer assumption predicts unchanged stress triaxiality in the carburised layer, which shows that the bi-layer model is a more conservative assumption compared to graded material models. Hence, if the steady-state is reached, carburisation could offer increased creep ductility for the bulk material, whereas the simplified homogeneous assumption would result in unchanged ductility.

The homogeneous assumption will result in an overly pessimistic assessment for components that are carburised while being subjected to load (Figure 5.10). For thin components with higher area fraction carburised, the disparity between

the failure initiation times for homogeneous and carburising models increases even further (Figre 5.13). Therefore, for a conservative assessment methodology, a smaller area fraction carburised should be used when a load controlled assessment is made using the bi-layer assumption.

If a structure is carburised before load application (pre-carburised), then an assessment using the homogeneous assumption will not necessarily lead to a conservative evaluation. At high stresses (or strain ranges) upon initial loading the carburised layer accumulates more creep strain compared to uncarburised structure (Figures 4.7a, 5.5, and 4.22). The bifurcation analysis clearly shows that there is a point of interception in ductility values below which the homogeneous assumption would overestimate creep damage initiation compared to the pre-carburised model. The point of intersection depends on stress magnitude, stress state and area fraction carburised. Triaxial tension can shift the point of intersection (Figure 5.5) above the assumed 0.75% ductility value, meaning that the homogeneous assumption would not be an appropriate assumption for lifetime prediction (Figure 5.7b).

6.3 Relative timescale comparison

For the results from parametric studies in Chapter 4 and the bifurcation weld analysis in Chapter 5, additional comments should be made here about the relative timescales involved and the applicability of analytical solutions from Chapter 3 for real component analysis. As discussed in Chapter 1, some plant components have now operated for periods in excess of 250,000 hours ($\sim 10^5$) [11]. In contrast, laboratory creep tests usually range from a few hundred hours to tens of thousand hours (from $\sim 10^2$ to $\sim 10^4$) [100]. It is believed that carburisation only mainly occurs at near the start of life when the chromium oxide present is broken down, and a duplex oxide starts to grow;, and the literature [14, 24, 76] indicates that time where most carburisation occurs is within $\sim 10^4$ hours from the start of operation.

From uniaxial specimen models (Chapter 4.4), the time needed to reach complete stress redistribution (t_{red}) in the stress interval of 140 - 270 MPa and 2.5% < a_f < 15% is in the range $\sim 10^4$ to $\sim 10^5$ hours. Considering that creep tests in laboratory conditions at $T = 550^oC$ are performed at stresses in excess of 240 MPa, the results from Chapter 4.4 suggest that for such specimens a complete stress redistribution is not possible ($t_{red} >> 10^5$) and specimens will reach the failure strain before complete stress redistribution is attained. However, these conclusions are based on models where primary creep is ignored, whereas from creep tests, it is known that primary creep can contribute significantly to the total creep strain. For a carburised structure, an accelerated initial creep rate would reduce the time to reach full stress redistribution that arises due to the material property mismatch. Therefore, if the

effects of primary creep were modelled, then more accurate predictions about creep redistribution times could be made.

From the bifurcation analysis it can be concluded that for such a complex geometry, complete stress redistribution is not achievable in realistic timescales due to significant regions of the structure being subjected to low stresses (Figure 5.4). If the carburised layer creep strains are considered relative to the homogeneous model, the time needed to reach a constant creep strain relative to the homogeneous test case is in the range ~ 10^5 to ~ 10^8 hours (Figure 5.5, 5.8, 5.11). The time for stress redistribution is strongly influenced by the area fraction carburised where higher area fraction carburised result in longer redistribution times (e.g. Figure 5.11). Hence a carburised component will develop creep damage whilst operating under non-steady state conditions.

By considering the timescales required to reach stress redistribution, it can be concluded that assuming a Norton creep law, $\dot{\varepsilon}^c = A\sigma^n$, fitted to secondary creep data, the steady state will often not be reached within plant operating lifetime. Therefore, the steady state solutions presented in Chapter 3 are of limited use for direct application. However, they are of value in evaluation of timescales and may also be of value in estimating the effects of primary creep by fitting the Norton creep law to describe the average creep rate under primary/secondary creep over relevant timescales.

6.4 Carburised structure assessment range of applicability

The range of applicability of the simplified methodology of [24] has been evaluated by finding the point of intersection at which the homogeneous assumption would predict a longer time to failure compared to the pre-carburised assumption. For thick components, where the carburised layer thickness is insignificant compared to the rest of the structure, below nominal stresses of ≈175 MPa the use of the homogeneous assumption with the proposed creep ductility of 0.75% will be acceptable (Figure 4.22c). Above stresses of 175 MPa the bi-layer assumption should be used for structural integrity assessments. For thin components, the stress magnitude (applied σ_{obs}) threshold increases due to increasing area fraction carburised. For uncracked components with 10% area fraction carburised (e.g. bifurcation weld geometry) the stress magnitude below which homogeneous assumption remains conservative is 220 MPa.

Although the analytical solutions in Chapter 3 do not consider stress redistribution effects, they can be used as a useful tool to mathematically predict at what

conditions a carburised layer might extend the lifetime of a component. The analytical solution in section 3.4 has shown that components with $a_f < 15\%$ do not get any increase in lifetime (Figure 3.6) [1]. However, carburised structures with $a_f > 38\%$ could, in theory, have a longer time to failure compared to a homogeneous component under the same load.

A significant limitation for the proposed limits is that the bounds do not consider stress triaxiality effects. The bifurcation study has shown that hydrostatic tension can significantly influence time for damage initiation (Figure 5.7b). This limitation could be addressed by running a series of parametric studies of carburised pressure vessels (e.g. pipe geometry) with different geometries. Gathering sufficient data from such a FE study, an SVM or ANN model could be built that would account not only for uncertainty in material properties but also for multiaxiality.

[1] Assuming ductility reduction by factor 3.5 and creep law multiplier reduction by factor of 22

Chapter 7

Conclusions and areas of future work

The UK's advanced gas-cooled reactors are approaching the end of their original design lives. Due to the high-temperature carbon-rich environment, several material issues have emerged. Predicting environmentally assisted microcrack formation due to carburisation and creep/creep-fatigue interaction has proven to be a challenging task. The existing assessment procedure for high-temperature assessments (R5) does not predict creep/creep-fatigue crack initiation under such conditions. This has led to development of a simplified approach for assessing carburised structures. The research presented in this thesis has helped to gain a better understanding of carburisation-creep interaction and has assessed the validity of the current simplified approach. This has produced a number of conclusions which are presented in Chapters 3-6. The main conclusions are summarised in this chapter along with selected areas identified where further research would be beneficial.

7.1 Mechanical response of a carburised material

7.1.1 Steady state creep

A mathematical proof using bounding theorems has shown that a non-homogeneous structure with a region of locally increased creep resistance will have a smaller creep energy dissipation rate on average than a homogeneous structure. Hence, this leads to the conclusion that, at the steady state, the carburised layer with reduced creep rate will lead to a reduced overall structural creep deformation rate.

An analytical solution based a the two-material structure under uniaxial load has been adapted to predict the carburised layer creep properties and stress state assuming graded material properties. The uniaxial solution showed that for the same

applied load, the creep resistant parts of the structure carry a higher part of the load to ensure compatible creep deformation. Hence, while the more creep resistant part is subjected to higher stress magnitude, the underlying bulk material is at lower stress. This shows that if the carburised layer is modelled as a homogeneous layer, the stresses at the surface can be greatly underestimated. The simplified analytical solution has also shown that carburised structures with a small carburised area do not gain any benefit in terms of increased time for creep damage initiation compared to a homogeneous material.

An analytical solution for a thick-walled cylinder has been developed by treating the cylinder as a number of concentric cylinders, this can account for any carburised layer property distribution profile. The concentric cylinder analytical model has provided an understanding of the effects of carburisation on the stress state in cylinders. For internally pressurised cylinders with a carburised outer layer, the stress triaxiality of the underlying bulk material is reduced. Hence, in such a structure carburisation has the potential to protect the bulk material at the steady state through increased ductility resulting from multiaxial effects. The creep stress triaxiality in the carburised layer is unchanged if the carburised layer is treated as having uniform properties. In addition, the effects of geometry were also investigated, and it was found that the normalised stress response in thin pipes resembles the normalised stress response of the uniaxial analytical solution.

7.1.2 The effects of material condition

As the analytical solutions are only valid in steady state creep, finite element models of an uniaxial specimen were analysed to understand stress redistribution effects. The 3-D uniaxial tensile specimen models have shown the impact of the carburised material tensile properties at high stresses. The models showed two completely different behaviours for materials which were carburised before or after the load application.

Material carburised before the load application

Finite element models have shown that under laboratory conditions, where tests are performed at high stresses, the global response of a test specimen with a layer of pre-carburised material shows accelerated creep deformation compared to the homogeneous specimen. Such an observation could be falsely interpreted as accelerated creep behaviour for the whole structure. However the results clearly indicate that additional creep relaxation processes occur only in the carburised layer and these lead to additional creep strain accumulation in the carburised layer. The additional creep strain cannot be deduced from the global deformation response;

hence the creep strain in the carburised layer can be underestimated. In addition, the deformation in the bulk material is largely caused by additional plastic strain accumulation instead of creep strain.

As the available carburised materials data in the literature are only available on pre-carburised specimens, a neural network model has been developed that can predict the carburised material properties based on the recorded global response from a uniaxial tensile test. The neural network was trained using the data gathered from thousands of finite element models and proved to be an effective tool for predicting the monotonic tensile properties by making some assumptions about the shape of the distribution of properties within the carburised layer. The trained neural network can be used as a tool to predict material properties in functionally graded materials avoiding time-consuming finite element analysis. The estimated material properties were used for the development of support vector machine models that were able to predict under what conditions the homogeneous material assumption would lead to conservative or non-conservative assessment.

Material carburised after the load application

Structures containing materials that are carburised after the load application have been shown to avoid the rapid damage accumulation that is seen in pre-carburised materials at high stresses. If the material is carburising while subjected to load, the damage calculations of uniaxial creep specimens at high stresses have shown that the creep damage is closer to the damage in homogeneous specimens; conversely the damage in pre-carburised material can be an order of magnitude higher. Analyses of a bifurcation weld geometry assuming various ductility values showed the importance of choosing the correct carburisation assumption[1]. Although carburising models still predicted early damage formation, these showed that assuming carburisation at short times after the load application would reduce unnecessary conservatism in the proposed homogeneous assumption methodology.

7.2 Carburised structure assessment

According to the evidence presented, the carburised layer tensile properties are key inputs that influence the life of pre-carburised specimens that are crept at laboratory conditions, i.e. high stresses. If the carburised layer tensile properties are deduced from an uniaxial hollow specimen under uniaxial loading, the carburised layer ductility can be increased through reduced stress triaxiality[2]. However, if the carburised

[1] Assuming pre-carburised or carburising after the load application

[2] If the bulk material is deforming plastically (ν_b = 0.5) and the carburised layer elastically (ν_b = 03).

layer yields, at higher stresses, any changes in the stress triaxiality are negligible in uniaxial specimens. Therefore, the fitted Ramberg-Osgood model (Eq. 2.32 from [24]) for the *average* carburised material properties is a reasonable assumption for predicting the global deformation and the local stress magnitude and stress state in the bulk section.

Creep damage accumulation is significant for components at high stresses, mainly stresses above the material yield strength. This research has clearly showed that for assessment of carburised structures, the material state is of major importance for determining the sustained creep damage. If a material is carburising following load application, a structure has a reduced creep strain rate and avoids the rapid stress relaxation phase which occurs if material is pre-carburised. However, the reduced creep strain does not imply that the creep damage initiation time of a component will be extended from that of a homogeneous component. Evidence clearly shows, if the carburising assumption holds true, that the proposed assessment procedure of treating a structure as uncarburised with reduced ductility, will lead to overly conservative creep assessment.

Support vector machine and artificial neural network models built using data gathered from parametric finite element studies have proven to be robust tools for accounting for the uncertainty in material property data. Considering the current advice on carburised material data, thick components with insignificant area fraction carburised of applied stress above 185 MPa should not use the homogeneous assumption. For thin components, the range of the homogeneous assumption increases to 220 MPa due to benefit of overall reduced creep strain. However these values are based on excluding any effects of stress triaxiality, which should be addressed with further research.

7.3 Suggestions for future work

This work has answered some of the questions regarding the creep response of carburised type 316H stainless steel components; however, the process of inquiry has opened new questions. As pre-carburisation can lead to rapid creep strain accumulation within the carburised layer, the carburised layer creep ductility value should be re-evaluated using FE modelling and/or testing. A more appropriate method for ductility evaluation would be incorporating creep damage in FEA, where elements drop load-bearing capacity once a failure condition is met. This approach would be more appropriate for re-evaluating creep ductility than the one presented in this work. In addition, there is strong evidence that carburisation during a creep test could lead to a more accurate estimate of creep ductility and evaluation of creep deformation properties. This type of test would allow for testing at higher stresses,

hence carburised layer materials data could be acquired in reasonable time-frames and avoid cracking due to initial loading. Therefore, such testing could offer significant benefits for materials data acquisition.

The current estimates of carburised layer creep properties are based on a single creep test. There is a significant experimental challenge to evaluate the reduction in creep law multiplier of carburised material relative to bulk material. Specimens cannot be loaded to high stresses because of the brittle nature of the carburised layer. This results in performing creep tests at lower stresses and they are time-consuming. In order to determine the creep law multiplier, a steady state must be reached, but due to the large time-frames it is often unclear whether or not this has been achieved. Hence the determination of the creep properties has been proven to be a challenging and expensive task. Material properties could be found numerically using finite element analysis in conjunction with machine learning methods. Similar to the method developed to determine the tensile properties, a neural network model could be built that could predict material creep properties based on the global response of a specimen at short times.

The bifurcation analysis showed how stress triaxiality could impact lifetime assessment. The proposed bounds for the range of applicability of the simplified assessment approach do not consider multiaxial effects; hence a parametric study could be performed on a pressurised cylinder under internal and/or external pressure assuming different geometries ($r_i : r_e$ and area fraction carburised). Gathering sufficient data from such simulations, an ANN or an SVM model could be developed that would take into account stress triaxiality effects. In addition, such models would provide bounds for actual AGR pipework, take into consideration any geometric effects, and account for variability in material properties.

In the work presented, only the effects of carburisation under forward creep has been addressed. During AGR operation, the boiler components are subjected to cyclic loading conditions with dwell times of about 10^4 hr. This raises important questions regarding creep-fatigue damage accumulation within the carburised layer. Research has shown that over extended time periods, the bi-layer assumption would give the same creep damage prediction compared with more complex graded material models. This might not be true during cyclic loading, especially when a component is subjected to higher service loads. The cyclic behaviour could considerably change the hysteresis loop due to cyclic hardening. It is unknown how graded material properties will change the stabilised hysteresis loop, or if the carburising model will provide any "benefit" compared to assuming pre-carburised material. In addition, current research has shown that the value of Young's modulus is not that significant for finding the range of applicability of the simplified approach, but considering material cyclic hardening behaviour, this might not be the case. Therefore

further analysis is needed to re-evaluate the current R5 advice on the appropriate carburised layer fatigue endurance and creep ductility values and provide a better understanding of carburisation and creep-fatigue interaction.

Finally, understanding carburised material behaviour under creep conditions could be further extended by considering cracked components. The literature suggests that the rate of carburisation is stress dependent. Therefore, this raises questions, such as how carburisation would influence the onset of crack propagation due to changes in material properties near a crack tip; how carburising and pre-carburisation behaviour would change the current procedure for assessing defects in R5 Volume 4/5.

References

[1] Radioactive Waste Management (RWM). *The UK's nuclear history*. 2018. URL: https://www.gov.uk/guidance/the-uks-nuclear-history (visited on Oct. 17, 2019).

[2] Parliament of the United Kingdom. "Climate Change Act 2008". In: *HM Government* (2008), pp. 1–103. ISSN: 0959-8138. DOI: 10.1136/bmj.39469.569815.47. URL: http://www.legislation.gov.uk/ukpga/2008/27/pdfs/ukpga%7B%5C_%7D20080027%7B%5C_%7Den.pdf.

[3] National Audit Office. *Nuclear power in the UK*. Tech. rep. The Department of Energy & Climate Change, 2016. URL: https://www.nao.org.uk/wp-content/uploads/2016/07/Nuclear-power-in-the-UK.pdf.

[4] Simon Shaw and Dean Thornton. "A History of Dosimetry for the Advanced Gas-cooled Reactors". In: *EPJ Web of Conferences* 106 (Feb. 2016). Ed. by A. Lyoussi, p. 02009. ISSN: 2100-014X. DOI: 10.1051/epjconf/201610602009. URL: http://www.epj-conferences.org/10.1051/epjconf/201610602009.

[5] EDF Energy. *Nuclear lifetime management*. 2018. URL: https://www.edfenergy.com/energy/nuclear-lifetime-management (visited on Oct. 17, 2019).

[6] British Energy Group. *How an AGR power station works*. 2006. URL: https://archive.uea.ac.uk/%7B~%7De680/energy/energy%7B%5C_%7Dlinks/nuclear/How%7B%5C_%7Dan%7B%5C_%7DAGR%7B%5C_%7Dpower%7B%5C_%7Dstation%7B%5C_%7Dworks.pdf.

[7] "Nuclear". In: *Energy Resources and Systems: Volume 1: Fundamentals and Non-Renewable Resources*. Ed. by Tushar K. Ghosh and Mark A. Prelas. Dordrecht: Springer Netherlands, 2009, pp. 453–647. DOI: 10.1007/978-90-481-2383-4_9. URL: https://doi.org/10.1007/978-90-481-2383-4_9.

[8] Bertrand Barré. "Gas-Cooled Reactors". In: *Handbook of Nuclear Engineering*. Ed. by Dan Gabriel Cacuci. Boston, MA: Springer US, 2010, pp. 2711–2748. ISBN: 978-0-387-98149-9. DOI: 10.1007/978-0-387-98149-9_22. URL: https://doi.org/10.1007/978-0-387-98149-9_22.

[9] P. J. Cameron and J. Walters. "The Design and Construction of Boilers for Advanced Gas-Cooled Reactors in the United Kingdom". In: *Nuclear Technology* 55.1 (Oct. 1981), pp. 151–162. ISSN: 0029-5450. DOI: 10.13182/NT81-A32838. URL: https://www.tandfonline.com/doi/full/10.13182/NT81-A32838.

[10] Erik Nonbol. *Description of the Advanced Gas Cooled Type of Reactor (AGR)*. Tech. rep. NKS/RAK2(96)TR-C2. Roskilde: Riso National Laboratory, 1996.

[11] David W. Dean and Julian G Johns. "Structural Integrity Issues in High Temperature Nuclear Plant: Experience from Operation of The UK Advanced Gas Cooled Reactor Fleet". In: *23rd Conference on Structural Mechanics in Reactor Technology*. Manchester, 2015. URL: https://repository.lib.ncsu.edu/bitstream/handle/1840.20/33886/SMiRT-23%7B%5C_%7DPaper%7B%5C_%7D459.pdf?sequence=1%7B%5C&%7DisAllowed=y.

[12] G. A. Webster and R. A. Ainsworth. *High Temperature Component Life Assessment*. First Edit. London: Chapman & Hall, 1994. ISBN: 978-90-481-4012-1. DOI: 10.1007/978-94-017-1771-7. URL: http://link.springer.com/10.1007/978-94-017-1771-7.

[13] S. Palkó, F. Scenini, and R. A. Ainsworth. "Factors Affecting the Oxidation and Carburisation Behaviour of an Austenitic Stainless Steel Used in the UK Advanced Gas-Cooled Reactors". In: *Proceedings of the ASME Pressure Vessel and Piping Conference*. 51593. Prague, Czech Republic: ASME, 2018, V01BT01A067. ISBN: 978-0-7918-5159-3. DOI: 10.1115/PVP2018-84279. URL: http://dx.doi.org/10.1115/PVP2018-84279.

[14] C. M. Younes. *Oxidation and Carburisation of Type 316 Stainless Steels in AGRs Environments*. Technical report CMY/IAC/15/C04. Interface Analysis Centre, University of Bristol, June 2015.

[15] Marc Chevalier. "The Assessment of Creep-Fatigue Crack Initiation in Carburized Austenitic Stainless Steel". In: *ASME 2018 Symposium on Elevated Temperature Application of Materials for Fossil, Nuclear, and Petrochemical Industries*. Seattle, WA: ASME, Apr. 2018, V001T03A003. ISBN: 978-0-7918-4076-4. DOI: 10.1115/ETAM2018-6713. URL: http://proceedings.asmedigitalcollection.asme.org/proceeding.aspx?doi=10.1115/ETAM2018-6713.

[16] D.H. Jones, A.Y. Nehru, and J. Skinner. "The impact fretting wear of a nuclear reactor component". In: *Wear* 106.1-3 (Nov. 1985), pp. 139–162. ISSN: 00431648. DOI: 10.1016/0043-1648(85)90107-3. URL: https://linkinghub.elsevier.com/retrieve/pii/0043164885901073.

[17] B. Chen, J. N. Hu, P. E. J. Flewitt, A. C. F. Cocks, R. A. Ainsworth, D. J. Smith, D. W. Dean, and F. Scenini. "Effect of thermal ageing on creep and oxidation behaviour of Type 316H stainless steel". In: *Materials at High Temperatures* 32.6 (2015), pp. 592–606. DOI: 10.1179/1878641315Y.0000000005. URL: https://doi.org/10.1179/1878641315Y.0000000005.

[18] Ana I. Martinez-Ubeda, Ian Griffiths, Oliver D. Payton, Charles M. Younes, Tom B. Scott, and Peter E. J. Flewitt. "Role of Long Term Ageing on the Creep Life of Type 316H Austenitic Stainless Steel Bifurcation Weldments". In: *Volume 6A: Materials and Fabrication*. American Society of Mechanical Engineers, July 2016. ISBN: 978-0-7918-5042-8. DOI: 10.1115/PVP2016-63467.

[19] M. P. O. Donnell, R. A. W. Bradford, D. W. Dean, C. D. Hamm, and M. Chevalier. "High Temperature Issues in Advanced Gas Cooled Reactors (AGR)". In: *TAGSI/FESI Symposium 2013*. 2013, pp. 1–8.

[20] "R5 high temperature creep-fatigue life assessment for austenitic weldments". In: *Procedia Engineering* 86 (2014), pp. 315–326. ISSN: 18777058. DOI: 10.1016/j.proeng.2014.11.044. URL: http://dx.doi.org/10.1016/j.proeng.2014.11.044.

[21] EDF Energy. *R5: Assessment procedure for high temperature response of structures*. Tech. rep. Issue 3, Rev 002. Gloucester, UK, 2015.

[22] R. A. Ainsworth. "R5 procedures for assessing structural integrity of components under creep and creep–fatigue conditions". In: *International Materials Reviews* 51.2 (Apr. 2006), pp. 107–126. ISSN: 0950-6608. DOI: 10.1179/174328006X79463. URL: http://www.tandfonline.com/doi/full/10.1179/174328006X79463.

[23] Sean Flannagan and Andrew Wisbey. *Summary of Amec Foster Wheeler Testing Activities in Support of ENVISINC Project - 2014*. Tech. rep. AMEC/203963-01/001 Issue 03. AMEC Foster Wheeler, May 2015.

[24] Marc Chevalier. *Carburised Material Properties for R5 Volume 2/3 Assessments*. Technical report E/REP/BBGB/0202/GEN/16, Rev 001. EDF Energy, 2018.

[25] Percy Phillips. "The Slow Stretch in Indiarubber, Glass, and Metal Wires when subjected to a Constant Pull". In: *Proceedings of the Physical Society of London* 19.1 (Dec. 1903), pp. 491–511. DOI: 10.1088/1478-7814/19/1/342. URL: https://doi.org/10.1088%2F1478-7814%2F19%2F1%2F342.

[26] Edward Andrade, Da Costa Neville, and Frederick Thomas Trouton. "On the viscous flow in metals and allied phenomena". In: *Proceedings of the Royal Society A*. Royal Society, June 1910. DOI: https://doi.org/10.1098/rspa.1910.0050.

[27] Terence G Langdon. "Grain boundary sliding revisited: Developments in sliding over four decades". In: *Journal of Materials Science* 41.3 (Feb. 2006), pp. 597–609. ISSN: 1573-4803. DOI: 10.1007/s10853-006-6476-0. URL: https://doi.org/10.1007/s10853-006-6476-0.

[28] Charles Mack. "Plastic Flow, Creep, and Stress Relaxation: Part III. Creep and Elastic After-Effect". In: *Journal of Applied Physics* 17.12 (Dec. 1946), pp. 1101–1107. ISSN: 0021-8979. DOI: 10.1063/1.1707682. URL: http://aip.scitation.org/doi/10.1063/1.1707682.

[29] R. K. Penny and D. L. Marriott. *Design for Creep*. Second Edition. London: Chpman & Hall, 1995. ISBN: 978-94-010-4248-2. DOI: 10.1007/978-94-011-0561-3. URL: http://link.springer.com/10.1007/978-94-011-0561-3.

[30] J Betten. *Creep Mechanics*. Berlin, Heidelberg: Springer Berlin Heidelberg, 2008. ISBN: 978-3-540-85050-2. DOI: 10.1007/978-3-540-85051-9. URL: http://link.springer.com/10.1007/978-3-540-85051-9.

[31] D. L. May, A. P. Gordon, and D. S. Segletes. "The Application of the Norton-Bailey Law for Creep Prediction Through Power Law Regression". In: *Volume 7A: Structures and Dynamics*. ASME, June 2013, V07AT26A005. ISBN: 978-0-7918-5526-3. DOI: 10.1115/GT2013-96008. URL: http://proceedings.asmedigitalcollection.asme.org/proceeding.aspx?doi=10.1115/GT2013-96008.

[32] Douglas L. Marriott, Arun Sreeranganathan, Peter Carter, and Shannon Read. "Experience in the Application of the Omega Creep Model in Creep Experiments and Component Analysis". In: *ASME 2014 Symposium on Elevated Temperature Application of Materials for Fossil, Nuclear, and Petrochemical Industries*. ASME, Mar. 2014, p. 151. ISBN: 978-0-7918-4074-0. DOI: 10.1115/ETAM2014-1019. URL: http://proceedings.asmedigitalcollection.asme.org/proceeding.aspx?doi=10.1115/ETAM2014-1019.

[33] J M Montes, F G Cuevas, and J Cintas. "New creep law". In: *Materials Science and Technology* 28.3 (Mar. 2012), pp. 377–379. ISSN: 0267-0836. DOI: 10.1179/1743284711Y.0000000029. URL: http://www.tandfonline.com/doi/full/10.1179/1743284711Y.0000000029.

[34] Ming Song, Tong Xu, Qijiang Wang, Weilian Wang, Yedong Zhou, Min Gong, and Chao Sun. "A modified theta projection model for the creep behaviour of creep-resistant steel". In: *International Journal of Pressure Vessels and Piping* 165 (Aug. 2018), pp. 224–228. ISSN: 03080161. DOI: 10.1016/j.ijpvp.2018.07.007. URL: https://linkinghub.elsevier.com/retrieve/pii/S0308016118300899.

[35] R. W. Evans and B. Wilshire. *Creep of metals and alloys*. London: The Institute of Metals, 1985. ISBN: 0904357597.

[36] F.H. Norton. *The Creep of Steel at High Temperatures*. Bulletin. McGraw-Hill Book Company, Incorporated, 1929. URL: https://books.google.co.uk/books?id=vswxAAAAMAAJ.

[37] J. Li and A. Dasgupta. "Failure-mechanism models for creep and creep rupture". In: *IEEE Transactions on Reliability* 42.3 (Sept. 1993), pp. 339–353. ISSN: 0018-9529. DOI: 10.1109/24.257816.

[38] O.A. Ruano, J. Wadsworth, J. Wolfenstine, and O.D. Sherby. "Evidence for Nabarro-Herring creep in metals: fiction or reality?" In: *Materials Science and Engineering: A* 165.2 (July 1993), pp. 133–141. ISSN: 09215093. DOI: 10.1016/0921-5093(93)90747-3. URL: https://linkinghub.elsevier.com/retrieve/pii/0921509393907473.

[39] E. Czoboly. "Basic Mechanisms of Creep and the Testing Methods". In: *Component Reliability Under Creep-Fatigue Conditions*. Ed. by J. Ginsztler and R. P. Skelton. 1st ed. Vienna: Springer Vienna, 1998, pp. 87–136. ISBN: 978-3-211-82914-1. DOI: 10.1007/978-3-7091-2516-8. URL: http://link.springer.com/10.1007/978-3-7091-2516-8.

[40] H J Frost and M F Ashby. "Deformation-mechanism maps: The plasticity and creep of metals and ceramics". In: *Oxford, Pergamon Press* (1982), p. 175. ISSN: 03783804. DOI: 10.1016/0378-3804(84)90015-9. URL: http://www.csa.com/partners/viewrecord.php?requester=gs%7B%5C&%7Dcollection=TRD%7B%5C&%7Drecid=A8415391AH%7B%5C%%7D5Cnpapers3://publication/uuid/2D64B33C-5D74-400D-AC62-1976E345C5A1.

[41] R. L. Coble. "A Model for Boundary Diffusion Controlled Creep in Polycrystalline Materials". In: *Journal of Applied Physics* 34.6 (June 1963), pp. 1679–1682. ISSN: 0021-8979. DOI: 10.1063/1.1702656. URL: http://aip.scitation.org/doi/10.1063/1.1702656.

[42] R.N. Stevens. "Grain Boundary Sliding: Experimental Observations". In: *Encyclopedia of Materials: Science and Technology*. Elsevier, 2001, pp. 3622–3624. DOI: 10.1016/B0-08-043152-6/00644-6. URL: https://linkinghub.elsevier.com/retrieve/pii/B0080431526006446.

[43] Jian-Feng Wen, Shan-Tung Tu, Fu-Zhen Xuan, Xue-Wei Zhang, and Xin-Lin Gao. "Effects of Stress Level and Stress State on Creep Ductility: Evaluation of Different Models". In: *Journal of Materials Science & Technology* 32.8 (2016), pp. 695–704. ISSN: 1005-0302. DOI: https://doi.org/10.1016/j.jmst.2016.02.014. URL: http://www.sciencedirect.com/science/article/pii/S1005030216300524.

[44] R Hales. "The Role of Cavity Growth Mechanisms in Determining Creep-Rupture Under Multiaxial Stresses". In: *Fatigue & Fracture of Engineering Materials and Structures* 17.5 (May 1994), pp. 579–591. ISSN: 8756-758X. DOI: 10.1111/j.1460-2695.1994.tb00257.x. URL: http://doi.wiley.com/10.1111/j.1460-2695.1994.tb00257.x.

[45] S R Holdsworth and G Merckling. *ECCC Developments in the Assessment of Creep-Rupture Properties*. URL: http://citeseerx.ist.psu.edu/viewdoc/summary?doi=10.1.1.510.6285.

[46] Stuart Holdsworth. "Creep-Ductility of High Temperature Steels: A Review". In: *Metals* 9.3 (Mar. 2019), p. 342. ISSN: 2075-4701. DOI: 10.3390/met9030342. URL: https://www.mdpi.com/2075-4701/9/3/342.

[47] R.W. Evans, B. Wilshire, Institute of Metals, and Metals Society. *Creep of Metals and Alloys*. Book (Institute of Metals). Institute of Metals, 1985. ISBN: 9780904357592. URL: https://books.google.co.uk/books?id=ethiQgAACAAJ.

[48] I. I. Trunin, N. G. Golobova, and Loginov E. A. "New method of extrapolation of creep test and long time strength results". In: *Proc. 4th Int. Symp. on Heat Resistant Metallic Materials*. Mala Fatra, 1971, p. 168.

[49] M.W. Spindler. "AN IMPROVED METHOD TO CALCULATE THE CREEP-FATIGUE ENDURANCE OF TYPE 316H STAINLESS STEEL". In: *Materials for Advanced Power Engineering*. Forschungszentrum Jülich GmbH, 2006, pp. 1673–1682. ISBN: 3-89336-436-6.

[50] M. W. Spindler. "The multiaxial creep ductility of austenitic stainless steels". In: *Fatigue & Fracture of Engineering Materials & Structures* 27.4 (Apr. 2004), pp. 273–281. ISSN: 8756-758X. DOI: 10.1111/j.1460-2695.2004.00732.x. URL: http://doi.wiley.com/10.1111/j.1460-2695.2004.00732.x.

[51] Warwick M. Payten, David W. Dean, and Ken U. Snowden. "A strain energy density method for the prediction of creep–fatigue damage in high temperature components". In: *Materials Science and Engineering: A* 527.7-8 (Mar. 2010), pp. 1920–1925. ISSN: 09215093. DOI: 10.1016/j.msea.2009.11.028. URL: https://linkinghub.elsevier.com/retrieve/pii/S0921509309012295.

[52] A. Mehmanparast, C. M. Davies, D. W. Dean, and K. M. Nikbin. "The Influence of Inelastic Damage on Tensile Deformation and Creep Crack Growth Behaviour of Type 316H Stainless Steel". In: *Volume 6A: Materials and Fabrication*. Imperial College London. ASME, July 2013, V06AT06A044. ISBN: 978-0-7918-5570-6. DOI: 10.1115/PVP2013-98001. URL: http://proceedings.asmedigitalcollection.asme.org/proceeding.aspx?doi=10.1115/PVP2013-98001.

[53] A. Mehmanparast, C. M. Davies, G. A. Webster, and K. M. Nikbin. "Creep crack growth rate predictions in 316H steel using stress dependent creep ductility". In: *Materials at High Temperatures* 31.1 (2014), pp. 84–94. DOI: 10.1179/0960340913Z.00000000011. eprint: https://doi.org/10.1179/0960340913Z.00000000011. URL: https://doi.org/10.1179/0960340913Z.00000000011.

[54] G. Sundararajan. "The Monkman-Grant relationship". In: *Materials Science and Engineering: A* 112 (June 1989), pp. 205–214. ISSN: 09215093. DOI: 10.1016/0921-5093(89)90360-2. URL: https://linkinghub.elsevier.com/retrieve/pii/0921509389903602.

[55] F. Dobeš and K. Milička. "The relation between minimum creep rate and time to fracture". In: *Metal Science* 10.11 (Jan. 1976), pp. 382–384. ISSN: 0306-3453. DOI: 10.1080/03063453.1976.11683560. URL: http://www.tandfonline.com/doi/full/10.1080/03063453.1976.11683560.

[56] P. W. Bridgman. "The Effect of Hydrostatic Pressure on the Fracture of Brittle Substances". In: *Journal of Applied Physics* 18.2 (Feb. 1947), pp. 246–258. ISSN: 0021-8979. DOI: 10.1063/1.1697610. URL: http://aip.scitation.org/doi/10.1063/1.1697610.

[57] J.R. Rice and D.M. Tracey. "On the ductile enlargement of voids in triaxial stress fields". In: *Journal of the Mechanics and Physics of Solids* 17.3 (June 1969), pp. 201–217. ISSN: 00225096. DOI: 10.1016/0022-5096(69)90033-7. URL: https://www.sciencedirect.com/science/article/pii/0022509669900337%20https://linkinghub.elsevier.com/retrieve/pii/0022509669900337.

[58] F. A. McClintock. "A Criterion for Ductile Fracture by the Growth of Holes". In: *Journal of Applied Mechanics* 35.2 (June 1968), pp. 363–371. ISSN: 0021-8936. DOI: 10.1115/1.3601204. eprint: https://asmedigitalcollection.asme.org/appliedmechanics/article-pdf/35/2/363/5449108/363_1.pdf. URL: https://doi.org/10.1115/1.3601204.

[59] A. C. F. Cocks and M. F. Ashby. "Creep fracture by coupled power-law creep and diffusion under multiaxial stress". In: *Metal Science* 16.10 (Oct. 1982), pp. 465–474. ISSN: 0306-3453. DOI: 10.1179/msc.1982.16.10.465. URL: http://www.tandfonline.com/doi/full/10.1179/msc.1982.16.10.465.

[60] M. Yatomi and K. M. Nikbin. "Numerical prediction of creep crack growth in different geometries using simplified multiaxial void growth model". In: *Materials at High Temperatures* 31.2 (May 2014), pp. 141–147. ISSN: 0960-3409. DOI: 10.1179/1878641314Y.0000000008. URL: http://www.tandfonline.com/doi/full/10.1179/1878641314Y.0000000008.

[61] A. Needleman, V. Tvergaard, and J. W. Hutchinson. "Void Growth in Plastic Solids". In: *Topics in Fracture and Fatigue*. Ed. by A. S. Argon. New York, NY: Springer New York, 1992, pp. 145–178. ISBN: 978-1-4612-2934-6. DOI: 10.1007/978-1-4612-2934-6_4. URL: https://doi.org/10.1007/978-1-4612-2934-6_4.

[62] S. Kweon. "Damage at negative triaxiality". In: *European Journal of Mechanics - A/Solids* 31.1 (Jan. 2012), pp. 203–212. ISSN: 09977538. DOI: 10.1016/j.euromechsol.2011.02.005. URL: https://linkinghub.elsevier.com/retrieve/pii/S0997753811000246.

[63] Viggo Tvergaard. "Behaviour of voids in a shear field". In: *International Journal of Fracture* 158.1 (July 2009), pp. 41–49. ISSN: 1573-2673. DOI: 10.1007/s10704-009-9364-1. URL: https://doi.org/10.1007/s10704-009-9364-1.

[64] Yingbin Bao and Tomasz Wierzbicki. "On fracture locus in the equivalent strain and stress triaxiality space". In: *International Journal of Mechanical Sciences* 46.1 (2004), pp. 81–98. ISSN: 0020-7403. DOI: https://doi.org/10.1016/j.ijmecsci.2004.02.006. URL: http://www.sciencedirect.com/science/article/pii/S0020740304000360.

[65] Kim Lau Nielsen and Viggo Tvergaard. "Effect of a shear modified Gurson model on damage development in a FSW tensile specimen". In: *International Journal of Solids and Structures* 46.3-4 (Feb. 2009), pp. 587–601. ISSN: 00207683. DOI: 10.1016/j.ijsolstr.2008.09.011. URL: https://linkinghub.elsevier.com/retrieve/pii/S0020768308003752.

[66] Yingbin Bao and Tomasz Wierzbicki. "On the cut-off value of negative triaxiality for fracture". In: *Engineering Fracture Mechanics* 72.7 (2005), pp. 1049–1069. ISSN: 0013-7944. DOI: https://doi.org/10.1016/j.engfracmech.2004.07.011. URL: http://www.sciencedirect.com/science/article/pii/S0013794404001869.

[67] K. Danas and P. Ponte Castañeda. "Influence of the Lode parameter and the stress triaxiality on the failure of elasto-plastic porous materials". In: *International Journal of Solids and Structures* 49.11-12 (June 2012), pp. 1325–1342. ISSN: 00207683. DOI: 10.1016/j.ijsolstr.2012.02.006. URL: https://linkinghub.elsevier.com/retrieve/pii/S0020768312000467.

[68] "The role of stress state and stress triaxiality in lifetime prediction of solder joints in different packages utilized in automotive electronics". In: *Microelectronics Reliability* 74 (2017), pp. 155–164. ISSN: 0026-2714. DOI: https://doi.org/10.1016/j.microrel.2017.04.013. URL: http://www.sciencedirect.com/science/article/pii/S002627141730104X.

[69] Mihkel Kõrgesaar. "The effect of low stress triaxialities and deformation paths on ductile fracture simulations of large shell structures". In: *Marine Structures* 63 (2019), pp. 45–64. ISSN: 0951-8339. DOI: https://doi.org/10.1016/j.marstruc.2018.08.004. URL: http://www.sciencedirect.com/science/article/pii/S0951833918300704.

[70] J. T. Boyle, J. Spence, and Z. P. Bažant. "Stress Analysis for Creep". In: *Journal of Applied Mechanics* 51.3 (1984), p. 708. ISSN: 00218936. DOI: 10.1115/1.3167710. URL: http://appliedmechanics.asmedigitalcollection.asme.org/article.aspx?articleid=1407748.

[71] Vincenzo Vullo. *Circular Cylinders and Pressure Vessels*. Vol. 3. Springer Series in Solid and Structural Mechanics. Cham: Springer International Publishing, 2014. DOI: 10.1007/978-3-319-00690-1. URL: http://link.springer.com/10.1007/978-3-319-00690-1.

[72] Harshad Bhadeshia and Robert Honeycombe. "Stainless Steel". In: *Steels: Microstructure and Properties*. Elsevier, 2017, pp. 343–376. ISBN: 9780750680844. DOI: 10.1016/B978-0-08-100270-4.00012-3. URL: https://linkinghub.elsevier.com/retrieve/pii/B9780081002704000123.

[73] Neil Birks, Gerald H. Meier, and Frederick S. Pettit. *Introduction to the High Temperature Oxidation of Metals*. 2nd ed. Cambridge University Press, 2006. DOI: 10.1017/CBO9781139163903.

[74] D. J. Young. *High Temperature Oxidation and Corrosion of Metals*. Corrosion Series. Elsevier Science, 2008. ISBN: 9780080445878. URL: https://books.google.co.uk/books?id=%5C_UnuDx7avkIC.

[75] H. S. Khatak and B. Raj. *Corrosion of Austenitic Stainless Steels: Mechanism, Mitigation and Monitoring*. Woodhead Publishing, 2002. URL: https://books.google.co.uk/books?id=LHleAAAACAAJ.

[76] M. J. Chevalier. *Carburisation of Type 316 Stainless Steel in an AGR Environment: Status of Current Understanding*. Technical report E/REP/BBGB/0120/ AGR/13 Rev 001. EDF Energy, Dec. 2014.

[77] K. A. Habib, M. S. Damra, J. J. Saura, I. Cervera, and J. Bellés. "Breakdown and Evolution of the Protective Oxide Scales of AISI 304 and AISI 316 Stainless Steels under High-Temperature Oxidation". In: *International Journal of Corrosion* 2011 (2011), pp. 1–10. ISSN: 1687-9325. DOI: 10.1155/2011/824676. URL: http://www.hindawi.com/journals/ijc/2011/824676/.

[78] Carmen Ostwald and Hans J. Grabke. "Initial oxidation and chromium diffusion. I. Effects of surface working on 9–20% Cr steels". In: *Corrosion Science* 46.5 (2004), pp. 1113–1127. ISSN: 0010-938X. DOI: https://doi.org/10.1016/j.corsci.2003.09.004. URL: http://www.sciencedirect.com/science/article/pii/S0010938X03002257.

[79] Aya Shin, Marc Chevalier, Eleanor Laney, and Jonathan Pearson. "Oxidation behaviour of steels in advanced gas cooled reactors". In: *Materials at High Temperatures* 35.1-3 (2018), pp. 30–38. DOI: 10.1080/09603409.2017.1389114. eprint: https://doi.org/10.1080/09603409.2017.1389114. URL: https://doi.org/10.1080/09603409.2017.1389114.

[80] F. Rouillard, G. Moine, L. Martinelli, and J. C. Ruiz. "Corrosion of 9Cr Steel in CO2 at Intermediate Temperature I: Mechanism of Void-Induced Duplex Oxide Formation". In: *Oxidation of Metals* 77.1 (Feb. 2012), pp. 27–55. ISSN: 1573-4889. DOI: 10.1007/s11085-011-9271-5. URL: https://doi.org/10.1007/s11085-011-9271-5.

[81] C. Liu, P. J. Heard, S. J. Greenwell, and P. E. J. Flewitt. "A study of breakaway oxidation of 9Cr–1Mo steel in a Hot CO2 atmosphere using Raman spectroscopy". In: *Materials at High Temperatures* 35.1-3 (2018), pp. 50–55. DOI: 10.1080/09603409.2017.1389424. eprint: https://doi.org/10.1080/09603409.2017.1389424. URL: https://doi.org/10.1080/09603409.2017.1389424.

[82] Sabrina Yan, Scott Doak, Rachel Thomson, and Rebecca Higginson. "An investigation on oxidation/carburisation of 9Cr-1Mo steel heat exchanger tube in an AGR environment". In: *Materials at High Temperatures* 35.1-3 (2018), pp. 56–65. DOI: 10.1080/09603409.2017.1392411. eprint: https://doi.org/10.1080/09603409.2017.1392411. URL: https://doi.org/10.1080/09603409.2017.1392411.

[83] Joy Sumner, Nigel Simms, Aya Shin, and Jonathan Pearson. "Kinetics of Duplex Oxide Growth on 9Cr Steels Exposed in CO2: Application of Dimensional Metrology". In: *Oxidation of Metals* 87.5 (June 2017), pp. 617–629. ISSN: 1573-4889. DOI: 10.1007/s11085-017-9766-9. URL: https://doi.org/10.1007/s11085-017-9766-9.

[84] G. B. Gibbs. "A model for mild steel oxidation in CO2". In: *Oxidation of Metals* 7.3 (Dec. 1973), pp. 173–184. ISSN: 1573-4889. DOI: 10.1007/BF00610578. URL: https://doi.org/10.1007/BF00610578.

[85] Gustavo C.C. Costa, Nathan S. Jacobson, Dorothy Lukco, Gary W. Hunter, Leah Nakley, Brandon G. Radoman-Shaw, and Ralph P. Harvey. "Oxidation behavior of stainless steels 304 and 316 under the Venus atmospheric surface conditions". In: *Corrosion Science* 132 (2018), pp. 260–271. ISSN: 0010-938X. DOI: https://doi.org/10.1016/j.corsci.2018.01.002. URL: http://www.sciencedirect.com/science/article/pii/S0010938X17308600.

[86] Gerald H. Meier, Keeyoung Jung, Nan Mu, Nazik M. Yanar, Frederick S. Pettit, J. Pirón Abellán, Tomasz Olszewski, L. Nieto Hierro, Willem J. Quadakkers, and Gordon R. Holcomb. "Effect of Alloy Composition and Exposure Conditions on the Selective Oxidation Behavior of Ferritic Fe–Cr and Fe–Cr–X Alloys". In: *Oxidation of Metals* 74.5 (Dec. 2010), pp. 319–340. ISSN: 1573-4889. DOI: 10.1007/s11085-010-9215-5. URL: https://doi.org/10.1007/s11085-010-9215-5.

[87] B. Chen, J. Lindsay, R. A. Ainsworth, and F. Scenini. "Oxidation Behavior of an Austenitic Stainless Steel Used in the UK Advanced Gas Cooled Reactors". In: *Proceedings of the NACE International conference*. Dallas, TX: NACE International, 2015. URL: https://www.onepetro.org/conference-paper/NACE-2015-5965.

[88] M. G. C. Cox, B. McEnaney, and V. D. Scott. "Vacancy condensation and void formation in duplex oxide scales on alloys". In: *Philosophical Magazine* 28.2 (Aug. 1973), pp. 309–319. ISSN: 0031-8086. DOI: https://doi.org/10.1080/14786437308217455. URL: http://www.tandfonline.com/doi/abs/10.1080/14786437308217455.

[89] EDF Energy. *CO_2 Oxidation Handbook*. Tech. rep. R67, Section 7, Issue 1. June 2015.

[90] S.R. Collins, P.C. Williams, S.V. Marx, A. Heuer, F. Ernst, and H. Kahn. "Low-Temperature Carburization of Austenitic Stainless Steels". In: *Heat Treating of Irons and Steels*. Vol. Vol 4D. ASM International, 2014. Chap. HEAT TREAT, pp. 451–460. DOI: 10.31399/asm.hb.v04d.a0005939. URL: http://www.asminternational.org/documents/10192/1849770/05352G%7B%5C_%7DSample.pdf/3841f98e-2bce-4f5d-9c97-f42726201e4a%20https://dl.asminternational.org/books/book/9/chapter/111210/low-temperature-carburization-of-austenitic.

[91] Olga Karabelchtchikova. "Fundamentals of Mass Transfer in Gas Carburizing". PhD thesis. Worcester Polytechnic Institute, 2007, pp. 5–13.

[92] D R Poirier and G H Geiger. "Fick's Law and Diffusivity of Materials". In: *Transport Phenomena in Materials Processing*. Cham: Springer International Publishing, 2016, pp. 419–461. ISBN: 978-3-319-48090-9. DOI: 10.1007/978-3-319-48090-9_12. URL: https://doi.org/10.1007/978-3-319-48090-9%7B%5C_%7D12.

[93] R.C. Lobb and H.E. Evans. "A determination of the chromium concentration for 'healing' layer formation during the oxidation of chromium-depleted 20cr-25ni-nb stainless steel". In: *Corrosion Science* 24.5 (1984), pp. 385–396. ISSN: 0010-938X. DOI: https://doi.org/10.1016/0010-938X(84)90065-9. URL: http://www.sciencedirect.com/science/article/pii/0010938X84900659.

[94] N. Terao and B. Sasmal. "Precipitation of M23C6 type carbide on twin boundaries in austenitic stainless steels". In: *Metallography* 13.2 (1980), pp. 117–133. ISSN: 0026-0800. DOI: https://doi.org/10.1016/0026-0800(80)90010-5. URL: http://www.sciencedirect.com/science/article/pii/0026080080900105.

[95] F. Rouillard, G. Moine, M. Tabarant, and J. C. Ruiz. "Corrosion of 9Cr Steel in CO2 at Intermediate Temperature II: Mechanism of Carburization". In: *Oxidation of Metals* 77.1 (Feb. 2012), pp. 57–70. ISSN: 1573-4889. DOI: 10.1007/s11085-011-9272-4. URL: https://doi.org/10.1007/s11085-011-9272-4.

[96] Mustafa Nasser, Catrin M. Davies, and Kamran Nikbin. "The Influence of AGR Gas Carburisation on the Creep and Fracture Properties of Type 316H Stainless Steel". In: V005T09A009. July 2016. DOI: 10.1115/PVP2016-63076. URL: https://doi.org/10.1115/PVP2016-63076.

[97] F. Biglari and K.M. Nikbin. "Environmental creep intergranular damage and multisite crack evolution model for engineering alloys". In: *Computational Materials Science* 84 (Mar. 2014), pp. 267–277. ISSN: 09270256. DOI: 10.1016/j.commatsci.2013.12.020. URL: https://linkinghub.elsevier.com/retrieve/pii/S0927025613007702.

[98] F.R. Biglari and K.M. Nikbin. "A diffusion driven carburisation combined with a multiaxial continuum creep model to predict random multiple cracking in engineering alloys". In: *Engineering Fracture Mechanics* 146 (Sept. 2015), pp. 89–108. ISSN: 00137944. DOI: 10.1016/j.engfracmech.2015.07.057. URL: https://linkinghub.elsevier.com/retrieve/pii/S0013794415004336.

[99] Farid R Biglari and Kamran M Nikbin. "Numerical predictions of carburisation and crack evolution using a combined diffusion rate and remaining multi-axial creep ductility damage model". In: *International Journal of Damage Mechanics* 26.6 (Aug. 2017), pp. 859–880. ISSN: 1056-7895. DOI: 10.1177/1056789516628317. URL: http://journals.sagepub.com/doi/10.1177/1056789516628317.

[100] Peter Deem. *ENVISINC Metallography Report, Summary of Results 2013-2015*. Tech. rep. 203634-TR-0001 Issue 04. Amec Foster Wheeler, Jan. 2017.

[101] Siti Khadijah Alias, Bulan Abdullah, Ahmed Jaffar, Syazuan Abdul Latip, Salmiah Kasolang, Mohd Faizul Izham, and Muhd Azimin Abd Ghani. "Mechanical Properties of Paste Carburized ASTM A516 Steel". In: *Procedia Engineering* 68 (2013), pp. 525–530. ISSN: 18777058. DOI: 10.1016/j.proeng.2013.12.216. URL: https://linkinghub.elsevier.com/retrieve/pii/S1877705813020705.

[102] MingHao Zhao, XueCheng Han, Gang Wang, and GuangTao Xu. "Determination of the mechanical properties of surface-modified layer of 18CrNiMo7-6 steel alloys after carburizing heat treatment". In: *International Journal of Mechanical Sciences* 148 (2018), pp. 84–93. ISSN: 0020-7403. DOI: https://doi.org/10.1016/j.ijmecsci.2018.08.021. URL: http://www.sciencedirect.com/science/article/pii/S002074031831556X.

[103] M.N. Gusev, O.P. Maksimkin, O.V. Tivanova, N.S. Silnaygina, and F.A. Garner. "Correlation of yield stress and microhardness in 08Cr16Ni11Mo3 stainless steel irradiated to high dose in the BN-350 fast reactor". In: *Journal of Nuclear Materials* 359.3 (2006), pp. 258–262. ISSN: 0022-3115. DOI: https://doi.org/10.1016/j.jnucmat.2006.09.005. URL: http://www.sciencedirect.com/science/article/pii/S0022311506004831.

[104] S. J. Kimmins. *Tensile Properties of ex-Heysham Superheater Forgings and a Correlation of Proof Strength with Hardness*. Tech. rep. EPD/GEN/REP/0008/96. Nuclear Elerctric plc., Feb. 1996.

[105] EDF Energy. "AGR Materials Data Handbook R66 Revision 9". In: *EDF Energy, Gloucester, UK* (2011).

[106] T. Sourmail. "Precipitation in creep resistant austenitic stainless steels". In: *Materials Science and Technology* 17.1 (2001), pp. 1–14. DOI: 10.1179/026708301101508972. eprint: https://doi.org/10.1179/026708301101508972. URL: https://doi.org/10.1179/026708301101508972.

[107] A D Warren, I J Griffiths, and P E J Flewitt. "Precipitation within localised chromium-enriched regions in a Type 316H austenitic stainless steel". In: *Journal of Materials Science* 53.8 (2018), pp. 6183–6197. ISSN: 1573-4803. DOI: 10.1007/s10853-017-1748-4. URL: https://doi.org/10.1007/s10853-017-1748-4.

[108] M. Godec and D. A. Skobir Balantič. "Coarsening behaviour of M23C6 carbides in creep-resistant steel exposed to high temperatures". In: *Scientific Reports* 6.1 (2016), p. 29734. ISSN: 2045-2322. DOI: 10.1038/srep29734. URL: http://www.nature.com/articles/srep29734.

[109] B. Chen, J. N. Hu, Y. Q. Wang, S. Kabra, A. C. F. Cocks, D. J. Smith, and P. E. J. Flewitt. "Internal strains between grains during creep deformation of an austenitic stainless steel". In: *Journal of Materials Science* 50.17 (2015), pp. 5809–5816. ISSN: 0022-2461. DOI: 10.1007/s10853-015-9128-4. URL: http://link.springer.com/10.1007/s10853-015-9128-4.

[110] T. Christiansen and M. A. J. Somers. "Low temperature gaseous nitriding and carburising of stainless steel". In: *Surface Engineering* 21.5-6 (Oct. 2005), pp. 445–455. ISSN: 0267-0844. DOI: 10.1179/174329405X68597. URL: http://www.tandfonline.com/doi/full/10.1179/174329405X68597.

[111] A. Gulli and S. Pal. *Deep learning with Keras*. Packt Publishing, Apr. 2017. ISBN: 978-1-78712-842-2. URL: http://link.springer.com/10.1007/978-3-540-85051-9.

[112] A. Singh, N. Thakur, and A. Sharma. "A review of supervised machine learning algorithms". In: *2016 3rd International Conference on Computing for Sustainable Global Development (INDIACom)*. Mar. 2016, pp. 1310–1315.

[113] Bernhard Scholkopf and Alexander J. Smola. *Learning with Kernels — Support Vector Machines, Regularization, Optimization and Beyond*. Cambridge, MA: Massachusetts Institute of Technology, 2002. ISBN: 0-262-19475-9.

[114] I. Griva, S.G. Nash, and A. Sofer. *Linear and Nonlinear Optimization*. 2nd ed. Other Titles in Applied Mathematics. Society for Industrial and Applied Mathematics, 2009. ISBN: 9780898717730. URL: https://books.google.co.uk/books?id=uOJ-Vg1BnKgC.

[115] Corinna Cortes and Vladimir Vapnik. "Support-Vector Networks". In: *Machine Learning* 20.3 (Sept. 1995), pp. 273–297. ISSN: 1573-0565. DOI: 10.1023/A:1022627411411. URL: https://doi.org/10.1023/A:1022627411411.

[116] Gopinath Rebala, Ajay Ravi, and Sanjay Churiwala. *An Introduction to Machine Learning*. Cham: Springer International Publishing, 2019. ISBN: 978-3-030-15728-9. DOI: 10.1007/978-3-030-15729-6. URL: http://link.springer.com/10.1007/978-3-030-15729-6.

[117] Fernandes de Mello Rodrigo and Antonelli Ponti Moacir. *Machine Learning*. Cham: Springer International Publishing, 2018. ISBN: 978-3-319-94988-8. DOI: 10.1007/978-3-319-94989-5. URL: http://link.springer.com/10.1007/978-3-319-94989-5.

[118] Barry J. Wythoff. "Backpropagation neural networks". In: *Chemometrics and Intelligent Laboratory Systems* 18.2 (Feb. 1993), pp. 115–155. ISSN: 01697439. DOI: 10.1016/0169-7439(93)80052-J. URL: https://linkinghub.elsevier.com/retrieve/pii/016974399380052J.

[119] Sandro Skansi. *Introduction to Deep Learning*. Undergraduate Topics in Computer Science. Cham: Springer International Publishing, 2018. ISBN: 978-3-319-73003-5. DOI: 10.1007/978-3-319-73004-2. URL: http://link.springer.com/10.1007/978-3-319-73004-2.

[120] Neha Yadav, Anupam Yadav, and Manoj Kumar. *An Introduction to Neural Network Methods for Differential Equations*. SpringerBriefs in Applied Sciences and Technology. Dordrecht: Springer Netherlands, 2015. ISBN: 978-94-017-9815-0. DOI: 10.1007/978-94-017-9816-7. URL: http://link.springer.com/10.1007/978-94-017-9816-7.

[121] Te-Ming Huang, Vojislav Kecman, and Ivica Kopriva. *Kernel Based Algorithms for Mining Huge Data Sets*. Vol. 17. Studies in Computational Intelligence. Berlin/Heidelberg: Springer-Verlag, 2006. ISBN: 3-540-31681-7. DOI: 10.1007/3-540-31689-2. URL: http://link.springer.com/10.1007/3-540-31689-2.

[122] Kurt Hornik, Maxwell Stinchcombe, and Halbert White. "Multilayer feedforward networks are universal approximators". In: *Neural Networks* 2.5 (Jan. 1989), pp. 359–366. ISSN: 08936080. DOI: 10.1016/0893-6080(89)

90020-8. URL: https://linkinghub.elsevier.com/retrieve/pii/0893608089900208.

[123] Warren S. McCulloch and Walter Pitts. "A logical calculus of the ideas immanent in nervous activity". In: *The bulletin of mathematical biophysics* 5.4 (Dec. 1943), pp. 115–133. ISSN: 1522-9602. DOI: 10.1007/BF02478259. URL: https://doi.org/10.1007/BF02478259.

[124] F. Rosenblatt. "The perceptron: A probabilistic model for information storage and organization in the brain." In: *Psychological Review* 65.6 (1958), pp. 386–408. ISSN: 1939-1471. DOI: 10.1037/h0042519. URL: http://doi.apa.org/getdoi.cfm?doi=10.1037/h0042519.

[125] Alex Krizhevsky, Ilya Sutskever, and Geoffrey E. Hinton. "ImageNet classification with deep convolutional neural networks". In: *Communications of the ACM* 60.6 (May 2017), pp. 84–90. ISSN: 00010782. DOI: 10.1145/3065386. URL: http://dl.acm.org/citation.cfm?doid=3098997.3065386.

[126] T. Sourmail, H. K. D. H. Bhadeshia, and D. J. C. MacKay. "Neural network model of creep strength of austenitic stainless steels". In: *Materials Science and Technology* 18.6 (June 2002), pp. 655–663. ISSN: 0267-0836. DOI: 10.1179/026708302225002065. URL: http://www.tandfonline.com/doi/full/10.1179/026708302225002065.

[127] D. Cole, C. Martin-Moran, A.G. Sheard, H.K.D.H. Bhadeshia, and D.J.C. MacKay. "Modelling creep rupture strength of ferritic steel welds". In: *Science and Technology of Welding and Joining* 5.2 (Apr. 2000), pp. 81–89. ISSN: 1362-1718. DOI: 10.1179/136217100101538065. URL: http://www.tandfonline.com/doi/full/10.1179/136217100101538065.

[128] V Srinivasan. "Low cycle fatigue and creep–fatigue interaction behavior of 316L(N) stainless steel and life prediction by artificial neural network approach". In: *International Journal of Fatigue* 25.12 (Dec. 2003), pp. 1327–1338. ISSN: 01421123. DOI: 10.1016/S0142-1123(03)00064-1. URL: https://linkinghub.elsevier.com/retrieve/pii/S0142112303000641.

[129] M.D. Mathew, Dae Whan Kim, and Woo-Seog Ryu. "A neural network model to predict low cycle fatigue life of nitrogen-alloyed 316L stainless steel". In: *Materials Science and Engineering: A* 474.1-2 (Feb. 2008), pp. 247–253. ISSN: 09215093. DOI: 10.1016/j.msea.2007.04.018. URL: https://linkinghub.elsevier.com/retrieve/pii/S0921509307006211.

[130] Young Il Kwon and Byeong Soo Lim. "A study of creep-fatigue life prediction using an artificial neural network". In: *Metals and Materials International* 7.4 (July 2001), pp. 311–317. ISSN: 1234-4320. DOI: 10.1007/BF03186074. URL: https://doi.org/10.1007/BF03186074.

[131] Amitava Ghatak and P. S. Robi. "Prediction of creep curve of HP40Nb steel using artificial neural network". In: *Neural Computing and Applications* 30.9 (Nov. 2018), pp. 2953–2964. ISSN: 0941-0643. DOI: 10.1007/s00521-017-2851-9. URL: http://link.springer.com/10.1007/s00521-017-2851-9.

[132] C. R. Calladine and D. C. Drucker. "Nesting surfaces of constant rate of energy dissipation in creep". In: *Quarterly of Applied Mathematics* 20.1 (Apr. 1962), pp. 79–84. ISSN: 0033-569X. DOI: 10.1090/qam/99965. URL: http://www.ams.org/qam/1962-20-01/S0033-569X-1962-99965-4/.

[133] J B Martin. "A Note on the Determination of an Upper Bound on Displacement Rates for Steady Creep Problems". In: *Journal of Applied Mechanics* 33.1 (Mar. 1966), pp. 216–217. ISSN: 0021-8936. URL: http://dx.doi.org/10.1115/1.3624992.

[134] T H Hyde, K Yehia, and W Sun. "Observations on the creep of two-material structures". In: *The Journal of Strain Analysis for Engineering Design* 31.6 (Nov. 1996), pp. 441–461. ISSN: 0309-3247. DOI: 10.1243/03093247V316441. URL: http://journals.sagepub.com/doi/10.1243/03093247V316441.

[135] R.P. Agarwala, M.C. Naik, M.S. Anand, and A.R. Paul. "Diffusion of carbon in stainless steels". In: *Journal of Nuclear Materials* 36.1 (July 1970), pp. 41–47. ISSN: 00223115. DOI: 10.1016/0022-3115(70)90060-7. URL: https://linkinghub.elsevier.com/retrieve/pii/0022311570900607.

[136] Luowei Cao, Guoshan Xie, Zhiyuan Han, and Fakun Zhuang. "Effect of Carburization on Creep Performance of Cr35Ni45Nb Heat Resistant Alloy". In: *Volume 6A: Materials and Fabrication*. ASME, July 2018, V06AT06A045. ISBN: 978-0-7918-5167-8. DOI: 10.1115/PVP2018-84226. URL: http://proceedings.asmedigitalcollection.asme.org/proceeding.aspx?doi=10.1115/PVP2018-84226.

[137] Mark Hudson Beale, Martin T. Hagan, and Demuth Howard B. *MatLab Deep Learning Toolbox Reference*. The MathWorks, Natick, MA, USA. 2019. URL: https://uk.mathworks.com/help/pdf_doc/deeplearning/nnet_ref.pdf.

[138] Mark Hudson Beale, Martin T. Hagan, and Demuth Howard B. *MatLab Deep Learning Toolbox User's Guide*. The MathWorks, Natick, MA, USA. 2019. URL: https://uk.mathworks.com/help/pdf_doc/deeplearning/nnet_ref.pdf.

[139] Kai Ming Ting. "Precision and Recall". In: *Encyclopedia of Machine Learning and Data Mining*. Boston, MA: Springer US, 2017, pp. 990–991. DOI: 10.1007/978-1-4899-7687-1_659. URL: http://link.springer.com/10.1007/978-1-4899-7687-1%7B%5C_%7D659.

[140] M.J. Stevens, R.J. Dennis, I.J.M. Bottomley, and R.A.W. Bradford. "Modelling the manufacturing history, through life creep-fatigue damage and limiting defect sizes of a pipework joint using finite element based methods". In: *International Journal of Pressure Vessels and Piping* 108-109 (Aug. 2013), pp. 13–27. ISSN: 03080161. DOI: 10.1016/j.ijpvp.2013.04.003. URL: https://linkinghub.elsevier.com/retrieve/pii/S0308016113000598.

Appendix A

Supplementary material for Chapter 3

A.1 Analytical solutions for elastic loading

Consider a hollow tube with internal radius, r_i, external radius, r_e. The tube consist of two materials that have different Young's modulus and Poisson's ratio values. There is an interface separating both materials at $r = r_{int}$. The hollow tube is strained in axial direction, hence the applied load is

$$\sigma_{obs} = (1 - af) \cdot \sigma_z^{(1)} + af \cdot \sigma_z^{(2)} \tag{A.1}$$

For linear elastic case stresses and strains must satisfy the Hooke's law:

$$\varepsilon_r^{(1,2)} = \frac{1}{E^{(1,2)}} \left(\sigma_r^{(1,2)} - \nu^{(1,2)} (\sigma_t^{(1,2)} + \sigma_z^{(1,2)}) \right) \tag{A.2}$$

$$\varepsilon_t^{(1,2)} = \frac{1}{E^{(1,2)}} \left(\sigma_t^{(1,2)} - \nu^{(1,2)} (\sigma_r^{(1,2)} + \sigma_z^{(1,2)}) \right) \tag{A.3}$$

$$\varepsilon_z^{(1,2)} = \frac{1}{E^{(1,2)}} \left(\sigma_z^{(1,2)} - \nu^{(1,2)} (\sigma_r^{(1,2)} + \sigma_t^{(1,2)}) \right) \tag{A.4}$$

where ε_r, ε_t, ε_z and σ_r, σ_t, σ_z are radial, hoop and axial strain and stresses respectively, E and ν are Young's modulus and Poisson's ratio, and superscripts $(1, 2)$ indicate inner (denoted as 1) or outer (denoted as 2) cylinders.

Assuming that there is induced interface pressure p_{int} that arises due to mismatch in material properties, then for axisymmetric structure radial compatibility (Eq.

A.5) and equilibrium condition (Eq. A.6) must be satisfied:

$$\frac{\partial \varepsilon_t}{\partial r} = \frac{\varepsilon_r - \varepsilon_t}{r} \tag{A.5}$$

$$\frac{\partial \sigma_r}{\partial r} = \frac{\sigma_t - \sigma_r}{r} \tag{A.6}$$

Radial compatibility is imposed from $\varepsilon_t(r_{int}) = \rho/r_{int}$ where ρ is radial displacement:

$$\begin{aligned}\varepsilon_t^{(1)}(r_{int}) = \frac{1}{E^{(1)}}\left(\sigma_t^{(1)}(r_{int}) - \nu^{(1)}(\sigma_r^{(1)}(r_{int}) + \sigma_z^{(1)}(r_{int}))\right) = \\ \frac{1}{E^{(2)}}\left(\sigma_t^{(2)}(r_{int}) - \nu^{(2)}(\sigma_r^{(2)}(r_{int}) + \sigma_z^{(2)}(r_{int}))\right) = \varepsilon_t^{(2)}(r_{int})\end{aligned} \tag{A.7}$$

The hoop and radial stresses can be expressed using Lamé equations for thick-walled cylinders in linear elastic regime:

$$\sigma_t^{(1)}(r_{int}) = -p_{int}\frac{r_{int}^2 + r_i^2}{r_{int}^2 - r_i^2}; \qquad \sigma_r^{(1)}(r_{int}) = -p_{int} \tag{A.8}$$

$$\sigma_t^{(2)}(r_{int}) = p_{int}\frac{r_e^2 + r_{int}^2}{r_e^2 - r_{int}^2}; \qquad \sigma_r^{(2)}(r_{int}) = -p_{int} \tag{A.9}$$

Combining Eqs. A.8–A.9 with Eq. A.7 gives the following equality:

$$\begin{aligned}\left[\frac{E^{(1)}}{E^{(2)}}\left(\nu^{(1)} - \frac{r_{int}^2 + r_i^2}{r_{int}^2 - r_i^2}\right) - \left(\nu^{(2)} + \frac{r_e^2 + r_{int}^2}{r_e^2 - r_{int}^2}\right)\right]p_{int} - \\ \frac{E^{(1)}}{E^{(2)}}\nu^{(1)}\sigma_z^{(1)} + \nu^{(2)}\sigma_z^{(2)} = 0\end{aligned} \tag{A.10}$$

Besides radial displacement compatibility at the interface, axial stain is assumed to be constant across the thickness of bi-layer specimen, hence combining Eqs. A.8–A.9 with Eq. A.4 gives

$$\begin{aligned}\left[\frac{E^{(1)}}{E^{(2)}}\left(2\nu^{(1)}\frac{r_{int}^2}{r_{int}^2 - r_i^2} + 2\nu^{(2)}\frac{r_{int}^2}{r_e^2 - r_{int}^2}\right)\right]p_{int} + \\ \frac{E^{(1)}}{E^{(2)}}\nu^{(1)}\sigma_z^{(1)} - \nu^{(2)} = 0\end{aligned} \tag{A.11}$$

In total there are three unknowns (p_{int}, $\sigma_z^{(1)}$, $\sigma_z^{(2)}$) and three equations (Eqs. A.1, A.11 and A.10), hence by solving this system of equations the multiaxial stress state can be found.

Figure A.1 shows a solution of two concentric cylinders loaded uniaxially to σ_{obs}, inner cylinder is assumed to be in fully plastic regime $\nu^{(1)} = 0.5$, $E^{(1)} = 157\,GPa$ and outer cylinder is elastic $\nu^{(2)} = 0.3$, $E^{(2)} = 205\,GPa$. From the results can be

seen that using the 2-bar model the axial stresses in the carburised layer will be overestimated compared to the axial stress when geometrical effects are considered. Nevertheless, the von Mises stress is increased in the hollow tube model compared to the 2-bar model. Figure A.1c show that for thick component the multiaxiality will promote early yielding in carburised layer.

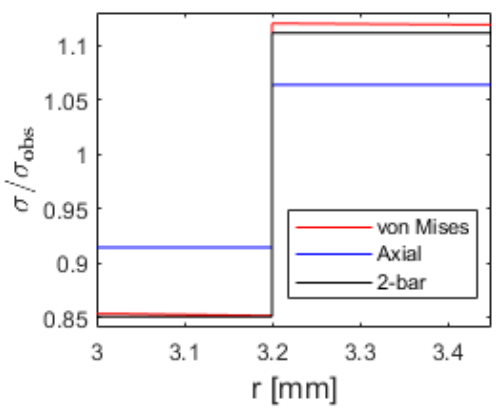

(a) Axial and von Mises stress, hollow tube af = 57%;

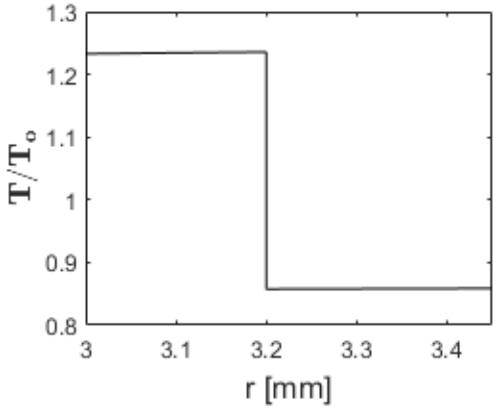

(b) Normalised stress triaxiality, hollow tube af = 57%;

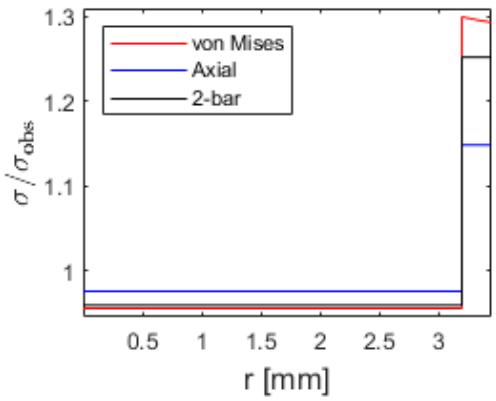

(c) Axial and von Mises stress, rod af = 14%;

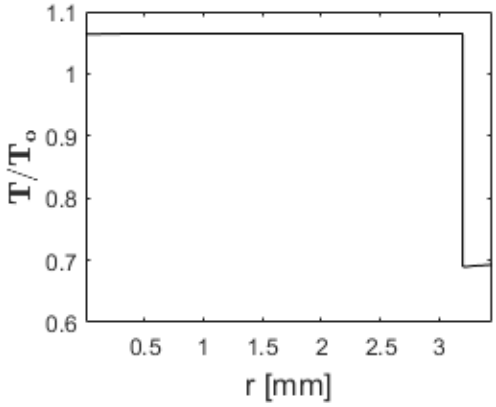

(d) Normalised stress triaxiality, rod af = 14%.

Figure A.1: Non-axial stress induced in a hollow tube and solid rod with a carburised layer (inner cylinder $\nu^{(1)}$ = 0.5, outer cylinder $\nu^{(1)}$ = 0.3).

A.2 Python code for concentric FG cylinders at steady state creep

The following program calculates the stress distribution of a functionally graded cylinder where creep law multiplier is a function of radius. The program allows to assume any distribution profile and provides a simple tool for stress and creep lifetime estimation.

```
"""
The calculation of redistributed stress state in a functionally
   graded cylinder by assuming some variation of creep properties
   through radius, such that A(r) can be any function. The code
   will discretise A(r) into N number of cylinders where each
   individual cylinder follows A_(r) = Ao_ * (r_/ri_)**m_.
@author: Janis Cakstins
"""

import numpy as np

# Number of cylinders assumed in bulk and carburised layer
N = 1000

# Geometry
ri = 1          # Internal radius [cm]
re = 1.01       # External radius [cm]
af = 0.5        # Area fraction carburised or 0.5192307692307693
   for 0.25 mm
rint = np.sqrt(re**2 - af*(re**2-ri**2))    # The interface
r_bulk = np.linspace(ri,rint,N+1)     # Radius through bulk
r_carb = np.linspace(rint,re,N+1)     # Radius through carburised
   layer
r_all = np.append(r_bulk,r_carb[1:])  # All radii
r_ints = r_all[1:-2]                  # All interface radii

# Loading
pi = 50         # Internal pressure [MPa]
pe = 0          # External pressure [MPa]

# Creep law properties through the thickness
n=10.18     # creep law exponent

# Homogeneous layer
Ab = 8.876*10**(-35) * 3600    # Creep law multiplier of the bulk
Ab_dist = Ab*np.ones(N)
m_bulk = 0 * np.ones(N)

# Carburised layer: calculates A(x) distribution in terms of m
def m(a, p):
    x = (r_carb**2 - rint**2)/(re**2-rint**2)
    A = Ab *10**(a*(x*100)**p)   # x**1 for lin and x**2 for
   parabolic. Modify this according to your A(x) function
    m = np.log(A[1:] / A[:-1]) / np.log(r_carb[1:]/r_carb[:-1])
    return m, A

# Calculate interface pressures
```

```
41 def press():
42     ri  = r_all[:-2]
43     rint= r_all[1:-1]
44     re  = r_all[2:]
45     k1 = (m_dist[:-1]+2)/n
46     k2 = (m_dist[1:]+2)/n
47     A1 = A_dist[:-1]
48     A2 = A_dist[1:]
49     C2 = (A1/A2)**(1/n) * k1/k2  * (ri/rint)**k1 * ( (1 - (rint/re)
       **k2)/(1- (ri/rint)**k1) )
50 
51     alpha = C2/(1+C2)
52     beta  = 1/(1+C2)
53     M = np.zeros((len(C2),len(C2)))
54     np.fill_diagonal(M[:,1:],beta[:-1])
55     np.fill_diagonal(M[1:]  ,alpha[1:])
56     M = np.matrix(M)
57     b = np.zeros(len(M)) # Boundary conditions
58     b[0]  = alpha[0] * pi
59     b[-1] = beta[-1] * pe
60     b=np.matrix(b)
61     I = np.identity(np.shape(M)[0]) # Identity matrix
62     p = np.linalg.inv(M-I) * np.transpose(-b)
63 
64     return np.array(p)
65 
66  # Creep properties
67 """2-bar: a=np.log10(1/22), p=0;
68  Lin a=-2.5386526490450867E-2, p=1; Para a=-3.5840310034492066E-4,
       p=2"""
69 #f = [1, 15, 20, 25, 30]
70 a_prop=[np.log10(1/22), -2.5618625880352637E-2, -3.6149972028914277
       E-4]
71 p_prop=[0,1,2]
72 
73 for i in range(len(a_prop)):
74     m_carb, A = m(a=a_prop[i], p=p_prop[i])
75     #m_carb, A = m(a=np.log10(f[i]), p=0)
76 
77     if m_carb[0]==m_carb[-1]:
78         Ac_dist = Ab_dist/22 #f[i]
79     else:
80         Ac_dist = Ab_dist
81 
82     A_dist = np.append(Ab_dist, Ac_dist)
83     m_dist = np.append(m_bulk, m_carb)
84 
```

```
85    pint  = press()     # All interface pressures
86    p_all = np.array([pi])
87    p_all = np.append(p_all,pint)
88    p_all = np.append(p_all,pe)
89
90    k = (m_dist+2)/n
91    stress_t  = (p_all[:-1]-p_all[1:]) * (-k)/((r_all[:-1]/r_all
      [1:])**k-1) - p_all[:-1]
92    stress_t  = np.append(stress_t, (p_all[-2]-p_all[-1])*((r_all
      [-2]/r_all[-1])**k[-1]*(1-k[-1])-1)/((r_all[-2]/r_all[-1])**k
      [-1]-1)- p_all[-2])
93    stress_r  = -p_all
94    stress_z  = 0.5 * (stress_t + stress_r)
95    stress_vM = (((stress_r-stress_t)**2+(stress_t-stress_z)**2+(
      stress_z-stress_r)**2)/2)**0.5
96
97    hydro = (stress_t + stress_r + stress_z)/3 # Hydrostatic stress
98    triax = hydro/stress_vM     # Stress triaxiality
99
100   cr = stress_vM**n * np.append(Ab_dist, A) # Carburised model
      creep rate
101
102   stress_r0 = (pi-pe) * ((ri/r_all)**(2/n)-1)/((ri/re)**(2/n)-1)
      - pi
103   stress_t0 = (pi-pe) * ((ri/r_all)**(2/n) * (1-2/n)-1)/((ri/re)
      **(2/n)-1)- pi
104   stress_z0 = 0.5 * (stress_r0 + stress_t0)
105   stress_vM0 = (((stress_r0-stress_t0)**2+(stress_t0-stress_z0)
      **2+(stress_z0-stress_r0)**2)/2)**0.5
106
107   hydro0 = (stress_t0 + stress_r0 + stress_z0)/3 # Hydrostatic
      stress (hom)
108   triax0 = hydro0/stress_vM0  # Stress triaxiality (hom)
109
110   cr0 = stress_vM0**n *Ab     # Homogeneous model creep rate
```

Appendix B

Supplementary material for Chapter 4

B.1 Additional data on the impact of material properties on accumulated creep strain

B.1.1 Test coupon geometry

A quarter of the following speciment was modelled in Chapter 4.2.1

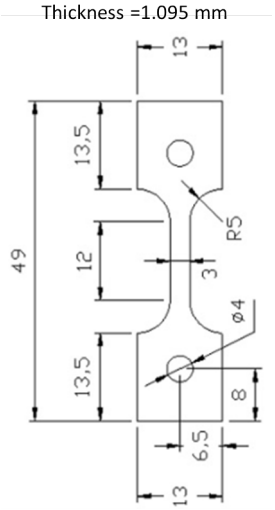

Figure B.1: The actual geometry of the specimen modelled (Courtesy of Palko [13])

B.1.2 Stress redistribution

Stress redistribution of pre-carbursied and carburising models where elastic, plastic and creep properties are changing are shown in Figure B.2. It can be seen from the

curve that 600 hr $M^*(El, Pl, Cr)$ and $M(El, Pl, Cr)$ have both reached the steady state solution of 480 MPa.

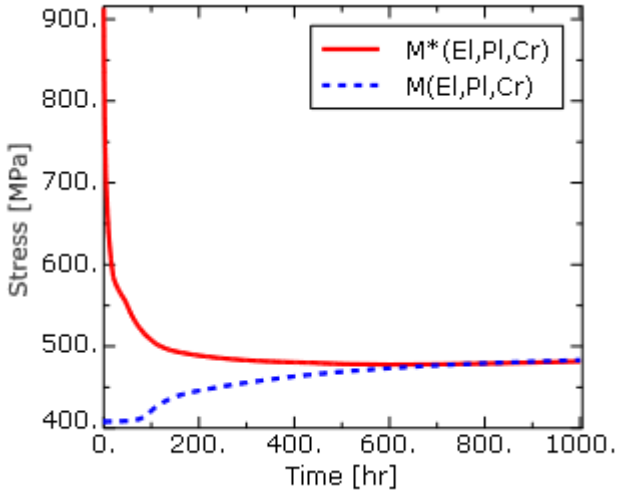

Figure B.2: Redistribution of stresses in pre-carburised and carburising models.

B.1.3 Creep damage after 500 hr

The creep damage of $M^*(El, Pl, Cr)$ (Figure B.3a) and $M(El, Pl, Cr)$ (Figure B.3b) at $t = t_{red} = 500\,hr$ assuming $\varepsilon_f = 2.6\%$. Creep damage through the thickness at various time steps shown in Figure B.3d and B.3e.

B.2 Tensile property neural network performance data

B.2.1 Parabolic material property distribution neural network

Figure B.4 shows the neural network performance of the single hidden layer (28 node) neural network for carburised layer von Mises stress estimation (Figure B.4a), and [28, 14] triaxiality classifier (Figure B.4b).

Figure B.5 shows an example of misclassification by the stress triaxiality neural network.

B.2.2 Linear material property distribution neural network

The estimated stress strain curves assuming linear distribution profile shown in Figure B.6.

Neural network performance summarised in Figures B.7.

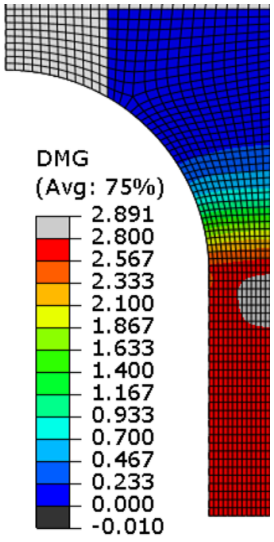

(a) Damage after 500 hr of the pre-carburised $M^*(El, Pl, Cr)$ model;

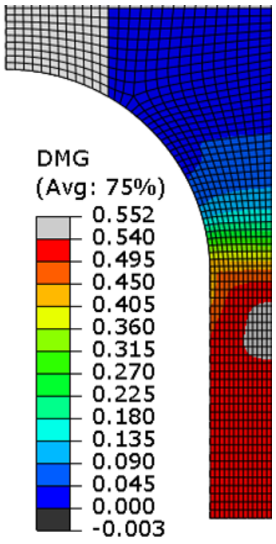

(b) Damage after 500 hr of the carburising $M(El, Pl, Cr)$ model;

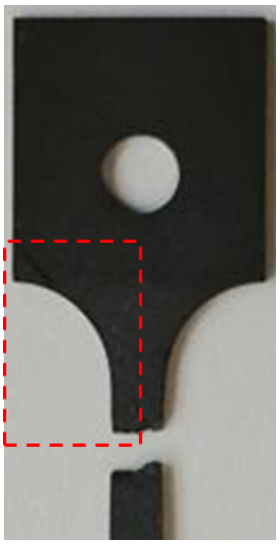

(c) Actual failure of carburising specimen [13].

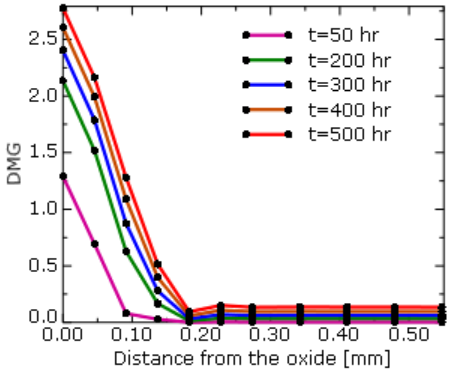

(d) Estimated creep in pre-carburised test case;

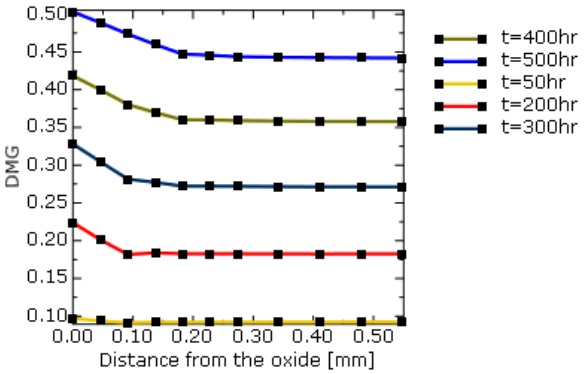

(e) Estimated creep in carburising test case.

Figure B.3: Creep damage comparison of pre-carburised and carburising specimens.

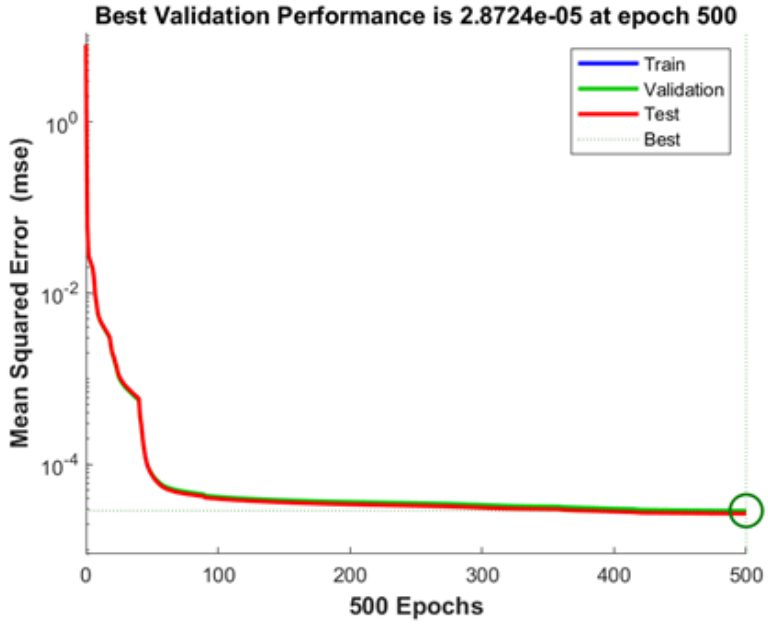

(a) Von Mises stress estimator;

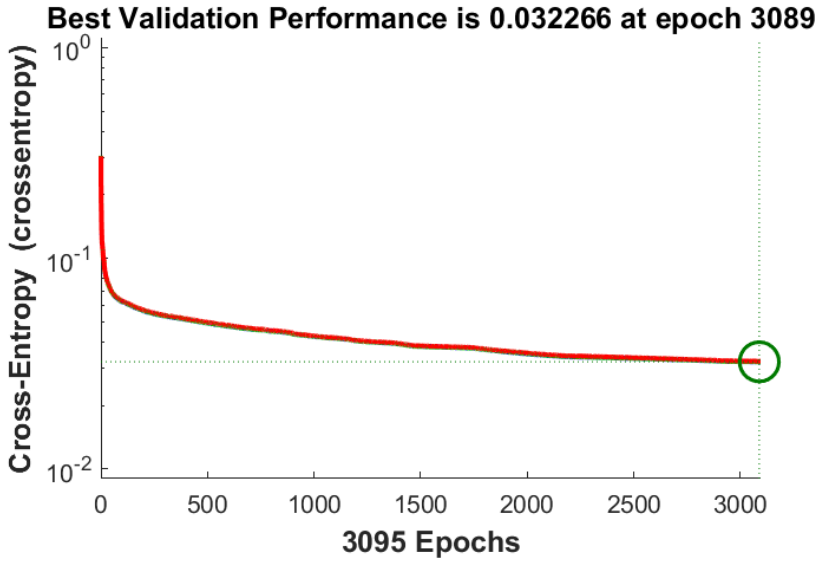

(b) Stress triaxiality estimator.

Figure B.4: The neural network performance over each iteration during the training stage.

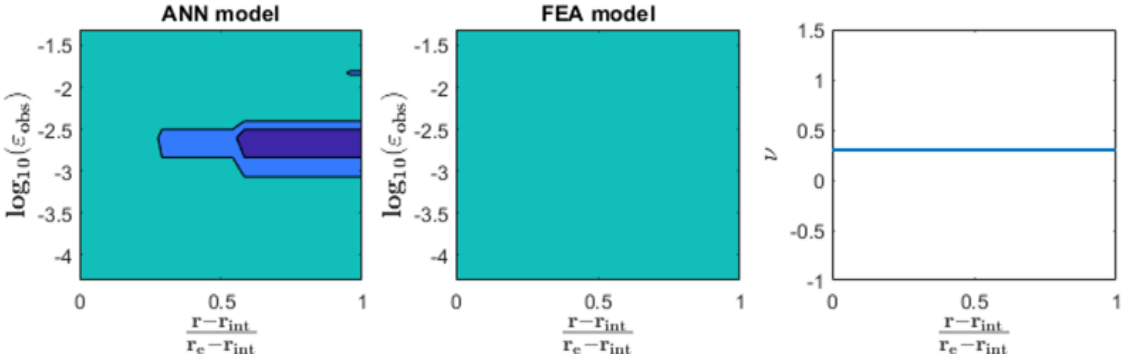

Figure B.5: An example of incorrectly labelled stress triaxiality values by the neural network.

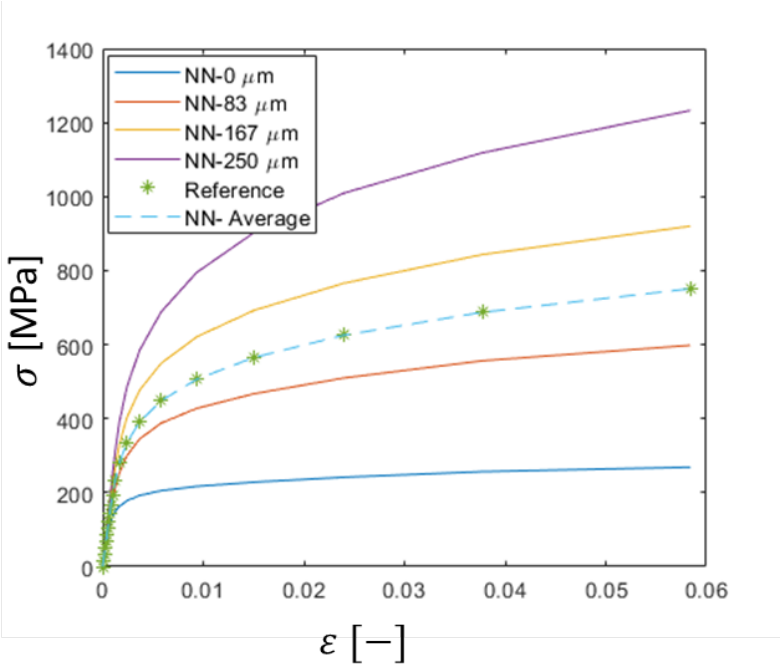

Figure B.6: The estimated distribution profile through the carburised layer using the trained linear distribution neural network model.

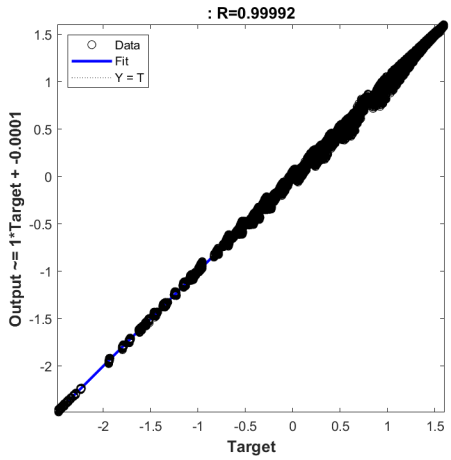

(a) The regression curve

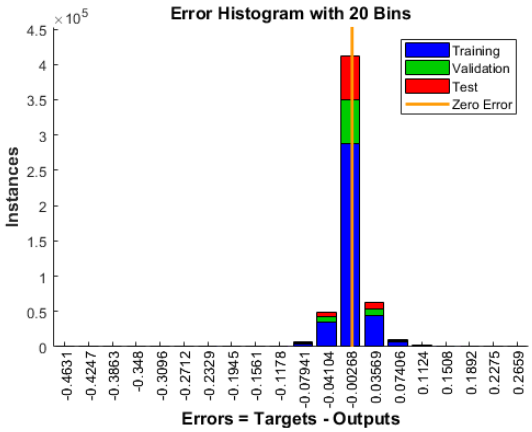

(b) The error histogram;

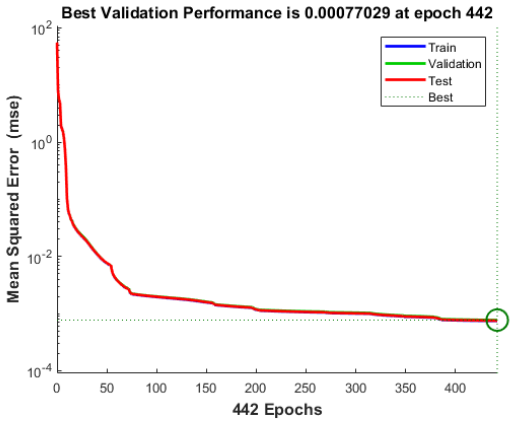

(c) Training performance with each iteration

Figure B.7: The training performance of the linear material property distribution neural network.

Appendix C

Supplementary material for Chapter 5

C.1 Normalised time to damage initiation

The following graphs time to damage initiation of carburised structure normalised to homogeneous structure assuming $\varepsilon_f = 2.6\%$ for the homogeneous model, where $t_f^{hom}(\omega^c(\varepsilon_f = 2.6\%)) = t_f^{hom} = 9.414 \times 10^6\,[hr]$ and $t_f^{hom}(\omega^{c*}(\varepsilon_f = 2.6\%)) = t_f^{hom*} = 6.0574 \times 10^6\,[hr]$. Figures in Figure C.1 represent the normalised failure times with respect to homogeneous model damage initiation according to Eqs. 5.2-5.3. For $t_f^N > 1$ or $t_f^{*N} > 1$ the structure will have longer creep lifetime compared to the homogeneous model.

Section 2.1.2 presents normalised time to creep damage initiation with respect to the homogeneous test case when homogeneous models reach creep ductility value of 2.6%. Table C.1 presents the same t_f^N and t_f^{N*} normalised with the homogeneous test case **assuming the same creep ductility value** as the carburised material:

$$t_f^{N'} = \frac{t_f(\varepsilon_f)}{t_f^{hom}(\varepsilon_f)} \tag{C.1}$$

$$t_f^{N'*} = \frac{t_f(\varepsilon_f)}{t_f^{hom}(\varepsilon_f)}. \tag{C.2}$$

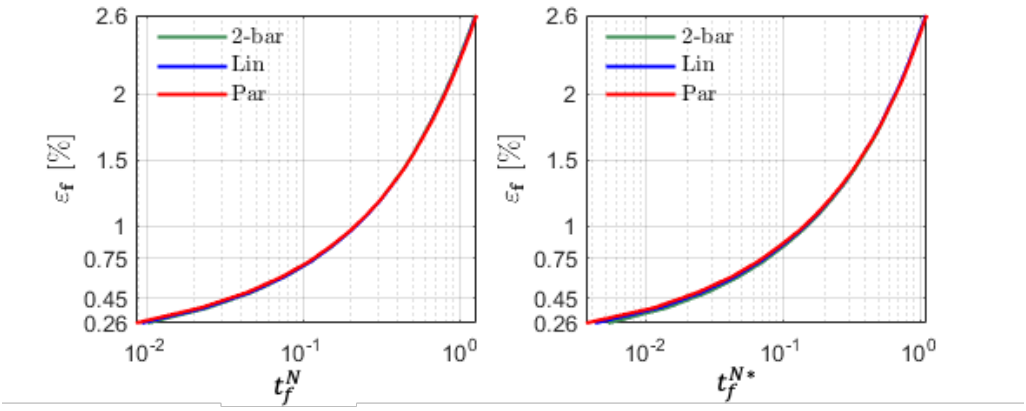

(a) The normalised plot of Figure 5.7

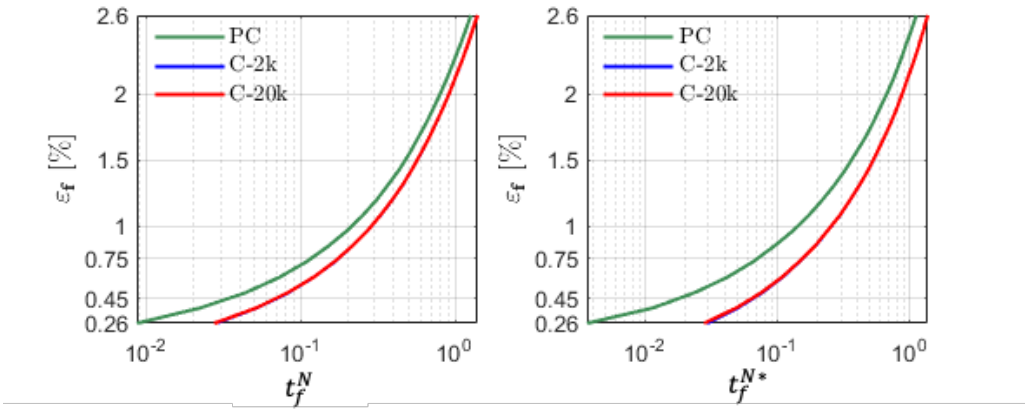

(b) The normalised plot of Figure 5.10

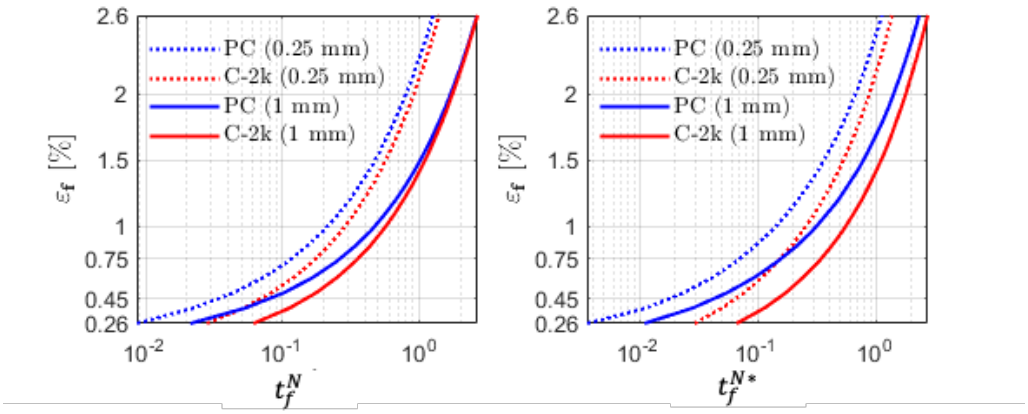

(c) The normalised plot of Figure 5.13

Figure C.1: Creep damage accumulation at the surface of the carburised layer normalised to homogeneous material (using ε_f = 2.6%).

Test case	ε_f = 2.6%		ε_f = 0.75%		ε_f = 0.45%	
	$t_f^{N'}$	$t_f^{N'*}$	$t_f^{N'}$	$t_f^{N'*}$	$t_f^{N'}$	$t_f^{N'*}$
PC 2-bar (0.25 mm)	1.24	1.11	1.05	0.79	0.87	0.60
PC Linear (0.25 mm)	1.26	1.10	1.04	0.75	0.84	0.54
PC Parabolic (0.25 mm)	1.26	1.12	1.02	0.81	0.81	0.50
C-2k (0.25 mm)	1.40	1.36	1.53	1.58	1.65	1.76
C-20k (0.25 mm)	1.40	1.36	1.53	1.57	1.64	1.73
PC Parabolic (1 mm)	2.66	2.31	2.31	1.61	1.91	1.18
C-2k Parabolic (1 mm)	3.03	2.98	3.72	4.09	4.32	4.92

Table C.1: The normalised failure time of all test cases according to Eqs. C.1–C.2.

C.2 Stress relaxation in pre-carburised bifurcation weld

Figure C.2 shows how different gradation of material properties could lead to different stress magnitudes in creep dwell. This is particularly important considering material cyclic response

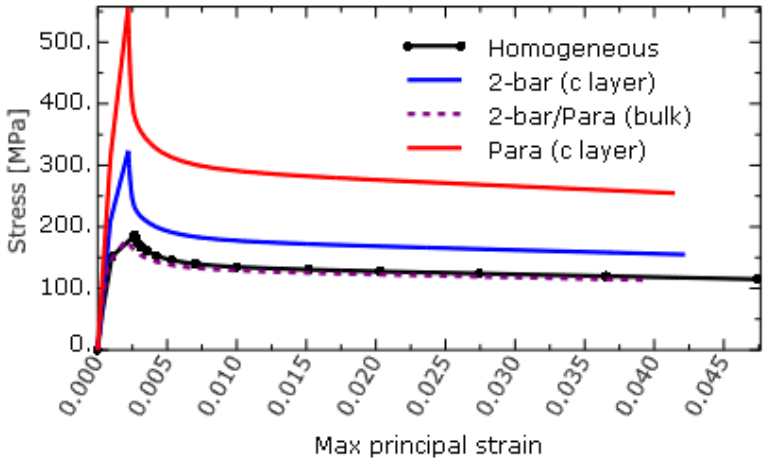

Figure C.2: Stress-strain curve of stress relaxation in the section sustaining the maximum damage (considering pre-carburised models only).